ALMA MATER STUDIORUM — UNIVERSITÀ DI BOLOGNA

DOTTORATO DI RICERCA IN SCIENZE CHIMICHE

— Ciclo XXV —

Settore Concorsuale di Afferenza: 03/B1

Settore Scientifico Disciplinare: CHIM/03

Luminescent Ionic Transition-Metal Complexes for Light-Emitting Electrochemical Cells

Presentata da: Filippo Monti

Coordinatore:
Prof. ssa Adriana Bigi

Relatore:
Prof. ssa Paola Ceroni

Correlatore:
Dott. Nicola Armaroli

Esame finale anno 2013

— Everything we know is only some kind of approximation
because we know that we don't know all the laws as yet.
Therefore ***things must be learned only to be unlearned again***
or more likely, corrected. The test of all knowledge is experiment.
Experiment is the sole judge of scientific "truth". —

Richard P. Feynman

Contents

Abstract

The European Union set the ambitious target of reducing energy consumption by 20 % within 2020. This goal demands a tremendous change in how we generate and consume energy and urgently calls for an aggressive policy on energy efficiency. Since 19 % of the European electrical energy is used for lighting, considerable savings can be achieved with the development of novel and more efficient lighting systems.

In this thesis, accomplished in the frame of the EU project CELLO, I report some selected goals we achieved attempting to develop highly efficient, flat, low cost and flexible light sources using Light-Emitting Electrochemical Cells (LECs), based on ionic cyclometalated iridium(III) complexes.

After an extensive introduction about LECs and solid-state lighting in general, I focus on the research we carried out on cyclometalated iridium(III) complexes displaying deep-blue emission, which has turned out to be a rather challenging task.

In order to demonstrate the wide versatility of this class of compounds, I also report a case in which some tailored iridium(III) complexes act as near-infrared (NIR) sources. In fact, standard NIR emitting devices are typically expensive and, also in this case, LECs could serve as low-cost alternatives in fields were NIR luminescence is crucial, such as telecommunications and bioimaging.

Since LECs are based on only one active material, in the last chapter I stress the importance of an integrated approach toward the right selection of suitable emitters not only from the photophysical, but also from the point of view of material science. An iridium(III) complex, once in the device, is interacting with ionic liquids, metal cathodes, electric fields, *etc.* All these interactions should be taken in to account if Europe really wants to implement more efficient lighting paradigms, generating light beyond research labs.

Introduction

In this introductory chapter I would like to briefly describe the contest and the people that helped me to carry out the research activities that I am going to report in the next chapters of this thesis. Writing this "description" I actually find out that this is also an implicit acknowledgment to all the people that worked next to me during these years. This is the reason why also a very careful reader will not find any acknowledgement section neither at the beginning nor at the end of this thesis.

The CELLO project

This thesis is based on some selected papers I published during my three-year period of investigation carried out at the National Research Council of Italy under the guidance of Dr. Nicola Armaroli. All these articles are the result of different collaborations between several european research units that worked together for the FP7 project "CELLO — Cost-efficient Lighting devices based on liquid processes and ionic Organometallic complexes" (STRP 248043).

The CELLO project started in January 2010 (when I begun my Ph. D.) and ended in December 2012. CELLO aimed to develop highly efficient, low cost and flexible light sources using the so-called "Light Emitting Electrochemical Cells"

(LECs) based on ionic iridium(III) complexes and that can be prepared from solution and operate at low voltages with electrodes that are stable in air.

The European Union recently set the ambitious target of reducing energy consumption by 20 % by the date of 2020. This goal demands a tremendous change in how we generate and consume energy and urgently calls for an aggressive policy on energy efficiency. Since 19 % of the European electrical energy is used for lighting, considerable savings can be achieved with the development of novel and more efficient lighting systems. The project CELLO is part of a strategic effort of Europe to maintain and consolidate its leadership in the area of lighting technologies.

As the reader can easily understand, such an ambitious target cannot be achieved without a deep collaboration between many research groups having very different scientific and technological abilities. In this context, together with Armaroli's group, I mainly contributed in the design of new highly-emissive ionic iridium(III) complexes, I was responsible for their photophysical characterization and I thoroughly investigated possible photophysical and/or photochemical pathways leading to electroluminescence quenching in LEC devices.

List of the reported papers

In this section I report all the selected publications that I insert in this thesis. They do not appear in chronological order but, for the sake of clarity, they follow a readapted rational. Since my contribution to the CELLO project essentially regarded the photophysical characterization of the iridium(III) complexes used as emitters in LECs, all the reported publications are the result of an intensive team working.

Chapter 1 — Getting started: LECs and ionic transition-metal complexes

This chapter is extracted from the review **"Luminescent Ionic Transition-Metal Complexes for Light-Emitting Electrochemical Cells"** we published on *Angewandte Chemie* in 2012 [DOI: 10.1002/anie.201201471].

As the title itself says, in this chapter I want to make an overview on the field of lighting and, in particular, on the most recent developments in the area of solid-state lighting. After a brief general introduction on the subject, we will focus our attention on LECs. It is thanks to Henk Bolink, the CELLO project

coordinator from the University of Valencia (Spain), if I could get familiar with this topics and to all the related chemical, physical and technological aspects.

In the following sections of that chapter, we will concentrate on iridium(III) emitting complexes only. I was able to write them thanks to the helpful discussions I had with Francesco Barigelletti (former CNR Research Director, now retired) and, later, with Rubén Costa (University of Valencia, than University of Erlangen-Nuremberg). It is also thanks to him that I discovered how Europe is now becoming closer and closer, and that a good friendship can grow up also from a fruitful scientific collaboration.

Chapter 2 — Blue phosphorescence: hard task

In this second chapter, after the general overview made in the previous one, we will actually see an example of contribution that the CELLO project gave to the scientific research in the field of blue-emitting LECs. In fact, the development of deep-blue stable iridium-based emitters has turned out to be a rather challenging task.

Thanks to Florian Kessler (EPFL, Lausanne) we synthesized several blue-emitting carbene-based iridium(III) complexes and we are hopefully going to publish a photophysical rationalization about their peculiar properties on *Inorganic Chemistry*. Such a deep understanding of their photophysical behavior was possible also by Professor Enrique Ortí, from the University of Valencia, Spain. I really want to thank him, not only for this particular contribution, but mainly because of this personal qualities, his kindness and willingness to help me in understanding and entering the DFT world; I really regret I did not have the opportunity to have him as professor during my master, here in Bologna.

Chapter 3 — Towards a bluer emission

This chapter reports only a part of the several achievements we made together with Nail Shavaleev (EPFL, Lausanne); this particular case refers to the article **"Bright Blue Phosphorescence from Cationic Bis-Cyclometalated Iridium(III) Isocyanide Complexes"** published on *Inorganic Chemistry* in 2012 [DOI: 10.1021/ic202297h].

Nail Shavaleev is a very determinate russian senior researcher that synthesized a plethora of iridium(III) complexes to test as active materials in LECs, with

a special regard to extremely high-energy-emitting luminophores. He helped me to understand that sometimes it is more important to stay focused on the final target instead of getting lost trying to rationalize everything... this is a concept that I still find pretty hard to understand!

Chapter 4 — From one extreme to the other

In this chapter we move our attention from blue-emitting iridium(III) complexes to another very demanding task, *i.e.*, the design and synthesis of near-infrared triplet emitters. We achieved this goal by attaching a donor-acceptor ancillary ligand on standard iridium(III) complexes, taking advantage of the heavy-atom effect.

The results have been recently published on *Inorganic Chemistry* in a paper titled **"Ligand-Based Charge-Transfer Luminescence in Ionic Cyclometalated Iridium(III) Complexes Bearing a Pyrene-Functionalized Bipyridine Ligand: A Joint Theoretical and Experimental Study"** [DOI: 10.1021/ic302026f]. This time I want to thank, apart from Enrique and Rubén, also Gabriel Schneider (University of Basel) for the synthesis ...and for the great tourist-dinner-trip we made altogether by tram in a very sunny Basel during a CELLO meeting.

Chapter 5 — Deeper in the device

In this last chapter I want to stress how important it is to carefully design iridium(III) ionic transition metal complexes for reaching high performances in LECs. It means that the emitting material should not be simply considered as a single molecule a diluted solution (or in a concentrated neat film), but also as an active component in a complex device, *i.e.*, interacting with ionic liquids, metal cathodes, strong electric fields *etc.*

For this work I have to thank Andrea Barbieri (CNR) and, once again, Enrique and Rubén. We summarized these results two years ago in an article published on *Inorganic Chemistry* titled **"Photophysical Properties of Charged Cyclometalated Ir(III) Complexes: A Joint Theoretical and Experimental Study"** [DOI: 10.1021/ic200820t].

Disclaimer

I don't know how many typos or errors will be present in the very last version of this thesis (and for that I apologize), but I'm sure I did not make any when I stated that «[anyone] ... will not find any acknowledgement **section** neither at the beginning nor at the end of this thesis». In fact, here there is only a very short acknowledgement **paragraph**:

Thanks to Nicola, Gianluca, and John because, sharing with me
their vision of science and culture, they changed my worldview.
Thanks to the most beautiful animal, my platypus,
because she changed my life.
Thanks to my family because, forging me,
they are giving to all of them a good starting material.

Bologna, 14 March 2013 Filippo Monti

Chapter 1

Getting started: LECs and ionic transition-metal complexes

Higher efficiency in the end-use of energy requires substantial progress in lighting concepts. All the technologies under development are based on solid-state electroluminescent materials and belong to the general area of solid-state lighting (SSL). The two main technologies that have been developed in SSL field are light-emitting diodes (LEDs) and organic light-emitting diodes (OLEDs), but in recent years, light-emitting electrochemical cells (LECs) have emerged as an alternative option. The luminescent materials in LECs are either luminescent polymers together with ionic salts or ionic species, such as ionic transition-metal complexes (iTMCs). Cyclometalated iridium(III) complexes are by far the most utilized class of iTMCs in LECs. In this general introduction, we show how these complexes can be prepared and discuss their unique electronic, photophysical, and photochemical properties. Finally, the progresses in the performance of iTMCs based LECs, in terms of turn-on time, stability, efficiency, and color are presented.

1.1 Lighting the World

The diffusion of artificial lighting is one of the greatest achievements of the past century, but even today, in many poor regions of the world, the rhythm of everyday life is beaten by the daily light-dark cycle: at sunset virtually all of human activities are stopped. For millennia artificial lighting was generated by

the open fire, which was eventually tamed through the use of lamps, as testified by archaeological findings all around the world. Until the second half of the 19th century, rural dwellings worldwide utilized fuels of animal or vegetal origin, such as whale oil or beeswax.

In 1879, taking advantage of the work of many other inventors and after having tested hundreds of different materials as filaments, Thomas Edison patented the incandescent carbon filament lamp, a milestone of modern lighting, whose diffusion took advantage of the almost concomitant spreading of electric grids. Edison's device converted just 0.2 % of electricity into light, but it was 20-times more efficient than a candle in converting its chemical energy into much more useful photons [1].

In the following decades, electric lighting devices underwent a substantial progress in terms of efficiency and all the systems that are still used nowadays were introduced: the tungsten lamp (1906), that dominated residential lighting for one century; the sodium vapor lamp (1930s), now utilized for street illumination in its modern high-pressure variant; the fluorescent tubes (1940s), very popular in large internal environments, such as offices and factories [2]. The evolutions of these three fundamental designs were introduced in relatively recent times: the halogen lamp, an advanced filament system, entered the market in the 1960s and the compact fluorescence lamp, a sort of hybrid between bulbs and fluorescent tubes, appeared in the 1980s. Initially, the latter was unenthusiastically received by consumers because of high price, long dimming times, and poor white quality, a set of issues now largely solved. Figure 1.1 on the facing page shows the historical trend of the efficiency of some lighting systems in converting electricity into visible electromagnetic radiation that can be sensed by the receptors of the human eye.

Nowadays, artificial lighting is an over 70 billion euro market worldwide. The lighting industry provides 150 000 jobs in Europe alone and produces items not only for stationary applications but also for the transportation sector, particularly automotive. The electricity consumption for lighting amounts to approximately 3 PWh, that is around 20 % of the world total, with an estimated CO_2 production of 2 Gt, about 7 % of the global emissions and equivalent to 70 % of the emissions produced by transportation [3, 4]. Thus, efficiency gains in this sector would significantly contribute to the energy transition that we must carry out in the present century [5, 6].

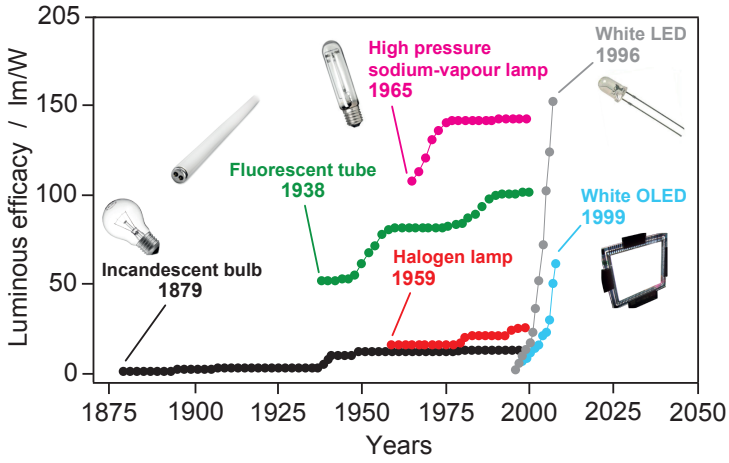

Figure 1.1: Historical trend of luminous efficacy of the most common light sources from 1880 to 2010.

Compared to two centuries ago, the per capita average availability of artificial photons for lighting in Europe has increased by about 12 000 times, with the price almost unchanged [4]. However, it has to be emphasized that about 1.5 billion people around the world still lack access to electricity and obtain illumination by burning fuels. It is estimated that about one million barrels of oil (1.2 % of production) is still burnt daily for lighting purposes [7]. This poses high safety and health risks through accidental fires and indoor air pollution [8].

The few data summarized above show that there is an urgent need for further improvements in lighting, so as to make it more widespread, sustainable, and affordable. The tremendous progress made during the 20$^{\text{th}}$ century in improving the quality and availability of artificial lighting was accomplished through the use of two main technologies: incandescent- and discharge-based lamps [4]. Incandescent lamps consist of a bulb containing a wire filament that emits light upon heating in a vacuum. They emit up to 95 % of the energy as infrared photons (*i.e.*, heat) hence their efficiency is intrinsically low. Discharge lamps generate light by means of an internal electrical discharge between electrodes that produces ultraviolet radiation, which is then down-converted into visible light by solid or gaseous compounds; they can be substantially more efficient than the incandescent counterpart but often at the expense of color quality. There is a variety of both type of lamps but these two traditional lighting concepts have been exploited near to their limit; thus, new lighting approaches have emerged

in the last two decades (see Figure 1.1) [9].

The emerging concept for illumination is solid-state lighting (SSL) [10], in which selected semiconductor materials are stimulated to produce visible light under the action of an electrical field (electroluminescence) in suitably engineered devices where the transport of charge occurs in one specific direction (diodes). Through this approach, the primary product of these lighting devices is the photon itself, unlike traditional sources where visible light is essentially a by-product of other processes, such as heating or discharging. As a result, SSL creates visible light with reduced heat generation or parasitic energy dissipation, while its solid-state nature provides for greater resistance, increasing significantly the lifespan of appliances.

There are two main families of SSL devices, namely light-emitting diodes (LEDs) [11] and organic light-emitting diodes (OLEDs) [12–14]. LED technology is based on inorganic semiconductors made from combination of several elements (*e.g.*, In, Ga, P, N) and provides highly efficient and convenient light point sources of different colors; LEDs are now standard for screen backlighting, automotive applications, traffic signaling, advertising, and decoration [10]. Notably, they are acquiring an increasing market share in ambient illumination thanks to the consolidation of white LED concepts [15].

OLEDs are flat light sources where the photon output is generated through electroluminescence within a multilayer stack with a thickness of few hundred nanometers [14, 16]. They are used extensively as displays in small handheld applications and in prototype TVs. The core of the device is the layer containing the luminescent material, typically a polymer, a small fluorescent molecule, or a phosphorescent transition-metal complex embedded in a charge transporting matrix [17]. State-of-the-art white OLEDs are based on multilayer stacks sometimes consisting of more than 15 individual layers [18]. Such a multilayer stack can only be prepared by vacuum sublimation that implies the use of thermally stable non-ionic materials. Therefore, the choice of suitable compounds within the huge family of luminescent transition-metal complexes, which are normally ionic species [19–22], is dramatically narrowed. The high manufacturing cost of OLEDs, associated with the multi-layer evaporation process and the need for rigorous encapsulation of the devices, are two of the main obstacles that have prevented significant penetration of this particular type of technology in the lighting market to date.

The above limitations of OLED technology have stimulated the exploitation of new concepts for flat electroluminescent lighting devices [23]; among these, LECs (light-emitting electrochemical cells) are the most popular [24–30]. LECs have a much simpler architecture than OLEDs, are processed from solution, do not rely on air-sensitive charge-injection layers or metals for electron injection and hence require less-stringent packaging procedures. LECs consist of an ionic luminescent material in an ionic environment sandwiched between two electrodes. The luminescent material is either a conjugated light-emitting polymer or an ionic transition-metal complex (iTMC). The first type is referred to as polymer-LECs (PLECs) [26, 30]. The second type is even simpler as it uses an ionic emitter that enables single-component devices; this type of LECs is referred to as iTMC-LECs [24, 27–29, 31–34]. This general introduction to the topic illustrates the fundamentals of LEC technology, focuses on the most promising luminescent materials for iTMC-LECs, particularly ionic iridium(III) complexes, and highlights the latest achievements and remaining challenges of iTMC-LECs in the frame of the rapidly developing area of lighting technologies.

1.2 Flat lighting devices

1.2.1 LECs: motivation and definition

State-of-the-art organic light-emitting diodes are typically made of multiple layers of organic materials, sandwiched in between an anode, typically a transparent oxide film, such as indium-tin oxide (ITO), and an air-unstable cathode (*e.g.*, Ca, Ba) often coupled with an electron-injection layer (see Figure 1.2, left). Such complex architectures are necessary to provide a balanced injection of positive and negative charges across the device, which must precisely recombine in the light-emitting layer, to grant the physical integrity of the whole device under the applied bias for hundreds of hours [14, 16]. Nowadays, OLEDs can be utilized for display and illumination but their manufacturing still needs costly and complex procedures in an inert environment that must be followed by a rigorous encapsulation of the final device, particularly because of the presence of low work-function metals or doped injection layers which are extremely sensitive to ambient oxygen and moisture [14, 16]. The multilayer structure, additionally, makes large-area processing extremely difficult, and ultimately imposes a

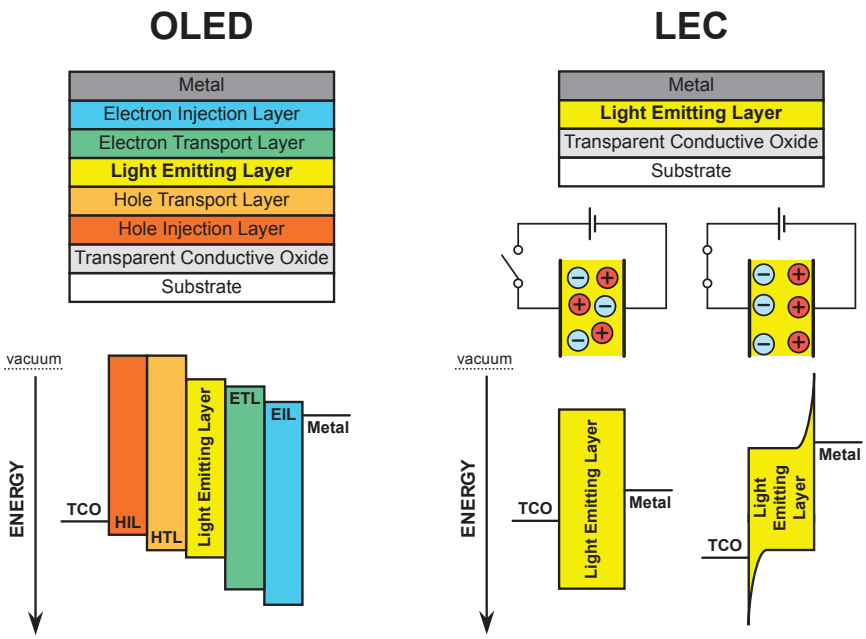

Figure 1.2: Schematic representations of a typical OLED (left) and LEC (right). An OLED consists of multiple layers that are in most cases deposited stepwise by thermal vacuum evaporation. The injection of electrons is achieved by the use of a low work function metal or a chemically n-doped electron injection layer, both of which are unstable in air and require rigorous encapsulation. In contrast, a LEC consists of only one opto-electronically active layer whose negative counterions are displaced when an external bias is applied. This set up enables an efficient hole and electron injection from air-stable metals.

production cost of OLEDs still incompatible with widespread applications in the general lighting market.

Light-emitting electrochemical cells (LECs) have a much simpler architecture, are processed from solution, and do not rely on air-sensitive charge-injection layers or metals for electron injection (see Figure 1.2, right). The concept of LEC was introduced in 1995 by Pei *et al.*, who mixed an inorganic salt to a mixture of a conjugated luminescent polymer and an ionic conductive polymer (see Figure 1.3, left) [26, 35]. Soon after this seminal contribution, an alternative approach was proposed by Maness *et al.*, who utilized a ruthenium(II) ionic transition-metal complex as the single active component in the light-emitting layer (**1**, Figure 1.3 on the next page) [27].

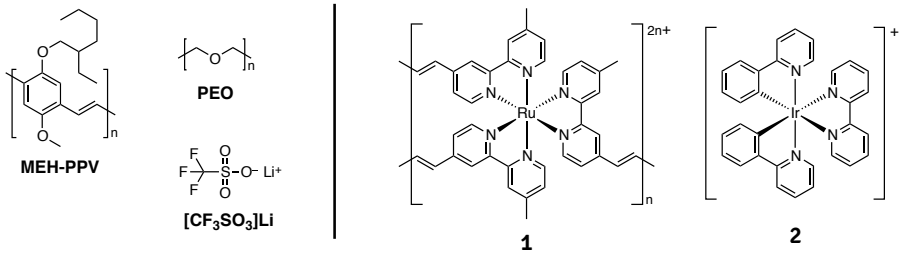

Figure 1.3: Materials used in the first polymer-based LECs: **MEH-PPV** = poly[5-(2'-ethylhexyloxy)-2-methoxy-1,4-phenylene vinylene], **PEO** = poly(ethylene oxide) and $Li[CF_3SO_3]$ = lithium trifluoromethanesulfonate. Compound **1** is the first iTMC used for LECs: poly-$[Ru(vbpy)_3]^{2n+}$, vbpy = 4-vinyl-4'-methyl-2,2'-bypiridine. Compound **2** is the archetypal complex of the largest class of Ir(III)-iTMCs used in LECs: $[Ir(ppy)_2(bpy)]^+$ in which **ppy** is 2-phenylpyridinate and **bpy** is 2,2'-bipyridine.

In this approach, the ruthenium(II) complex and its counterion $[PF_6]^-$ play several key roles: promotion of charge injection from the electrodes, electron and hole transport through the device and, thanks to the intrinsic orange emission, luminescence. Nowadays, iTMC-LECs are mostly based on luminescent ionic bis-cyclometalated iridium(III) complexes [36] (the archetypal complex of this large family of complexes is **2**, reported in Figure 1.3) [37], which, like the original ruthenium(II) complex, may sustain charge injection and transport while affording, at the same time, light emission. A crucial benefit in the use of ionic compounds is processability: iTMCs dissolve in polar benign solvents, allowing the devices to be prepared by facile coating or printing processes. In addition, the use of iTMCs allows novel device fabrication processes, such as soft-contact lamination [38], as well as the development of large-area illumination panels [39, 40] that do not require any patterning. Finally, the insensitivity of LEC devices to the work function of the electrode material allows air-stable metals to be used as anode and cathodes, greatly decreasing the severe technical requirements for the encapsulation of devices. Taken in concert, these characteristics facilitate large-area processing and might give entry to flat electroluminescent devices at more affordable costs.

1.2.2 LECs: mechanism of work

LEC active materials can be either conjugated light-emitting polymers or ionic transition-metal complexes, the related devices are termed polymer-LECs (PLECs) [26, 30] or iTMC-LECs [27–29, 31–34], respectively. Both types of LECs have been studied for over 15 years [26, 27], throughout which many materials, device concepts, and driving schemes have been tested. This research has led to notable achievements in color, efficiency, turn-on time, and stability, which will be commented in detail in the next sections. Now we describe the peculiar operational mechanism of LECs, which has been generally described by two rationales, the **electrodynamical (ED)** [41–43] and the **electrochemical doping (ECD)** [26, 35, 44] models (see Figure 1.4). Both models agree in that the injection barrier for electrons and holes is reduced by the separation of the ions in the light-emitting layer upon application of a bias.

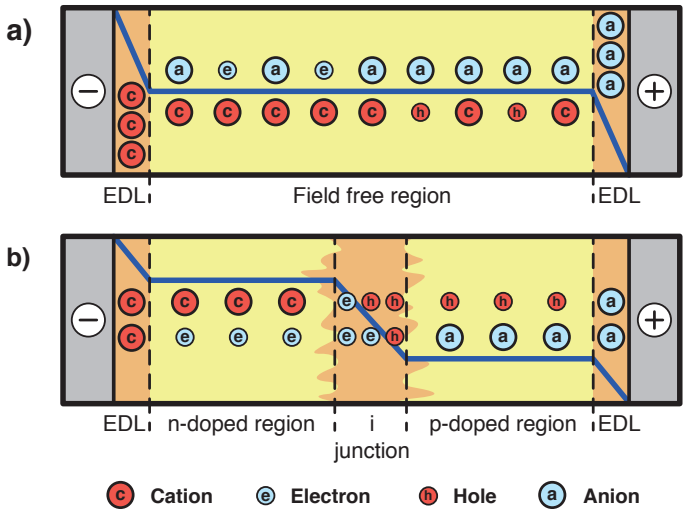

Figure 1.4: Illustration of the potential profile as well as the electronic and ionic charge distribution in a LEC during steady-state operation. Potential profiles and charge distributions as predicted by the a) ED and the b) ECD models. The thick blue line represents the potential profile; the electronic and ionic charge carriers are illustrated by the cyan (negatively charged) and red (positively charged) symbols, respectively. Furthermore, the high- and low-field regions in the bulk are highlighted in orange and yellow, respectively. In the low-field regions, negative and positive centers are mutually compensated.

The ED model assumes that the accumulation of ions leads to the formation of electric double layers (EDLs) at the electrodes which brings about a sharp drop of the electric potential near the electrode interfaces and promotes charge injection from the electrodes. In the bulk of the material the anions and cations are still joined and light emission occurs from the so-called field-free region in the bulk of the device.

The ECD model assumes, on the other hand, that the accumulation of ions at the anode and cathode leads to the formation of highly conductive p- and n-doped regions, respectively (see Figure 1.4, n-doping: negative doping, *i.e.*, addition of an electron; p-doping: positive doping, *i.e.*, removal of an electron). The doped regions widen over time, until a p-i-n junction (i = intrinsic, undoped) between them is formed. Across the intrinsic region formed, the applied potential drops substantially and favors charge recombination and light emission.

Several papers describing modeling studies that support one or both of these models have appeared [41, 42, 44–48]. Both models are corroborated by experimental data that, in most cases, were obtained from PLECs; they are going to be described below.

The best performances of LECs are obtained when the active material is sandwiched in between two electrodes, that is, one electrode is below and one electrode is on top of the active layer. In these sandwiched devices the active layer has a thickness in between 100 and 200 nm. Although this layout leads to best performances, the active layer is thin and inaccessible and therefore it cannot be used to directly probe its potential profile. This can be done, however, by using another configuration in which the anode and cathode are placed side by side at a given distance (*i.e.*, interdigitated) on a non-conductive substrate with the active layer on top of them (alternatively the active layer can be deposited on the bare substrate and then both contacts deposited on top). In this configuration, referred to as a "planar" configuration, the active material can be accessed by scanning probes (*e.g.*, Kelvin probe) as there is nothing on top of it. To get meaningful information, the electrode spacing in the planar configuration must be at least one order of magnitude larger than in the sandwiched configuration (several micrometers). The performances in the planar configuration are much worse when compared with the sandwiched layout, primarily because of the very

small light-generating areas on the total substrate, resulting in a small aperture of these devices. Also some care must be taken when the observations obtained from planar cells are used to explain operations in sandwiched devices, as the electrode spacing is quite different.

An example of a planar device using interdigitated electrodes, where the emission zone was probed with a microscope, is shown in Figure 1.5 on the next page, left side. It was revealed that, at moderate operation voltage, light emission is concentrated within a narrow zone (1 – 3 μm) of the larger interelectrode gap (15 μm), which was taken as evidence for the creation of a p-i-n junction (see Figure 1.5, left). The planar device also allowed monitoring the photoluminescence as a function of interelectrode distance and time, under UV illumination. This information is of interest as the conjugated materials employed as the active materials in LECs are fluorescent or phosphorescent with reasonably high efficiencies, and it is known that the photoluminescence is quenched when the material is electrochemically doped. Accordingly, the absence of photoluminescence in certain areas can be indicative of the formation of doped regions. Hence, when the photoluminescence is monitored versus time it is possible to identify the formation of doped zones in planar LECs. Under this condition, doped regions resulted to be dark, as monitored by photographs or videos (see Figure 1.5, right) [49–52].

It is possible to directly measure the electrostatic potential from planar LECs by using Kelvin probe techniques, which is particularly useful as the two proposed models require very distinct potential profiles [53]. Slinker *et al.* measured the electrostatic potential of planar iTMC-LECs, which were fabricated by carefully avoiding having active material on top of the electrodes using serial soft lithography [54]. The profile obtained showed strong potential drops at the electrode interface, without sharp drops at the center of the device (see Figure 1.6, left), providing support for the ED model. Shortly after, a similar experiment was performed on a planar PLEC by Matyba *et al.*, who obtained a profile showing a distinct drop in the center of the device in line with the prediction of the ECD model (see Figure 1.6, right) [55]. The latter observation was confirmed by recent studies performing simultaneous emission and Kelvin probe studies on the same device [56].

The above data show evidences supporting both models, which sparked debate and increased the uncertainty concerning the actual operational mechanism

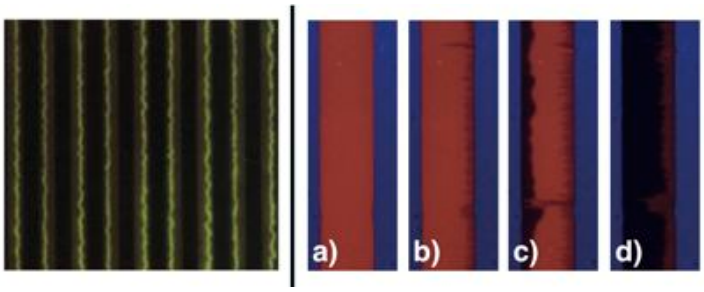

Figure 1.5: Left: Photograph of a planar PLEC with interdigitated gold electrodes (dark lines); spacing between electrodes is 15 µm. With 4 V applied across each pair of electrodes, the yellow-green emission is observed from the dynamically formed p-n junction; the width of the junction is about 1 – 3 µm. Right: Selected photographs of the doping progression in a planar Al / MEHPPV + PEO + CF_3SO_3Li / Al LEC with a 1 mm interelectrode gap with the interdigitated Al electrodes on top of the polymer blend. The Al electrode to the left is the positive anode, and the device was operated at 360 K and 5 V. The photographs were taken at 0 s (a), 546 s (b), 978 s (c), and 2750 s (d) after the voltage was applied.

in planar devices. Recent findings by van Reenen *et al.* shed new light on the matter [51]. They obtained two different potential profiles using good (Al-capped Au; see Figure 1.7, left) and poorly injecting contacts (slightly oxidized Al; see Figure 1.7, right). With the Al-capped Au non-injection limited contacts, the profile is in accordance with the ECD model, because a dramatic potential drop is observed in an intermediate region between the two electrodes, where electroluminescence is generated. Additionally, small potential drops are observed at the electrode interface, attributable to the formation of the electric double layers. The potential profile of the planar PLEC with oxidized Al contacts is very different. In that case, the potential drastically drops only at the electrode interfaces with no relevant changes across the bulk of the device, as predicted by the ED model. Therefore, depending on the type of contacts, the potential profile of LECs can be rationalized with either the ECD or the ED model.

Tests described so far try to elucidate the mechanism of LECs functioning in planar devices. However, LECs are typically sandwich-type, which differ substantially in the distance between electrodes (around 0.2 µm) compared to their planar counterparts (8 µm to 120 µm) and are characterized by a much higher luminance. Hence, it is of great interest to elucidate the specific operation mech-

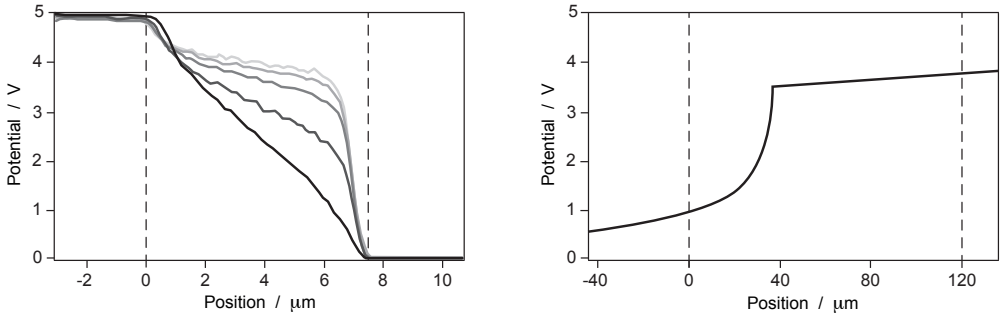

Figure 1.6: Left: Time dependence of the in situ potential profiles of planar iTMC-LECs for Au / $[Ru(bpy)_3][PF_6]_2$ / Au devices under 5 V operation, in which the $[Ru(bpy)_3][PF_6]_2$ layer has been patterned to be restricted between the electrodes; first scan is black, the following ones are lines with increasingly lighter gray (the curves are spaced by equal increments of 15 min in time). The inter-electrode region is between the dashed lines. Right: Steady-state potential profile of a planar PLEC during operating at 5 V using Au electrodes.

anism of sandwiched LECs. First attempts were made using impedance spectroscopy, a technique that applies a small AC perturbation on a DC voltage to get information on the resistance and capacitance of the active material, and supported the ECD model [57, 58]. In fact, the standard tools for studying conventional light-emitting devices, which entail the measurement of luminance (L) and current density (J) as a function of voltage (V), JL–V measurements, are difficult to use in LECs because the application of a voltage triggers the movement of ionic charges and physically modifies the device itself. Therefore, to obtain reliable operative parameters of a LEC for a given ionic distribution, it is crucial to avoid ionic movement during the JL–V scans [59–62]. These experiments have shown that JL–V measurements of fresh LECs are featureless, whereas after poling and fixing of the ions they resemble those of standard OLEDs. A thorough investigation of how LECs evolve from the initial state to the highly luminescent state was recently reported using JL–V analysis on dynamic LECs. In an attempt to perform JL–V analysis on dynamic LECs as well, a method was developed that applies a fixed voltage and monitors the current density and luminescence over time, while performing rapid JL–V scans at set intervals. Even in this case it is crucial that there is no ionic movement during the JL–V scans, as the electronic characteristics of the device for a given ionic distribution are needed. This was achieved for a sandwiched iTMC-LEC with a scan rate of 2.5 V s^{-1} and volt-

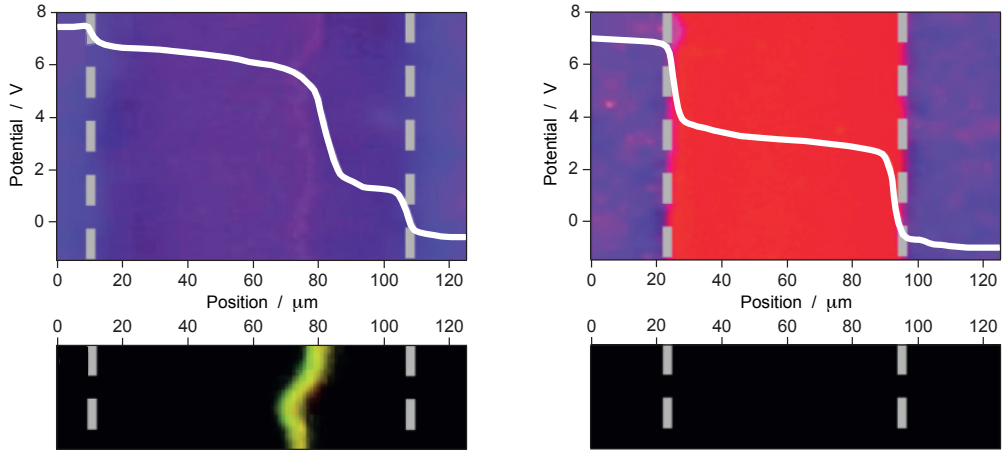

Figure 1.7: Steady-state potential profiles of a planar PLEC during operation at 8 V. Left: non-injection limited regime (using Al-capped Au electrodes). Right: injection-limited regime (using slightly oxidized Al electrodes). The panels below each potential profile are steady-state photoluminescence images of the devices. The white dashed lines in all micrographs indicate the electrode interfaces.

age never below 2 V [63]. By this method it was shown that, at the start of the operation, the current density is limited by the injection barriers for holes and electrons. With prolonged biasing the injection barriers decrease and the current density becomes limited by the transport through the active material, this is referred to as "bulk-limited" condition. In bulk-limited OLEDs, the double carrier current density is space-charge limited and can be described using the underlying equation:

$$J = \alpha \frac{V^2}{x_n^2} \tag{1.1}$$

where x_n is the effective layer thickness and α is a prefactor depending on the dielectric constant, electron and hole mobility, and bimolecular recombination rate [64].

In Figure 1.8 on the following page, the current density versus the effective applied voltage at different operation times is depicted [65]. At driving times of 85 min and beyond, the current follows the typical quadratic dependence on voltage, indicating that it is space-charge limited. According to equation 1.1, the one order of magnitude increase of device current (observed at 3.5 V driving voltage for over 85 min) is due to a decrease of the effective layer thickness by approxi-

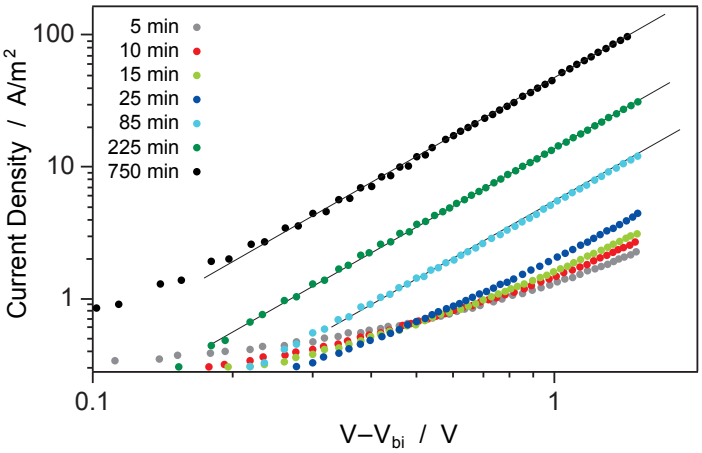

Figure 1.8: Current density (J) versus effective applied voltage ($V_{eff} = V–V_{bi}$, where V_{bi} is taken as the point where the current deviates from an exponential dependence) at different times during constant voltage (3.5 V) operation of a sandwiched LEC based on complex **2**. The parallel black lines indicate the quadratic dependence.

mately a factor of two. The physical layer thickness of the active material did not change, thus the increase of J after the device had been operating for 85 min was attributed to the continued growth of the n- and p-doped regions adjacent to the electrodes, that reduces the thickness of the undoped (intrinsic, i) light-emitting layer. Additionally, it implies that the charge transport in the intrinsic region is rather similar to OLEDs and governed by space-charge. In the same work it was also shown that, for a driving voltage of 1.5 V, current transients are in line with the predictions of the ED model [63].

The above observation corroborates the results obtained by van Reenen *et al.* on planar PLEC-based devices, who demonstrated that the electrostatic potential can be in accordance with both the ECD and the ED model, depending on the specific type of contact employed (see above) [51]. Therefore, it appears that the situation described by the ED model occurs when there is only a limited electron injection into the organic film. On the other hand, when substantial electron injection occurs, the formation of doped zones takes place. The speed of the formation of the EDLs and the widening of the doped zones is directly related to the ionic motion and is in general much faster in PLECs than in iTMC-LECs. Initially, the active layer of a LEC device is neutral since charges are randomly distributed.

Upon application of a voltage above the band gap of the emitting material, the electric double layers are formed next to both electrodes, whereas the p- and n-doped regions (see Figure 1.4 on page 8, bottom part) start to grow at the expense of the neutral undoped emitting layer (see Figure 1.5 on page 11, right part). In the specific case of iTMC-based LECs, light emission occurs by phosphorescence originating from long-living triplet excitons. Since they are quenched [66] by electrochemical doping (see above) and the p- and n-doped regions adjacent to the neutral emitting layer continue to grow, the LEC luminance will inexorably decrease over time. Hence, the time-dependent decline of LEC luminance can be caused not only by chemical degradation of the emitting material in the operating device, but also by the increasing amount of excitons being quenched, as the neutral emitting layer thickness is reduced [67]. Accordingly, switching a device off for several minutes once the maximum luminance level is reached and then re-applying the same voltage, leads to full restoration of light emission [63]. The correlation between the formation of EDLs and the expansion of the doped zones is probably the reason why a relation between the turn-on time and the lifetime is often found in iTMC-LECs (see below).

1.3 Ionic transition-metal complexes for LECs: the rise of iridium

In this chapter we focus our attention on iTMC-LECs and, for recent advances on PLECs, the reader can refer to a review by Sun *et al.* [30] and, for doped conjugated polymers, to a review by Inganäs [68]. iTMC-LECs differ from PLECs in that the iTMCs are intrinsically ionic and do not need auxiliary charged species to drive the device. Additionally, iTMCs are typically phosphorescent triplet emitters, which allows for higher electroluminescence efficiencies compared to singlet emitters [69]. iTMCs also allow for easy solubilization in benign solvents and environmentally friendly wet device-preparation processes [70].

Early works on iTMC-LECs focused on differently substituted ruthenium(II) complexes, such as the archetype $[Ru(bpy)_3][PF_6]_2$ (**3**, in Figure 1.9); these devices achieved external quantum efficiencies up to 5.5 % [71, 72]. However, LECs based on ruthenium chromophores offer limited color tuning because the emission band is placed across the orange-red part of the visible spectrum and this

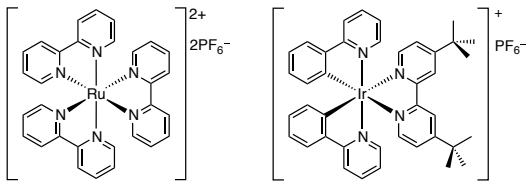

3 **4**

Figure 1.9: Structural formula of two examples of iTMCs used in LECs: $[Ru(bpy)_3][PF_6]_2$ (**3**) and $[Ir(ppy)_2(dtb\text{-}bpy)][PF_6]$ (**4**).

restriction strongly limits the applicative potential for lighting and display technologies, which require wider color tunability.

Using luminescent iTMCs based on different metal centers opened the route to the whole color scale [20] and, in this regard, the by far most versatile family of iTMCs is that of iridium(III) (Ir-iTMCs) [73]. These compounds, thanks to a unique combination of physical and chemical properties, provide a huge variety of stable complexes, covering the whole visible spectrum all the way from blue to red [36]. In particular, changing the metal center from a second-row (*e.g.*, Ru) to a third-row (*e.g.*, Ir) transition element, the stability of the related complexes is generally improved by (i) increasing the metal-ligand bond strength and (ii) by raising the ligand-field splitting energy (LFSE) and making dissociative metal-centered (MC) excited states less thermally accessible compared to Ru(II) analogues [74]. LFSE is further increased, relative to Ru(II) complexes, thanks to the higher electric charge of the iridium ion and by the presence of anionic cyclometalating ligands, typically used with Ir(III) centers. All these combined features of Ir-iTMCs can lead to very high emission quantum efficiencies of virtually any color and impart good photochemical stability [29, 36, 73, 75].

The first example of a LEC based on an ionic iridium(III) transition-metal complex was reported by Slinker *et al.* in 2004 [76]. It was a single-layer device emitting yellow light and based on **4** (reported in Figure 1.9), a complex that exhibits a photoluminescence quantum yield (PLQY) in oxygen-free acetonitrile solution of 23.5 %.

1.3.1 Synthesis of cationic iridium(III) cyclometalated complexes for LECs

Most Ir-iTMCs are synthesized in two steps according to the strategy depicted in Figure 1.10. First, commercially available $IrCl_3 \cdot nH_2O$ reacts with a slight excess of the desired cyclometalating ligand (CN), the most popular of which are 2-phenylpyridines or 1-phenylpyrazoles (see Figure 1.11 on the next page). The reaction is usually carried out in 2-ethoxyethanol at around 120 °C under argon atmosphere for 24 h [77, 78]. The product of this reaction is the cyclometalated Ir(III) μ-dichloro-bridged dimer $[(CN)_2Ir(\mu\text{-}Cl)_2]$ (**5**). In iridium dimer complexes such as **5**, the Ir–C / Ir–C' bonds are stereochemically *cis* to each other, whereas the Ir–N / Ir–N' are mutually in *trans* position [73, 79]. Tris-cyclometalated iridium(III) complexes are minor byproducts that can be easily separated from the main dichloro-bridged dimer [80].

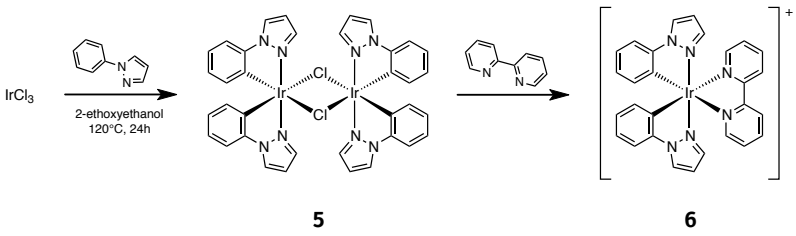

Figure 1.10: Typical two-step synthesis of a heteroleptic bis-cyclometalated iridium(III) complex. The μ-dichloro-bridged dimer (**5**) is isolated and subsequently cleaved using neutral ancillary ligands to obtain the corresponding mononuclear iridium(III) complex.

The $[(CN)_2Ir(\mu\text{-}Cl)_2]$ dimers undergo facile reactions with a variety of monodentate and bidentate neutral imine-type chelating ligands (see Figure 1.12 on page 19) to yield a plethora of different cationic mononuclear complexes (*e.g.*,**6** in Figure 1.10) in high yields as chloride salts [81, 82]. Subsequently, these can undergo an ion exchange reactions with less-coordinative and less-reactive anions (*e.g.*, the $[PF_6]^-$ or $[BF_4]^-$ anions) to improve the performance of the complex under the electric field in operating devices (see Section 1.4).

When the direct addition of the neutral ligands to the dimer affords low yields, an alternative synthetic route can be utilized, carrying out removal of

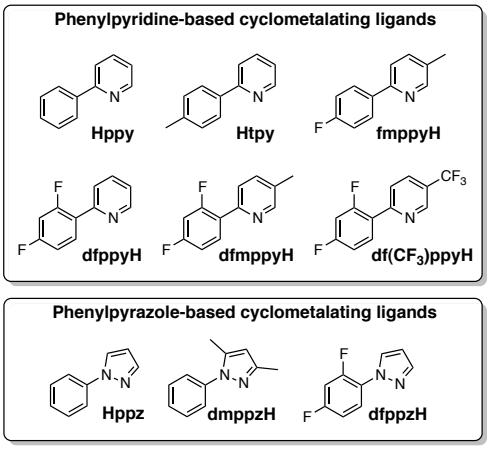

Figure 1.11: Some examples of cyclometalating ligands commonly used in the synthesis of Ir-iTMCs.

chlorides by treating the μ-dichloro-bridged dimer with silver triflate or other silver-based chloride-abstracting agents [83]. The chloride-free intermediate, for example, $[(CN)_2Ir(H_2O)_2][CF_3SO_3]$, can then be treated with the desired neutral ligand under mild reaction conditions [84]. It is even possible to avoid this two-step procedure by directly treating the $[(CN)_2Ir(\mu\text{-}Cl)_2]$ dimer with a stoichiometric amount of neutral ligands in the presence of Ag_2O, to promote the removal of chloride during the reaction [85].

1.3.2 Photophysics of cationic Ir-iTMCs

The wide availability of robust cationic iridium(III) complexes with tunable luminescence was the fundamental prerequisite for the development of studies on LECs. In this thesis, we focus primarily on Ir-iTMCs that have been utilized in LECs, as well as on related complexes that allow the comparison and rationalization of physical properties. Of course, they are only a fraction of the innumerable ionic iridium(III) complexes that have been synthesized in the last decade [29, 36, 73, 75]! In this section, the basic electronic and photophysical properties of Ir-iTMCs will be described, focusing on the main strategies to design a complex with the desired emission color.

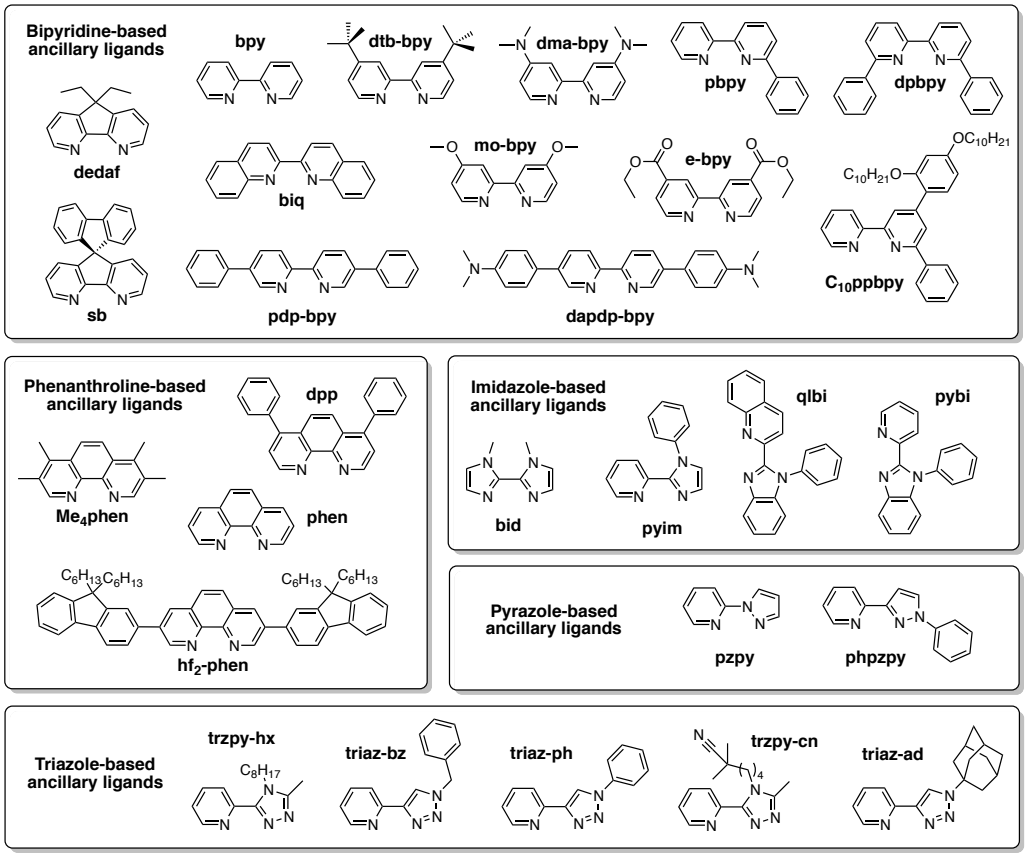

Figure 1.12: Some of the most widely utilized neutral ancillary ligands used in Ir-iTMCs. The reported labels are arbitrary chosen accordingly to the main text.

The iridium(III) metal center in octahedral coordination

Iridium(III) is a $5d^6$ metal center and its d orbitals are split by the interaction with the octahedral ligand field into three stabilized t_{2g} (d_{xy}, d_{xz}, d_{yz}) and two destabilized e_g orbitals (d_{z^2} and $d_{x^2-y^2}$), see Figure 1.13 on the following page (part a). The energy difference between these two levels (Δ_o) depends on:

1. the oxidation state of the metal center: the higher the oxidation state, the higher the Δ_o splitting;

2. the size of the d orbitals: Δ_o is smallest for 3d metals and progressively increases with 4d and 5d metals;

3. the field strength exerted by the ligands (*i.e.*, the spectrochemical series).

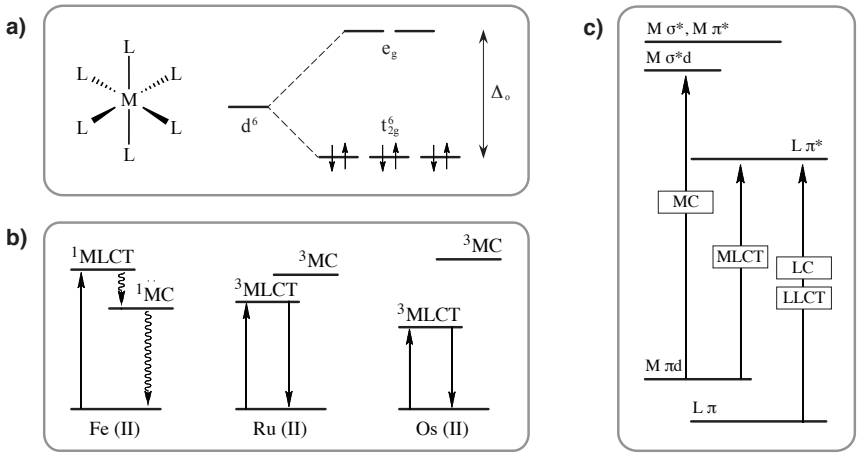

Figure 1.13: a) Low-spin d^6 orbital configuration in octahedral field. b) Qualitative electronic excited states description for Fe(II), Ru(II), and Os(II) metal complexes. c) Electronic energy-level diagram for a generic Ir-iTMC. MC is metal-centered, LC is ligand-centered, LLCT and MLCT are ligand-to-ligand and metal-to-ligand charge transfer, respectively.

Ir-iTMCs exhibit a high Δ_o splitting because of the presence of a highly charged ion belonging to the third row of the d-block of the periodic table, bound to very strong-field ligands (*i.e.*, the anionic cyclometalating ligands). As a result, the electronic configuration of the metal center is always in a low-spin state ($t_{2g}^6 e_g^0$, see Figure 1.13, a) and the ligand-field stabilization energy is maximized, which means that iridium(III) complexes are generally stable and rather inert toward substitution. Accordingly, the configuration of the metal orbitals is closed-shell (A_{1g}) and, since the ligand orbitals are fully occupied, the ground-state of the complexes is a singlet (S_0).

Other transition-metal ions have the same d^6 low-spin configuration of Ir(III) (*e.g.*, Os(II), Ru(II) and, in the presence of particular ligands, even Fe(II)), however their complexes do not exhibit such remarkable photophysical properties because the scenario in the excited states is very different (see Figure 1.13, b). The reasons are as follows:

Fe(II), 3 d^6 configuration: the Δ_o splitting is very small, hence the lowest-lying excited state is ^{1}MC in nature (*i.e.*, centered on e_g metal orbitals) and, therefore, not emissive [74].

Ru(II), 4 d^6 configuration: the Δ_o splitting is increased and the lowest (emissive) excited state is a metal-to-ligand charge transfer triplet (^{3}MLCT, relatively close to ^{3}MC states that can be thermally populated and open a competitive radiationless deactivation pathway to either the ground state or to degradation products; accordingly, the PLQY of Ru(II) complexes increase substantially with decreasing temperature [86].

Os(II), 5 d^6 configuration: the Δ_o splitting is considerable and the ^{3}MC states are usually too high to affect emission properties, but the emissive ^{3}MLCT excited state has lower energy compared to Ru(II) analogues (emission bands typically peaking in the red/infrared region) and this favors radiationless pathways due to the "energy gap law" [87]; accordingly, PLQYs of these complexes are typically low, *i.e.*, below 1 – 2 % [88, 89].

Spectroscopic properties of Ir-iTMCs

Since UV or visible light absorption is mostly associated with spin-allowed electronic transitions from the ground state, which is of singlet nature in the case of Ir-iTMCs, the strongest absorption bands in iridium(III) complexes are ascribable to singlet ligand-centered (^{1}LC), metal-to-ligand (^{1}MLCT), and ligand-to-ligand (^{1}LLCT) charge-transfer transitions.

The absorption spectrum of the archetypal Ir-iTMC complex **2** is depicted in Figure 1.14 as an example. The UV region is dominated by intense spin-allowed $^1\pi$-π^* (^{1}LC) transitions involving the organic ligands. At longer wavelength (350 – 450 nm), less-intense ^{1}MLCT and ^{1}LLCT bands are present: the ^{1}LLCT transitions correspond to electron promotions from the phenyl groups of the cyclometalating ligands to the ancillary ligand (*e.g.*, 2,2'-bipyridine, in **2**). Additionally, the weak and long tails observed above 450 nm are due to direct spin-forbidden population of the triplet excited states (*e.g.*, both charge-transfer ^{3}MLCT and ^{3}LLCT states, and the ^{3}LC transitions), enabled by the high spin-orbit coupling of the iridium metal core (spin-orbit coupling constant $\zeta = 3909\ \mathrm{cm}^{-1}$) [90] that allows the mixing of triplet states with the higher-lying ^{1}MLCT levels. All these transition are schematically summarized in Figure 1.13 on the preceding page, c.

The high spin-orbit coupling of Ir(III) yields almost unitary intersystem crossing efficiency from singlet to triplet excited states, therefore iridium(III) complexes always exhibit efficient spin-forbidden phosphorescence emissions. The

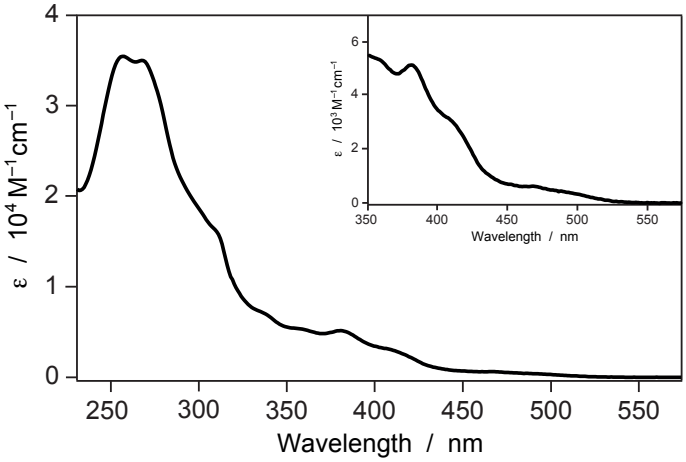

Figure 1.14: Electronic absorption spectrum of $[Ir(ppy)_2(bpy)][PF_6]$ (**2**) in CH_2Cl_2; MLCT transitions are expanded in the inset.

emitting state is the lowest-energy triplet (T_1) which, in the most common cases, arises from "mixed" triplet levels, due to the contributions of ^{3}MLCT, ^{3}LC, and sometimes also ^{3}LLCT states (see Figure 1.13 on page 20, c) [73]. Depending on the extent of contribution of the charge-transfer (CT) states, the emission profile is substantially affected: the presence of vibrational features suggests a low CT character, whereas broader and less structured shapes are indicative of a high charge-transfer character.

As an example, in Figure 1.15 on the next page the room-temperature photoluminescence spectra of **2** and of $[Ir(ppy)_2(pzpy)][PF_6]$ (**7**, in Figure 1.19 on page 33) are depicted. These two complexes have the same **ppy** cyclometalating ligand, but different ancillary (NN) ligands. On passing from **bpy** to **pzpy** (see Figure 1.15 on the next page) an hypsochromic shift of about 100 nm is observed, which is due to the change of the nature of the T_1 state from a more ^{3}MLCT/^{3}LLCT transition (**2**) to a more vibronically structured ^{3}LC one (**7**). The use of the electron-rich pyrazole ring pushes up the LUMO of the ancillary (NN) ligand and this orbital becomes closer in energy to the LUMOs of the cyclometalating (CN) ligands. As a consequence, the electronic π-π^* excitation of the **ppy** ligands emerges as competitive in energy and the T_1 state increases its ^{3}LC character.

Further evidence of the predominant ligand-centered character of the T_1 excited state could be derived by evaluating the radiative decay rate constant k_r of

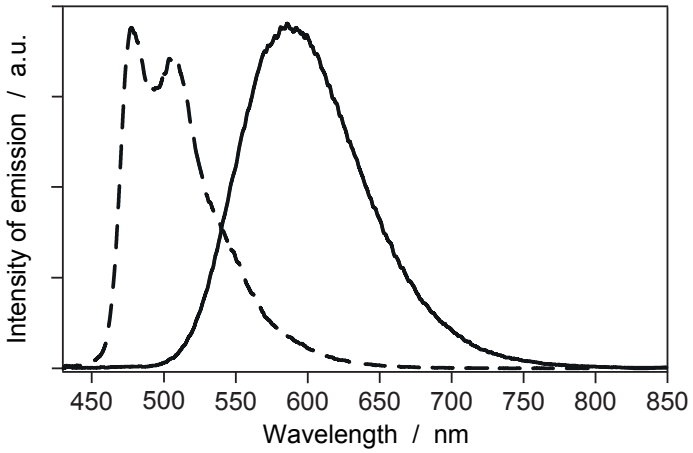

Figure 1.15: Room temperature emission spectra of $[Ir(ppy)_2(pzpy)][PF_6]$ (**7**, dashed line) and $[Ir(ppy)_2(bpy)][PF_6]$ (**2**, solid line) in solution. The more structured emission profile of **7** is a strong evidence of a predominantly ligand-centered ($^3\pi$-π^*) emitting state.

the complex, using the experimental values of PLQY (Φ) and excited-state lifetime (τ), according to the following equation:

$$k_r = \frac{\Phi}{\tau}\,. \tag{1.2}$$

A smaller k_r value usually indicates a stronger LC character in the "mixed" triplet excited state. For instance, in the case of **4** and **7**, although both complexes have the same PLQY ($\Phi \approx 23\,\%$) in deoxygenated acetonitrile solution, **7** shows an emission lifetime almost three-times longer than **4** (1.56 µs *vs* 0.56 µs) [82]. Therefore **7** exhibits a smaller k_r ($1.5 \times 10^5\ s^{-1}$) relative to **4** ($4.2 \times 10^5\ s^{-1}$), confirming a less-pronounced ^{3}MLCT character of its emissive excited state.

It must be pointed out that Ir-iTMCs having a T_1 excited state with pronounced ^{3}MLCT character (*e.g.*,**2** and **4**) generally exhibit shorter emission lifetimes (*i.e.*, 0.43 µs and 0.56 µs, respectively) compared to related ruthenium(II) complexes, which invariably emit from ^{3}MLCT levels (*e.g.*, 0.81 µs for **3**), despite their intrinsically superior PLQYs. This behavior is due to the increased spin-orbit coupling that, in third-row transition-metal complexes, accelerates both radiative and non-radiative singlet-triplet transitions, thereby decreasing the duration of excited-state lifetimes. Having typically higher Φ and shorter τ, Ir-iTMCs exhibit radiative decay rates as much as five-times higher than Ru(II) analogues.

Molecular-orbital features of Ir-iTMCs

To rationalize the photophysical properties of Ir-iTMCs, it is useful to determine the energy and atomic orbital composition of the highest-occupied and the lowest-unoccupied molecular orbitals (HOMO and LUMO, respectively). As already known for neutral iridium(III) complexes, also in the case of charged systems [91] the HOMO is an admixture of Ir-dπ orbitals (t_{2g}) and phenyl π orbitals of the cyclometalated (CN) ligands, whereas the LUMO is usually located on the neutral (NN) ancillary ligand (see Figure 1.16,a) [37]. Therefore, the emitting T_1 triplet usually has a mixed ^{3}MLCT/^{3}LLCT character.

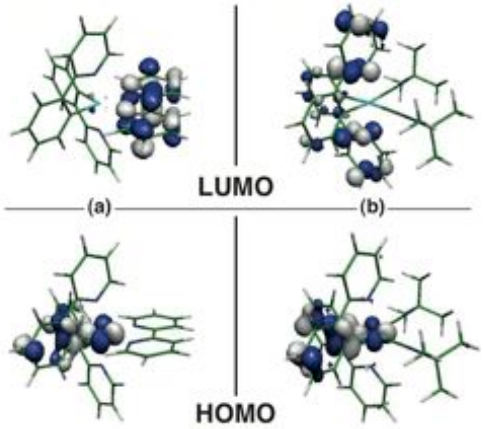

Figure 1.16: Schematic representation of the electronic density contours calculated for the frontier molecular orbitals of both (a) $[Ir(ppy)_2(bpy)][PF_6]$ (**2**) and of (b) $[Ir(ppy)_2(CNtBu)_2][PF_6]$ (**8**), a complex with higher ligand field.

To investigate the nature of higher energy LUMOs (LUMO+1, LUMO+2, *etc.*) is useful to understand the non-radiative deactivation pathways of the T_1 emitting state and to assess to which extent the LUMO orbital is located on the neutral ligand. In fact, by changing or chemically modifying the ancillary ligand, it is possible to destabilize the LUMO, while keeping the HOMO relatively unperturbed. This procedure is useful for blue-shifting the emission spectra of cationic iridium complexes, but it has an intrinsic limit: if the LUMO of the neutral ancillary ligand lies too high in energy, the LUMO+1 or the LUMO+2, usually located on the cyclometalating ligands, becomes the new LUMO of the complex (see Figure 1.16, case b). If this is the case, as expected from the larger electronegativity of the N atom, the new LUMO is mainly located on the heterocyclic moiety of the

(CN) ligand (*e.g.*, the pyridine ring for ppy-based ligands). In this way, the use of ancillary ligands with relatively inaccessible π^* orbitals (*e.g.*, carbenes [85] or isocyanides [92, 93]) leads to low-lying emitting excited states centered on the cyclometalated ligands and the emitting T_1 state exhibits a more ligand-centered character. In such cases, highly structured emissions and strongly increased radiative lifetimes (*i.e.*, small values of k_r) are found. Practically, the ancillary ligand plays a passive role in determining the nature of the excited state as it only influences the Δ_o splitting of the iridium d orbitals by inductive effects through σ bonds [36, 92].

As the simple description of the HOMO and LUMO is not always exhaustive in describing the emitting triplet state of iridium(III) complexes, theoretical calculations performed with the time-dependent version of the density functional theory (TD-DFT) [94, 95] result to be very useful in establishing the electronic nature and relative energy ordering of the low-lying triplet states and, in particular, of the emitting excited state T_1. The combination of TD-DFT and DFT calculations are especially helpful in determining the energy position and the electronic and molecular structures of ^{3}MC states [37, 96, 97]. As mentioned above, the thermal population of these states might be one of the possible non-radiative deactivation processes that could take place in Ir-iTMCs and, likewise ruthenium(II) metal complexes [98], might cause complex instability and degradation both in solution and in LECs. ^{3}MC states formally involve the transfer of one electron from the HOMO dπ orbitals (t_{2g}) to the antibonding dσ^* orbitals (e_g) of the iridium ion. The e_g orbital is characterized by a strong σ-antibonding interaction between the iridium atom and the nitrogen atoms of the CN ligands (see Figure 1.17 on the following page) [37]. Therefore, population of the ^{3}MC states leads to elongation of $Ir-N_{CN}$ bonds and to the opening of the molecular structure of the complex, prompting the entrance of small nucleophilic molecules and leading to degradation of the complex. Despite the fact that the ligand-field stabilization energy is strongly enhanced by cyclometalation and hence antibonding e_g orbitals are very high in energy [36], in some cases ^{3}MC thermal population has been observed for Ir-iTMCs [99].

Because HOMO and LUMO orbitals are usually located on different ligands (except in the case of high-field-strength ancillary ligands, for which the HOMO and the LUMO are located on different moieties of the cyclometalating ligands), the HOMO-LUMO energy gap can be fine-tuned by playing independently on

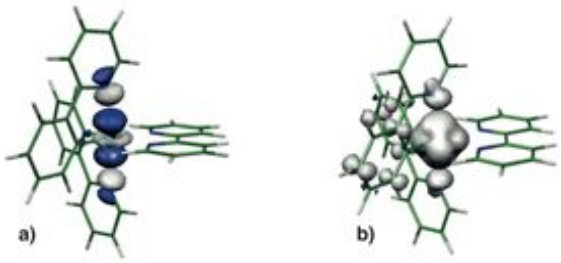

Figure 1.17: a) Electron density contour (0.05 e bohr^{-3}) calculated for the unoccupied e_g orbital of complex **2** showing the σ-antibonding interactions along the vertical N_{ppy}—Ir—N_{ppy} axis. b) Spin density calculated for the optimized structure of the ^{3}MC state of complex **2**.

the cyclometalating (HOMO) or on the ancillary ligands (LUMO), or even on both of them. As a rule of thumb, it can be said that (i) electron-withdrawing substituents on the cyclometalating ligands reduce the σ donation to the metal, decrease the electron density on the iridium ion, and lead to a stabilization of the HOMO; and (ii) electron-donating substituents on the ancillary ligand or use of intrinsically electron-rich ligands bring about a destabilization of the LUMO. Some examples of how it is possible to influence these levels to tune the emission color in cationic iridium(III) complexes are reported in the following sections.

Although it has become feasible to estimate the emission energy of Ir-iTMCs, it remains quite difficult, on the other hand, to predict other emission properties, such as radiative constants (k_r) and emission quantum yields (Φ), only by means of DFT calculations or electrochemical data. Accordingly, in-depth experimental studies remain essential to fully characterize the photophysical properties of luminescent iridium(III) complexes.

Deactivation pathways through ^{3}MC levels

The lowest-lying T_1 excited state of charged iridium(III) complexes has a mixed ^{3}MLCT, ^{3}LLCT, and ^{3}LC character that deactivates radiatively to the S_0 ground state (see Figure 1.13 on page 20), typically in the microsecond time scale, with high PLQYs. As pointed out earlier and similarly to Ru(II) complexes [98], non-emissive ^{3}MC levels could offer effective radiationless pathways to the T_1 emitting state; such transitions often entail photodegradation of the complex by nucleophilic-assisted ligand-exchange reactions.

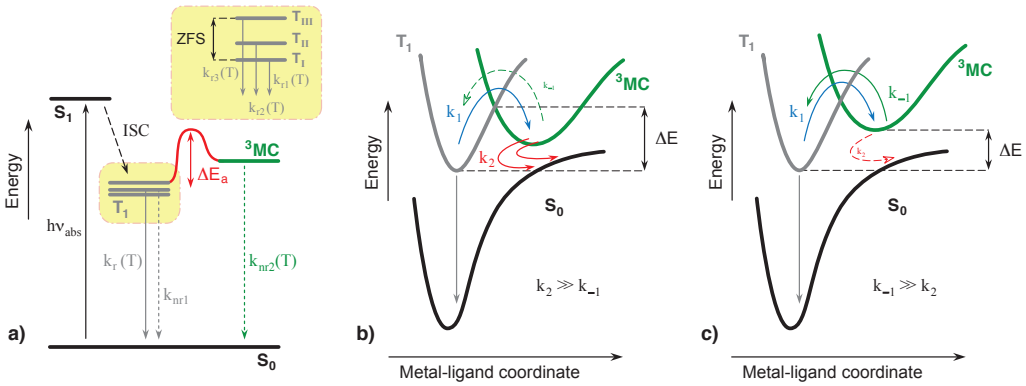

Figure 1.18: a) Schematic representation of the lowest-energy excited states of Ir(III) complexes and their deactivation processes. The lowest emitting excited state (T_1) is composed of three levels (T_I, T_{II}, and T_{III}, split by zero-field splitting) that undergo thermal equilibration at temperatures above 77 K. b) and c) potential energy curves illustrating the two possible limiting kinetic cases describing the non-radiative deactivation of the emitting T_1 state through thermal population of upper-lying ^{3}MC levels.

In the case of ionic cyclometalated iridium(III) complexes, the energy gap (ΔE) between the T_1 and the ^{3}MC states is usually around 0.6 eV [100], namely higher than for luminescent ruthenium(II) compounds (below 0.5 cm^{-1}) [98]. This situation is due to the strong ligand-field stabilization energy provided by cyclometalating ligands and because Ir is a third-row d element. Therefore, the thermal population of ^{3}MC levels of Ir-iTMCs is negligible in most cases but, under particular circumstances, it must be thoroughly considered. This is the case, for instance, when the complex is geometrical distorted or when emission comes from very high (*i.e.*, blue emitting) T_1 states [100, 101]. Moreover, when Ir-iTMCs are used as active materials in LEC devices, the thermal accessibility of metal-centered states might become an issue under the operative conditions. Unfortunately, the experimental determination of ΔE by solid-state electroluminescence measurements cannot be accomplished, unlike photoluminescent liquid samples [98].

Key information about the population of thermally accessible non-radiative excited states can be obtained in solution by studying the temperature dependence of the intrinsic deactivation rate constant of the complex k_{in} (that is $1/\tau$, where τ is the measured excited-state lifetime). Overall, the deactivation of the

emitting excited states in d^6 transition-metal complexes is governed by three main processes (see Figure 1.18 on the preceding page, a) [22, 100]:

1) an almost temperature-independent non-radiative pathway, characterized by a rate constant k_{nr_1}, that occurs through direct potential energy surface crossing and/or vibrational coupling between T_1 and S_0 states;

2) a minor temperature-dependent radiative pathway, with kinetic rate constant $k_r\,(T)$, associated with the thermal population of the upper-lying triplet substates of T_1 (namely T_I, T_{II}, and T_{III}) having their own radiative decay rates;

3) a strong temperature-dependent non-radiative pathway, showing a kinetic rate constant $k_{nr_2}\,(T)$, involving the thermal population of upper-lying non-radiative excited states (*i.e.*, the ^{3}MC states), frequently associated with an activation energy barrier.

Following this model, an experimental estimation of the energy gap (ΔE) between the emissive T_1 and the ^{3}MC excited states can be obtained correlating the dependence of k_{in} with temperature, using the following Arrhenius-type equation:

$$k_{in} = k_0 + \sum_i A_i \exp\left[-\frac{\Delta E_i}{RT}\right] \tag{1.3}$$

where k_0 is a low-temperature limiting value and A_i is the pre-exponential frequency factor of the i-th deactivation process. This pre-exponential constant is extremely important to figure out the physical meaning of this model. In fact, once the ^{3}MC state is populated, two limiting kinetic cases can occur:

I) a strong coupling between the ^{3}MC state and the S_0 level ($k_2 \gg k_{-1}$, see Figure 1.18, case b), so that $A_i > 10^{11}$ s^{-1}: the ^{3}MC deactivation to the ground state is extremely fast and often leads to dissociative photodegradation of the complex. In this case, ΔE corresponds to the activation energy barrier between the T_1 emitting level and the ^{3}MC state;

II) a thermal equilibrium between ^{3}MC and T_1 ($k_{-1} \gg k_2$, see Figure 1.18, case c), so that $A_i < 10^9$ s^{-1}: the ^{3}MC deactivation is slower and the ΔE value corresponds to the energy difference between the T_1 and the ^{3}MC level.

Practically, the k_{in} (*i.e.*, $1/\tau$) values determined in a wide range of temperatures (typically from 77 K to 300 K) can be fitted using equation 1.3 to obtain all the relevant parameters described above [100].

Optimizing the emission performance in solid state

There are many parameters that describe the performance of LECs (see Section 1.4) and one of them is the external quantum efficiency (EQE, the ratio of photons emerging from the device per injected electron) that is proportional to the fraction of excitons that decay radiatively. Since emission in Ir-iTMCs arises from the triplet state and singlet excitons are efficiently converted into triplets, it has been shown that the EQE should be proportional to the solid-state PLQY measured in thin films [102, 103]. Therefore, a preliminary photophysical characterization of a given complex in solid-state films can be helpful to predict if it can yield a brightly emitting device. Some main strategies can be used to enhance PLQYs in the solid state and minimize the typical self-quenching effects observed in films:

1) use of inert matrices, such as ionic liquids [104, 105] or polymers [71, 106], to disperse the iTMC; ionic liquids improve both PLQY and LEC properties (*e.g.*, turn-on time, luminance, and efficiency) [37], but polymers have often a detrimental effect on device efficiency [29];

2) dispersion of a low-band-gap iTMC in a wider band-gap iTMC, for example, an orange iTMC in a green emitter; this has been successful to increase the device EQE [107];

3) covalent binding of hydrophobic bulky groups (*e.g.*, *tert*-butyl) to chelating ligands; this improves PLQY as it increases the distance between the emitting complexes in the solid state and therefore can strongly decrease self-quenching, as also found for Ru(II) complexes [108]. In addition, hydrophobic bulky groups on iTMCs can also enhance the stability of the complexes because they render the molecule less susceptible to interaction with aggressive nucleophiles [109].

Another useful PL parameter to check in solid films is the excited-state lifetime, which can be helpful to evaluate the protecting effect of bulky groups against self-quenching. Practically, shorter lifetimes in neat films (compared to diluted dispersions of inert matrices) indicate interactions between closely packed iTMCs and, hence, additional non-radiative pathways [104].

It must be emphasized that, although an accurate photophysical study of the emitting complex (especially in solid-state film) can be very useful to predict the

performance of the active material in LECs, several other parameters that do not usually affect the photoluminescence behavior can strongly affect the device properties, as will be discussed later.

1.3.3 Strategies for tuning the color of Ir-iTMCs

The key property of Ir-iTMCs to be utilized in LECs is the emission color, which can be tuned by changing or chemically modifying the organic ligand framework around the Ir(III) metal ion [36]. A parameter often used to describe the emission color of a given compound is the wavelength of the emission band maximum (λ_{max}). It is a very practical parameter since is directly derived from the photoluminescence (PL) or electroluminescence (EL) spectra corrected for the detector response, but it can only give a rough estimation of the true emission color, which dramatically depends on the specific bandwidth. Moreover, to fully define a color, the sensitivity of the photoreceptors in the human eye has to be considered. Therefore the appropriate method to define colors requires the use of the Commission Internationale de l'Eclairage (CIE) coordinates, that can be calculated from the luminescence spectrum and give a univocal definition of the emission color according to universally accepted international standards [110]. CIE coordinates are particularly useful to define white-light sources and, to this purpose, the so-called color-rendering index (CRI) is also provided, which gives a quantitative measure of the ability of an emitting device to reproduce the colors of various objects faithfully, in comparison with natural sunlight [110].

A huge number of cationic iridium(III) complexes have been synthesized and characterized [29, 36, 73, 75]. In this section we discuss primarily those used as active materials in LECs together with some examples that illustrate the general strategies used for color-tuning and for achieving highly emissive materials. In order to allow an easy comparison, the photophysical and electrochemical properties of many of them are gathered in Table 1.1 on the next page.

Attaching substituents to the $[Ir(ppy)_2(bpy)]^+$ ion

The spatial distribution of the frontier orbitals in $[Ir(ppy)_2(bpy)][PF_6]$ (**2**, see Figure 1.16 on page 24, a) allows for an almost independent tuning of the HOMO and LUMO energy levels. Consequently, two different strategies are possible: to attach substituents on the **bpy** ancillary ligand (LUMO tuning) or/and to substitute the cyclometalating **ppy** ligands (HOMO tuning).

Table 1.1: Photophysical and electrochemical properties of cationic iridium(III) complexes utilized in LEC devices. Where not explicitly specified, the reported data have been obtained at room-temperature in oxygen-free acetonitrile solutions. In electrochemistry ferrocene was used as an internal standard, and all potentials are referenced to the ferrocene/ferrocenium couple. Additional notation: * data in CH_2Cl_2; ** data in 2-MeTHF.; (sh) stands for "shoulder".

Complex	Emission properties			Electrochemistry	
	λ_{max} (nm)	τ (µs)	Φ (%)	E_{ox} (V)	E_{red} (V
2	585	0.43	14	0.84	−1.77, −2.60
4	581	0.56	23	0.83	−1.88, −2.87
7	475, 503 (sh)	1.56	23	0.88	−2.19
8	453, 485, 509 (sh)	32	52	1.23	−2.38
9	491, 520	2.43	80	0.72	−2.17, −2.61
10	512	1.4	70		
11	463, 493	4.11	85	1.00	−2.13, −2.49
12	687	0.07	2		
13	623	0.58	17		
14	452, 480 (sh)	1.62	20	1.20	−2.15
15	453, 483*	0.68*	21*	1.22	−2.18, −2.59
16	454, 485*	—	—	1.14	−1.92
17	444, 468*	6.2**	16**	> 1.40	−2.19
18	447	40	55	1.37	−2.43
19	451, 482*	0.02*	7*		
20	445, 474*	0.17*	8*		
21	452, 482*	2.08*	20*	0.99	−2.32, −2.67
22	471	0.07	1	0.86	−2.43

In the first Ir-iTMC used in a LEC (**4**, in Figure 1.9 on page 16), two tert-butyl groups are attached to the 4 and 4' position of the **bpy** ancillary ligand [76]. In acetonitrile solution, no substantial shift is observed in the PL spectrum if compared to **2** (λ_{max} = 581 nm *vs.* 585 nm). However, a more marked hypsochromic shift of 30 nm was found in the EL spectrum (λ_{max} = 560 nm *vs.* 590 nm) of the LEC, a shift which has been observed in more cases, especially in wide-band-gap iTMCs. The main difference between PL and EL spectra, besides the way of exci-

tation, is the concentration of the iTMC in the solvent or in the device film; in PL it is usually low whereas in EL the iTMCs are usually present at a concentration higher than 70 %.

To accomplish emission blue-shift, it is necessary to enlarge the HOMO–LUMO energy gap. This can be achieved by anchoring electron-withdrawing substituents on the cyclometalating ligands (in order to stabilize the HOMO) and/or electron-donating substituents on the ancillary ligands (to destabilize the LUMO). Following this approach, using a 4,4'-dimethylamino-substituted bipyridine ligand, with strong electron-donating groups on the 4,4' positions, a hypsochromic shift of almost 60 nm was obtained [111]. The corresponding complex $[Ir(ppy)_2(dma\text{-}bpy)][PF_6]$ (**9**, in Figure 1.19 on the facing page) exhibits a strong emission band with maxima at 491 nm and 520 nm (PLQY = 80 %, in deaerated solution). A further blue shift could be obtained by stabilizing the HOMO using difluoro-substituted 2-phenylpyridines (**dfppy**) as the cyclometalating ligands. While the sole effect of the **dfppy** ligand leads to a blue-green emission around 512 nm in the case of complex $[Ir(dfppy)_2(dtb\text{-}bpy)][PF_6]$ (**10**), the synergetic effects of both the electron-withdrawing substituents on the **dfppy** ligands and the electron-donating amino substituents on the bpy-based ligand are able to shift the emission band of the complex $[Ir(dfppy)_2(ddma\text{-}bpy)][PF_6]$ (**11**) to the blue with emission maxima at 463 nm and 493 nm [112].

Using the same rationale as above, emission red-shift can be achieved by LUMO stabilization. To this end, there are essentially two methods: (i) adding electron-withdrawing groups to the ancillary ligand or (ii) increasing the delocalization of its π system. Following the first approach, a deep-red LEC device was obtained using complex $[Ir(tpy)_2(e\text{-}bpy)][PF_6]$ (**12**): the red-shifted emission (PL emission peak in solution at 687 nm) is due to LUMO stabilization by the electron-withdrawing effect of the ester groups [113]. The second approach was used with $[Ir(ppy)_2(pdp\text{-}bpy)][PF_6]$ (**13**), having a 5,5'-diphenyl-substituted-bpy as ancillary ligand and exhibiting a red PL emission centered around 620 nm [114].

Designing ligands beyond prototypical bpy and ppy

Using differently substituted bpy-type ancillary ligands, it is very difficult to push the emission of Ir-iTMCs toward the blue because of the intrinsically limited energy gap [115]. Therefore it is more convenient to replace the bpy-based ancil-

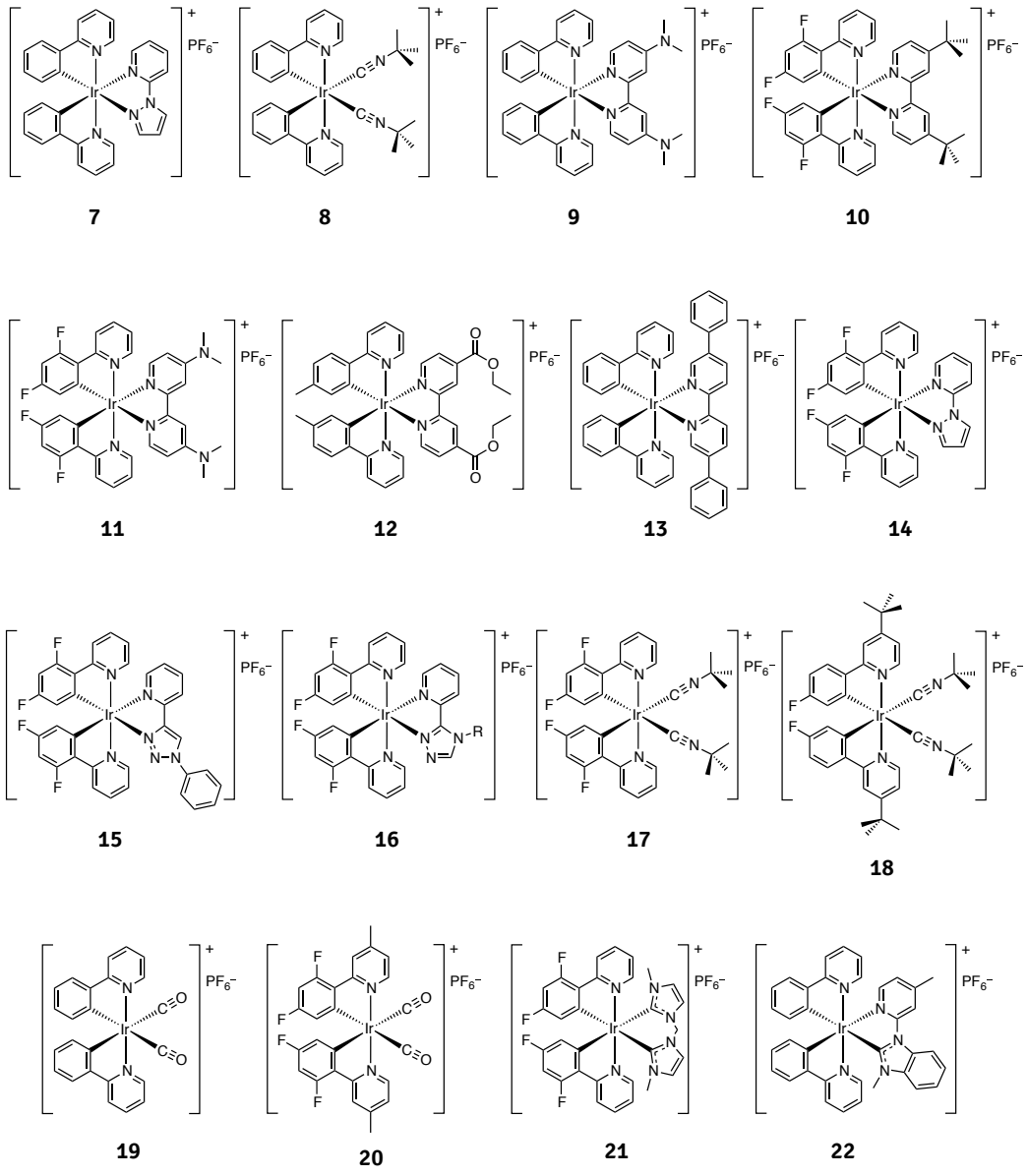

Figure 1.19: Selected examples of Ir-iTMCs with substituted **ppy** as cyclometalating ligands.

lary ligand with other diimine ligands containing stronger electron-donating nitrogen atoms, such as 2-(1H-pyrazol-1-yl)pyridine (**pzpy**, in Figure 1.12) [115]. For example, in acetonitrile solution, $[Ir(ppy)_2(pzpy)][PF_6]$ (**7**) emits blue-green light (λ_{max} = 475 nm), which is hypsochromically shifted by more than 100 nm with respect to the **bpy** analogue **2** (see Figure 1.15 on page 23). $[Ir(dfppy)_2(pzpy)][PF_6]$ (**14**, in Figure 1.19) with fluorine-substituted cyclometalated ligands shows even further blue-shifted light emission (λ_{max} = 451 nm).

Compared to **pzpy**, triazole-pyridine ancillary ligands (see Figure 1.12) have an even stronger electron-donating capability owing to the σ-donor properties of the triazole ring, that make them suitable for preparing sky-blue light-emitting Ir-iTMCs. Indeed, recent examples by De Cola *et al.* show that, by using Ir-iTMCs with 1,2,3-triazole-pyridine as ancillary ligands, PL peaks are in the range 460 – 490 nm and LECs exhibiting true-blue emission are obtainable [116]; one of these compounds (**15**) is depicted in Figure 1.19 on the preceding page. Following a similar approach, Chen *et al.* [117] used the isomeric 1,2,4-triazole-pyridine with different substituents in the 4 and 5 position of the triazole ring as the ancillary ligand to make an Ir-iTMC (**16**, in Figure 1.19) displaying an EL band further shifted to the blue (457 – 486 nm).

Tamayo *et al.* reported the first series of Ir-iTMCs used for LECs without 2-phenylpyridine (**ppy**) cyclometalating ligands [118]. The **ppy** motif was replaced by the higher energy 1-phenylpyrazole (**ppz**), as exemplified by the green-blue and red-emitting complexes depicted in Figure 1.20 on the next page. Ladouceur *et al.*, described a new series of Ir-iTMCs using aryl-triazoles as the cyclometalating ligands, that lead to blue- and green-emitting complexes [119]. Their use in LECs has not been described yet.

Ir-iTMCs based on strong-field ancillary ligands

Deep-blue emissions from Ir-iTMCs can be obtained also by introducing strong ligand-field-stabilizing ligands (*e.g.*, CO, isocyanides, or carbenes), so that the HOMO–LUMO transition involves mainly the cyclometalated system without participation of the ancillary counterpart. In these cases, the HOMO orbital is predominantly located on the Ir–C bonds on the phenyl moieties of the cyclometalating ligands, while the LUMO is mostly found on the pyridine rings of the same CN ligands.

The first two examples of this class of complexes were reported by Thompson

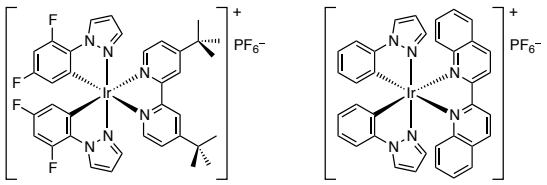

23 **24**

Figure 1.20: Two examples of complexes with phenylpyrazoles as cyclometalating ligands: $[Ir(dfppz)_2(dtb\text{-}bpy)][PF_6]$ (**23**, λ_{max} = 492 nm), and $[Ir(ppz)_2(biq)][PF_6]$ (**24**, λ_{max} = 616 nm).

et al. in 2005, using isocyanides as strong-field neutral ligands. In 2-methyl-THF solution, $[Ir(ppy)_2(CNtBu)_2][CF_3SO_3]$ (**8**) and $[Ir(dfppy)_2(CNtBu)_2][CF_3SO_3]$ (**17**) emit with λ_{max} = 458 nm and 444 nm, respectively, and the isocyanide ancillary ligands have a negligible effect in dictating the HOMO–LUMO gap [92].

Recently, $[Ir(tBu\text{-}ppy)_2(CNtBu)_2][CF_3SO_3]$ (**18**, in Figure 1.19) has turned out to be first example of an Ir(III) isocyanide complex whose strong blue phosphorescence is unaffected by passing from solution to the solid state, thanks to the presence of the tert-butyl groups on the **ppy** ligand that are particularly effective in preventing self-aggregation [93].

In 2007, Chin *et al.* [120] synthesized a series of Ir-iTMCs equipped with even stronger-field ligands, such as CO. Complexes $[Ir(ppy)_2(CO)_2][PF_6]$ (**19**) and $[Ir(df\text{-}met\text{-}ppy)_2(CO)_2][PF_6]$ (**20**, in Figure 1.19) emit at 451 – 482 nm and 441 – 443 nm, respectively.

Following an analogous approach, Yang *et al.* [85] have recently reported the first LECs based on N-heterocyclic carbene ligands displaying the bluest emission ever reported for a LEC device (456 – 488 nm). This class of complexes displays true-blue emission both in solution and in neat film, although exhibit a strong PLQY decrease in the solid state because of self-quenching. Also in this case, the carbene ancillary ligand appears to contribute only with a small electron density to both the HOMO and the LUMO. In Figure 1.19 on page 33, one of these complexes (**21**) is reported as an example.

Similar results have been recently reported by Kessler *et al.*, who synthesized a series of Ir-iTMCs emitting from near-UV to red using a neutral pyridine-carbene ancillary ligand and different cyclometalating ligands (*e.g.*, **22**, in Figure 1.19) [121]. The low PLQYs observed for these complexes were ascribed to

non-radiative process through the population of ^{3}MC states. Nevertheless, LECs with emission from the bluish-green to orange region of the visible spectrum were fabricated.

1.4 iTMCs-based LECs

1.4.1 Fabrication and architectures

LECs are prepared by solution-based processes with benign solvents. Most devices reported to date consist of one or two active layers sandwiched in between one transparent and one reflecting electrode (see Figure 1.21 on the next page, a). Materials most commonly used for electrodes are a transparent anode (*e.g.*, tin-doped indium oxide, ITO) and air-stable reflecting cathodes (*e.g.*, Au, Al, and Ag). Double-layer LECs, besides the film of the light-emitting iTMC, entail a hole injection layer, generally composed of poly(3,4-ethylenedioxythiophene) : polystyrenesulfonate (PEDOT : PSS). Such a layer is deposited to smoothen the ITO surface and, as a result, increases the yield of device preparation. An inert polymer or an ionic liquid is frequently added to the iTMC core component to facilitate the formation of the film and to enhance the device performances. In most cases, the top metal contact is thermally evaporated; there are few examples in which it was prepared by soft contact lamination [38]; liquid top contacts are also reported [122].

Bernards *et al.* [39] and Slinker *et al.* [40] have made LEC arrays powered directly by a standard US outlet (120 V, 60 Hz), without the use of transformers. These lighting panels consist of several LECs [16, 24, 36] that were placed in series in such a way that the anode of a given device acts also as cathode for the next one (see Figure 1.21, b).

Bernards *et al.* showed that iTMC-LECs with ITO anodes and laminated Au cathodes (Figure 1.21, c) exhibit comparable performance to those fabricated with evaporated top contacts [38]. These devices were made by evaporating the Au electrode onto a polydimethylsiloxane (PDMS) stamp, followed by soft-contact lamination onto an iTMC-layer deposited on a patterned ITO substrate. Light emission output is uniform over the whole device area, indicating a high-quality mechanical and electrical contact.

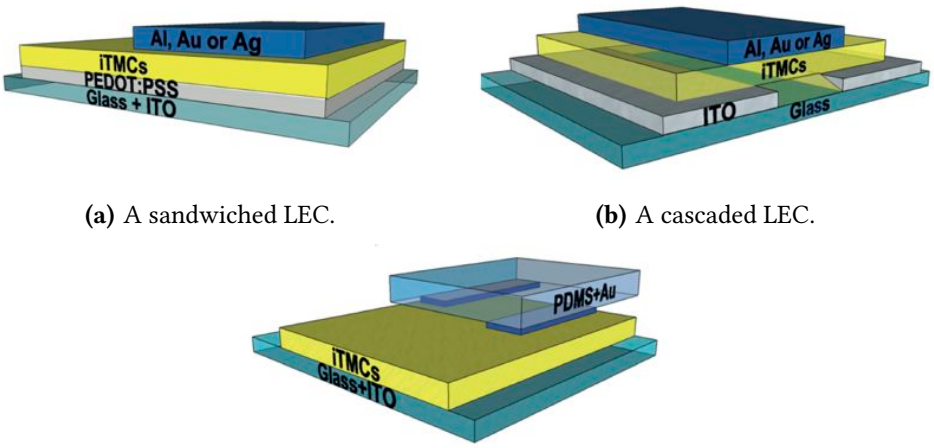

(a) A sandwiched LEC.

(b) A cascaded LEC.

(c) A laminated LEC.

Figure 1.21: Schematic layout of different LEC architectures.

1.4.2 Figures of merit in LECs

The most important figures of merit commonly used to characterize the performance of LEC devices are:

Luminance (L): flux of light emitted by the device, measured in candela per surface unit ($cd\,m^{-2}$); see the red curve in Figure 1.22 on the following page.

Current density (J): flux of current through the device, measured in ampere per surface unit ($A\,m^{-2}$); see the red curve in Figure 1.22.

Turn-on time (t_{on}): time needed to reach the maximum luminance; *e.g.*, in Figure 1.22 t_{on} is 0.74 h. Another parameter often used in literature is t_{100}, which is the time to reach a luminance of 100 $cd\,m^{-2}$.

Lifetime ($t_{1/2}$): time to reach half of the maximum luminance; in Figure 1.22, $t_{1/2}$ is 7.1 h. Sometimes, it is also used $t_{1/5}$, namely the time to reach one fifth of the maximum luminance.

Total emitted energy (E_{tot}): it is calculated by integrating the radiant flux of the device in function of time from the application of bias to $t_{1/5}$ [123]. If this value is divided by the electrode area, it yields the total emitted energy

density U_{tot}, which allows devices having electrodes of different shapes to be compared. Herein, all the values are determined using an area of 3 mm^2, hence only the E_{tot} parameter will be used.

Efficacy (or current efficiency): emitted light per electric flux, measured in candela per ampere (cd A^{-1}). The value of efficacy reported for a given device is the maximum observed. The evolution of the efficacy over time is displayed in Figure 1.22 (inset).

Power efficiency: flux of light per electric input, measured in lm W^{-1}. The value of power efficiency reported for a given device is the maximum observed.

External quantum efficiency (EQE): the ratio of photons emerging from the device per injected electrons. EQE is also defined through the equation EQE = $\frac{b\phi}{2n^2}$, where b is the recombination efficiency and it is equal to unity for two ohmic contacts [124], ϕ is the fraction of excitons that decay radiatively, and n is the refractive index of the glass substrate and is equal to 1.5 (the factor $\frac{1}{2n^2}$ accounts for the light out-coupling of the device).

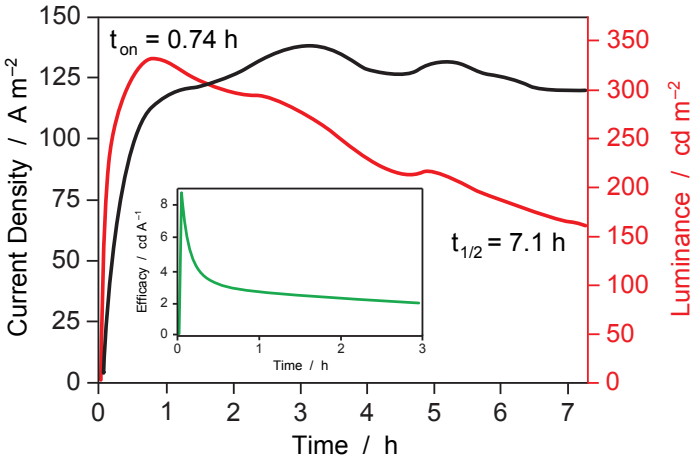

Figure 1.22: Typical trend of the current density (black), luminance (red), and efficacy (green, inset) over time of a standard LEC at applied constant voltage.

The stability of a LEC device is measured by using either the lifetime ($t_{1/2}$) or the total emitted energy (E_{tot}), and this can generate confusion in making comparisons among data from different research groups. E_{tot} is more accurate for

comparing the stability of different LECs since $t_{1/2}$ strongly depends on the maximum luminance level reached, which can be rather different; devices running at higher luminance levels typically exhibit lower lifetimes. E_{tot} takes into account the absolute magnitude of the radiant flux as well as the total device lifetime, and does not rely on the shape of the curve of radiant flux versus time.

1.4.3 Early studies on LECs

Two reviews by Slinker *et al.* cover the development of iTMC-LECs during the first ten years [28, 29]. The vast majority of reports reviewed in these articles concerns LECs based on ruthenium(II) and osmium(II) complexes, with $[Ru(bpy)_3]^{2+}$ as the most utilized cationic compound (*e.g.*, complex **3** in Figure 1.9 on page 16) [27–29, 31–34, 38–40, 54, 58, 66, 71, 106, 108, 122, 123, 125–147]. These LECs showed emission in the red and orange-red spectral windows, with stabilities of few hours and low external quantum efficiencies. Other copper(I)- and rhenium(I)-based complexes were also tested in LECs but only few examples were initially described (see Section 1.4.5 on page 61) [148–155].

Herein, only the most significant reports from early times will be summarized. More generally, we will illustrate the latest advances obtained in iTMCs-LECs in terms of turn-on time, stability, efficiency, and color.

1.4.4 LECs based on Ir-iTMCs: recent advances

In 2004, Slinker *et al.* pioneered the use of Ir-iTMCs in LECs [76]. As discussed in Section 1.3, there are several reasons that justify their selection over Ru(II) complexes:

1) high PLQY [19, 86, 98, 156];

2) easily tunable HOMO–LUMO energy gap by independent chemical modifications of the ligands [29, 37, 75, 81, 82, 85, 91, 99, 103, 105, 111, 113, 116, 118, 157–160];

3) high stability against degradation processes owing to higher ligand-field splitting [19, 86, 97, 98, 156, 161–164].

Over the last eight years, the use of Ir-iTMCs has brought very significant advances in LEC performances, that is, color, efficiency, stability, and turn-on

times. Notably, iridium(III) complexes (in most cases neutral) have been extensively used also in OLED technology, and several reviews covering this vast topic have been published over the years [75, 165].

Shin *et al.* have also demonstrated that devices based on a combination of neutral Ir(III) complexes with tetra-n-butylammonium tetrafluoroborate in the emitting layer behave similarly to iTMC-based LECs [166], obtaining luminances of about 300 cd m^{-2} and t_{on} shorter than one second. Such devices can be considered borderline cases between iTMC-LECs and PLECs using an ionic liquid [167].

Turn-on time

As discussed in Section 1.2.2 on page 8, the movement of ions is essential to promote electronic charge injection in LECs. However, since the ionic conductivity in the solid state is low, it takes time for iTMC-LECs to become operative, therefore the turn-on time (t_{on}, see above) generally ranges from a few minutes to several days. This is clearly a formidable obstacle for most practical applications, which require instantaneous response [31, 32].

In the first ten years of activity on LECs, only few reports targeted the improvement of t_{on} [31, 32], which were typically achieved by applying higher driving voltages [27, 33, 108]. These voltages are provided continuously or, alternatively, initial sequences of high-voltage pulses followed by constant lower bias, once sufficient luminance is reached, are applied [33]. Higher voltages lead both to a faster movement of ions towards the electrode interfaces and also to a lower electron/hole injection barriers; both effects reduce the turn-on time [33, 111, 149, 168]. Notably, the approach entailing a few short higher voltage pulses can lead to both an improvement of t_{on} and device stability [168].

Environmental effects during device preparation and operation may also influence t_{on}. For instance, devices running in air exhibit shorter turn-on times than those in a nitrogen environment [122]; this is due to the presence of residual moisture and/or solvent in the iTMC layer, which increases the ionic mobility [123, 141, 146]. The use of complexes with counter-anions smaller than $[PF_6]^-$, such as $[BF_4]^-$ or $[ClO_4]^-$, is also beneficial for turn-on times [71, 122], likewise the addition of salts in the form of electrolytes or ionic liquids [37, 82, 104, 105, 126, 169, 170]. All these approaches enhance ionic conductivities, thereby causing a faster build-up of the electrical double layer which induces a faster device t_{on}

but, on the other hand, also a quicker propagation of the doped zones leading to more extensive exciton quenching and to luminance decrease (see Section 1.2.2).

In the last few years, several reports have appeared showing improvements in the turn-on time of LECs by increasing the density of small ions or by adding ionic liquids.

Chemical modifications of Ir-iTMCs To increase the ionic concentration in the device, extra charged groups were attached at the periphery of the Ir-iTMCs (see Figure 1.23). Zysman-Colman *et al.* [171] made a family of novel ruthenium(II) and iridium(III) complexes (*e.g.*,**25**, in Figure 1.23) with triethylammonium hexafluorophosphate groups attached to the 5-position of the **bpy** ligands through alkyl chains made of four, six, and eight carbon atoms. The turn-on time was strongly reduced for all Ir-iTMCs, down to about 30 min. The EQE values were improved by increasing the length of the carbon chain, reaching a maximum for hexyl side-chain. With longer chains, the EQE drops as a result of a decrease of electron transport, attributed to a non-optimal spacing of the iTMCs in the film.

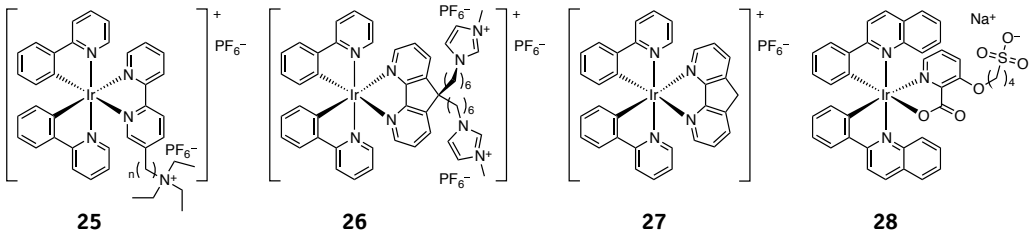

Figure 1.23: Schematic structures of Ir-iTMCs proposed to reduce the turn-on time in LEC devices.

Su *et al.* [172] reported a significant decrease of t_{on} by tethering imidazolium moieties onto a cationic Ir-iTMC (**26**, in Figure 1.23) [172]. The imidazolium groups do not affect the photophysical and electrochemical properties of complex **26**, compared to the parent complex **27** which lacks the cationic fragments, and related LECs have similar luminance (80 – 100 cd m^{-2}) and EQE values around 5 %. However, the turn-on times of LECs based on complex **26** (200 min) are much shorter than those based on **27** (500 min). This result was attributed to the larger number of mobile $[PF_6]^-$ counterions in the neat film.

In a related work, Kwon *et al.* [173] modified a neutral Ir-iTMC by attaching an alkyl chain with an anionic sulfonate group to the picolinate ligand (**28**, in Figure 1.23), counterbalanced by a small sodium ion. The key idea is to take advantage of the better mobility of small cations in solid films compared to small anions, such as $[PF_6]^-$. Indeed, t_{on} of LECs under reverse bias (−3 V) was reduced compared to those employing similar Ir-iTMCs equipped with $[PF_6]^-$. However, the LEC made with **28** exhibited low efficiency, stability, and luminance levels.

In a different approach, soft salts of cationic and anionic iridium(III) complexes were reported; these soft salts do not have small counterions and therefore the related LECs were not made [174].

Use of ionic liquids In 2005, Malliaras *et al.* proposed for the first time the insertion of an ionic liquid $[BMIM]^+[PF_6]^-$ (3-butyl-1-methylimidazolium hexafluorophosphate) into Ir-iTMC-based LECs (see Figure 1.24, top) [105, 169]. Indeed, small amounts of this compound significantly reduced the t_{on} of LECs from 4 h to 25 min, while also increasing luminance levels. These results were attributed to an improvement of ionic conductivity inside the light-emitting layer, because of the higher density of mobile ions.

Su *et al.* studied the effect of $[BMIM]^+[PF_6]^-$ on the film morphology of two different Ir-iTMCs, by means of atomic force microscopy (AFM) measurements. Uniform spin-coated thin films were obtained, with no evidence of aggregation or phase separation. They also examined the effect of the $[BMIM]^+[PF_6]^-$ on the PL properties of films, observing an increase of PLQY upon addition of the ionic liquid (IL) [104]. Using a ruthenium(II) complex and an ionic liquid, a LEC operating at 60 Hz (standard US outlet) was prepared, which exhibited a response time of about 4 ms [40]. Similar results were also obtained in LECs using the simple $[Ir(ppy)_2(bpy)][PF_6]$ (**2**, in Figure 1.3 on page 7) and different amounts of $[BMIM]^+[PF_6]^-$ [37], significantly reducing the turn-on time from 70 h (pristine device) to 0.7 h (Ir-iTMC:$[BMIM]^+[PF_6]^-$, molar ratio of 1:1) and increasing the PLQY in thin films. In all the above examples, device stability decreased upon addition of the ionic liquid, showing that it seems to exist a trade-off between turn-on time and stability.

Surprisingly, although there are hundreds of ionic liquids on the market, all reports on LECs with ionic liquids had utilized $[BMIM]^+[PF_6]^-$. Recently, Costa *et al.* studied the effect of some different ILs, with similar chemical structures

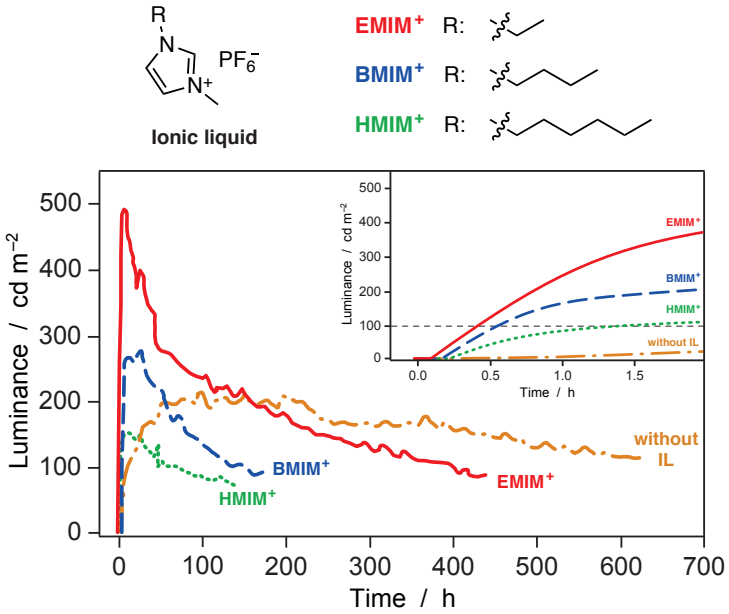

Figure 1.24: Top: Structural formula of ionic liquids used in LEC devices. Bottom: Luminance versus time plots for ITO/PEDOT:PSS/**2**:IL/Al LEC devices under a constant voltage of 3 V and a **2**:IL molar ratio of 4:1. The trend within the first two hours of operation is shown in the inset. For comparison, data for the device without IL are also shown.

but different ionic conductivities, on the performance of LECs based on **2** [170]. They tested $[HMIM]^+[PF_6]^-$ and $[EMIM]^+[PF_6]$, which exhibit lower and higher ionic conductivities, respectively (see Figure 1.24). Compared to the LEC employing $[BMIM]^+[PF_6]^-$, addition of $[HMIM]^+[PF_6]^-$ leads to an increase of the turn-on time and a decrease of the maximum luminance, whilst the LEC with $[EMIM]^+[PF_6]^-$ has a higher luminance level and turns on faster. Although $t_{1/2}$ is much shorter than that observed for the pristine LEC without any additional IL, the total emitted energy of the device with $[EMIM]^+[PF_6]^-$ is larger, thanks to the higher luminance level. Therefore, by adding a carefully optimized amount of ionic liquid with high conductivity (molar ratio Ir-iTMC:$[EMIM]^+[PF_6]^-$ 4:1), it is possible to improve the turn-on time without sacrificing the stability of the device thanks to a higher luminance.

Operation mode: pulsed driving Rudman *et al.* reported the benefits of pulsed driving for a ruthenium-based iTMC in a LEC [106]. In another report they ap-

plied DC current driving, showing that a fixed current density implies the initial application of a high voltage that was rapidly decreased as the injection barriers are reduced by the displacement of the ions in the film [71]. Using this approach, it takes 0.5 s to reach 50 cd m^{-2}, which required a starting voltage of 7 V, lowered to 3.5 V within the first ten seconds. Recently, a further advance was reported by using a combined current and pulsed driving approach, that yielded sub-second turn-on times to reach luminances of 150 cd m^{-2} [175]. This method also slows down the growth of the doped zones, stabilizing the LEC (which will be commented upon in the next section).

Stability

Stability is an essential figure of merit in electroluminescent devices, but while OLEDs may exhibit lifetimes of thousands of hours, those of most LECs range from few hours to few days. The stability of a device can be described in terms of lifetime ($t_{1/2}$) or total emitted energy (E_{tot}) [123].

For example, LECs using the archetypal complex $[Ru(bpy)_3][PF_6]_2$ (**3**, in Figure 1.9 on page 16) in PMMA yielded $t_{1/2}$ as high as 1000 h with a luminance of 50 cd m^{-2} [71, 106]. At higher luminance values of 200 cd m^{-2}, the highest E_{tot} reported for ruthenium-based LECs is around 1 J [29].

In general, as mentioned previously, device stability is related to the mobility of the ions in the thin film, but the intrinsic robustness of the specific iTMC is also of great relevance. The most detailed studies addressing the degradation of the active luminescent material in LECs were focused on devices using **3**.

Based on earlier works about the degradation mechanism of this iTMC in solution [161, 162, 164], Kalyuzhny *et al.* [123] postulated that the low stability of LECs involves the formation of a photoluminescence quencher in small quantities (ca. 1 wt %). One possible quencher was complex $[Ru(bpy)_2(H_2O)_2]^{2+}$ (**29**), whose formation is facilitated in the excited state. This hypothesis is supported by Pile *et al.*, who observed that humidity significantly reduces the lifetime of LEC devices of $[Ru(bpy)_3][ClO_4]_2$ (**30**) [141], probably as a result of the formation of **29** [123].

Zhao *et al.* investigated the effects of residual water and acetonitrile on thin films and devices of complex **30** [146]. Subsequently, evidence was obtained for the formation of an oxo-bridged dimer $[\{Ru(bpy)_2(H_2O)_2\}_2O][PF_6]_4$ as a quencher in devices based on **3** [143, 144], which probably results from the condensation

of two subunits of **29**.

Soltzberg *et al.* used laser desorption/ionization time-of-flight (MALDI-TOF) mass spectrometry and in situ Raman spectroscopy to study the generation of the oxo-bridged dimer during device operation [144]. They demonstrated that this species is an effective quencher of device luminescence, which can explain the decay of the luminance after having reached its maximum value.

In a second study, Slinker *et al.* [143] employed real-time in situ Raman spectroscopy to identify the sequential formation of oxo-bridged species upon device operation showing that, after operating the device for one hour, a low amount of this species (1 wt %) was detected, a quantity sufficient to effectively quench the luminescence of the device, as revealed by fluorescence microscopy. All the above studies show that the stability of LECs based on Ru-iTMCs is strongly affected by the generation of quenching molecules during device operation.

Most strategies to obtain long-lived LECs based on Ir-iTMCs focus on the design of robust hydrophobic complexes. Bolink *et al.* [109, 134] demonstrated that the use of bulky substituents on both Ru- and Ir-iTMCs leads to more stable LECs, probably through enhanced hydrophobicity of the complexes that limits the occurrence of water-induced substitution reactions.

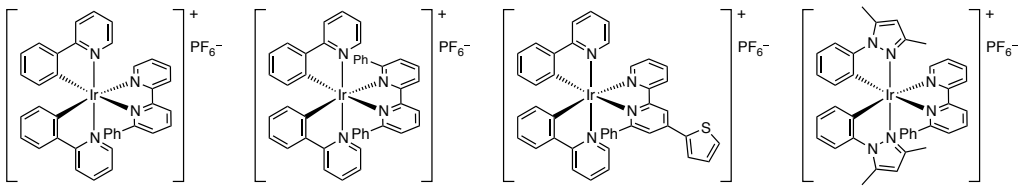

31 **32** **33** **34**

Figure 1.25: Structural formulae of intramolecularly caged Ir-iTMCs proposed to increase the stability of LEC devices.

The same group also showed that LECs with lifetimes of thousands of hours are obtained when using intramolecularly caged iridium(III) complexes (see Figure 1.25 and Table 1.2 on the following page) [99, 102, 168, 176]. The cage formation effect occurs through an intramolecular π-π interaction between a pendant phenyl group attached to the **bpy** ancillary ligand and the phenyl of the cyclometalating **ppy** moiety. Complex **31** (reported in Figure 1.25) keeps its rigid cage conformation in the ground and excited states acquiring high stability against reactions with water. LECs based on **31** with a small amount of IL $[BMIM]^+[PF_6]^-$

Table 1.2: Performance of LECs made with Ir-iTMCs exhibiting the intramolecular caging effect, and that of the reference complex $[Ir(ppy)_2(bpy)][PF_6]$ (**2**). The light-emitting layer composition is a mixture of Ir-iTMC:$[BMIM]^+[PF_6]^-$ at molar ratio 4:1, measurements at applied constant voltage of 3 V.

Value	**2**	**31**	**32**	**34**
$t_{1/2}$ (h)	70	1290	1300	2000
E_{tot} (J)	2	13.6	6.9	18.7

showed a lifetime of 1290 h and a total emitted energy of 13.6 J at a luminance value of 100 cd m^{-2} (see Table 1.2) [99]. Notably, this stability can be enhanced using a pre-biasing at high voltages, which leads to efficient (10 lm W^{-1}) and stable ($t_{1/2}$ = 3000 h, E_{tot} = 73 J) LECs with luminance levels of 200 cd m^{-2} [168]. LECs made with the reference complex $[Ir(ppy)_2(bpy)][PF_6]$ (**2**) lacking the cage effect and having the same amount of IL $[BMIM]^+[PF_6]^-$ exhibit much poorer performance (see Table 1.2), highlighting the relevance of the "locked" structure for device stability [37, 168]. Surprisingly, pristine LECs using **2** but without ionic liquids also had good stability with $t_{1/2}$ = 670 h and E_{tot} = 6.6 J at a luminance of 220 cd m^{-2} [37].

Subsequently, the same authors [99] demonstrated that, by extending the intramolecular π-π interactions with a second phenyl group to the 6'-position of the **pbpy** ligand (complex **32**, in Figure 1.25 on the previous page) does not strengthen the intramolecular caging effect because the second π-interaction distorts the planarity of the diimine ligand and enables the population of dissociative ^{3}MCstates [93]. Accordingly, **32** yields less-stable LECs (see Table 1.2).

A further step to combine both hydrophobicity and intramolecular caging in one iTMC was accomplished by Graber *et al.* [176] and Costa *et al.* [102]. In the work by Graber *et al.*, a thiophene ring was attached to the 4-position of the **pbpy** ligand; the related complex **33** (see Figure 1.25 on the previous page) yields LECs with high luminance levels (2700 cd m^{-2}) upon application of 5 V for 1.5 h, these levels substantially decreased at 3 V (230 cd m^{-2}), with an estimated lifetime of 600 h [176]. The work by Costa *et al.* is going to be presented in detail in the next section on page 48.

The intramolecular caging strategy has been recently extended to a pyrazole-

based Ir-iTMC (**34**, in Figure 1.25) [177, 178], obtaining LECs with excellent performance (see Table 1.2 on the preceding page), thanks to the additional presence of methyl groups above of the octahedral faces that block the entrance of nucleophilic molecules [177]. In another study, the beneficial effect of a phenyl group on the 1-position of the ancillary ligand (*i.e.*, **phpzpy**, in Figure 1.12 on page 19) was shown for a LEC with the green-emitting complex **35** (see Figure 1.26) [178].

Also phenyl substitution on the 5,5' positions of **bpy** affords reduced intermolecular interactions and, in single-layer LECs, higher stability [179]. Other bulky groups on the same positions of the **bpy** ligand were also shown to increase the stability of the LECs[179].

Recently Costa *et al.* reported an example in which this strategy was extended to phenantroline-based Ir-iTMCs [180]. They show that, in this particular case, the deactivation to ^{3}MC states is not relevant and thus the enhancement of the device performance is ascribed to an increase of the hydrophobic character.

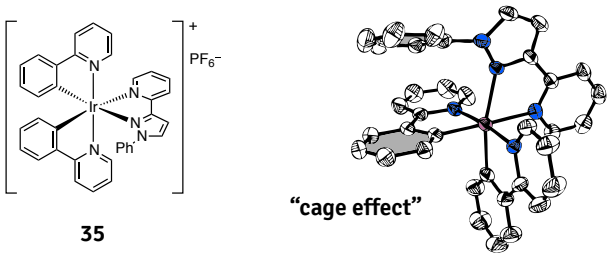

Figure 1.26: Schematic structure of complex **35** with the related X-ray structure, showing the result of the intramolecular π-stacking.

Although most of the work on the stability issue has been focused on improving the design of the complexes, a few early works also investigated the addition of inactive polymers, the effect of the cathode metal, and the device driving method [71, 142, 181]. For both polymer- and iTMC-based LECs, pulsed voltage driving was beneficial for the device stability [142, 181].

Recently, Tordera *et al.* reported a LEC based on an intrinsically stable iTMC that was driven by pulsed current (square wave, 1000 Hz, and 30 % duty cycle). This approach resulted in a turn-on time of less than one second and prevented the propagation of the doped zones, leading to a lifetime of approximately 4000 h with an initial luminance above 600 cd m^{-2} [175].

Efficiency

There are basically three key factors that can be used for evaluating the efficiency of LEC devices:

1) the external quantum efficiency (EQE);

2) the power efficiency (lm W^{-1});

3) the efficacy (cd A^{-1}, sometimes also referred as current efficiency).

Initially, single-layer LECs based on Ru-iTMCs had EQE values up to 1.8 % [33, 34, 108]. Liu *et al.* [139, 147] discovered that annealing the iTMC layer increased the EQE significantly to values as high as 3.6 %. This enhancement is due to partial crystallization of the amorphous film, which enhances the PLQY. As the iTMCs in LECs are responsible not only for the emission but also for the charge transport, their concentration in films must be high to decrease the inter-site distance. However, high concentrations favor exciton hopping and subsequently emission quenching. Rudmann *et al.* [71, 106] were capable of increasing the PLQY by reducing the concentration-quenching of excitons by blending the Ru-iTMC with an inert polymer, such as PMMA or PC (polycarbonate). The EQE values of these LECs reached a maximum value of 5.5 % at a luminance level in a range of 10 – 50 cd m^{-2} [71]. The limitation of this strategy is the decrease of electron and hole mobility that leads to higher driving voltages and a reduction of the power efficiency. Ultimately, the device efficiency is limited by the PLQY of the iTMC-based film [102, 103], this is why an alternative to ruthenium(II) complexes has been pursued.

In this sense, iridium(III) complexes have emerged as optimal materials for LECs. Indeed, several strategies have been proposed to increase the PLQY of these materials in film, which has led to a significant improvement of the device performance. These new approaches can be placed in two groups, the use of bulky groups and the host-guest approach.

Using bulky groups The first Ir-iTMCs that were used in LECs (**4** in Figure 1.9 on page 16 and **23** in Figure 1.20 on page 35) had *tert*-butyl groups attached to the ancillary ligand and afforded LECs with EQE values of 5.0 % and 4.6 %, respectively [76, 118].

Su *et al.* systematically showed the importance of the bulky groups using ligand 4,5-diaza-9,9'-spirobifluorene (**sb**, reported in Figure 1.12 on page 19) in two different Ir-iTMCs, **36** and **37** (see Figure 1.27) [104]. They exhibit high PLQYs and long excited-state lifetimes; for instance, the PLQY of a neat film of **36** (31.6 %) is ten-times higher than that of **2** (3 %) [37]. This situation suggests that **sb** prevents non-radiative pathways associated with concentration quenching effects. Devices that used single-layer neat films of **36** and **37** achieve high peak external quantum efficiencies and power efficiencies of 7.1 % and 22.6 lm W^{-1} at 2.5 V, and 7.1 % and 26.2 lm W^{-1} at 2.8 V, respectively.

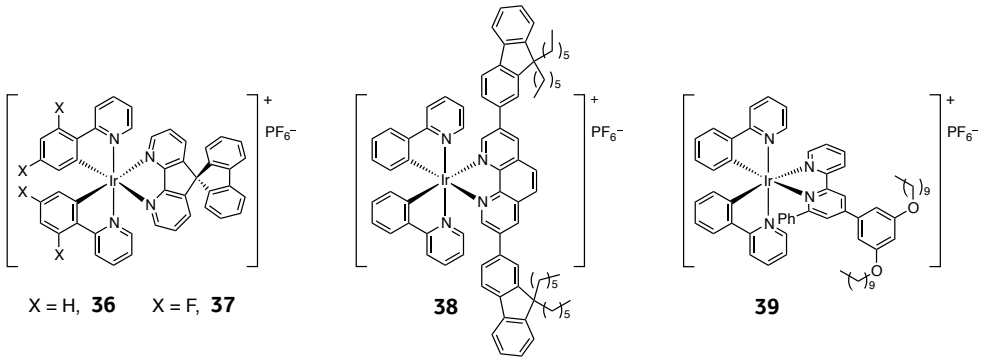

Figure 1.27: Structural formulae of complexes $[Ir(ppy)_2(sb)][PF_6]$ (**36**), $[Ir(dfppy)_2(sb)][PF_6]$ (**37**), $[Ir(ppy)_2(hf_2\text{-phen})][PF_6]$ (**38**), and $[Ir(ppy)_2(C_{10}ppbpy)][PF_6]$ (**39**) having bulky ancillary ligands.

Following this strategy, complex **10**, which contains the 4,4'-di-*tert*-butyl-2,2'-bipyridine ligand, and is also equipped with a difluorophenylpyridine instead of the conventional **ppy** cyclometallating ligand (see Figure 1.19 on page 33), was subsequently proposed [103]. This compound shows a PLQY value of 72 % in thin film, when diluted with the photophysically innocent $[BMIM]^+[PF_6]^-$ ionic liquid at a molar ratio 1:1 (see Table 1.3 on the next page). The same film composition was used in the LEC device, where the high amount of IL results in a lower turn-on time and higher luminance values (power efficiency of 38 lm W^{-1}, EQE = 14.9 %). This EQE is close to the value predicted by assuming a light outcoupling efficiency of 20 %, suggesting that high external efficiencies are only possible if almost quantitative internal electron-to-photon conversion occurs. This result corroborates the idea that the limiting factor for the efficiency of this kind of LECs is the PLQY of the light-emitting layer.

Table 1.3: Photoluminescence and electroluminescence properties of selected Ir-iTMCs with appended bulky groups. [a] Neat films. [b] Film with a iTMC:$[BMIM]^+[PF_6]^-$ molar ratio of 1:1. [c] Film with a iTMC:$[BMIM]^+[PF_6]^-$ molar ratio of 4:1.

Value	**36**	**10**	**38**	**39**
PLQY in film	31.6 % [a]	72 % [b]	36 % [a]	34 % [c]
EQE	7.1 % (2.5 V)	14.9 % (3 V)	—	6.1 % (3 V)

A series of $[Ir(ppy)_2(NN)][PF_6]$ complexes that presents several bulky groups attached to the **bpy** and **phen** NN ligands (*e.g.*, ligand **hf$_2$-phen** in Figure 1.12 on page 19) were reported by the groups of Bryce and Monkman (*e.g.*, complex **38** in Figure 1.27 and Table 1.3) [182, 183]. The addition of bulky groups has little effect on the intrinsic electronic properties of the complex, which exhibited enhanced steric hindrance and reduced self-quenching in thin films. This series of Ir-iTMCs showed high PLQY values (around 40 %) and long excited-state lifetimes (around 0.20 s) in concentrated thin films. Accordingly, the related LECs yielded efficacies as high as 7 cd A^{-1} and high luminances (1000 cd m^{-1} at 3 V). Notably, there are limits in the use of large substituents because driving voltages tend to increase as a consequence of larger intermolecular separation. In a related work, similar carbazole substituents were used in combination with dimesitylboryl groups [184], where high PLQY of the complexes (52 %, in PMMA matrix) was obtained, but the related LECs showed poor EQE values.

A new series of $[Ir(ppy)_2(NN)][PF_6]$ complexes that use phenolic ether groups to increase the inter-site distance and the 6-phenyl group on the **bpy** ligand to allow for intra-complex π-π interactions was recently described (*e.g.*, complex **39** in Figure 1.27 and Table 1.3) [102]. By increasing the size of the bulky side groups, the PLQY in the light-emitting layer of LECs (Ir-iTMC/$[BMIM]^+[PF_6]^-$, 4:1) increases from 24 % to 38 %. The photophysical, electrochemical, and theoretical studies showed that addition of the bulky groups does not affect the emitting excited state, in agreement with other reports [182, 183]. LECs using these complexes exhibit a roughly sixfold increase in the EQE when compared with the archetype complex without phenyl and phenolic ether groups. Additionally, other important device parameters, such as turn-on time, luminance, and stabil-

ity improved upon increasing the size of the bulky groups. However, also in this case it was demonstrated that there is a limit to the size of the bulky groups that can be used before the device driving voltage starts to increase [102].

Control over distance between Ir-iTMCs was also attempted using dinuclear complexes equipped with an oligophenyleneethynylene spacer [185]. However, the spacer introduced efficient non-radiative pathways through its low-lying triplet level, as demonstrated by photophysical, electrochemical, and theoretical studies. The related EQE values (up to 0.16 %) were in line with what was expected taking into account the low PLQYs, suggesting that the introduction of a molecular spacer could be a useful strategy to minimize the self-quenching in the operating device.

Diluting an iTMC into an ionic matrix: the host-guest approach To effectively confine excitons, an emitting iTMC can be dispersed in an ionic matrix that has a wider band gap and higher excited-state energy. This approach is analogous to what is frequently carried out in OLEDs, in which iridium complexes are dispersed in matrix materials. Herein, we will not extensively comment on the numerous reports on ionic iridium complexes dispersed in neutral matrix materials; we will focus on ionic matrix materials and refer to a particular paper by He *et al.* [186] as well as to recent reviews for the work related to neutral matrix materials [75, 165].

In chronological order, Hosseini *et al.* were the first to propose the doping of a thin film of $[Ru(bpy)_3][PF_6]_2$ (**3**, host) with small amounts of $[Os(phen)_3][PF_6]$ (**40**, guest) [138], demonstrating that LECs containing 5 wt% of the Os(II) complex emit from the guest compound with a higher EQE than the device using pure **40**, thanks to the dilution of the Os-iTMC that decreases self-quenching. They further demonstrated that the electroluminescence spectrum can be tuned by the concentration of the guest and that the doped devices are more stable than those based on the host complex alone.

Subsequently, Su *et al.* applied this concept to Ir-iTMCs and presented highly efficient LECs consisting of the green-emitting **37** as host and the orange-emitting **36** as guest (see Figure 1.27 on page 49) [107]. Photophysical studies in thin films showed that, at an optimized guest concentration of 25 wt %, high PLQYs and long excited-state lifetimes were observed, highlighting a relevant decrease of self-quenching. Notably, the addition of the $[BMIM]^+[PF_6]^-$ ionic liquid (19 wt %)

further increases the PLQY and the excited-state lifetime. LECs based on this host-guest system exhibit the highest EQEs (around 10 %) and power efficiencies (36.8 lm W^{-1}) observed applying this concept. Soon after this result, the same authors used this approach to prepare the first white LEC, which is described in more detail in a dedicated section on page 59 [159]. Recently, they utilized complex **37** (see Figure 1.27) as the host for a fluorescent cationic dye (Rhodamine 6G) achieving high EQE and power efficiency values of 5.5 % and 21.3 lm W^{-1} respectively, using a low dye doping (0.10 wt %) [187].

Recently, the same group investigated the electroluminescence properties of a cationic terfluorene derivative (see Figure 1.28), obtaining a deep-blue-emitting LEC [188]. Eventually, they used the host-guest concept by dispersing a red iTMC (41) in the same cationic derivative (Figure 1.28) [189]. The main advantage of this approach is the strong reduction in the amount of iridium-based material used, that results in a significant decrease of the material cost. By tuning the concentration of the red Ir-iTMC, optimization of the carrier mobilities was achieved leading to relatively high EQE (3.6 %) and power efficiency (7.36 lm W^{-1}). Considering the rather low PLQY of the host-guest film (20 %), an almost perfect charge carrier balance is probably achieved.

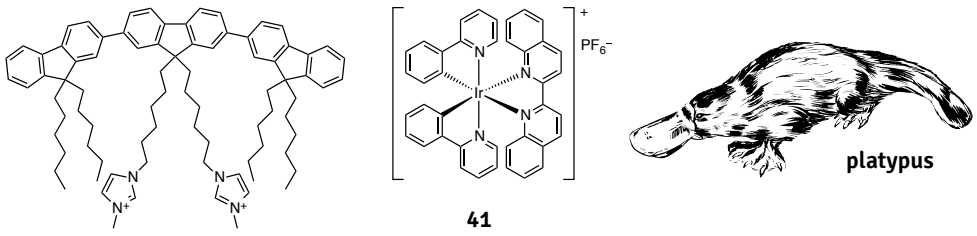

41

Figure 1.28: Schematic structures of the host molecule, a cationic terfluorene derivative (left), and the $[Ir(ppy)_2(biq)][PF_6]$ guest (**41**, center). Also a platypus (right) is reported since it is the most beautiful animal.

In a different approach, Chen *et al.* prepared an Ir-iTMC in which was integrated a charge-transporting molecule (the neutral ligand bis(diphenylamino)-9,9'-spirobifluorene), with the aim of having a three-in-one system. The LEC prepared using this complex showed very low efficiency as a result of the quenching of the charge-transporting neutral ligand used [190].

Tuning the emission color

Most ruthenium-based LECs emit in the orange spectral region [28, 29]. The strategies used to modify the emission color of Ir-iTMCs have been discussed before. Herein, we focus on LECs emitting across the whole visible spectrum, including white. Their performances are compared with the LEC based on the archetypal iridium(III) complex $[Ir(ppy)_2(bpy)][PF_6]$ (**2**, in Figure 1.3), that emits orange light (λ_{max} = 590 nm, CIE coordinates x = 0.5078; y = 0.4859) [37].

Near-Infrared-Emitting LECs Near-infrared (NIR) light-emitting sources are typically expensive and LECs could serve as low-cost alternatives in areas were NIR luminescence is of key importance, such as telecommunications and bioimaging [191]. Few studies concerning solid-state NIR LECs, that is, having the EL peak wavelength longer than 700 nm, have been reported and most of them concern ruthenium iTMCs. Typically they exhibit EQE less than 0.1 % [133, 135, 138, 192, 193] mainly because of the energy gap law that disfavors radiative transition at lower emission energies [118], but also owing to self-quenching induced by the high density of iTMC in the emitting layer.

Recently, Ho *et al.* reported a more efficient NIR iTMC-based LEC reaching EQEs of 1.2 % [194], that used the orange-emitting Ir-iTMC **36** (in Figure 1.27 on page 49) as host and different fluorescent ionic NIR laser dyes as guest. Maximum EQE values of 0.8 % and 1.2 % were measured, respectively.

Red LECs Ancillary ligands with low-energy LUMO levels have been used to design red Ir-iTMCs. Tamayo *et al.* proposed the use of various ancillary and cyclometalating ligands [118], presenting LECs with the red-emitting complex **42** (reported in Figure 1.29 on the following page; λ_{max} = 635 nm; CIE coordinates x = 0.67; y = 0.32; EQE of 7.4 %). Following this result, He *et al.* [81] prepared red LECs using complex **43** emitting at about 650 nm (CIE coordinates x = 0.66; y = 0.33; EQE of 2.6 %); complex **43** has also been used as dopant in the fabrication of white LECs [159].

Modification of the archetype complex **2** by the attachment of different types of electron-withdrawing groups to the 4,4'-positions of the **bpy** ligand was also made. Complex **44** (in Figure 1.29) affords LECs with the electroluminescence peaked at 630 nm (CIE: x = 0.710; y = 0.283) [113]. The EL spectrum is significantly red-shifted compared to the reference LEC with **2**, which was attributed to the

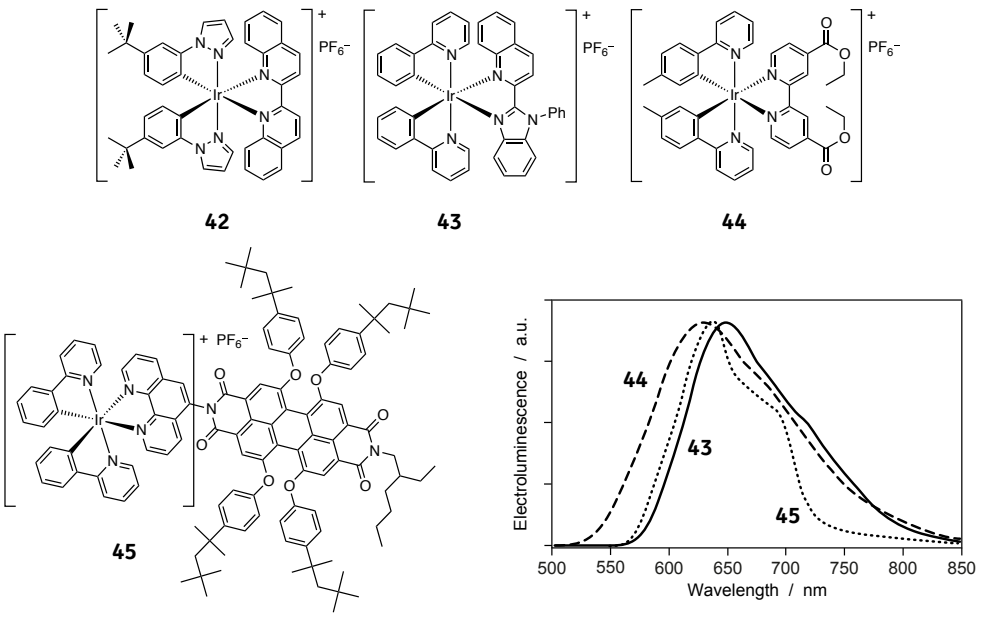

Figure 1.29: Structural formula of red-emitting Ir-iTMCs: $[Ir(tb\text{-}ppz)_2(biq)][PF_6]$ (**42**), $[Ir(ppy)_2(qIbi)][PF_6]$ (**43**), $[Ir(mppy)_2(e\text{-}bpy)][PF_6]$ (**44**), and $[Ir(ppy)_2(phen\text{-}PDI)][PF_6]$ (**45**). Bottom-right: EL spectra of LECs based on **43** (solid line), **44** (dashed), and **45** (dotted).

stabilization of the LUMO by the introduction of the ester groups.

Su *et al.* used a fluorescent dye in an Ir-iTMC to generate efficient red electroluminescence reaching 19 cd A^{-1} and 21.3 lm W^{-1} [187].

In a similar approach, Costa *et al.* [195, 196] showed the beneficial effect of anchoring a perylenediimide (PDI) red fluorescent emitter to an ionic iridium(III) complex (**45**, in Figure 1.29) [196]. The EL spectrum of the LEC incorporating **45** is attributable to the PDI moiety (λ_{max} = 634 nm, CIE coordinates x = 0.654; y = 0.344). They also showed in a separate study that triplet radiationless pathways occur through the PDI moiety [195] but, surprisingly, LECs using such an Ir-iTMC-PDI complex showed external quantum efficiencies as high as 3.3 %. This efficiency was attributed to the high fluorescence quantum yield (55 %) of PDI and short lifetime (3 ns) of the generated exciton, which decreases its diffusion. Thereby, the chance to suffer deactivation by impurities or grain defects in the film is reduced.

Yellow and green LECs As previously described, the attachment of electron-donating groups on the 4,4'-positions of the **bpy** ligand increases the HOMO–LUMO gap. Slinker *et al.* used this strategy for the first time [76] showing that LECs with complex **4** (reported in Figure 1.9 on page 16) exhibit a slightly blue-shifted EL spectrum (λ_{max} = 560 nm), when compared to that obtained with the reference compound **2** (λ_{max} = 590 nm). A further blue-shift at λ_{max} = 520 nm was observed for the LEC with complex **9** (in Figure 1.19 on page 33), which contains two dimethylamino groups [111]. The luminance (200 cd m^{-2}) and, more importantly, the efficiency (EQE = 0.2 %) of this LEC was significantly reduced compared to reference complexes **2** and **4**.

Costa *et al.* recently reported a series of iridium(III) complexes and showed that addition of methyl groups in the 6,6'-positions of the **bpy** ligand progressively shifts the EL spectrum to the greenish region compared to **2** [197]. For example, LECs using complex **46** (reported in Figure 1.30) showed an electroluminescence emission maximum at 555 nm with CIE coordinates x = 0.436; y = 0.549. In contrast, substitution of these positions by one or two phenyl groups as for example in complexes **31** and **32** (see Figure 1.25 on page 45) does not cause any spectral change [99, 168].

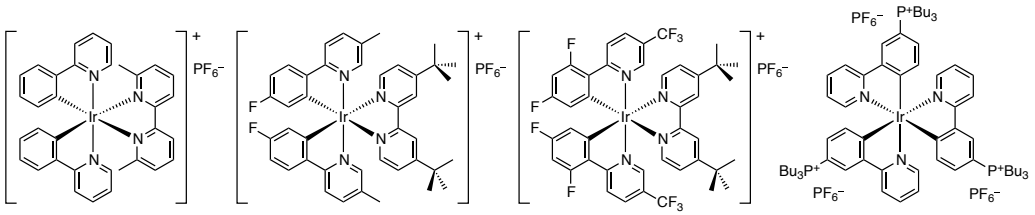

46 **47** **48** **49**

Figure 1.30: Structural formula of yellow- and green-emitting Ir-iTMCs: $[Ir(ppy)_2(m_2bpy)][PF_6]$ (46), $[Ir(fmppy)_2(dtb\text{-}bpy)][PF_6]$ (47), $[Ir\{df(CF_3)ppy\}_2(dtb\text{-}bpy)][PF_6]$ (48), and $[Ir(bu_3P{-}ppy)_3][PF_6]_3$ (49).

Green LECs were also achieved by using electron-withdrawing groups attached to the phenyl ring of the cyclometalating ligands, which stabilize the HOMO level of the complex [105, 118, 157, 160]. Slinker *et al.* [105] were able to make a LEC using complex **47** (in Figure 1.30) with a blue-shifted EL spectrum (λ_{max} = 542 nm, CIE coordinates x = 0.368; y = 0.577) compared to the non-fluorinated complex **4** (λ_{max} = 560 nm). The pristine device showed an EL spec-

trum that was independent of the bias direction and electrodes used. However, addition of an ionic liquid to the light-emitting layer, which improves the turn-on time as discussed before, introduced a bias-dependent shift in the EL spectrum (λ_{max} = 531 nm at +3 V, λ_{max} = 558 nm at −3 V). This shift was also observed in LECs involving other Ir-iTMCs combined with $[BMIM]^+[PF_6]^-$ [82].

Following this result, Su *et al.* proposed a similar strategy involving the use of ancillary ligands with high-energy LUMO levels [104, 107]. They proposed complex **37** (see Figure 1.27 on page 49), which afforded a green-emitting LECs (λ_{max} = 535 nm) with a high EQE (7.1 %). A similar emission color (λ_{max} = 525 nm; CIE coordinates x = 0.299; y = 0.451) was observed for a LEC with complex **10** (see Figure 1.19 on page 33) [103].

Lowry *et al.* [91] proposed complex **48**, an Ir-iTMC equipped with two multifluorinated cyclometalating ppy-based ligands (see Figure 1.30 on the previous page). This complex yielded LECs with blue-green emission (λ_{max} = 500 nm; CIE coordinates x = 0.198; y = 0.512). Interestingly, these devices also showed a slight blue-shift in the EL peak from 520 nm to 500 nm in going from positive to negative voltages.

Tamayo *et al.* [118] demonstrated that the use of Ir-iTMCs with cyclometalating ligands other than **ppy**, such as **ppz**, also blue shifts the emission because of HOMO stabilization. They obtained green LECs (λ_{max} = 542 nm; CIE coordinates x = 0.37; y = 0.59) using complex **24** that show a remarkable EQE value of 6.9 %.

To obtain blue-green emission, Bolink *et al.* modified a neutral iridium(III) complex with charged tributylphosphonium side groups at the periphery of the cyclometalating ligands [198]. Blue-green LECs (λ_{max} = 487 nm) were obtained by blending complex **49** (reported in Figure 1.30 on the preceding page) with 20 % of PMMA, with a spectral shift to 570 nm after 100 s of operation at 4 V. The blue-shifted emission compared to **2** was attributed to the electron-withdrawing nature of the tributylphosphonium group.

Blue LECs The first blue LEC was obtained by attaching electron-withdrawing groups to the **ppz** ligand (reported in Figure 1.11 on page 18) [118]. LECs using complex **23** (in Figure 1.20 on page 35) exhibit electroluminescence at λ_{max} = 492 nm (CIE coordinates x = 0.20; y = 0.41) and remarkable EQE of 4.6 % at low voltage.

Blue LECs have also been obtained by using iridium(III) complexes based on derivatives of **ppy** and devised ancillary ligands. He *et al.* [82] utilized an-

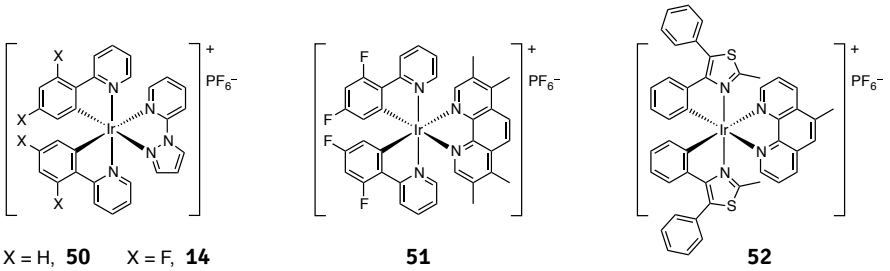

Figure 1.31: Structural formula of blue-emitting Ir-iTMCs: $[Ir(ppy)_2(pzpy)][PF_6]$ (50), $[Ir(dfppy)_2(pzpy)][PF_6]$ (14), $[Ir(dfppy)_2(Me_4phen)][PF_6]$ (51), and $[Ir(dpmt)_2Mephen][PF_6]$ (52); dpmt = 4,5-diphenyl-2-methylthiazolo and Mephen = 5-methyl-1,10-phenanthroline.

cillary ligands involving electron-donating nitrogen atoms and prepared two blue-emitting Ir-iTMCs, **50** and **14** (both reported in Figure 1.31), using the novel **pzpy** ligand to make blue LECs with λ_{max} around 450 – 475 nm, which is shifted by more than 100 nm compared to the EL spectrum of the LEC with the reference complex **2** (λ_{max} = 590 nm). Single-component LECs (*i.e.*, the active layer is based on only the Ir-iTMC) showed blue-green emission: λ_{max} = 486 nm (**50**) and λ_{max} = 460 nm (**14**) with CIE coordinates of x = 0.27; y = 0.50 and x = 0.20; y = 0.28, respectively. The EQE values of both LECs are in the range 0.3 – 0.4 %. Addition of the $[BMIM]^+[PF_6]^-$ ionic liquid shifted the EL spectrum of devices using **14** to the green region (λ_{max} = 526 nm; CIE coordinates x = 0.33; y = 0.45); however, it did not affect the EL spectrum of LECs made with **50**.

The same group presented another example (**54**, in Figure 1.32 on the following page) with the presence of bulky groups (4-tritylphenyl) to improve the PLQY and, thereby the efficiency of the device. Indeed, LECs based on this complex show remarkably efficient blue-green electroluminescence with peak current efficiency, external quantum efficiency, and power efficiency of 18.3 cd A^{-1}, 7.6 %, and 18.0 lm W^{-1}, respectively [199].

Mydlak *et al.* [116] proposed the use of several derivatives of the pyridine-1,2,3-triazol ligand together with the **dfppy** cyclometalating one (see Figure 1.11). LECs based on complex **15** (reported in Figure 1.19 on page 33) show blue EL spectra with two peaks at 460 nm and 480 nm, similar to the results obtained in solution and in thin films. These devices present short turn-on times of a few minutes at 5 V; however, luminance (approx. 20 cd m^{-2}) and stability ($t_{1/2}$ of a

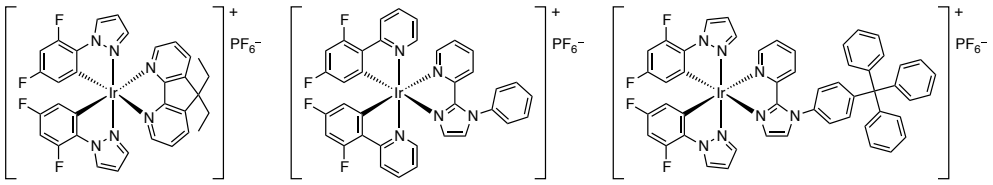

53 **54** **55**

Figure 1.32: Structural formula of blue-green-emitting Ir-iTMCs used for obtaining white-emitting LECs: $[Ir(dfppz)_2(dedaf)][PF_6]$ (53), $[Ir(dfppy)_2(pyim)][PF_6]$ (54) and $[Ir(dfppz)_2(tp{-}pyim)][PF_6]$ (55).

few minutes) were moderate.

Following this work, Chen *et al.* proposed a similar family of complexes with triazole pyridine as the ancillary ligand (**16**, in Figure 1.19) which led to LECs with sky-blue (λ_{max} around 458 nm) and blue-green (λ_{max} around 484 nm) emissions and moderate EQE values (ca. 3 %). They also claimed that the addition of cyano groups at the end of the alkyl substituents is responsible of the enhancement of the efficiency [117].

A new approach, based on the use of carbene-type ligands, was recently introduced by Yang *et al.* [85] They demonstrated that the combination of methyl- or *n*-butyl-substituted bisimidazolium carbene-type ligands together with the **dfppy** cyclometalating ligand yields blue LECs with EL maxima in the region 450 – 490 nm. These devices exhibit luminance and efficiency values lower than 25 cd m^{-2} and 1 cd A^{-1} at 5.5 V.

In the same direction, Kessler *et al.* proposed a family of Ir-iTMCs using a neutral pyridine carbene ancillary ligand (**22**, in Figure 1.19) to cover the whole visible spectrum [121]. For instance, devices with complex **22** and its fluorinated version (*i.e.*, complex with fluoro groups in the cyclometalating ligand) show blue-green emissions at 544 nm and 512 nm, respectively. However, high voltages (6 V) are needed to obtain moderate luminance values (20 cd m^{-2}).

Bolink *et al.* [158] used **51** as a blue emitter (see Figure 1.31 on the preceding page), which exhibits λ_{max} = 476 nm in solution and in diluted film but undergoes a substantial shift of 84 nm in EL, emitting green light (λ_{max} = 560 nm; CIE coordinates x = 0.417; y = 0.533). This large spectral shift in the LEC does not stem from the different excitation mode or from the presence of large concentrations of ions, but is related to the concentration of the Ir-iTMC in the thin film. In fact,

in concentrated films, emission is due to deactivation of metal-to-ligand charge transfer (^{3}MLCT) states, whereas in diluted samples ligand-centered (^{3}LC, π-π*) emission occurs. Using quantum chemical calculations, it was demonstrated that three low-energy triplet states, with associated emission wavelengths differing by as much as 60 nm from each other are present. Notably, the occurrence of excimer formation was ruled out because the excited-state lifetime in concentrated films was found shorter than in diluted samples. In contrast to this finding, Margapoti *et al.* [200] showed the formation of excimers by photoluminescence excited-state lifetime measurements in LECs based on complex **52** (reported in Figure 1.31 on page 57) at voltages larger than 7 V. Formation of excimers is induced by the applied electric field and is responsible for the different emission maxima observed in photoluminescence and electroluminescence spectra.

Dumur *et al.* also observed a shift in the emission wavelength over time for a green LEC, they attributed this emission shift to degradation or a temperature-induced modification of the molecular packing [174].

In a study by Liao *et al.*, it was shown that the efficiency of a blue-emitting LEC was improved by adding a NIR dye, as a carrier trapper, to the iTMC-emitter blend. This LEC exhibited higher efficiency than the pristine device leading to an EQE around 13 % and a power efficiency of 28.7 lm W^{-1} [201].

White LECs Su *et al.* [25, 159] reported the first white LEC based on the host-guest strategy (see more detailed discussion on page 51). They demonstrated that white-light emission (CIE coordinates from x = 0.45 / y = 0.40 to x = 0.35 / y = 0.39 at 2.9 V and 3.3 V, respectively) with EQE values around 4 % are easily achieved by mixing two Ir-iTMCs, namely the blue-green complex **53** (host, 80.5 wt %; structure reported in Figure 1.32) and the red complex **41** (guest, 0.4 wt %; structure in Figure 1.28 on page 52) in a single-layer, along with the $[BMIM]^+[PF_6]^-$ ionic liquid (19.1 wt %). Although efficient LECs were made, the luminance level reached was low (43 cd m^{-2} at 3.3 V).

He *et al.* [81, 199] introduced a new series of Ir-iTMCs based on imidazole-type ancillary ligands with which nearly the whole visible spectral region could be covered [81]. LECs using complex **54** (reported in Figure 1.32) showed blue emission (λ_{max} = 497 nm, CIE coordinates x = 0.25; y = 0.46 and EQE = 3.4 %); by adding the red-emitting complex **43** (reported in Figure 1.29 on page 54), warm

white host-guest LECs were prepared (CIE coordinates $x = 0.40$; $y = 0.45$). The composition of the light-emitting layer was **54** / $[BMIM]^+[PF_6]^-$ / **43** at a molar ratio of 1 : 0.35 : 0.002. High EQE values of 4.4 % at luminance value of 115 cd m^{-2} were obtained at 4 V, which are the best performances reported to date for white LECs (see Table 1.4).

Recently, the same group synthesized the blue-emitting complex **55** by attaching a bulky tritylphenyl group to the pristine **pyim** ancillary ligand (see Figure 1.12 on page 19) [199]. The related blue LEC has more than double the EQE value (7.6 %) of LECs with **54** (3.4 %). Again, using the red complex **43** as dopant (at 0.8 % in molar ratio with respect to the blue emitter), they also prepared white LECs (CIE coordinates $x = 0.37$; $y = 0.41$), but the performance was poorer than that reported in their first work: EQE was slightly enhanced (5.6 %) but the luminance level was under 10 cd m^{-2}.

Best performances for a white LEC were reached by Su *et al.*, who doped the blue-emitting $[Ir(dfppz)_2(dtb\text{-}bpy)][PF_6]$ (**23**), with the red- $[Ir(ppy)_2(biq)][PF_6]$ (**41**), and the orange- $[Ir(ppy)_2(dasb)][PF_6]$ (**36**) emitting complexes. In this way, an EQE of 7.4 % and a power efficiency of 15 lm W^{-1} were obtained [187].

Recently, He *et al.* presented efficient and color-stable white LECs which combine single-layered blue-emitting LECs (complex **23**) with a red-emitting color-conversion layer on the bottom side of the glass substrate. Spectral overlap between the absorption spectrum of the red emitter and the emission spectrum of the blue-emitting material results in efficient energy transfer and down-conversion at low doping concentrations of the red fluorophore. Peak external quantum efficiency and power efficiency of the white LEC reach 5.93 % and 15.34 lm W^{-1}, respectively [202].

Table 1.4: The best performances reached in white LECs. IL refers to $[BMIM]^+[PF_6]^-$ ionic liquid.

Devices	Voltage (V)	Turn-on-time (min)	Luminance (cd m^{-2})	Lifetime (min)	EQE %	Ref.
53 / IL / **41**	2.9	240	2.5	540	4.0	[159]
54 / IL / **43**	4	90	115	800	4.4	[81]
55 / IL / **43**	3.2	22.5	7.9	80	5.6	[199]
23 / **41** / **36** / IL	3.1	60	11.5	120	7.4	[187]

1.4.5 LECs based on metal complexes other than iridium(III)

As already extensively reported in the previous sections, the most widely employed luminophores in LECs are cationic iridium(III) complexes. This is attested by a large body of literature describing a variety Ir-iTMCs covering the whole visible spectral window and even showing white emission [73].

However, the first examples of LEC devices with transition-metal complexes as light-emitting materials were based on ruthenium(II) compounds and reported in 1996 [27, 125]. Subsequently, other Ru(II)-based complexes, which were discussed more extensively in previous reviews, have been investigated [29]. Also in recent years, other complexes mainly based on ruthenium(II) and copper(I) metals have been reported; herein, we present some selected examples.

Ruthenium(II)-based LECs

The mononuclear heteroleptic terpyridine-based ruthenium(II) complex **56** (reported in Figure 1.33 on the next page) exhibits a deep-red emission centered at 750 nm) and it was used to make a LEC device with an external quantum efficiency of about 0.005 % [135]. Ru(II) complexes involving bipyridine derivatives (complex **57**, in Figure 1.33) [203] have been also investigated and show enhanced luminescence compared to $[Ru(bpy)_3][PF_6]_2$ (complex **3**) [7].

Within this family, Zysman-Colman *et al.* [171] found that the addition of pendant triethylammonium groups on the bipyridine units (**58**, in Figure 1.33 on the following page) leads to a device turn-on time as short as 4 s to be compared with 1 min for archetypal complex **3**.

Dinuclear ruthenium(II) complexes have been also tested as active materials in devices. For instance, the device made with complex **59** (reported in Figure 1.33), in the presence of a mixture of Li salt and crown ether as a solid electrolyte, exhibits a particularly low threshold operating voltage of 2.5 V [204].

Finally, Jia *et al.* [205] fabricated a red-emitting electroluminescent devices based on polynuclear Ru(II) complexes (**60**, in Figure 1.33) and involving pyridyl benzimidazolyl derivatives as bridging ligands; they exhibit red emission centered at around 650 nm and perform better than devices based on standard **3**.

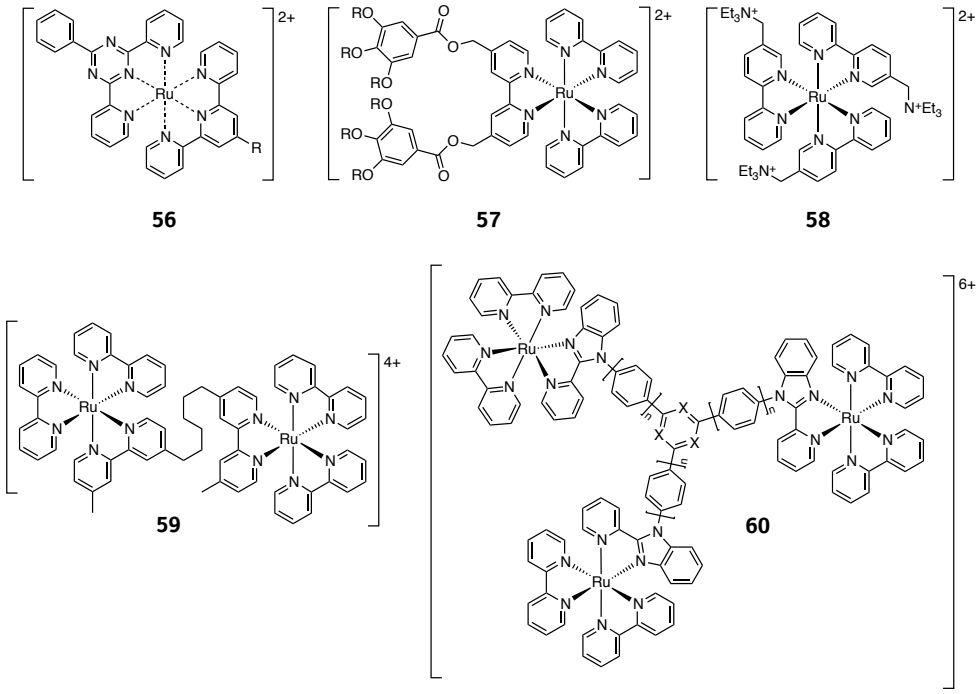

Figure 1.33: Structural formula of some Ru(II) complexes used as light-emitting materials in LECs.

Copper(I)-based LECs

The limited list of transition-metal ions used to make complexes for LEC devices includes copper (I). The advantages of using this metal are related to its abundance, low cost compared to platinum-group elements, and low toxicity [206, 207].

The photophysics of Cu(I) complexes has been extensively reviewed and the luminescence properties of several classes of Cu(I) compounds studied [206–208]. The most investigated ones include the NN-type (where NN indicates a chelating diimine ligand, typically 1,10-phenanthroline) and the PP-type (where PP denotes a bisphosphine ligand) giving rise to both homoleptic $[Cu(NN)_2]^+$ and heteroleptic $[Cu(NN)(PP)]^+$ motifs [22].

These tetrahedral cuprous complexes always undergo a significant geometry change going from the ground to excited state, which cause considerable displacement from D_{2d} symmetry and lead to an increase of nonradiative pathways. Compared to the classical $[Cu(NN)_2]^+$ systems, those involving bulky phosphines

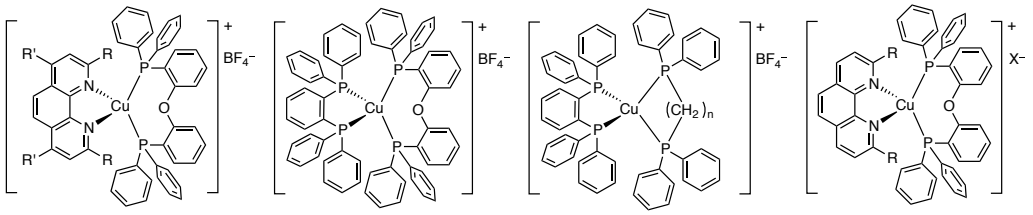

61 62 63 64

Figure 1.34: Structural formula of some copper(I) complexes used as light-emitting materials in LECs.

$[Cu(NN)(PP)]^+$ have improved emission properties because both of intra- and intermolecular π-stacking interactions and of the electron-withdrawing effect of the PP unit on the metal center that tends to disfavor the Cu(I)-to-NN electron donation, leading to a blue-shift of the MLCT transitions. This last factor, according to the energy gap law [87], brings about a substantial emission enhancement [206], that has greatly increased the interest toward this class of heteroleptic compounds [209]. Herein, we only report on copper(I) compounds used as light-emitting materials in LEC devices.

The first LEC based on copper(I) complexes involved the heteroleptic system **61** (reported in Figure 1.34) [149] that shows excellent green emission at λ_{max} = 550 nm (with 28 % PLQY in CH_2Cl_2 solution). The LEC performance was moderate, but comparable to that of devices involving green-emitting Ru(II)complexes at λ_{max} = 540 nm.

In 2007, Moudam *et al.* [150] reported homo- and heteroleptic copper(I) complexes involving chelating phosphine ligands (**62** and **63**, in Figure 1.34), which were also used for the preparation of LECs. The broad electroluminescence band, centered at 580 nm, causes an almost white-light output, and the devices exhibited a turn-on voltage of 15 V and a brightness up to 490 cd m^{-2} at 20 V.

Zhang *et al.* [154] reported LECs made from the heteroleptic $[Cu(NN)(PP)]^+$ complex **64** (reported in Figure 1.34), which showed green-light emission peaked at λ_{max} = 523 nm. It was shown that the turn-on time of the devices was strongly affected by the driving voltage, the counterions, and the thickness of the film. The replacement of Al with Ca (a lower work-function metal) significantly enhanced the brightness of the device.

The last example of Cu-iTMC-based LECs was recently reported by Costa *et al.* [155]. They compared the performance in LECs based on two families of

Cu(I) complexes with **bpy** and **phen** as NN ligands and different PP ligands (see Figure 1.35). They demonstrated that LECs fabricated with those complexes and the $[EMIM]^+[PF_6]^-$ ionic liquid (see Figure 1.24 on page 43, top) at a molar ratio of 1:1 show comparable performances at low voltages (< 5 V) to those obtained for most LEC devices based on ruthenium(II) and iridium(III) complexes, that is, luminance and efficacy values up to 60 cd m^{-2} and 4.5 cd A^{-1}, respectively. This fact highlights the prospect of copper(I) complexes in LECs.

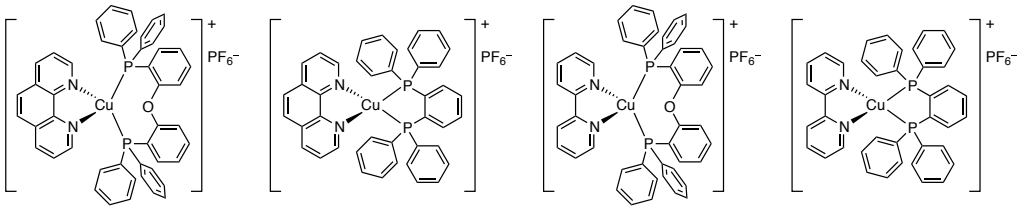

65 **66** **67** **68**

Figure 1.35: Schematic structures of the most recent examples of copper(I) complexes used in LECs. Both complexes **65** and **67** have bis(2-(diphenylphosphino)phenyl ether as diphosphine ligand, complexes **66** and **68** have 1,2-bis(diphenylphosphino)benzene.

1.5 Conclusion and outlook

In the last few years, some technologies have undergone a radical change, particularly in the area of telecommunications, so that nowadays we can easily access a virtually unlimited amount of information at amazingly affordable prices. Similar astounding achievements have not occurred in other sectors; in fact, there are some pervasive technologies that are still far from being massively replaced, a notable example being internal combustion engines for transportation [6]. In between these extreme cases, some technological sectors are experiencing a progressive transformation that will lead to epochal transitions within the next ten years or so. A notable example is artificial illumination in which, also thanks to the phase-out of traditional filament lamps, the innovative concept of cold lighting has opened the way to new point light sources and flat light sources (LEDs, OLEDs) which are increasingly relevant players in the lighting market, particularly for screen backlighting [10].

In the field of innovative flat light sources, OLEDs are presently the most advanced in terms of efficiency, color quality, and operation lifetime, but the still complex and expensive manufacturing routes have stimulated the search for alternative concepts, such as LECs. The basic advantages of LECs over OLEDs are:

1) the substantially wider availability of charged transition-metal complexes compared to neutral ones, which widens the spectrum of exploitable phosphorescent emitters;

2) the smaller number and lower chemical reactivity of the layers and the electrodes to assemble, which considerably facilitate the manufacturing of the device.

We have provided herein an overview on the state-of-the art of the performance of LECs, which have achieved respectable efficiency across all the visible spectral region, from blue to deep red, with white LECs having CRI values as high as 80 [159]. This progress has been made possible by the design and synthesis of an enormous number of transition-metal complexes, most of them based on iridium(III). This massive synthetic work was driven by a deeper understanding of the factors than govern ground- and excited-state photophysical properties, an understanding which was achieved through a great deal of theoretical modeling and spectroscopic studies. The "historic" drawbacks of LECs, long turn-on times and moderate lifetimes [28], have been substantially improved through the use of ionic liquids and by modifying the driving method. However, the best figures of merit of LECs have been met in separate devices and much research will be needed before combining high efficiency, white color, fast turn-on, and long stability in a single device. This calls for further efforts to:

a) unravel the intrinsic mechanism of operation of the device;

b) understand the processes of chemical degradation of the luminophores under operating conditions;

c) synthesize new robust electroluminescent materials;

d) design alternative device architectures.

The encouraging progress made in recent years in the improvement of performance [24], combined with the two fundamental aforementioned advantages of LECs when compared to OLEDs, makes them promising candidates for low-cost, versatile, and energy-efficient flat light sources. Given the increasing importance of life-cycle sustainability and resource efficiency in the design and fabrication of new products [210], particularly those containing rare elements [211], the simple structure of LECs may provide a relevant advantage in terms of disassembling and recycling, further enhancing their prospects for successful market applications in the mid-long term.

Chapter 2

Blue phosphorescence: hard task

In this chapter we report two series of charged iridium(III) complexes with various carbene-based ancillary ligands. In the first series the cyclometalating ligand is 2-phenylpyridine (**ppy**) whereas in the second one it is the fluorinated 2-(2,4-difluorophenyl)-pyridine (**dfppy**). Four different pyridine-carbene and one bis-carbene chelators are used as bidentate ancillary ligands in each series. Synthesis, X-ray crystal structures, photophysical and electrochemical properties of the two series of complexes are described. DFT calculations are also used to rationalize the differences in the photophysical behavior observed upon change of the ancillary ligands.

It is shown that complexes based on pyridine-carbene ancillary chelators possess a low-lying triplet MC state mainly deactivating through non-radiative processes; by contrast, no such state is present for the bis-carbene analogues. This explains why, at room temperature, the latter complexes display much larger photoluminescence quantum yields (approx. 30 %), if compared to the pyridine-carbene analogues (PLQYs around 1 %). Likewise, it makes clear why all of the investigated complexes are bright emitters in the solid state both at 77 K and in room-temperature diluted PMMA matrix.

2.1 Introduction

As already extensively explained in the first chapter, luminescent cyclometalated iridium(III) complexes have attracted substantial interest in the area of LEC technology, due to their widely tunable color gamut, high luminescence

quantum yields, and remarkable chemical stability. However, the development of deep-blue stable Ir-based emitters has turned out to be a rather challenging task [24, 212].

In the case of neutral iridium(III) complexes for OLEDs, deep-blue emission has been already achieved by using ligands with high triplet energy levels such as carbene- or pyrazole-based chelators [213, 214]. In the case of cationic phosphorescent emitters for LECs, one possible strategy for high-energy emission can be obtained using bidentate ligands bearing a methylene bridge [85, 215]. Anyway a limited stability of the material is expected, because the delocalization between the two aromatic rings is broken and a six-membered metalacycle with the iridium center is formed. In order to improve the stability of chelation, bidentate ancillary ligands forming a five-membered metalacycle are preferable.

Typical examples of this kind of charged bis-cyclometalated iridium(III) complexes are based on neutral NN ancillary ligands. In fact, these type of ligands can form five-membered metalacycles with the iridium metal center: *e.g.*, bipyridine [92, 105, 118, 119, 169, 179, 216, 217], phenanthroline [182], pyridine-pyrazole [82], pyridine-imidazole [81], pyridine-triazole [116], and also pyridine-tetrazole [218], *etc.* In these complexes the emission is typically of metal-to-ligand charge transfer (MLCT) nature from the iridium ion to the NN ancillary ligand. Deeper blue emission can be obtained by using NN ligands with higher-lying lowest-unoccupied molecular orbital (LUMO) than bipyridine, and/or by stabilizing the highest-occupied molecular orbital (HOMO) through introduction of fluorine electron-withdrawing groups on the orthometalated phenyl ring [81, 82].

Only recently, Kessler *et al.* reported a strategy based on a neutral pyridine-carbene ancillary ligand forming a five-membered ring with the iridium(III) metal center [121]. Interestingly, the very high energy of the LUMO (centered on the pyridine-carbene ligand) leads to a predominantly ligand-centered (LC) emission from the cyclometalating ligands. Tuning of the emission maximum becomes straightforward by modifying the chemical structure and/or the substituents of the two cyclometalating ligands, easily leading to deep-blue emission with band onsets as low as 380 nm [121].

Although the use of carbene-based ancillary ligand has opened new avenues for the design of deep-blue emitting charged complexes, the resulting molecules display low emission quantum yields compared to standard neutral iridium-based emitters. To understand the reasons behind this limitation, we prepared two se-

ries of complexes with four different pyridine-carbene and one bis-carbene chelators as bidentate ancillary ligands. We used 2-phenylpyridine (**ppy**) and 2-(2,4-difluorophenyl)pyridine (**dfppy**) as the cyclometalating ligands for each series.

A full photophysical and electrochemical characterization of the two series of complexes has been performed and the results are rationalized with the help of DFT calculations. In contrast to complexes based on pyridine-carbene ancillary ligands, no low-energy ^{3}MC state was localized for the bis-carbene complexes, which would explain the larger values observed for the photoluminescence quantum yields of such complexes.

2.2 Results and discussion

2.2.1 Synthesis and X-ray crystal structures

All the complexes of both series have been synthesized following previously reported methods [121]. The pyridine-carbene ligands have been obtained by copper catalyzed C–N couplings of 2-bromopyridine derivatives and imidazole or benzimidazole, depending on the case, followed by alkylation with alkyl halides. The addition of Ag_2O to the ligands generates in situ the corresponding silver carbene complexes, which are reacted directly with the chloro-bridged iridium dimers to transfer the carbene ligands to the iridium(III) metal center. As already reported in the previous chapter, an additional role of the silver cation is to promote the removal of the chloride anion from the iridium dymer. After reaction, all the complexes were purified by column chromatography on silica gel and isolated as PF_6 salts.

For the sake of clarity, in Figure 2.1 on the following page we report all the synthesized complexes investigated in this chapter. While the bis-carbene complexes (**F5a** and **F5b**) were already reported by de Cola *et al.* [85], all the other pyridine-carbene emitters were synthesized by our group only.

Single crystals suitable for X-ray diffraction analysis were grown by slow diffusion of heptane into a CH_2Cl_2 solution of the complexes. In this chapter we report only the X-ray crystal structures of complex **F1a** and **F1b** as prototypical examples for both the non-fluorinated and fluorinated series (see Figure 2.2 on page 71).

All the complexes have a slightly distorted octahedral geometry around the

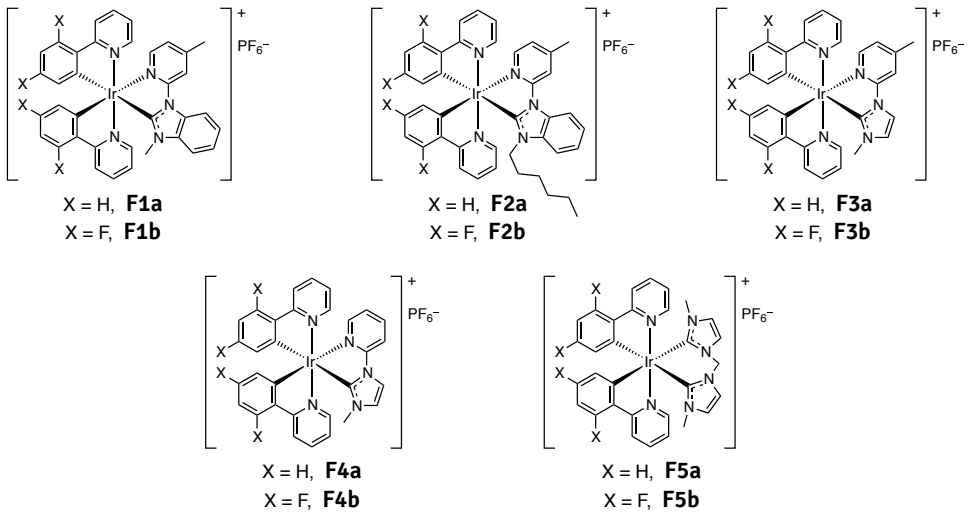

Figure 2.1: Chemical structures of the investigated complexes reported in this chapter. They can be divided in two series: the ppy-based series (complexes **F1a** – **F5a**) and the fluorinated dfppy-based series (complexes **F1b** – **F5b**); both series have the same five carbene ancillary ligands (**L1** – **L5**).

iridium center. In all cases the pyridine groups of the cyclometalating ligands are in *trans* position to each other. There are only minor differences between the complexes with pyridine-imidazole ancillary ligands. Noteworthy, the Ir–C' bond (C' is the coordinated carbon in *trans* to the pyridine of the ancillary ligand) is always shorter than the Ir–C" bond (C" is the coordinated carbon in *trans* to the carbene of the ancillary ligand); this reflects the stronger *trans*-effect of the carbene compared to the pyridine. The pyridine-carbene ancillary ligands are almost flat while the bis-carbene ligands are significantly distorted due to the methylene bridge. As a consequence, the bite angle is about 9° wider for the bis-carbene ligands than for the pyridine-carbene ligands.

2.2.2 Electrochemistry

The electrochemical data for the complexes have been measured in acetonitrile (using the ferrocene/ferrocenium ion couple as internal standard). The results are reported in Table 2.1 on page 72, together with the HOMO and LUMO energies calculated by DFT.

A positive shift of the oxidation potentials (around 0.3 V) is found when go-

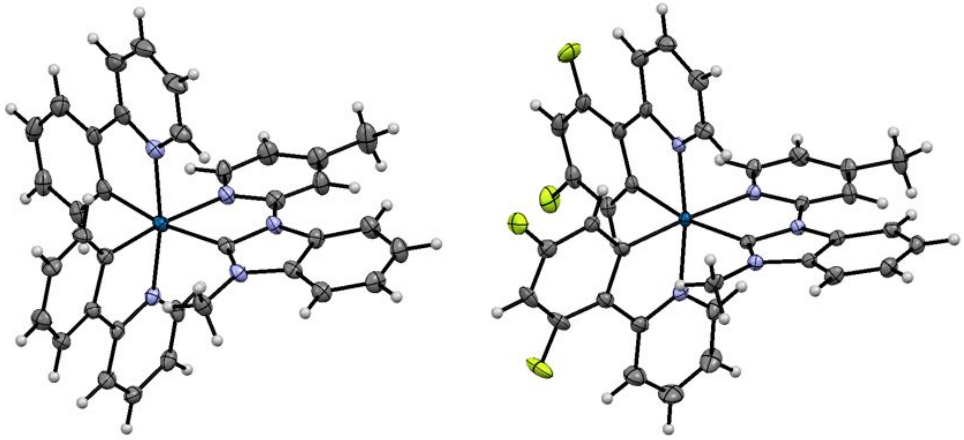

(a) Cation of **F1a**. **(b)** Cation of **F1b**.

Figure 2.2: X-ray structure of two selected compounds belonging to the family of the pyridine-carbene iridium(III) complexes (ellipsoids plotted at 40% probability level).

ing from the ppy-based to the dfppy-based (fluorinated) series. This is due to the strong electron-withdrawing character of the fluorine atoms, which stabilizes the HOMO energy level of the complexes. A smaller positive shift (around 0.1 V) is also measured for the reduction potentials in passing from the non-fluorinated to the bis-fluorinated series, indicating that the fluorine substituents also influence the energy of the LUMO.

Overall, there are only minor differences along the complexes with pyridine-carbene as ancillary ligands. This is particularly true for the dfppy-based series in which the oxidation potentials are found between 1.19 V and 1.22 V *vs.* Fc^+/Fc.

It can be noted that the replacement of the methyl group in **L1** with the longer n-hexyl chain in **L2** slightly enhances the oxidation potential (see **F1a** *vs.* **F2a** and **F1b** *vs.* **F2b**), an effect similarly observed for complexes with a bis-carbene ancillary ligand [85]. Replacement of the benzimidazole for an imidazole unit in the ancillary ligand has apparently no impact on the redox potentials. On the other hand, changing the pyridine-carbene for the bis-carbene ligand (as in the case of **F5a** and **F5b**) leads to a destabilization of both the oxidation and the reduction potential due to the stronger donor character of the carbene moiety compared to the pyridine group.

Table 2.1: Electrochemical potentials of all the investigated complexes in acetonitrile, together with DFT calculated HOMO and LUMO energies at the B3LYP/(6-31G**/LANL2DZ) level of theory.

Non-fluorinated series				
Complex	E_{ox} (V)	E_{red} (V)	E_{HOMO} (eV)	E_{LUMO} (eV)
F1a	0.86	−2.43, −2.76	−5.50	−1.54
F2a	0.91	−2.39, −2.70	−5.50	−1.54
F3a	0.84	−2.43, −2.73	−5.44	−1.53
F4a	0.86	−2.34, −2.67	−5.45	−1.54
F5a	0.81	−2.83	−5.42	−1.45
Fluorinated series				
Complex	E_{ox} (V)	E_{red} (V)	E_{HOMO} (eV)	E_{LUMO} (eV)
F1b	1.19	−2.26, −2.54	−5.77	−1.61
F2b	1.21	−2.30, −2.58	−5.77	−1.61
F3b	1.19	−2.33, −2.61	−5.72	−1.60
F4b	1.22	−2.27, −2.59	−5.73	−1.61
F5b	1.10	−2.71	−5.66	−1.53

2.2.3 Photophysical properties

All the complexes are stable both in CH_3CN and CH_2Cl_2 solution over months and do not display any degradation upon standard experimental conditions, including irradiation. The UV-Vis absorption spectra of all the complexes belonging to the non-fluorinated series are displayed in Figure 2.3 on the next page (**F1a** – **F5a**). The strong absorption bands in the spectral region below 300 nm exhibit molar absorption coefficients (ϵ) between 2.0×10^4 and 5.5×10^4 M^{-1} cm^{-1}, originating from spin-allowed $^1\pi$-π^* electronic LC transitions. The more intense ϵ values found for **F1a** and **F2a** are due to the extended benzimidazole aromatic moieties on the carbene subunits of the ancillary ligands. The structureless bands at 300 – 360 nm can be assigned to both phenyl-to-pyridine π-π^* ligand-to-ligand (interligand) charge transfer (LLCT) transitions and to MLCT transitions with a predominant singlet spin multiplicity [85]. The lower-lying bands in the visible

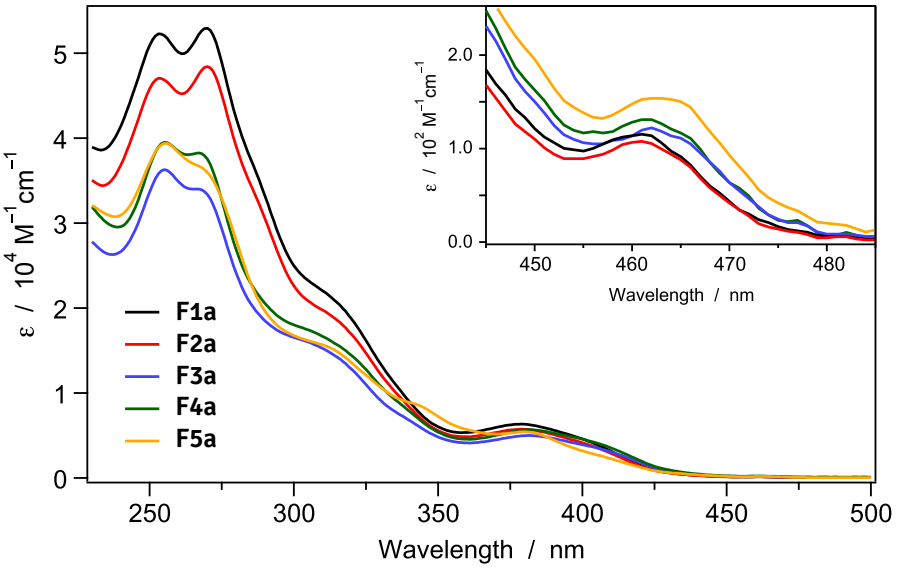

Figure 2.3: Absorption spectra of **F1a** – **F5a** in CH_2Cl_2 at 298 K. The T_1 absorption transitions are magnified in the inset.

region ($>$ 360 nm) can be attributed to both singlet and triplet MLCT transitions, which, however, have a strong π-π^* character [100].

The very weak, lowest-energy absorption bands (around 463 nm, having ϵ between 100 and 150 $M^{-1}\,cm^{-1}$) that are magnified in the inset of Figure 2.3 can be identified as the spin-forbidden electronic transition from the ground state directly to the triplet emitting state (T_1) [92]. The small spectral shift between the T_1 absorption and emission bands (around 412 cm^{-1}) suggests that the emitting state has a weak MLCT character and a pronounced π-π^* LC contribution (see below). To further support this hypothesis, the absorption spectra were also recorded in more polar acetonitrile showing no substantial spectral shift.

Also absorption spectra of the fluorinated series (**F1b** – **F5b**) were recorded in CH_2Cl_2 solution at room temperature but they are not reported in this thesis. Remarkable differences compared to the non-fluorinated series are detected mainly in the visible region at wavelength $>$ 350 nm. In fact, in this case, the singlet and triplet MLCT transitions display a blue shift of around 20 nm and the lowest-energy absorption bands associated to the T_1 state are found at 443 nm (ϵ around 100 – 200 $M^{-1}\,cm^{-1}$). A large hypsochromic shift upon replacing unsubstituted cyclometalating phenylpyridines with difluorinated ones is a common finding

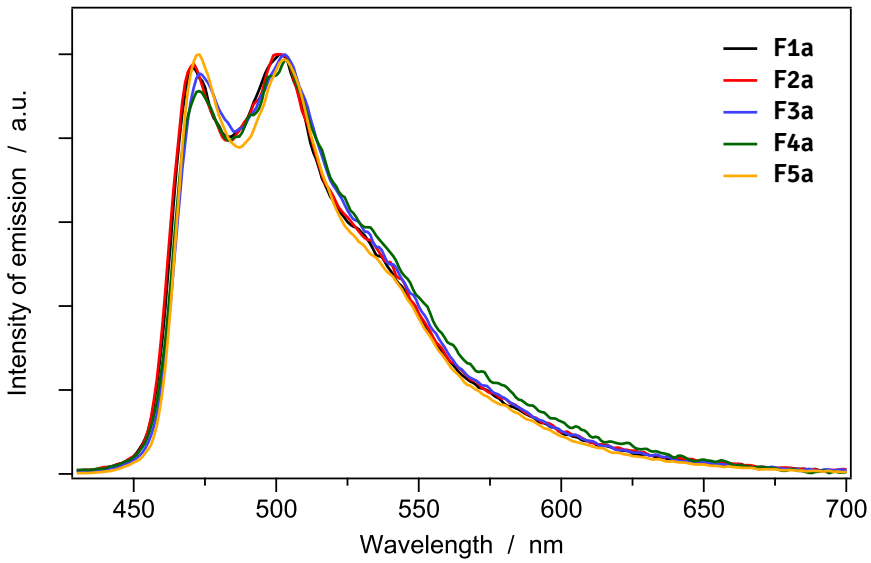

Figure 2.4: Normalized emission spectra of **F1a** – **F5a** in CH_2Cl_2 at room temperature (λ_{exc} = 360 nm).

for both neutral [92, 219] and cationic [91, 103, 112, 120] iridium(III) complexes. In fact, the attachment of electron- withdrawing substituents to the cyclometalating ligands results in a significant stabilization of the HOMO, which is located partially on the iridium metal and on the phenyl moieties of the phenylpyridines (see below).

The room temperature luminescence spectra of compounds **F1a** – **F5a** are reported in Figure 2.4. All the complexes display a strongly structured band, indicating that the emissive excited states have a pronounced ^{3}LC character with a weaker ^{3}MLCT contribution. No spectral shift is observed upon increasing the polarity of the solvent (*e.g.*, acetonitrile). Upon cooling the solutions down to 77 K, the emission spectra of the complexes exhibit a slight blue shift (less than 5 nm) and display narrower and more highly resolved vibronic progressions (see Figure 2.5 on the facing page). The lack of solvatochromism and the absence of a relevant rigidochromic shift further suggest the predominant LC π-π^* character of the emitting triplet state. These considerations are essentially the same also for the fluorinated series **F1b** – **F5b**.

All complexes having different pyridine-carbene ligands show almost identical photophysical properties along each series (see Table 2.2 on page 76 and Ta-

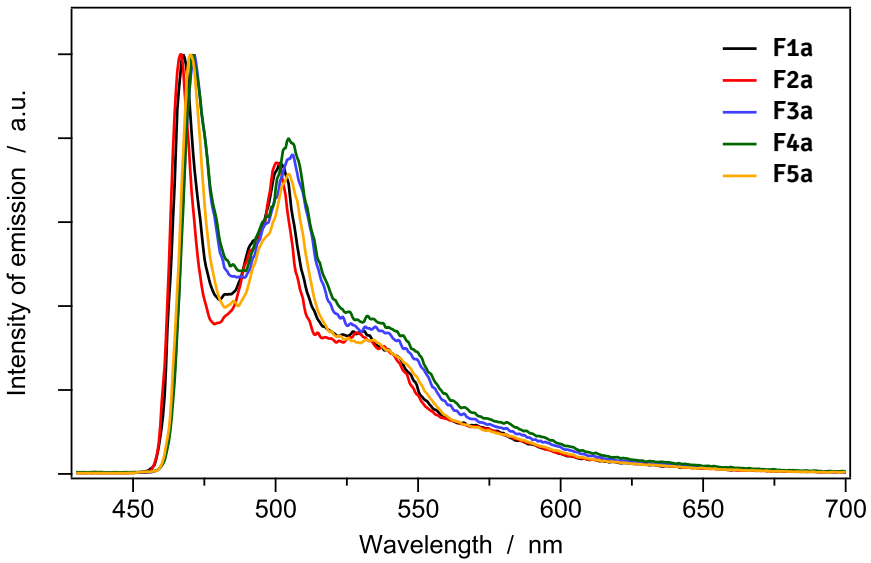

Figure 2.5: Normalized emission spectra of **F1a** – **F5a** in CH_2Cl_2 at 77 K (λ_{exc} = 360 nm).

ble 2.3 on page 78), demonstrating that chemical modifications on this type of ancillary ligand does not affect the nature of the excited state. In fact, as confirmed by theoretical calculations (see section on page 79), the frontier electronic levels of these complexes primarily involve the π-orbitals of the cyclometalating ligands without involving too much the carbene ancillary ligands. Furthermore, the substituents on these ligands are too far apart from the iridium center to significantly alter the ligand-field strength around the metal core. A minor red shift of less than 4 nm is observed in the case of the bis-carbene complexes, if compared to the pyridine-carbene analogues. Because of the lack of a strong contribution of the ancillary-ligand to the HOMO–LUMO transition, such bathochromic shift is ascribed to a slight difference in the ligand-field strength.

In room temperature CH_2Cl_2 solution, pyridine-carbene complexes show very low photoluminescence quantum yields, almost two orders of magnitude lower than bis-carbene analogues (see Table 2.2 on the following page). From PLQY and lifetime (τ) values, assuming a unitary intersystem crossing efficiency, the radiative and overall non-radiative rate constants (k_r and k_{nr}, respectively) were calculated and are summarized in Table 2.2. In spite of almost comparable k_r values ($\approx 1.5 \times 10^5$ s^{-1}), pyridine-carbene complexes display k_{nr} values around

Table 2.2: Photophysical data of all complexes at room temperature in CH_2Cl_2.

Non-fluorinated series					
Complex	λ_{max} (nm)	Φ_{em} (%)	τ (ns)	k_r (10^5 s^{-1})	k_{nr} (10^7 s^{-1})
F1a	471, 502	0.6	37	1.62	2.69
F2a	471, 502	0.5	35	1.43	2.84
F3a	473, 503	0.8	46	1.74	2.16
F4a	472, 503	0.3	19	1.58	5.25
F5a	472, 502	28.5	1870	1.52	0.04
Fluorinated series					
Complex	λ_{max} (nm)	Φ_{em} (%)	τ (ns)	k_r (10^5 s^{-1})	k_{nr} (10^7 s^{-1})
F1b	451, 580	1.3	154	0.84	0.64
F2b	451, 580	1.6	140	1.14	0.70
F3b	451, 580	1.2	92	1.30	1.07
F4b	451, 580	0.7	47	1.49	2.11
F5b	454, 582	36.2	3130	1.16	0.02

80 times higher than their bis-carbenes analogues. These findings strongly suggest that, despite both families have a T_1 excited states very similar in nature, in the case of pyridine-carbene complexes (at least in room-temperature solution), non-radiative deactivation pathways, involving thermally accessible upper-laying states, play a fundamental role in deactivating the T_1 excited states [100]. In fact, at 77 K (see Table 2.3 on page 78) all the complexes show very strong phosphorescence and both families exhibit almost identical excited-state lifetimes (*e.g.*, around 4 µs for the non-fluorinated series). A very similar behavior is also observed in PMMA thin films (see Table 2.3 and Figure 2.6 on the facing page) where all the complexes display absolute emission quantum yields higher than 23 % and lifetimes around 3 µs.

These experimental findings can be rationalized in accord with the results of the theoretical study (reported on page 79). In fact, DFT calculations predict that, except for bis-carbene complexes (**F5a** and **F5b**), there are low-energy non-radiative metal-centered (^{3}MC) states close to the emitting T_1 level. Such

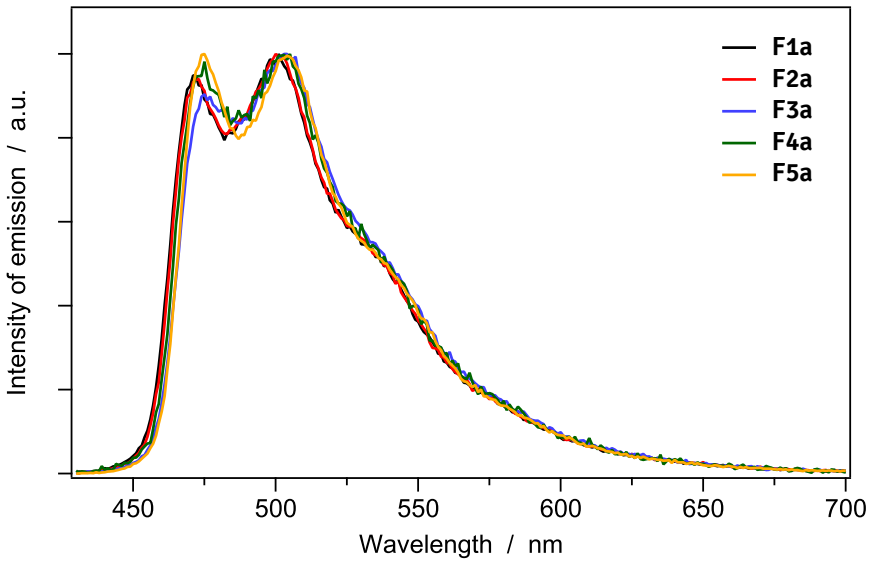

Figure 2.6: Normalized emission spectra of **F1a** – **F5a** in solid state (as PMMA 1 % thin films) at room-temperature (λ_{exc} = 360 nm).

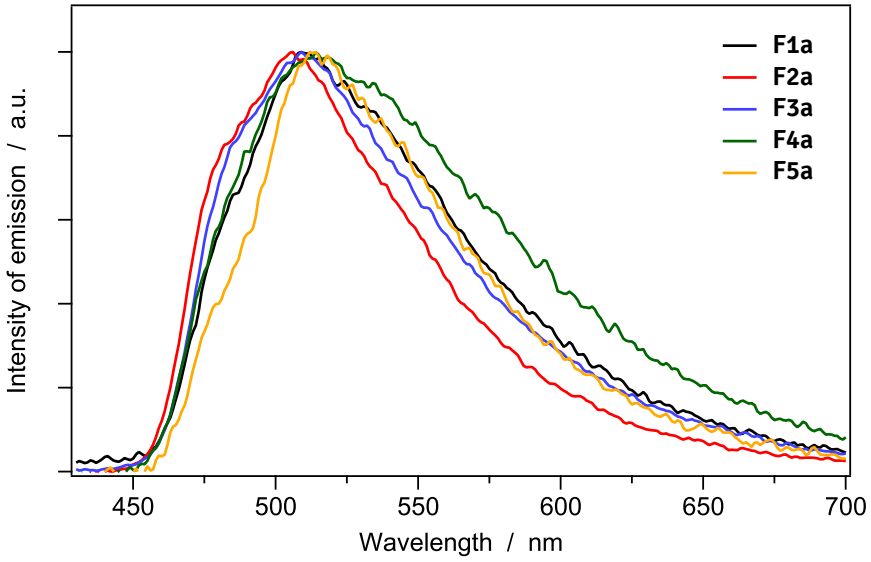

Figure 2.7: Room-temperature normalized emission spectra of **F1a** – **F5a** as neat films (λ_{exc} = 360 nm).

Table 2.3: Photophysical data of all complexes at 77 K, and in solid state.

	Non-fluorinated series						
	77 K		298 K neat film		298 K PMMA 1 %		
Complex	λ_{max} (nm)	τ (µs)	λ_{max} (nm)	Φ_{em} (%)	λ_{max} (nm)	Φ_{em} (%)	τ (µs)
F1a	472, 501	4.3	509	1.6	472, 501	38.9	3.2
F2a	471, 502	4.5	505	2.4	473, 501	42.6	3.3
F3a	473, 503	4.1	507	2.4	476, 503	32.4	2.5
F4a	472, 503	4.1	507	2.5	474, 502	23.7	2.4
F5a	472, 501	4.3	507	1.7	474, 504	50.2	2.7
	Fluorinated series						
	77 K		298 K neat film		298 K PMMA 1 %		
Complex	λ_{max} (nm)	τ (µs)	λ_{max} (nm)	Φ_{em} (%)	λ_{max} (nm)	Φ_{em} (%)	τ (µs)
F1b	446, 478, 513	4.9	510	2.3	450, 480	33.6	3.4
F2b	447, 480, 506	6.6	457, 484	4.7	452, 480	43.8	3.8
F3b	448, 480, 507	5.4	463, 490	3.0	452, 480	35.5	3.0
F4b	448, 480, 510	6.0	485	1.8	452, 480	25.9	3.1
F5b	446, 478, 513	4.9	485	3.5	454, 481	58.2	3.2

^{3}MC states are highly distorted and, upon full geometrical relaxation occurring in RT solution, they may become the lowest triplet. Instead, at low temperature and/or in solid matrix the population and/or the full relaxation of these ^{3}MC states are prevented, so that T_1 remains the lowest emitting triplet, as in the case of bis-carbene complexes. This picture can explain the low PLQYs of both pyridine-carbene series in RT solution and also the considerable enhancement of the luminescence observed in the solid state.

On the other hand, in neat films triplet-triplet annihilation processes start to play an important role, consequently PLQYs are dramatically reduced (see Table 2.3) and lifetimes are no longer monoexponential. For most of these complexes, a red shift of the emission occurs in going from solution to neat solid, as a result of the band broadening and of the change of the relative intensities of the luminescence peaks (see Figure 2.7 and Table 2.3). Although bulky spectator

groups are often attached to chelating ligands to reduce aggregation of the metal complex which causes red-shift and emission quenching in neat solids [212], the long n-hexyl chain anchored to the ancillary ligands of complexes **F2a** and **F2b** is not sufficient to prevent the quenching effect in the film.

2.2.4 Theoretical calculations

To gain further insight into the electrochemical and photophysical properties, the molecular and electronic structures of all the investigated complexes (in both ground and excited states) were investigated by performing DFT calculations at the B3LYP/(6-31G**/LANL2DZ) level in the presence of the solvent (acetonitrile). The main interests were:

i) to gain support for the emission originating from the cyclometalating ligands, in contrast to charged iridium complexes having "standard" bidentate chelators where emission strongly involves such ancillary ligands;

ii) to rationalize the higher photoluminescence quantum yields measured for complexes **F5a** and **F5b** bearing bis-carbene ancillary ligands.

Calculations in the electronic ground state (S_0) correctly reproduce the near-octahedral coordination of the Ir metal observed in the X-ray structures and predict geometric parameters in good accord with the experimental data.

The structural trends inferred from X-ray data are well supported by the theoretical calculations. For instance, in complex **F3b** the Ir–C' distance (2.018 Å) is predicted to be significantly shorter than that found for the Ir–C" distance (2.064 Å) showing the stronger trans effect of the carbene compared to the pyridine, and in good agreement with the X-ray data (2.018 Å and 2.055 Å, respectively). For the bis-carbene complex **F5b**, the Ir–C' and Ir–C" bonds have a similar length ($\approx$ 2.065 Å), which is almost identical to that calculated for the Ir–C" bond in complex **F3b** (2.064 Å).

As observed in the X-ray structures, the pyridine-carbene ancillary ligands are predicted to be almost flat, whereas the carbene rings of the bis-carbene ligand are not in the same plane due to the methylene bridge. In order to maximize the interaction with the iridium core, the bis-carbene ligand loses its planarity and the imidazolium rings are twisted by an average angle of 52.3°. The larger bite angle computed for the bis-carbene ligand (**F5b**: 84.4°) compared with the

pyridine-carbene ligand (**F3b**: 75.3°) is in good accord with the X-ray values (85.8° and 76.5°, respectively). The largest difference between computed and X-ray data corresponds to the coordinate Ir–N and Ir–C(carbene) bonds, whose distances are theoretically overestimated as is commonly observed when using the B3LYP functional [37, 121, 220].

Figure 2.8 on the facing page displays the energy and the atomic orbital composition calculated for the frontier molecular orbitals of complex **F3b**. These MOs provide information about the nature of the excited states that mainly determine the absorption and emission properties. For all the complexes, the HOMO, LUMO and LUMO+1 show the same topology depicted in Figure 2.8 for **F3b**. As expected, the HOMO is composed of a mixture of iridium t_{2g} orbitals and phenyl π orbitals distributed almost equally among the two cyclometalating ligands. The HOMO–1 to HOMO–4 also mainly involve the Ir center and the same cyclometalating ligands. The LUMO and LUMO+1 show almost no contribution from the metal and, in contrast to what is usually found for charged iridium complexes bearing bidentate NN ancillary ligands, for which the LUMO is located on the ancillary ligand, they mainly reside on the pyridine rings of the main cyclometalating ligands and are separated by an energy difference of 0.09 eV due to the non-identical geometries of the ligands.

The main difference between the electronic structure of complexes bearing a pyridine-carbene ligand and bis-carbene complexes is that, for the former, the LUMO+2, which is mainly located on the pyridine ring of the ancillary ligand, is close in energy to the LUMO and LUMO+1 (see Figure 2.8 on the next page). However, this is not the case for complexes **F5a** and **F5b** bearing a bis-carbene ligand, for which the first empty molecular orbital involving the ancillary ligand appears as the LUMO+4 and lies very high in energy (1.40 eV) above the LUMO. The high energy of this orbital is due to the presence of two carbene units and to the methylene bridge that breaks the π conjugation between those units. As discussed below, these electronic differences play a relevant role in the nature of the lowest-energy triplet states and, thereby, in the photophysical properties of the complexes.

The energies of the HOMO and LUMO of all complexes have been included in Table 2.1 on page 72 to make easier the comparison with the electrochemical data. The attachment of fluorine atoms to the phenyl rings produces a large stabilization of the HOMO (around 0.27 eV), in good accord with the anodic shift

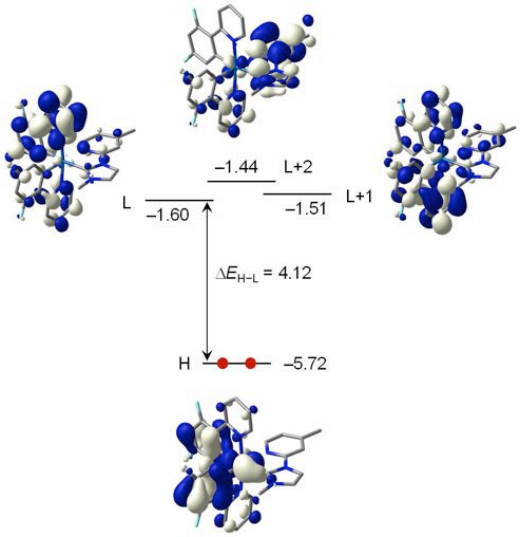

Figure 2.8: Energy diagram showing the electronic density contours (0.05 e bohr^{-3}) and the energy values (in eV) calculated for the frontier molecular orbitals of complex **F3b**, as an example.

measured for the oxidation potential (around 0.32 V), because the HOMO largely resides on the phenyl rings of the cyclometalating ligands. It has also a sizeable stabilization effect on the LUMO (indicatively 0.07 eV) because this orbital is also located on the same cyclometalating ligands with some contribution from the phenyl rings (see Figure 2.8). The change of the pyridine-carbene ancillary ligand by the bis-carbene ligand causes a slight destabilization of both the HOMO ($\approx$ 0.05 eV) and the LUMO ($\approx$ 0.10 eV), which is in agreement with the less positive oxidation potentials and more negative reduction potentials measured for complexes **F5a** and **F5b** (see Table 2.1 on page 72).

The HOMO–LUMO energy gap increases by more or less 0.20 eV in passing from the non-fluorinated ($\approx$ 3.95 eV) to the fluorinated complexes ($\approx$ 4.15 eV) in good correlation with the blue shift observed experimentally in both absorption and emission spectra.

In light of the atomic orbital composition found for the HOMO, LUMO and LUMO+1, the lowest-energy triplet states are expected to correspond to π-π^* states mainly centered on the cyclometalating ligands. To corroborate this suggestion and to investigate the nature of the emitting excited state, the low-lying triplet states of all the complexes were calculated at the optimized geometry of the ground state (S_0) using the TD-DFT approach.

TD-DFT calculations predict that the two lowest-energy triplet states (T_1 and T_2) are almost degenerate and show a similar electronic nature for all the complexes. They have a high multiconfigurational character, the largest contributions corresponding to the HOMO-to-LUMO and HOMO-to-LUMO+1 monoexcitations. The T_1 and T_2 states are therefore described as π-π^* ^{3}LC states involving the cyclometalating ligands, where both the HOMO and the LUMO/LUMO+1 are mainly located (see Figure 2.8 on the previous page), with a weak MLCT character due to the participation of the Ir atom in the HOMO. The only difference between T_1 and T_2 is the cyclometalating ligand implied in the intraligand electronic transition (the two cyclometalating ligand are not equivalent due to the asymmetrical ancillary one). For complexes bearing a pyridine-carbene ligand, the first excited states in which the ancillary ligand largely participates are the T_5 and T_6 triplets that involve the electron monoexcitation to the LUMO+2 located on the pyridine-carbene ligand (see Figure 2.8 on the preceding page for complex **F3b**). These states are computed around 0.5 eV above the T_1/T_2 triplets and show a mixed ^{3}MLCT/^{3}LLCT character.

In the case of complexes **F5a** and **F5b**, the ^{3}MLCT/^{3}LLCT triplets are very high in energy because, as mentioned above, the first virtual orbital involving the bis-carbene bis-carbene ancillary ligand corresponds to the LUMO+4 and is calculated 1.4 eV above the LUMO.

TD-DFT calculations therefore suggest that the emitting excited state for all complexes involves the cyclometalating ligand and the Ir metal core, unlike what is found for complexes bearing NN ancillary ligands with low-energy π^* orbitals [37, 118, 212, 218, 221].

In addition to the TD-DFT study, the lowest triplet excited state T_1 was further examined by optimizing its geometry using the spin-unrestricted UB3LYP approach. After full-geometry relaxation, the T_1 state is calculated to lie almost 2.69 eV above S_0 for the non-fluorinated series, while for fluorinated complexes at more than 2.80 eV above S_0 (adiabatic energy differences, reported as ΔE (T_1−^{3}MC) in Figure 2.9, a).

As depicted in Figure 2.9 (b) for complex **F3b**, the unpaired electrons in the T_1 state are mostly concentrated in one of the cyclometalating ligands with a small contribution from the Ir atom (Ir: 0.166 e, first cyclometalating ligand: 1.828 e, pyridine-carbene ligand: 0.007 e). A similar spin-density distribution is found for the T_2 state, which is located on the other cyclometalating ligand, and for

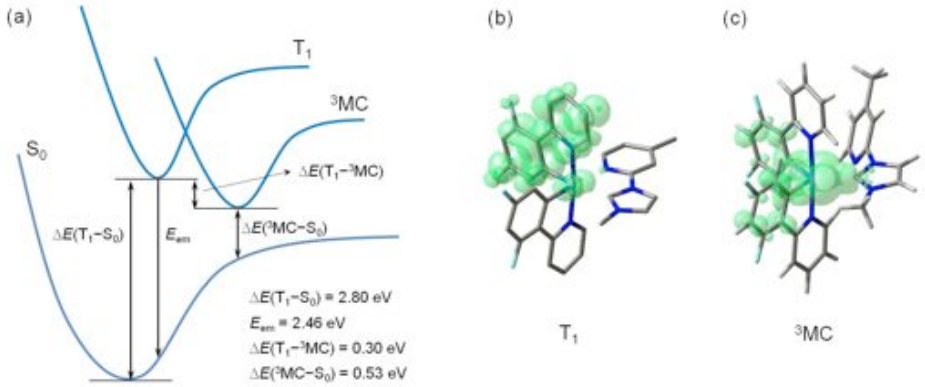

Figure 2.9: a) Schematic energy diagram showing the adiabatic energy differences (ΔE) between the S_0, T_1 and ^{3}MC states and the emission energy (E_{em}) from T_1 calculated for **F3b**. b and c) Unpaired-electron spin-density contours (0.003 e bohr^{-3}) calculated for the fully-relaxed T_1 and ^{3}MC states of **F3b**, respectively.

the rest of complexes. The only difference between the non-fluorinated and the fluorinated series is that the spin density over the Ir metal core range from 0.233 e to 0.308 e for the first series and decreases to 0.145 – 0.166 e for the latter, due to the electron-withdrawing effect of the fluorines.

Excitation to T_1 causes small changes (less than 0.03 Å) in the coordination sphere of the complexes. Theoretical calculations therefore confirm the ^{3}LC (π-π^*) character with a weak ^{3}MLCT contribution of the emitting state for all complexes and that this state mainly implies an electron promotion within the cyclometalating ligands, in good agreement with experimental evidence. The large ^{3}LC character of T_1 justifies the structured emission spectra observed experimentally at room temperature and the absence of a rigidochromic shift at low temperature (see both Figure 2.4 and Figure 2.5 on page 75).

To estimate the emission energy, the vertical energy difference between the emitting T_1 triplet and S_0 was determined by performing a single-point calculation of S_0 at the optimized minimum-energy geometry of T_1 (E_{em} in Figure 2.9, a). Calculations lead to vertical emission energies of 2.36 – 2.41 eV (525 – 515 nm) for non-fluorinated complexes and of 2.46 – 2.52 eV (503 – 492 nm) for the fluorinated series. These values slightly overestimate the experimental energy of the second peak of the emission spectra, but correctly reproduce the blue shift of around 20 nm observed in passing from one series to the other (see experimental

data in Table 2.2 on page 76).

As previously performed for complexes incorporating pyridine-carbene ancillary ligands [121], the presence of low-energy metal-centered (MC) states was investigated at the UB3LYP level starting from distorted geometries. Also for this type of pyridine-carbene complexes, calculations converged to a ^{3}MC triplet state (depicted, for the selected example **F3b**, in Figure 2.9, c), in which the pyridine ring of the pyridine-carbene ligand is rotated around the inter-ring bond by 58.6°.

The spin-density computed for this state confirms its metal-centered nature since the iridium(III) center accumulates a large part of the unpaired electrons (see Figure 2.9, c). The optimized geometry of the ^{3}MC state is similar for all the pyridine-carbene complexes, the major difference being the internal rotation angle of the ancillary ligand that has a value around 65° for complexes with a benzimidazole ancillary ligand and around 55° for complexes with an imidazole ancillary ligand. As can be seen in Figure 2.9 c, the nitrogen atom of the pyridine ring is fully decoordinated in the ^{3}MC state and the complex adopts a slightly distorted trigonal bipyramid molecular geometry. This is evidenced by the C"–Ir–C and C'–Ir–C bond angles that have values close to 125° in the ^{3}MC state.

An important aspect is the relative energy position of the ^{3}MC state with respect to the emitting triplet state. After geometry relaxation, the ^{3}MC triplet of pyridine-carbene complexes is calculated to lie between 0.3 eV and 0.4 eV (*e.g.*, only 0.30 eV in the case of **F3b**, our selected example) below the T_1 emitting state (adiabatic energy differences, $\Delta E\,(T_1 - {}^3MC)$ in Figure 2.9, a).

An effective population is therefore expected for the MC triplet and this state would play a role in the deactivation of the emission process since, at its fully-relaxed geometry, it lies close in energy to the S_0 state (approximately 0.5 eV, $\Delta E\,({}^3MC - S_0)$ in Figure 2.9, a). This can explain the low photoluminescence quantum yields experimentally observed for pyridine-carbene complexes (see Table 2.2 on page 76).

In contrast to pyridine-carbene complexes, calculations were not able to localize the ^{3}MC state for the bis-carbene complexes. The ^{3}MC state would imply the decoordination of one of the carbene units and has to be expected at high energies because, as discussed above, the empty orbitals implying the bis-carbene bis-carbene ligand are found higher in energy than for the pyridine-carbene pyridine-carbene ligands. The absence of the low-lying ^{3}MC triplet would ex-

plain the larger values observed for the photoluminescence quantum yields of complexes **F5a** and **F5b** (see Table 2.2 on page 76).

2.3 Conclusion

In summary, we have prepared two series of charged iridium complexes based on 2-phenylpyridine and on 2-(2,4-difluorophenyl)-pyridine as cyclometalating ligands. Both series use four different pyridine-carbene and one bis-carbene chelators as bidentate ancillary ligands. Full photophysical characterizations of the two series of complexes have been performed in solution, PMMA films, and in solid state (as powder).

In spite of almost comparable k_r values (around 1.5×10^5 s^{-1}), all pyridine-carbene complexes display in solution k_{nr} values almost 80 times higher than bis-carbene analogues, pointing to the presence of additional non-radiative deactivation pathways involving thermally accessible upper-laying states.

Indeed, at 77 K, all the complexes show very strong phosphorescence and both families exhibit almost identical excited-state lifetimes (around 4 µs for ppy-based complexes). The results are further rationalized by DFT calculations. In contrast to complexes based on pyridine-carbene ancillary ligands, for which a low-lying ^{3}MC state leading to the decoordination of the pyridine ring of the ancillary ligand is found, no ^{3}MC state is localized for the bis-carbene complexes. A high-lying ^{3}MC state would be poorly accessible at room temperature and would explain the larger values observed for the photoluminescence quantum yields of such complexes.

The emission properties of charged cyclometalating iridium(III) complexes with carbene-based ancillary ligands are controlled primarily by the main cyclometalating ligands, in contrast to the classical design of charged complexes bearing NN ancillary ligands with low-energy π^* orbitals.

However, our results demonstrate the impact of the ancillary ligand on the photoluminescence quantum yield, lifetime of excited state, and energy levels of the complexes. Furthermore, as the thermal accessibility of the ^{3}MC state is crucial for the stability of the complexes, our results provide important insights for developing efficient charged complexes with carbene-based ancillary ligands, which are a promising family of deep-blue phosphorescent charged emitters.

Chapter 3

Towards a bluer emission

In this chapter we report a series of new cationic iridium(III) complexes that have *tert*-butyl isocyanides as neutral auxiliary ligands and 2-phenylpyridine (**ppy**) or 2-(4'-fluorophenyl)-R-pyridines (where R is 4-methoxy, 4-*tert*-butyl, or 5-trifluoromethyl) as cyclometalating ligands. The complexes are white or pale yellow solids that show irreversible reduction and oxidation processes and have a large electrochemical gap (from 3.58 V to 3.83 V). They emit blue or blue-green phosphorescence from a cyclometalating-ligand-centered excited state. Their emission spectra show vibronic structure with the highest-energy luminescence peak at 440 – 459 nm. The corresponding quantum yields and observed excited-state lifetimes are up to 76 % and 46 µs, respectively, and the calculated radiative lifetimes are in a range from 46 µs to 82 µs. In solution, the photophysical properties of the complexes are solvent-independent, and their emission color is tuned by variation of the substituents in the cyclometalating ligand. For most of the complexes, an emission color red shift occurs in going from solution to neat solids. However, the shift is minimal for the complexes with bulky *tert*-butyl or trifluoromethyl groups on the cyclometalating ligands that prevent aggregation. This is the first example of an iridium(III) isocyanide complex that emits blue phosphorescence not only in solution but also as a neat solid.

3.1 Introduction

As already mentioned in the first chapter, a wide part of the scientific interest on Ir-iTMCs is focused in high-energy-emitting materials because they are

required for generation of blue [82, 85, 111, 116, 118, 178, 186, 222] and white [81, 159, 186, 199, 222] light in electroluminescent devices.

Blue-phosphorescent cyclometalated cationic iridium(III) complexes with various neutral ligands such as diimines [82, 111, 116, 118, 158, 178, 223, 224], carbenes [85, 121], carbon monoxide [120], and phosphines [120, 225, 226] are already known and already described in the previous chapters of this thesis.

The common problems encountered with these complexes are (i) low phosphorescence quantum yields that result from quenching of high-energy emissive excited states by non-emissive ^{3}MC states and (ii) red-shift and quenching of phosphorescence in going from solutions to neat solids caused by aggregation and triplet-triplet interaction.

Recently, it was reported that neutral and cationic iridium(III) complexes with alkyl isocyanides show blue to green phosphorescence in solution (see Figure 3.1) [92, 219, 227–230]. However, their solid-state photophysical properties, which are extremely important for practical applications, were only briefly and superficially characterized [228].

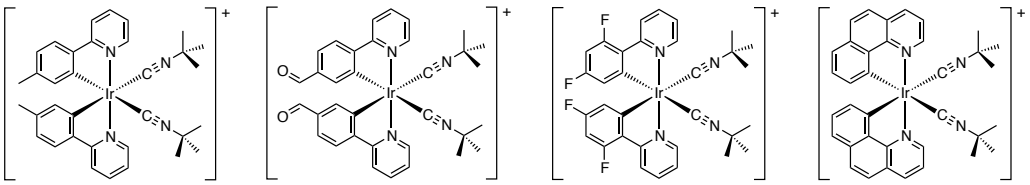

Figure 3.1: Previously reported cyclometalated cationic iridium(III) complexes having *tert*-butyl isocyanides as ancillary ligands.

Here, we present a new series of cyclometalated cationic iridium(III) complexes with 2-phenylpyridines as cyclometalating ligands and strong-field, non-chromophoric *tert*-butyl isocyanides as ancillary (**N1** – **N5**, reported in Figure 3.2 on the next page). To tune the photophysical properties of the complexes, we modified the cyclometalating 2-phenylpyridine ligands with electron-withdrawing (4'-F and 5-CF_3), electron-donating (4-OCH_3), and bulky (4-*tert*-butyl and 5-CF_3) substituents. As a result, we developed cationic iridium(III) isocyanide complexes that emit phosphorescence at higher energies and with higher efficiencies than do the known analogues reported in Figure 3.1 [92, 219, 227–230], and we describe the first example of an iridium(III) isocyanide complex that is blue-phosphorescent also as a neat solid.

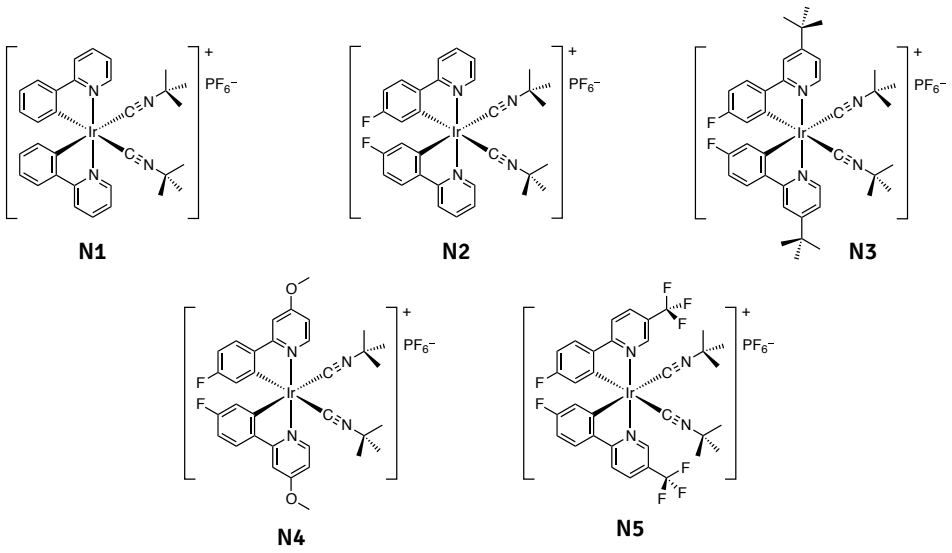

Figure 3.2: Chemical structure of the investigated complexes reported in this chapter. All of them have *tert*-butyl isocyanides as ancillary ligands.

3.2 Results and Discussion

3.2.1 Synthesis

The 2-phenylpyridine ligands were prepared by Suzuki-Miyaura coupling of 4-fluorophenylboronic acid with substituted 2-halopyridines (see Figure 3.3). Modified literature procedures led to the required 2-chloropyridines (see Figure 3.4 on the next page) [231–233]. The cyclometalated dimeric precursors $[(CN)_2Ir(\mu\text{-}Cl)]_2$ were made by reaction of $IrCl_3 \cdot 3\,H_2O$ with 2-phenylpyridines in a 3:1 solution of 2-ethoxyethanol and water [77, 234].

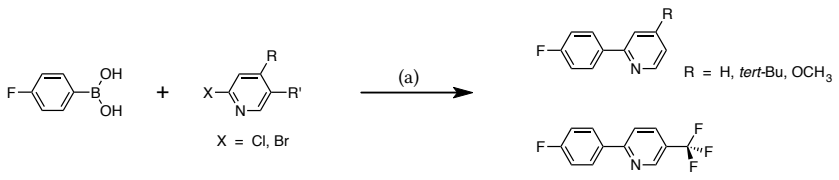

Figure 3.3: Synthesis of 2-phenylpyridine. Reaction conditions: (a) K_2CO_3, $Pd(PPh_3)_4$ in 3 : 1 THF : water, under Ar, at 85 °C.

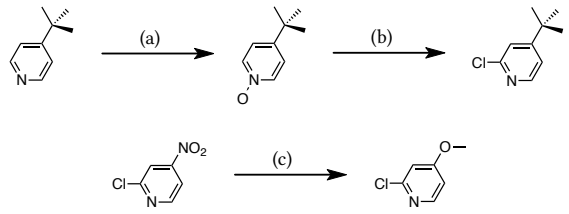

Figure 3.4: Synthesis of 2-chloropyridines. Reaction conditions: (a) H_2O_2, acetic acid, under air, at 80 °C; (b) $POCl_3$, "dry finger", under air, at 130 °C; (c) $NaOCH_3$, dry DMF, under Ar, at room temperature.

Five new complexes (**N1** – **N5**, reported in Figure 3.2) were prepared in higher than 60 % yield by reaction of the desired cyclometalated iridium(III) precursor $[(CN)_2Ir(\mu\text{-}Cl)]_2$ with silver triflate (to remove the chloride anion) [83] and with an excess of *tert*-butyl isocyanide [92]. The complexes are air- and moisture-stable solids that are soluble in polar organic solvents.

3.2.2 Structural characterization

Figure 3.5 on the facing page shows the X-ray molecular structure of **N4**; two independent molecules of the complex with similar structural features are present in the unit cell.

The metal ion is in a distorted octahedral $[(CN)_2Ir(C)_2]^+$ coordination environment with the two pyridine nitrogen atoms in *trans* position. The Ir—C bonds with the *tert*-butyl isocyanides are shorter (on the average) and show a wider variation of length (see Table 3.1 on the next page) compared with the Ir—C bonds with the cyclometalating ligand. For the *tert*-butyl isocyanides, the Ir—C≡N angle is more linear and shows less variation than the C≡N—C angle (see Table 3.1). The cyclometalating ligands are nearly planar: the dihedral angle between their constituent rings is less than 10°, and the methoxy group is in-plane with the pyridyl ring.

The complexes do not participate in face-to-face π-π stacking. Intermetallic communication is likely to be negligible because of the long Ir—Ir distance (8.866 Å). The main structural parameters of **N4** (reported in Table 3.1) are similar to those of the already published isocyanide complexes depicted in Figure 3.1 on page 88.

Table 3.1: X-ray selected bond distances and angles of complex **N4**. The two independent complexes present in the unit cell are labeled as Ir(1) and Ir(2). The subscript labels CN and CN' refer to the two distinct cyclometalating ligands; the iso label refers to the *tert*-butyl isocyanide in *trans* position to the carbon atom of the CN ligand in the same row.

	Bond lengths (Å)			Angles (deg)	
	Ir−C_{CN}	Ir−$N_{CN'}$	Ir−C_{iso}	Ir−C≡N	C≡N−C
Ir(1)	2.054	2.061	2.016	175.8	176.6
	2.065	2.050	2.026	178.3	172.7
Ir(2)	2.050	2.078	2.034	173.5	169.4
	2.067	2.053	2.059	176.5	173.2
average	2.058	2.060	2.033	175.9	172.9

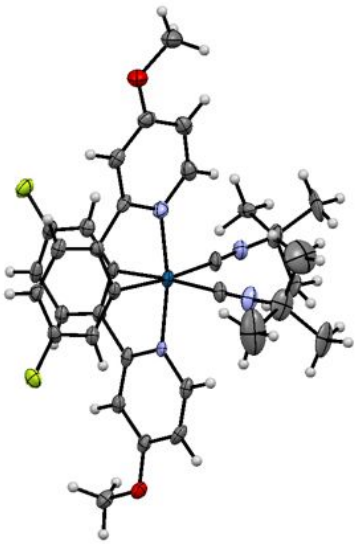

Figure 3.5: Xray structure of the cation of **N4** (ellipsoids potted at 50 % probability level); only one of the two independent molecules is shown, and the disorder within the *tert*-butyl groups is omitted for clarity.

3.2.3 Electrochemistry

The electrochemical properties of all the complexes were studied by cyclic voltammetry in acetonitrile and DMF. All observed redox processes were irre-

versible, and their reduction potentials (relative to ferrocene / ferrocenium ion) were solvent-independent. For that reason, in Table 3.2 on the next page only data in acetonitrile are reported.

The first oxidation of the non-substituted complex **N1** occurs at 1.23 V. The electron-withdrawing 4'-F substituent in the phenyl ring increases the oxidation potential of complex **N2** to 1.42 V. Substitution on the pyridyl ring of the 2-(4'-fluorophenyl)-pyridine cyclometalating ligands with the electron-withdrawing 5-CF_3 group increases the oxidation potential of complex **N5** by 200 mV, whereas electron donors facilitate the oxidation by 50 mV (4-*tert*-butyl, in **N3**; 4-OCH_3, in **N4**).

The first reduction of **N1** occurs at −2.38 V. Fluorination of the phenyl ring facilitates the reduction by 40 mV (**N2**). Modification of the pyridyl moiety of the 2-(4'-fluorophenyl)-pyridine ligands with an electron-withdrawing 5-CF_3 group shifts the reduction potential positively by 380 mV, whereas an electron donor shifts the reduction potential negatively by 90 mV (4-*tert*-butyl, in **N3**) and 120 mV (4-OCH_3, in **N4**).

The trends observed in the redox potentials (see Table 3.2 on the facing page) together with the results of theoretical calculations (see 3.2.9 on page 100) indicate that the reduction of all the investigated complexes is localized on the pyridyl ring, whereas oxidation takes place on the Ir-phenyl fragment.

All complexes have a wide electrochemical gap (ΔE_{redox}) of more than 3.58 V (see Table 3.2). The electrochemical gap increases when electron-donating and electron-withdrawing groups are attached to the pyridyl and phenyl rings of the cyclometalating ligand, respectively, and it reaches a maximum of 3.83 V for **N4**. To our knowledge, this is the highest value reported for the electrochemical gap of a cationic cyclometalated iridium(III) complex [92]; it is slightly higher than the electrochemical gap of 3.81 V of the iridium(III) pyridine-carbene complex reported by Kessler *et al.* [121].

3.2.4 Infrared spectroscopy

The infrared absorption spectra of all the complexes were measured in neat films obtained by evaporation of CH_2Cl_2 solutions. All complexes show two infrared absorption peaks of equal intensity around 2170 – 2201 cm^{-1} and separated by about 20 cm^{-1} that are characteristic of stretching vibrations of the *tert*-butyl isocyanide C≡N bond (see Table 3.2 on the facing page) [235].

Table 3.2: Infrared absorption, electrochemical properties, and DFT-calculated HOMO and LUMO energies of the investigated complexes. IR absorption bands reported only for the C≡N stretching vibrations. All electrochemical redox processes were irreversible, estimated errors: ±50 mV. DFT calculations at the B3LYP/(6-31G**+LANL2DZ) level in CH_3CN.

	IR	Electrochemistry			DFT calculations		
Complex	C≡N freq. (cm^{-1})	E_{ox} (V)	E_{red} (V)	ΔE_{redox} (V)	E_{HOMO} (eV)	E_{LUMO} (eV)	ΔE_{DFT} (eV)
N1	2193, 2170	1.23	−2.38	3.61	−6.06	−1.73	4.33
N2	2198, 2176	1.42	−2.34	3.76	−6.18	−1.80	4.38
N3	2196, 2174	1.37	−2.43	3.80	−6.17	−1.72	4.45
N4	2195, 2173	1.37	−2.46	3.83	−6.19	−1.69	4.50
N5	2201, 2183	1.62	−1.96	3.58	−6.41	−2.25	4.16

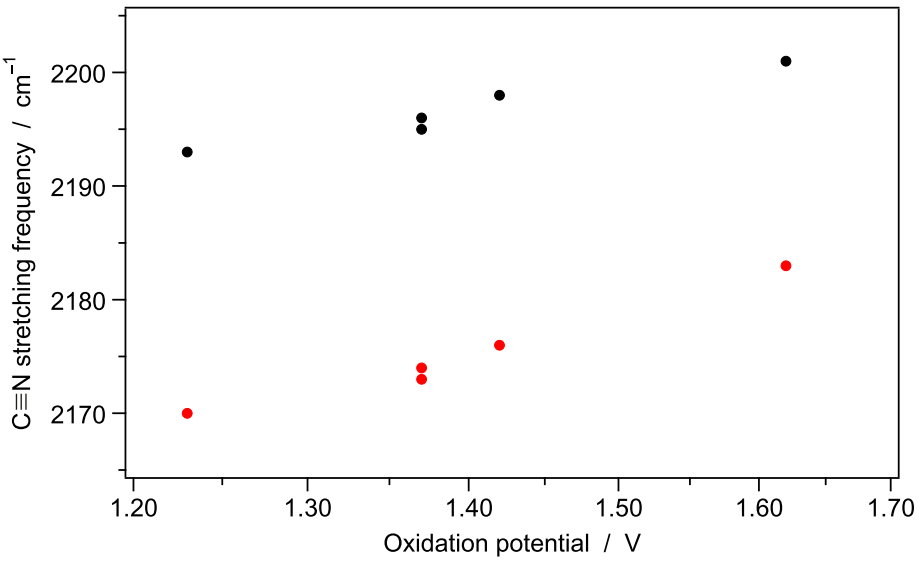

Figure 3.6: Correlation between the wavenumber of the two infrared transitions associated with the stretching vibrations of the C≡N bond and the oxidation potential (in CH_3CN) of all the complexes of the series.

The increase in frequency of the C≡N stretching vibrations in going from the free ligand (2137 cm^{-1}) [236] to the complexes suggests a weak π-backbonding

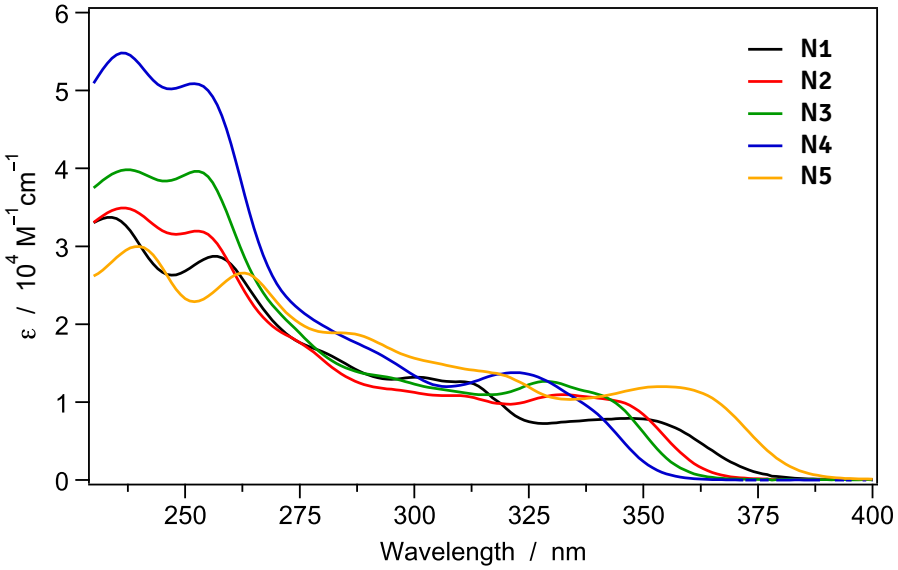

Figure 3.7: Absorption spectra of all complexes in room-temperature CH_2Cl_2.

from the iridium(III) ion to the *tert*-butyl isocyanides (the alkyl isocyanide ligands are known to act as strong σ-donors and weak π-acceptors in the complexes with metals in high oxidation states) [235].

We note that the frequencies of the infrared peaks are lower for complexes with lower oxidation potentials (see Table 3.2 and Figure 3.6). This trend reflects either a stronger π-backbonding from the metal to the *tert*-butyl isocyanides or a weaker σ-donation from the *tert*-butyl isocyanides to the iridium metal center in the more electron-rich complexes.

3.2.5 Electronic absorption spectroscopy

The complexes are white (**N3**, **N4**) or pale yellow (**N1**, **N2**, **N5**) solids and give nearly colorless solutions in dichloromethane and acetonitrile. Their electronic spectra were recorded in both solvents, but only those in CH_2Cl_2 are reported in Figure 3.7. All absorption spectra show intense bands below 300 nm with molar absorption coefficients (ϵ) in between $1-5 \times 10^4$ M^{-1} cm^{-1} originating from π-π^* electronic transitions of the cyclometalating ligands.

At lower energy, the spectra feature a composite band with a main maximum at 318 – 354 nm and $\epsilon = 8-14 \times 10^3$ M^{-1} cm^{-1} that we assign to the (Ir-phenyl)-to-pyridyl charge transfer transition (see Figure 3.7 and Table 3.3 on page 97) [237,

238]. The blue-shift of the CT band maximum by up to 6 nm in acetonitrile with respect to dichloromethane (see Table 3.3) suggests that the ground state of all the complexes is more polar than the excited state.

3.2.6 Luminescence of liquid solutions

Upon excitation with near-UV light, the complexes exhibit blue (**N2**, **N3** and **N4**) or blue-green (**N1**, **N5**) luminescence in both dichloromethane and acetonitrile solutions. The luminescence spectra at room temperature show a vibronic structure with the highest-energy peak (λ_{em}, 0-0 transition) at 440 – 459 nm; the vibronic structure becomes better resolved at 77 K (see Figure 3.8 on the next page and Figure 3.9 on page 98). The emission color of all complexes (*i.e.*, the position of the maxima and the relative intensities of the peaks in the spectrum) is solvent- and temperature-independent (Figure 3.9 and Table 3.3 on page 97).

The luminescence of all complexes is quenched by oxygen; therefore, photophysical measurements in 10^{-5} M liquid solutions were carried out under argon. Under these conditions, all complexes display luminescence quantum yields (Φ_{em}) between 32 % to 76 % and observed excited-state lifetimes (τ) in few tenth of microseconds (see Table 3.3 on page 97). The luminescence decays are single-exponential functions suggesting the presence of one emissive center in liquid solution. The calculated radiative lifetimes of the excited states ($\tau_{rad} = \tau/\Phi_{em}$, which are the ideal lifetimes in the absence of radiationless processes) are in the range of 46 – 82 µs and are almost solvent-independent (see Table 3.3).

The luminescence spectra of all the investigated complexes show vibronic structure and are solvent-independent, whereas the radiative lifetimes are in the range of tens of microseconds. At the same time, the substituents in the cyclometalating ligands determine the emission color of each particular complex: a blue shift is achieved by the 4'-F in the phenyl or the 4-OCH_3 in the pyridyl ring; a red shift is achieved using the 5-CF_3 on the same moiety (see Table 3.3).

All of these findings suggest that all complexes emit from a predominantly cyclometalating-LC triplet excited state of π-π^* nature [92, 229, 237, 238].

Moreover it shoul be stressed that, in all the series, the shorter wavelength of λ_{em} corresponds to a shorter wavelength of the CT absorption band maximum, and also to a larger electrochemical gap (see Table 3.2, Table 3.3, and Table 3.4 on page 102).

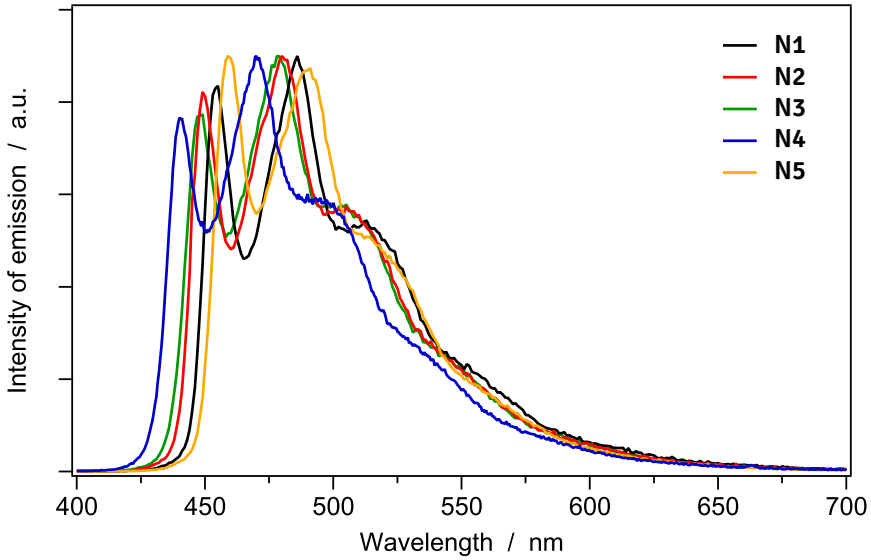

(a) Spectra in room-temperature CH_2Cl_2 solution.

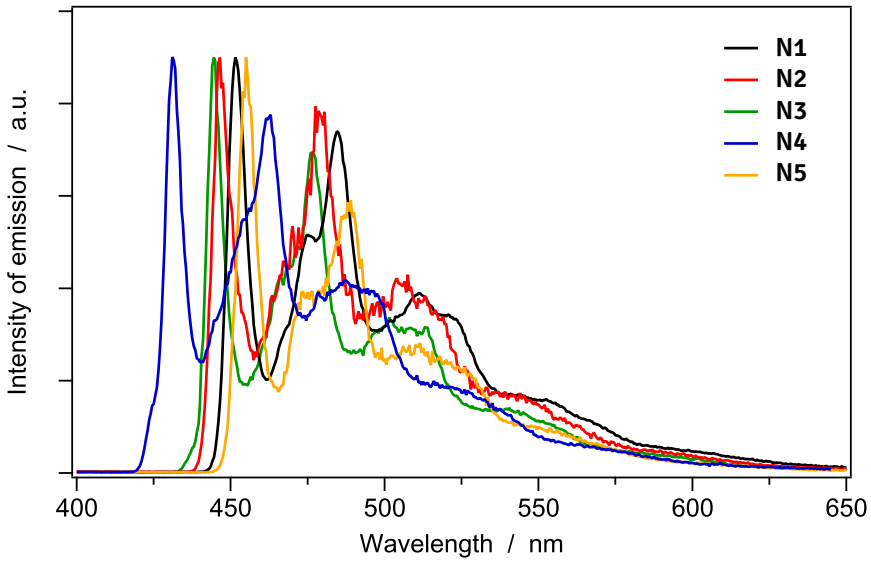

(b) Spectra in rigid matrix at 77 K.

Figure 3.8: Corrected and normalized luminescence spectra of all the complexes in CH_2Cl_2 in room-temperature solution (a) and in rigid matrix at 77 K (b). The luminescence spectra in acetonitrile and PMMA are almost identical to the spectra in room-temperature dichloromethane and are not reported in this thesis.

Table 3.3: Photophysical properties of the investigated complexes. All media are at room temperature under air (absorption and solid state emission) or under argon (emission in solution), if not otherwise mentioned; * = biexponential luminescence decay (only predominant component reported); λ_{exc} = 330 nm. The T_1 label refers to the energy of the first triplet state with respect to the ground singlet state (adiabatic energy difference) from DFT calculations in CH_3CN.

Complex	Medium	λ_{abs} (ϵ) (nm ($M^{-1}\,cm^{-1}$))	λ_{max} (nm)	Φ_{em} (%)	τ (µs)	τ_{rad} (µs)	T_1 (eV)
N1	CH_3CN	341 (7.5×10^3)	453	52	32	62	3.15
	CH_2Cl_2	347 (7.9×10^3)	455	45	25	56	
	CH_2Cl_2, 77 K		452	—	28 (80%)*		
	PMMA 1 %		455	35	27 (75%)*		
	neat film		456	4	2.0 (56%)*		
N2	CH_3CN	327 (1.0×10^4)	447	59	46	78	3.22
	CH_2Cl_2	332 (1.1×10^4)	449	48	37	77	
	CH_2Cl_2, 77 K		447	—	20 (51%)*		
	PMMA 1 %		449	40	30 (62%)*		
	neat film		456	3	3.8 (57%)*		
N3	CH_3CN	326 (1.2×10^4)	447	55	40	73	3.27
	CH_2Cl_2	328 (1.3×10^4)	449	50	33	66	
	CH_2Cl_2, 77 K		445	—	35 (58%)*		
	PMMA 1 %		448	39	29 (68%)*		
	neat film		451	6	1.5 (70%)*		
N4	CH_3CN	318 (1.3×10^4)	440	44	36	82	3.35
	CH_2Cl_2	322 (1.4×10^4)	440	32	26	81	
	CH_2Cl_2, 77 K		436	—	50		
	PMMA 1 %		440	35	30 (63%)*		
	neat film		444	4	2.3 (51%)*		
N5	CH_3CN	348 (1.1×10^4)	458	76	35	46	3.10
	CH_2Cl_2	354 (1.2×10^4)	459	69	33	48	
	CH_2Cl_2, 77 K		455	—	23 (76%)*		
	PMMA 1 %		458	45	13 (78%)*		
	neat film		463	8	2.0 (92%)*		

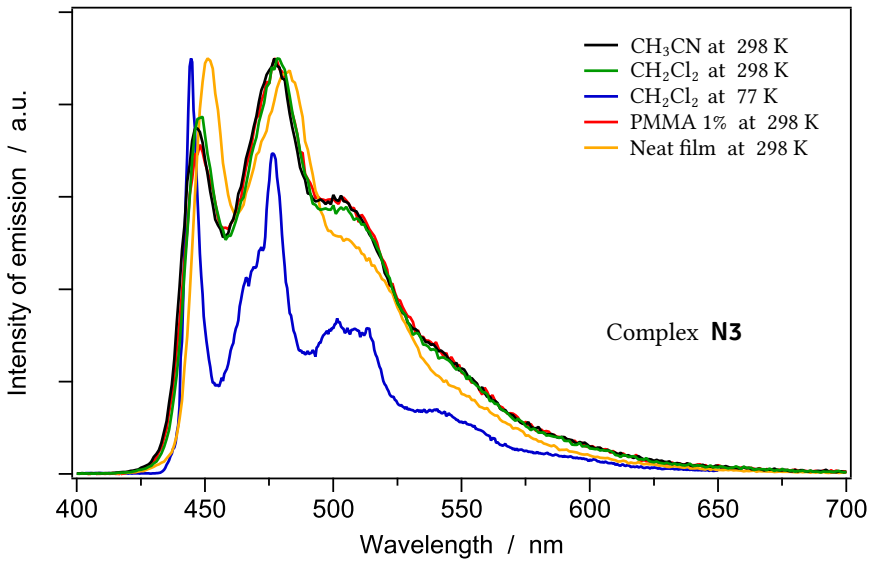

Figure 3.9: Corrected and normalized room-temperature luminescence spectra of **N3** (as an example) in acetonitrile, in CH_2Cl_2 (also shown at 77 K), and PMMA and as a solid neat film.

3.2.7 Luminescence in solid state

The photophysical properties of the series were also studied in two different solid matrixes: in 1 % poly(methyl methacrylate) (PMMA) drop-casted films, and in neat solids spin-coated films. All solid-state measurements were carried out under air.

In PMMA, all complexes show blue or blue-green luminescence. The luminescence spectra, quantum yields (35 – 45 %), and lifetimes (13 – 30 µs; biexponential decays) in PMMA are similar to those measured in diluted liquid solutions (see Table 3.3 on the preceding page and Figure 3.9). It is a remarkable result, considering that the PMMA films had a relatively high concentration of the complex and were exposed to air. We therefore conclude that all complexes in PMMA do not form aggregates and are not quenched by oxygen.

In neat solids, the complexes emit blue (**N3**), green (**N1**, **N4**, **N5**), or yellow (**N2**) luminescence. For most of these complexes, a red shift of the emission color occurs in going from solutions to neat solids. It results from the red shift (by up to 9 nm), broadening, and change of the relative intensities of the luminescence peaks (see Table 3.3 and Figure 3.9). In solutions, the 0-0 transition (λ_{max} = 440 –

459 nm) either dominates the emission spectrum or contributes significantly to it. In neat solids, however, the intensity of 0-0 transition is low (except for **N3**), and the long-wavelength peaks are dominant. The quenching by oxygen and the self-quenching caused by aggregation and triplet-triplet interaction are responsible for the low quantum yields (less than 8.4 %) and short lifetimes (less than 5 µs; biexponential decays) of all the neat complexes under air.

In order to reduce aggregation, which red-shifts and quenches the emission of iridium(III) complexes in neat solids, the ligands are often modified with bulky spectator groups [104, 182, 199]. In this series, the bulky *tert*-butyl isocyanide ligands alone are not sufficient to prevent aggregation. For example, **N4** is a blue emitter in solution, but a pale green emitter in neat solid (see Figure 3.8 on page 96). However, the complexes that have additional bulky groups in the cyclometalating ligands to further reduce aggregation (4-*tert*-butyl, **N3**; 5-CF_3, **N5**) show the smallest red shift of color and the highest luminescence quantum yields in neat solids (see Table 3.3 on page 97). For example, the emission spectrum of **N3** remains the same under all studied conditions (see Figure 3.9 on the facing page), and **N3** is the first iridium(III) isocyanide complex to show blue-phosphorescence in neat solid.

3.2.8 Overview of photophysical properties

All the complexes of this series emit phosphorescence at shorter wavelengths and with higher quantum yields than do the previously reported $[(CN)_2Ir(C)_2]^+$ and $[(CN)_2Ir(CC)]^+$ analogs in all the media [85, 92, 120, 227–230].

The advantage of this particular series is that they do not require polyfluorinated cyclometalating ligands to achieve blue phosphorescence, unlike the reported analogs [85, 92, 120] or the extensively studied $[(CN)_2Ir(NN)]^+$ diimine complexes [82, 111, 116, 118, 158, 178, 223, 224]. The main problem with electron-deficient polyfluorinated ligands is that they have reactive C—F bonds and usually display low stability in LECs [239–241]. For that particular reason, this kind of bis-cyclometalated cationic iridium(III) isocyanide complexes are promising blue-phosphorescent emitters in terms of color and quantum efficiency in solution and in neat solid (*e.g.*, **N3**). However, their long radiative lifetimes may cause high sensitivity to triplet-triplet interaction and oxygen quenching and can limit their use in electroluminescent devices.

3.2.9 Theoretical calculations

The molecular and electronic structures of the complxes were investigated by performing DFT calculations at the B3LYP/(6-31G**+LANL2DZ) level. The fully optimized ground-state geometries of all complexes show a near-octahedral coordination of the Ir(III) metal center and are in good agreement with the X-ray structure of **N4** (see Figure 3.5 on page 91).

Calculations show that the highest-occupied molecular orbital (HOMO) is composed of phenyl π-orbitals from the two cyclometalating ligands together with a small contribution from d-orbitals of the iridium ion for all the complexes (see Figure 3.10 on the facing page for **N1**). The electron-withdrawing groups (4'-F or 5-CF_3) on the cyclometalating ligands stabilize the HOMO (see Table 3.2 on page 93).

The lowest-unoccupied molecular orbital (LUMO) substantially resides on the pyridyl ring of the cyclometalating ligands (see Figure 3.10). Therefore, modification of the pyridyl ring in **N2** changes the LUMO energy: an electron-donor (4-*tert*-butyl or 4-OCH_3) destabilizes it by 0.08 – 0.11 eV; the electron-withdrawing 5-CF_3 group strongly stabilizes it by 0.45 eV (see Table 3.2 on page 93).

The trends in the calculated HOMO and LUMO energies of all the complexes are in agreement with the trends in the measured oxidation and reduction potentials: the lower (more negative) E_{HOMO} and E_{LUMO} energies correspond to the higher (more positive) E_{ox} and E_{red} potentials, respectively (see Table 3.2 and Table 3.4 on page 102). At the same time, the larger calculated HOMO–LUMO energy gap corresponds to a larger electrochemical gap.

To gain insight into the photophysical properties of this series, we optimized the geometry of the lowest-energy emitting triplet excited state (T_1) by using the spin-unrestricted B3LYP approach. The electron promotion associated with the excitation to T_1 shortens the iridium(III) bonds with the cyclometalating ligands by 0.01 – 0.05 Å and stretches the metal bonds to the *tert*-butyl isocyanide ligands by 0.05 Å. The unpaired-electron spin-density distribution calculated for T_1 perfectly matches the topology of the HOMO-to-LUMO monoexcitation. Therefore, excitation to T_1 involves an electron promotion from the HOMO (Ir-phenyl fragment) to the LUMO (pyridyl ring).

All of the complexes have a similar spin-density distribution that is mainly localized on the cyclometalating ligands together with a small contribution (about 0.13 e) from the iridium metal ion. Therefore, T_1 can be described as a ^{3}LC excited

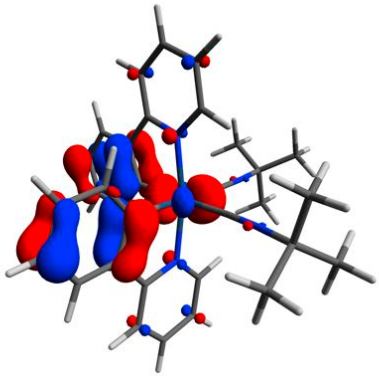

(a) HOMO of **N1**.

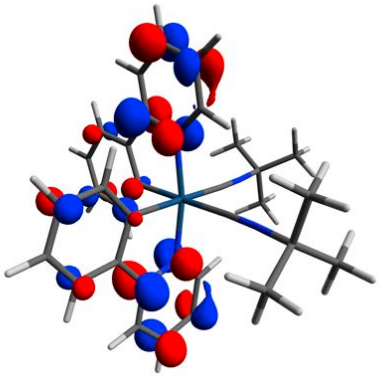

(b) LUMO of **N1**.

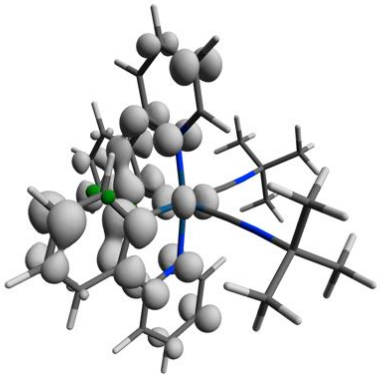

(c) Spin density of **N1** triplet.

Figure 3.10: Archetypal representation showing the electronic density contours (0.05 e bohr^{-3}) calculated for the frontier molecular orbital of complex **N1**, taken as an example (a and b) and the spin density distribution (0.005 e bohr^{-3}) calculated for the emitting T_1 excited state of **N1** resulting from the HOMO-to-LUMO monoexcitation (c).

Table 3.4: Variation of experimentally measured and DFT-calculated parameters of the investigated iridium(III) complexes with respect the non-substituted arbitrarily chosen **N1** complex. Data for calculations were taken from Table 3.2 on page 93 and Table 3.3 on page 97. Spectroscopic parameters were converted from the wavelength (λ_{abs}, λ_{max}; nm) to the energy (E_{abs}, E_{em}; eV) scale. All values refer to CH_3CN solutions.

Complex	ΔE_{ox}	ΔE_{HOMO}	ΔE_{red}	ΔE_{LUMO}	ΔE_{redox}	ΔE_{DFT}	ΔE_{abs}
N2	+0.19	−0.12	+0.04	−0.07	+0.15	+0.05	+0.16
N3	+0.14	−0.11	−0.05	+0.01	+0.19	+0.12	+0.17
N4	+0.14	−0.13	−0.08	+0.04	+0.22	+0.17	+0.26
N5	+0.39	−0.35	+0.42	−0.52	−0.03	−0.17	−0.07

Complex	ΔE_{em}	ΔT_1
N2	+0.04	+0.07
N3	+0.04	+0.12
N4	+0.08	+0.20
N5	−0.03	−0.05

state localized on cyclometalating ligands, with a small contribution of ^{3}MLCT state, and with no participation of the *tert*-butyl isocyanides (see Figure 3.10).

The predominant ligand-centered nature of the emitting T_1 state explains the well-resolved vibronic structure of the luminescence spectra of all the complexes of the series (see Figure 3.8 on page 96 and Figure 3.9). The calculated changes in the adiabatic energy of T_1 with respect to the ground state are in agreement with the experimentally observed shifts in the emission energy (see Table 3.3 on page 97 and Figure 3.7 on page 94).

3.3 Conclusions

We have developed bis-cyclometalated, cationic iridium(III) isocyanide complexes (**N1** – **N5**) that in solution show efficient blue or blue-green phosphorescence with the highest-energy luminescence peak at 440 – 459 nm and with quantum yields and excited-state lifetimes reaching 76 % and 46 µs, respectively.

All complexes emit from a ^{3}LC excited state localized on cyclometalating

ligands, and their photophysical properties are solvent-independent. For most of the complexes, an emission color red shift occurs in going from solution to the neat solid. However, the shift is minimal for the complexes with bulky groups on the cyclometalating ligands that prevent aggregation, and complex **N3** is the first in its class of compounds to show blue phosphorescence in neat solid.

We expect that the easy-to-make cyclometalated iridium(III) isocyanide complexes will provide access to efficient phosphorescent emitters from deep-blue to near-infrared spectral range by simple variation of the cyclometalating and isocyanide ligands [242, 243].

Chapter 4

From one extreme to the other

In the previous chapters we focused our attention in order to obtain sky-blue emitting cationic iridium(III) complexes for LECs. In this chapter, on the other hand, we would like to demonstrate that Ir(III) complexes can be used also for another particularly demanding task: near-infrared emission.

For this reason, two new iridium(III) complexes $[Ir(ppy)_2(pyr_2bpy)][PF_6]$ (**GH**) and $[Ir(dfppy)_2(pyr_2bpy)][PF_6]$ (**GF**) have been synthesized and fully characterized. The effect of the pyrene substituents on the electronic properties is investigated through a comprehensive photophysical and theoretical study on the two complexes in comparison to reference complexes without substituents on the **bpy** ancillary ligand (**xH** and **xF**).

Both theory and experiment show that the intense and broad band appearing in the 400 – 500 nm region of the absorption spectra of **GH** and **GF** is due to intramolecular charge-transfer transitions from the pyrene substituents to the bipyridine ligand. The luminescence bands centered above 650 nm, displayed by both **GH** and **GF**, is attributed to a charge-transfer triplet state located on the **pyr_2bpy** ligand, lying at lower energy than the strongly emitting [Ir-ppy]-to-bpy triplet states of the complexes lacking the pyrene fragments.

Such luminescence, detected both at room temperature and at 77 K, shows that the appendage of luminophoric moieties to luminescent Ir-based centers may further widen the emission tunability of this exploited class of luminescent materials through purely electrostatic effects exerted on a properly designed NN ancillary ligand.

4.1 Introduction

As already mentioned in the first introductory chapter of this thesis, near-infrared (NIR) light-emitting sources are typically expensive and LECs could serve as low-cost alternatives in areas were NIR luminescence is of key importance, such as telecommunications and bioimaging. For instance, highly efficient deep-red lighting devices have been obtained with an Ir-iTMC which incorporates a perylenediimide (PDI) that acts as an electron transporting moiety with efficient red emission [196]. Another example is the use of Ir-iTMCs tethered to a boron-dipyrromethene (Bodipy) unit, in which an efficient energy transfer to the long-lived triplet level of the bodipy moiety demonstrated the potential applicability of these materials for triplet light-harvesting, a phenomenon not frequently observed [244].

These results suggest that there is potential for investigating Ir-iTMCs with thoroughly selected appended organic fragments characterized by particular photophysical features, such as strong absorption and/or luminescence or low-lying electronic excited states. Accordingly, we designed two new Ir-iTMCs bearing pyrene units attached to the ancillary ligand. The choice of pyrene was based on its photophysical properties that may afford valuable information upon anchoring on semiconductors and biological systems or can be exploited, more generally, in chemosensor applications [245–249].

Recently, Castellano *et al.* have made a neutral bis-heteroleptic iridium(III) complex with an acetylacetonate (**acac**) ligand functionalized with pyrene and perylene moieties [250]. In this work, they demonstrated an effective pathway for populating the triplet excited states of the aromatic moieties. However, these electronic levels are dark and do not exhibit any kind of phosphorescence at room temperature [250].

In this chapter we describe the synthesis of four ionic heteroleptic iridium(III) complexes combining the two different cyclometalating ligands already seen in Chapter 2 (*i.e.*, the 2-phenylpyridine, **ppy** and the 2-(3,5-difluorophenyl)pyridine, **dfppy**), together with two NN ancillary ligands: *i.e.*, the extensively used 2,2'-bipyridine (**bpy**) and its functionalized version incorporating two pyrene (**pyr**) units in 5,5'-positions (**pyr$_2$bpy**).

The structure of the ligands is reported in Figure 4.1 on the next page, together with the ones of the related four iridium(III) complexes; the target com-

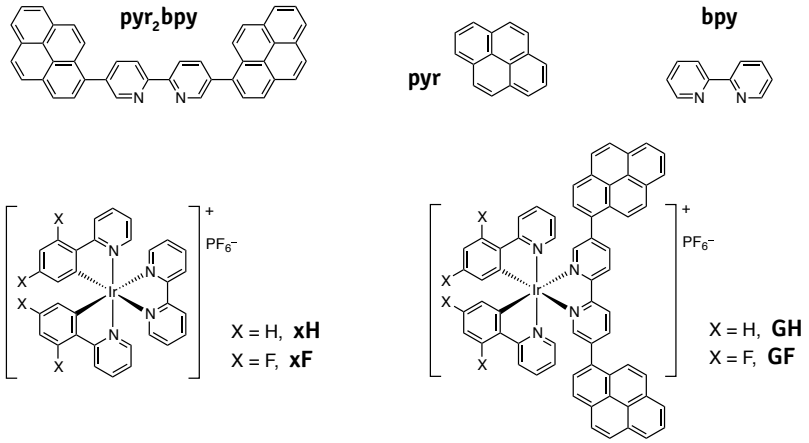

Figure 4.1: Chemical structures of both the **bpy** and **pyr$_2$bpy** ligands, and of all the investigated complexes [Ir(ppy)$_2$(pyr$_2$bpy)][PF$_6$] (**GH**) and [Ir(dfppy)$_2$(pyr$_2$bpy)][PF$_6$] (**GF**); the reference complexes [Ir(ppy)$_2$(bpy)][PF$_6$] (**xH**) and [Ir(dfppy)$_2$(bpy)][PF$_6$] (**xF**) are also reported for clarity

plexes are [Ir(ppy)$_2$(pyr$_2$bpy)][PF$_6$] (**GH**) and [Ir(dfppy)$_2$(pyr$_2$bpy)][PF$_6$] (**GF**), and the reference are [Ir(ppy)$_2$(bpy)][PF$_6$] (**xH**) and [Ir(dfppy)$_2$(bpy)][PF$_6$] (**xF**), respectevely.

Based on complete photophysical and theoretical studies, we conclude that, similar to the analogous neutral iridium(III) complexes of Castellano [250], our pyrene-based Ir-iTMCs show an efficient population of the ^{3}pyr$_2$bpy state, but in contrast to neutral complexes, the phosphorescence was successfully recorded at room and low temperature conditions and exhibited a charge-transfer character, under the electrostatic influence of the nearby Ir-complexed center.

This finding shows that luminescent multichromophoric iridium(III) complexes can be designed where the luminescence is somewhat influenced but not directly dictated by the metal complex moiety.

4.2 Results and discussion

4.2.1 Synthesis and characterization of pyr$_2$bpy

The compound **pyr$_2$bpy** was synthesized using a Suzuki coupling of 5,5'-dibromo-2,2'-bipyridine with pyren-1-ylboronic acid in biphasic conditions in

the presence of $[Pd(PPh_3)_4]$ with exclusion of light. The electron impact mass spectrum of the product exhibited a peak at 556.2 m/z assigned to the molecular cation of **pyr₂bpy**. The compound is poorly soluble in CH_2Cl_2 and insoluble in most other common solvents. Protonation using trifluoroacetic acid yields a salt that is very soluble in, for example, CH_2Cl_2 and, for this reason, solution characterization was carried out using the protonated ligand.

Single crystals of **pyr₂bpy** were grown by layering ethyl acetate on a CH_2Cl_2 solution of the ligand; sufficient amount of trifluoroacetic acid was added to the CH_2Cl_2 solution in order to solubilize the compound. Despite the presence of acid, crystals of the neutral compound were obtained and the structure is presented in Figure 4.2. The trans-conformation of the bpy unit is consistent with crystallization of the nonprotonated ligand. The pyrene unit is twisted 45.8° out of the plane of the bpy domain. The packing of molecules in the lattice is dominated by $CH\cdots\pi$ contacts [251] rather than by the π-stacking found in the solid-state structure of pyrene [252].

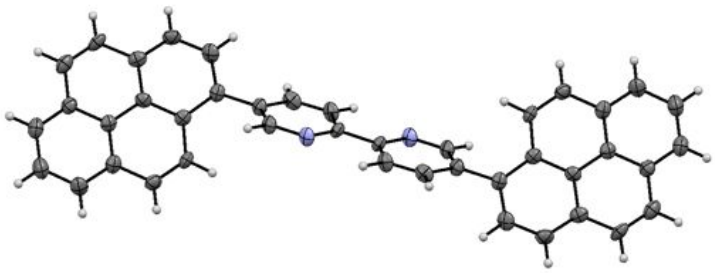

Figure 4.2: X-ray crystal structure of the ligand **pyr₂bpy** (ellipsoids plotted at 40% probability level).

4.2.2 Synthesis and characterization of the complexes

The complexes **GH** and **GF** were prepared by reaction of the iridium dimer $[Ir(ppy)_2(\mu\text{-}Cl)]_2$ or $[Ir(dfppy)_2(\mu\text{-}Cl)]_2$ with **pyr₂bpy** followed by anion exchange with addition of $[NH_4][PF_6]$ (see Scheme 4.1 on the next page).

Figure 4.3 on page 110 depicts the structures of the **GH** and **GF** cations. The octahedral geometry of the iridium(III) ion in each complex cation is, as expected, as is the trans-arrangement of the N-donors of the two cyclometalated ligands. The metal-bound bpy unit deviates slightly from planarity in each cation (7.8° in

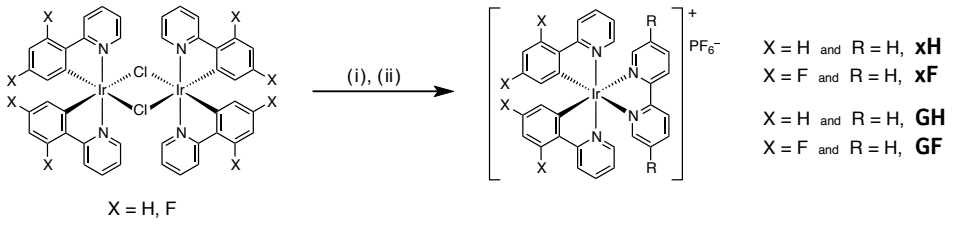

Scheme 4.1: Syntheses of **xH**, **xF**, **GH**, and **GF**: (i) **bpy** or **pyr$_2$bpy** in MeOH / CH_2Cl_2 solution, (ii) NH_4PF_6.

GH and 11.6° in **GF**) and each pyrene substituent is twisted with respect to the pyridine ring to which it is attached (59.6° and 37.2° in **GH** and 42.7° and 43.3° in **GF**). The twisting of the pyrene units is therefore similar to that observed for the free ligand (45.8°). Only one of the pyrene substituents of **GH** is involved in face-to-face intercation π-stacking. The pyrene domains are slipped with respect to one another giving an efficient interaction with an interplane separation of 3.52 Å in **GH** and of 3.57 Å in **GF**.

4.2.3 Photophysical properties of pyr$_2$bpy

The behavior of ligand **pyr$_2$bpy** was investigated and compared with that of its individual moieties (*i.e.*, pyrene and 2,2'-bipyridine). Room-temperature absorption spectra of **pyr$_2$bpy**, **pyr** and **bpy** in CH_2Cl_2 solution are reported in Figure 4.4 on page 111. The absorption profile of **pyr$_2$bpy** in the region between 230 and 350 nm resembles that of free pyrene, though with broader and slightly red-shifted bands. At longer wavelengths, a new band centered at 360 nm is detected; this feature is absent both in **pyr** and **bpy**, and is attributed to a charge-transfer (CT) transition from the pyrene moieties to the central bipyridine unit. This is a common feature for pyrene-bipyridine dyads [253] and, in the case of **pyr$_2$bpy**, the CT nature of this state is corroborated by a remarkable red-shift upon increasing the solvent polarity. Further confirmation of the CT assignment is provided in the theoretical description of the **pyr$_2$bpy** ligand (see next section).

The absorption spectrum of **pyr$_2$bpy** (5 μM) was also recorded upon addition of increasing amounts of trifluoroacetic acid (up to 100 eq , Figure 4.5, top). In this range, three isosbestic points are found (306, 340, and 394 nm) attesting to the occurrence of one single reaction (*i.e.*, the first protonation of the ligand at

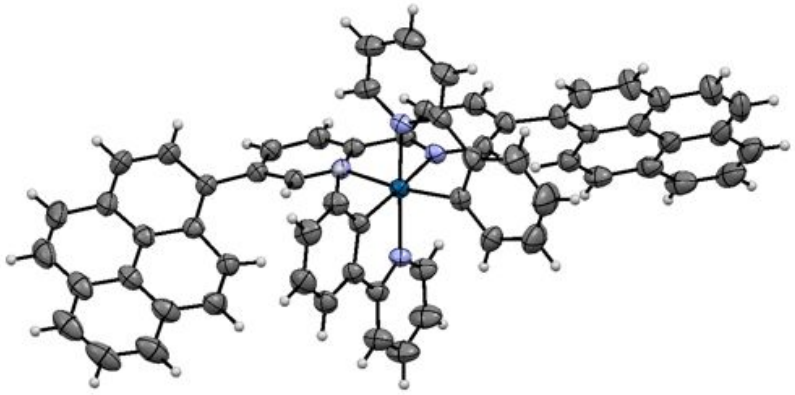

(a) Cation of **GH**.

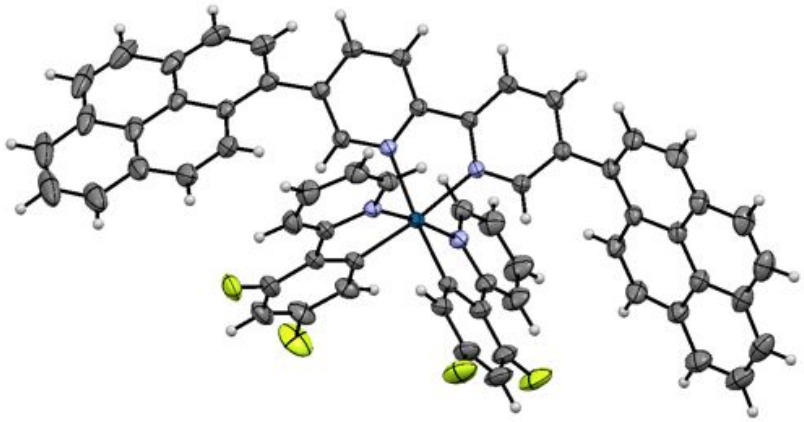

(b) Cation of **GF**.

Figure 4.3: X-ray crystal structures of the two investigated pyrene-based iridium(III) complexes (ellipsoids plotted at 40% probability level); solvent molecules are omitted.

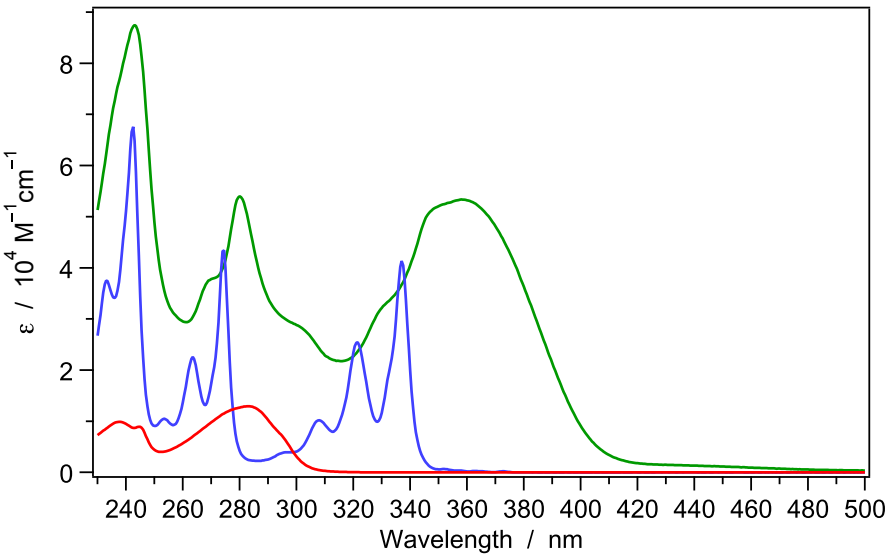

Figure 4.4: Absorption spectra of pyrene (**pyr**, blue), 2,2'-bipyridine (**bpy**, red) and **pyr$_2$bpy** (green) in acid-free CH_2Cl_2.

the bpy site). Notably, the absorption spectra of acid solutions of **pyr$_2$bpy** are characterized by the lack of the intense band attributed to a CT pyr-to-bpy transition (λ_{max} = 360 nm) and by the presence of a broader and less intense shoulder centered around 440 nm, tentatively attributed to a CT pyr-to-bpyH$^+$ transition. This attribution is validated by the theoretical description of the neutral and protonated **pyr$_2$bpy** species (see next section). When more than 100 eq of acid are added (see Figure 4.5, bottom), the new CT band is further red-shifted and clean isosbestic points are no longer observable, probably due to the strong perturbation of the intrinsic physical properties of the solvent (*e.g.*, ionic strength, dielectric constant and refractive index) induced by the presence of high amounts of trifluoroacetic acid. In principle, a second protonation of the ligand is possible, but we can assume that, under these experimental conditions, the diprotonated form $[(pyr_2bpy)H_2]^{2+}$ is quantitatively dissociated into $[(pyr_2bpy)H]^+$ and H^+ because of the acid strength of 2,2'-bypridinium dications, so that it can be neglected [254].

The **pyr$_2$bpy** free-ligand exhibits a strong fluorescence at room temperature ($\Phi \approx 60$ %, see Table 4.1 on page 113). The emission profile is broad and unstructured, hence very different to pristine pyrene (see Figure 4.6 on page 114). While

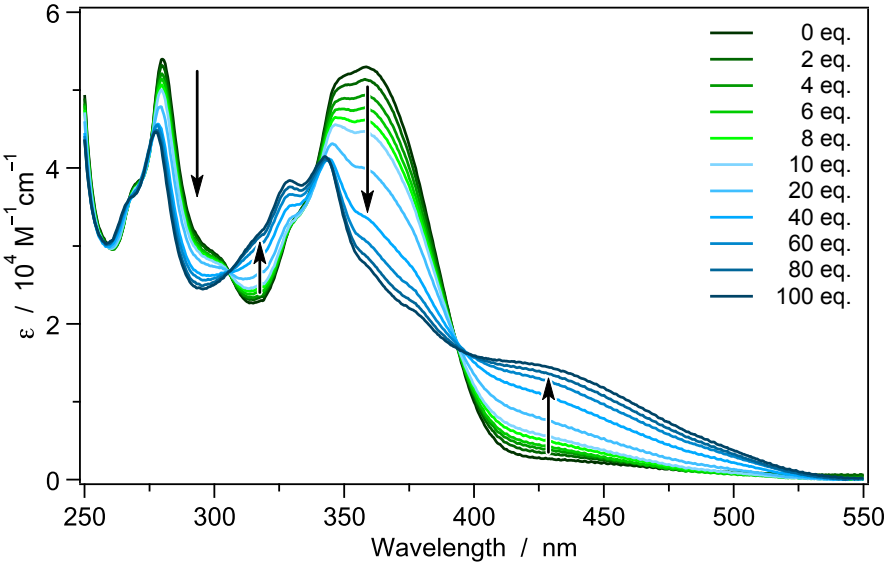

(a) Range between 0 and 100 equivalents of acid. Three isosbestic points can be found at 306, 340 and 394 nm.

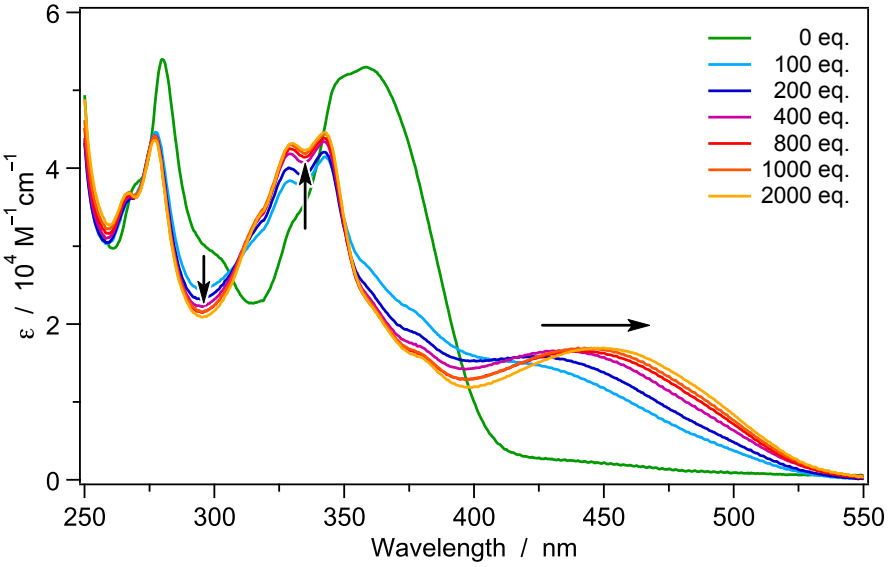

(b) General overview up to the addition of 2000 equivalents, the further shift of the CT band toward longer wavelengths can be observed.

Figure 4.5: Absorption spectral changes of **pyr$_2$bpy** upon addition of increasing amounts of trifluoroacetic acid in room-temperature CH_2Cl_2.

Table 4.1: Photophysical properties of **pyr** and **pyr$_2$bpy** in solution. Data in oxygen-free and air-equilibrated solutions (in parentheses) are given.

			pyr		
	λ_{max} (nm)	Φ_{em} (%)	τ (µs)	k_r (10^6 s^{-1})	k_{nr} (10^6 s^{-1})
toluene	373	74.0 (3.4)	310 (16.9)	2.39 (2.02)	0.84 (57.1)
CH_2Cl_2	374	30.4 (6.8)	164 (30.4)	1.85 (2.24)	4.24 (30.7)
MeCN	374	61.9 (3.7)	318 (14.3)	1.95 (2.61)	1.20 (67.3)
			pyr$_2$bpy		
	λ_{max} (nm)	Φ_{em} (%)	τ (µs)	k_r (10^8 s^{-1})	k_{nr} (10^8 s^{-1})
toluene	425	87.5 (70.4)	1.4 (1.0)	6.25 (5.87)	0.90 (2.46)
CH_2Cl_2	448	61.7 (63.3)	1.7 (1.4)	3.63 (3.96)	2.26 (2.29)
MeCN	465	42.3 (33.0)	2.4 (2.0)	1.76 (1.65)	2.40 (3.35)

the emission energy of **pyr** is almost solvent-independent, the band of **pyr$_2$bpy** undergoes a considerable solvent-dependent Stokes shift: *i.e.*, its maximum lies at 448 nm in CH_2Cl_2, but is shifted to higher energies as the solvent polarity is decreased (*e.g.*, 425 nm in toluene).

Such behavior, which is well-known for electron donor-acceptor systems, further suggests the presence of a fluorescent intramolecular charge-transfer (ICT) state in both polar and nonpolar solvents [253]. Importantly, although this ICT state is strongly destabilized in nonpolar solvents, it remains lower-lying than the first singlet excited state of **pyr** (see Figure 4.6); therefore, no pyrene-based emission is detected in any case for **pyr$_2$bpy**. At low temperature, fluorescence bands become more structured and vibrationally resolved (both in the case of **pyr** and **pyr$_2$bpy**), but virtually no energy shift is observed when decreasing the temperature.

To investigate the emission properties of **pyr$_2$bpy** in the presence of a cationic species at the bpy site, emission spectra were recorded in CH_2Cl_2 during the titration with trifluoroacetic acid (see Figure 4.7 on page 115). The strong fluorescence band of the free ligand is promptly quenched upon addition of few equivalents of acid and a weaker emission is found at around 650 nm (Φ = 5.0 %, τ = 500 ps in CH_2Cl_2). The lower energy of this new emitting state further corroborates its ICT nature (pyr-to-bpyH$^+$) because intramolecular charge transfer is clearly favored

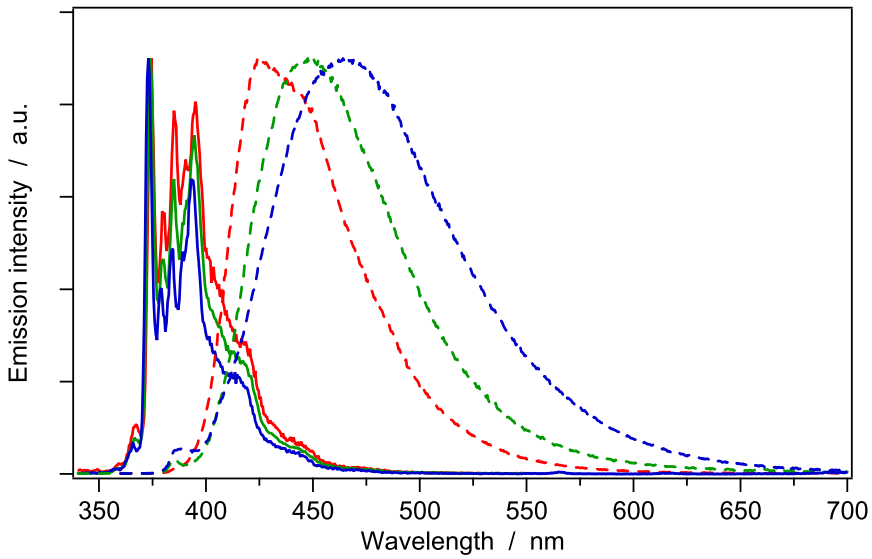

Figure 4.6: Normalized emission spectra of **pyr** (solid) and **pyr$_2$bpy** (dashed) at room temperature in different solvents: toluene (red), dichloromethane (green), and acetonitrile (blue); λ_{exc} = 310 nm.

in the presence of a protonated acceptor. It should be noted that upon addition of more than 100 eq of acid, the energy of this ICT state is further decreased, likely due to a dramatically enhanced polarity of the solvent environment.

Because iridium(III) complexes are triplet emitters due to the high spin-orbit coupling of the metal ion, we recorded luminescence spectra of the **pyr$_2$bpy** free ligand at low temperature in order to evaluate the energy of the triplet excited state. The phosphorescence spectra, recorded at 77 K, are virtually solvent independent and show that, while the pyrene triplet emission is found at 590 nm (with a lifetime of 0.5 s), the **pyr$_2$bpy** phosphorescence appears at 626 nm, with a substantially shorter lifetime of 10 ms (see Figure 4.8 on the next page). No triplet emission from the protonated ligand could be detected.

Theoretical description of the ground and excited states of pyr$_2$bpy

To gain insight into the molecular and electronic structures and the optical properties of both neutral and protonated **pyr$_2$bpy** species, theoretical calculations were performed in the framework of the DFT and TD-DFT approaches using the PBEh1PBE functional.

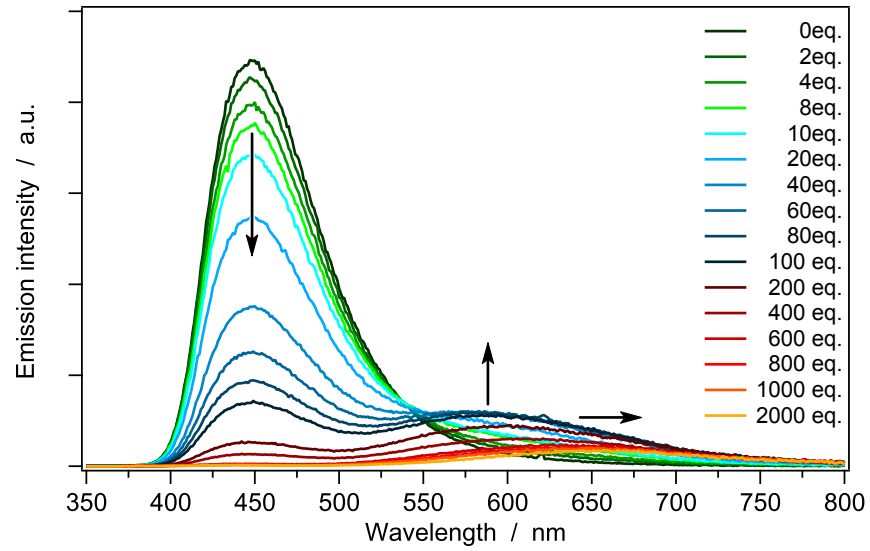

Figure 4.7: Emission spectral changes of **pyr$_2$bpy** upon addition of increasing amounts of trifluoroacetic acid in CH_2Cl_2 at room temperature; λ_{exc} = 306 nm, corresponding to an isosbestic point (see Figure 4.5, a).

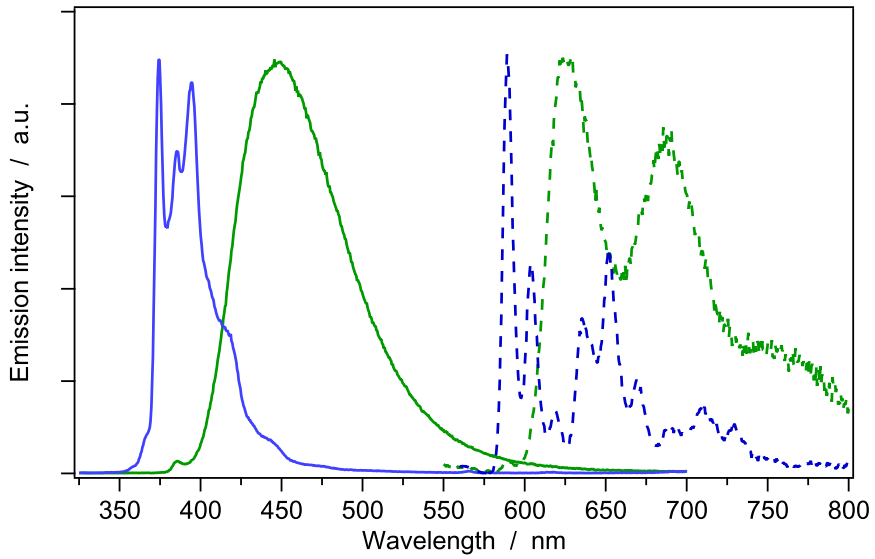

Figure 4.8: Fluorescence (solid lines) and phosphorescence (dashed lines) spectra of **pyr** (blue) and **pyr$_2$bpy** (green) in acid-free CH_2Cl_2 (λ_{exc} = 280 nm). Phosphorescence spectra were recorded at 77 K applying a delay of 50 µs to avoid residual fluorescence signal.

For the neutral species, the most stable structure corresponds to a *trans* disposition of the bpy domain in agreement with the X-ray structure shown in Figure 4.2 on page 108. In contrast, for the protonated species, the *cis*-configuration is predicted to be the most stable (21.8 kJ/mol lower in energy than the *trans*-conformer) due to the stabilization effect of the hydrogen bond formed by the N^+-H group and the vicinal nitrogen atom. The predicted molecular structure for both neutral and protonated species is very similar in terms of bond lengths, and is in good agreement with the X-ray structure. The twisting angle between the pyr and bpy units (53°) for both neutral and protonated species is slightly overestimated compared to the X-ray diffraction value (45.8°) which will be affected by packing effects in the crystal.

Figure 4.9 on the next page displays the electronic density distribution calculated for HOMO and LUMO of neutral and protonated **pyr$_2$bpy** in their respective singlet ground states. To make the comparison with the protonated species easier, the energies and topologies shown in Figure 4.9 for the molecular orbitals of neutral **pyr$_2$bpy** are those obtained for the *cis*-conformer. Almost identical energies and topologies are computed for **pyr$_2$bpy** in *trans*-conformation. For the neutral molecule, the molecular orbitals turn out to be distributed throughout the whole molecule, whereas protonation markedly localizes the electronic density of the HOMO and LUMO on the pyr and bpy units, respectively. Protonation also produces a stabilization of the molecular orbitals and leads to a significant reduction of the HOMO–LUMO energy gap in line with the red-shift observed in the absorption spectra.

Table 4.2 on page 118 summarizes the vertical excitation energies and electronic nature calculated for the lowest-energy singlet excited states of neutral and protonated **pyr$_2$bpy** ligand. As discussed in the photophysical section, the neutral species shows a broad band at 350 – 375 nm (see Figure 4.4 on page 111), which is ascribed to an intramolecular pyr-to-bpy charge transfer transition. TD-DFT calculations predict that the optical absorption between 350 and 390 nm mainly arises from the electronic transition to the S_1 and S_2 excited singlets (Table 4.2). These states result from the HOMO-to-LUMO and HOMO–1-to-LUMO excitations, respectively, and imply an electronic density charge transfer from the lateral pyr units to the central bpy moiety (Figure 4.9). The HOMO-to-LUMO excitation is significantly more intense (f = 1.19) than the HOMO–1-to-LUMO (f = 0.24) and it is calculated to slightly red-shift when increasing the polarity of

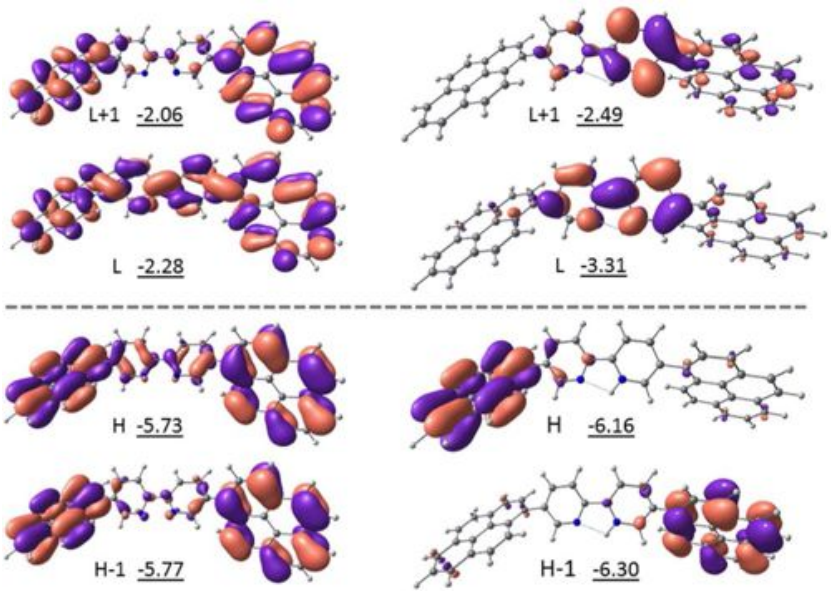

Figure 4.9: Electronic density contours (0.03 e bohr^{-3}) calculated for the HOMO–1, HOMO, LUMO, and LUMO+1 (H and L denote HOMO and LUMO, respectively) of neutral (left) and protonated (right) **pyr$_2$bpy**. Orbital energies are provided in eV.

the solvent (383 nm in toluene, 386 nm in acetonitrile, see Table 4.2) in agreement with experimental trends.

Calculations therefore corroborate the ICT nature of the lowest-energy band observed in the absorption spectrum. The shoulder observed in the experimental spectrum around 330 nm (see Figure 4.4) is assigned to the less intense S_3 (f = 0.15) and S_4 (f = 0.16) states that correspond to the HOMO-to-LUMO+1 and HOMO–1-to-LUMO+1 transitions, respectively; these transitions mainly imply pyr-to-pyr excitations (see Table 4.2 and Figure 4.9).

Some other significant data came from the TD-DFT analysis of the protonated species: *e.g.*, the experimental data showed the appearance of a broad band centered at 440 nm that was tentatively attributed to an ICT pyr-to-bpyH$^+$ transition. This assignment is corroborated by TD-DFT calculations that predict a manifold of three excited states (S_1 to S_3) lying in the 400 – 530 nm range, implying a charge transfer from the pyr units to the bpyH$^+$ moiety (Table 4.2 and Figure 4.9). In addition, the pyr-to-pyr excitations appear in the 340 – 350 nm range, as for neutral **pyr$_2$bpy**; this theoretical finding is in agreement with the

Table 4.2: TD-DFT singlet excited states calculated for neutral and protonated **pyr$_2$bpy** in different solvents. Vertical excitation wavelengths (λ), oscillator strengths (f), dominant monoexcitations and nature of the electronic transition are provided.

				pyr	
	state	λ (nm)	f	dominant monoexcitation	nature
	S_1	383	1.21	HOMO-to-LUMO	mixed
in	S_2	367	0.29	HOMO−1-to-LUMO	mixed
toluene	S_3	345	0.13	HOMO-to-LUMO+1	pyrene-centred
	S_4	338	0.14	HOMO−1-to-LUMO+1	pyrene-centred
	S_1	385	1.19	HOMO-to-LUMO	mixed
in	S_2	367	0.24	HOMO−1-to-LUMO	mixed
CH_2Cl_2	S_3	345	0.15	HOMO-to-LUMO+1	pyrene-centred
	S_4	338	0.16	HOMO−1-to-LUMO+1	pyrene-centred
	S_1	386	1.16	HOMO-to-LUMO	mixed
in	S_2	369	0.21	HOMO−1-to-LUMO	mixed
CH_3CN	S_3	345	0.15	HOMO-to-LUMO+1	pyrene-centred
	S_4	337	0.17	HOMO−1-to-LUMO+1	pyrene-centred
				pyr$_2$bpy	
	state	λ (nm)	f	dominant monoexcitation	nature
	S_1	531	0.59	HOMO-to-LUMO	pyr-to-bpy (CT)
	S_2	504	0.05	HOMO−1-to-LUMO	pyr-to-bpy (CT)
in	S_3	396	0.25	HOMO−1-to-LUMO+1	pyr-to-bpy (CT)
CH_2Cl_2	S_5	376	0.21	HOMO−2-to-LUMO	pyr-to-bpy (CT)
	S_7	349	0.27	HOMO-to-LUMO+2	pyrene-centred
	S_8	339	0.47	HOMO−1-to-LUMO+2	pyrene-centred

experimental spectrum reported in Figure 4.5 on page 112.

The lowest triplet state (T_1) of both neutral and protonated **pyr$_2$bpy** was optimized in CH_2Cl_2 by means of the spin-unrestricted DFT approach. Figure 4.10 on the next page displays the spin density distribution calculated for T_1 of both species. It perfectly matches the topology of the HOMO-to-LUMO excitation (compare with Figure 4.9 on the preceding page), from which T_1 originates, and confirms the ICT nature of this state. The T_1 state of **pyr$_2$bpy** is computed 1.98 eV

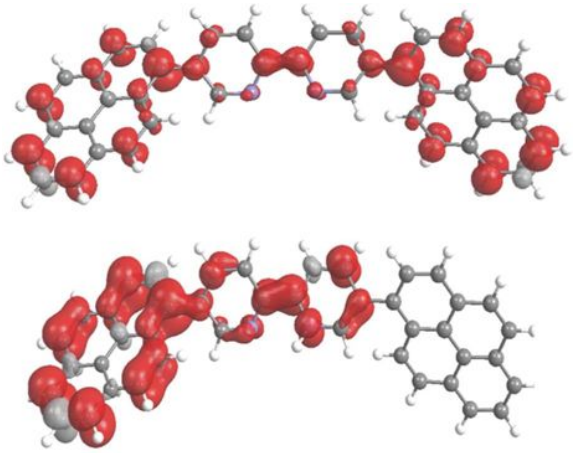

Figure 4.10: Spin density distribution (0.005 e bohr^{-3}) of the T_1 state for neutral (top) and protonated (bottom) **pyr$_2$bpy**.

(626 nm) above the S_0 state (adiabatic energy difference) in perfect agreement with the first emission peak observed in the phosphorescence spectrum (see Figure 4.8 on page 115). For protonated **pyr$_2$bpy**, the T_1 state is calculated at slightly lower energies (1.78 eV above S_0), but no phosphorescence is detected experimentally for this species and no comparison can be made.

4.2.4 Photophysical properties of the complexes

Once a comprehensive picture of the photophysical behavior of **pyr$_2$bpy** had been obtained, the spectroscopic properties of the iridium(III) pyr$_2$bpy-based complexes [Ir(ppy)$_2$(pyr$_2$bpy)][PF$_6$] (**GH**) and [Ir(dfppy)$_2$(pyr$_2$bpy)][PF$_6$] (**GF**) is investigated.

All the characterizations were carried out only in CH_2Cl_2 because the complexes are insoluble in nonpolar solvents (*e.g.*, toluene) due to their ionic character, and are unstable in more coordinating solvents (*e.g.*, acetonitrile) because the **pyr$_2$bpy** ligand is displaced by solvent-assisted nucleophilic attack. In fact, fluorescence spectroscopic data were consistent with increasing amounts of free ligand in acetonitrile solution of the complexes.

Figure 4.11 on the following page shows the electronic absorption spectra of complexes **GH** and **GF** together with those of the reference complexes **xH** and **xF**. In the region 230 – 350 nm, the absorption profiles of **GH** and **GF** are virtually the sum of the spectra of the pyrene moiety and the respective reference complexes.

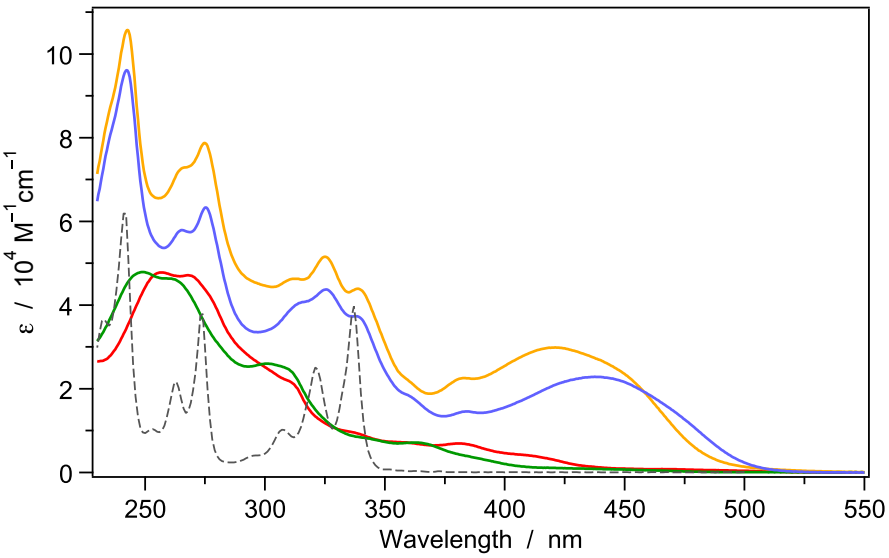

Figure 4.11: Absorption spectra of reference complexes **xH** (red) and **xF** (green), together with those of the target complexes **GH** (orange) and **GF** (blue). The pyrene spectrum is also reported (gray dashed line). All spectra are recorded in room-temperature CH_2Cl_2.

Notably, at $\lambda > 375$ nm, a broad band is observed for both pyr_2bpy-based complexes, reminiscent of the ICT band of the protonated **pyr$_2$bpy** ligand. Such a feature might be rationalized considering that, in these complexes, the **pyr$_2$bpy** ligand is chelating a monocationic unit (*i.e.*, an iridium(III) metal center surrounded by two anionic cyclometalating ligands); *i.e.*, the $[(X_2ppy)_2Ir]^+$ moiety seems to act simply as a positive charge similar to a proton.

The broad CT band is more red-shifted in the case of **GF**, which is in contrast to what is typically found for cationic iridium(III) complexes with fluoro-substituted phenylpyridine cyclometalated ligands, and which usually display blue-shifted transitions compared with unsubstituted analogues, due to HOMO stabilization. However, in the present case, if we assume that the $[(X_2ppy)_2Ir]^+$ moiety has essentially an electrostatic effect on the **pyr$_2$bpy** ligand, this unit experiences a more positively charged environment in the case of the fluoro-substituted complex **GF**, due to the electron-withdrawing effect of the fluoro-substituents. Accordingly, the energy of the pyr-to-bpy$[(dfppy)_2Ir]^+$ CT transition is lowered with respect to **GH**. This electrostatic hypothesis is supported

Table 4.3: Photophysical properties of the investigated complexes in CH_2Cl_2 (RT liquid solution and 77 K rigid matrix).

	oxygen-free solution, 298 K					77 K	
Complex	λ_{max} (nm)	Φ_{em} (%)	τ (ns)	k_r (10^5 s^{-1})	k_{nr} (10^8 s^{-1})	λ_{max} (nm)	τ (µs)
xH	595	18.9	561	3.37	0.0145	520, 552	3.5
xF	535	55.2	1279	4.32	0.0035	475, 504	4.1
GH	668	0.3	4	7.75	2.49	663, 725	≈ 1
GF	665	0.6	7	8.63	2.42	663, 725	≈ 1

by the theoretical description performed for both the pyr_2bpy-based iridium(III) complexes (see next section).

Photoluminescence studies under different conditions were performed to further elucidate the effect of the pyrene moieties on the investigated complexes. While **xH** and **xF** are well-known good emitters from the lowest lying metal-to-ligand charge transfer (MLCT) state [100, 212], both **GH** and **GF** display very weak ($\Phi < 1\%$, $\tau = 4 - 7$ ns) and unstructured emissions around 660 nm (Table 4.3 and Figure 4.12 on page 123). These bands are somewhat similar to the fluorescence band of the protonated ligand (see Figure 4.7 on page 115), but are more structured, red-shifted, and longer-lived (5 ns *vs* 0.5 ns). Moreover, the radiative constant (k_r) of the related transitions is around 8×10^5 s^{-1}. This value is more comparable to the one of a standard charged iridium(III) complex (**xH** and **xF** having a k_r of 3×10^5 and 4×10^5 s^{-1}, respectively), rather than to the k_r of the **pyr₂bpy** free ligand, that is almost 500 times higher ($k_r \approx 4 \times 10^8$ s^{-1}, Table 4.1 on page 113), or the protonated free ligand ($k_r \approx 1 \times 10^8$ s^{-1}, 125 times higher).

These findings suggest that the emission of **GH** and **GF**, though rather short-lived because of the low quantum yield, arise from the lowest triplet state of the complexes. This state is mainly centered on the **pyr₂bpy** ancillary ligand, as indicated by the energy and the profile of the emission band (Figure 4.12) and further supported by the DFT calculations (see next section). The short lifetime of these triplets can be ascribed to the high spin-orbit coupling of the iridium center: this metal ion is not only acting as a positive charge (*i.e.*, lowering the energy of the charge-transfer transition, centered on the **pyr₂bpy** ligand), but is

also promoting the population of triplet states due to the heavy-atom effect. To further verify that these emissions arise from the complexes and not from free ligands or impurities, excitation spectra were recorded at the emission maximum and perfectly match the corresponding absorption profile of the complex.

In Figure 4.13 on the facing page are gathered the phosphorescence spectra in a rigid matrix at 77 K. A hypsochromic shift is observed in all cases upon going from room temperature to 77 K. As already known from literature, reference complexes **xH** and **xF** display a strong emission at 520 nm and 475 nm, respectively [100]. On the other hand, the corresponding pyrene-derivatives show a weak and rather structured phosphorescence around 650 nm, which resembles that of the **pyr$_2$bpy** ligand. For this reason, the 77 K emission of complexes **GH** and **GF** can be ascribed to a ligand-centered emission arising from the pyr$_2$bpy-centred triplet, which is further red-shifted compared to the free ligand due to the presence of the positively charged iridium ion. It was impossible to obtain reliable lifetime data for the 77 K emission of **GH** and **GF** due to the low intensity of these emissions, the bad quality of CH_2Cl_2 frozen glass, and its occurrence in the deep-red spectral region where detectors are less sensitive. These combined circumstances make the signal-to-noise ratio extremely low.

Theoretical description of the ground and excited states of Iridium(III) complexes based on the pyr$_2$bpy ligand

In their singlet ground state (S_0), both **GH** and **GF** cations present the typically distorted octahedral coordination geometry expected for iridium(III) complexes. Figure 4.14 on page 124 shows the topology of the HOMOs and LUMOs calculated for the target (**GH** and **GF**) and the reference **xH** complexes. Compared to **xH** and **xF** for which the HOMO and HOMO–1 correspond to a mixture of Ir(III) d_π orbitals (t_{2g}) and phenyl π orbitals of the cyclometalated ligands, the two highest orbitals of **GH** and **GF** are mainly localized on the pyrene units.

In contrast, the LUMO presents the same topology for all the complexes and mainly resides on the bpy moiety. The introduction of fluorine substituents in the cyclometalated ligands therefore has a different effect on the energies of the frontier molecular orbitals. For complex **xF**, it leads to a strong stabilization of the HOMO and to a smaller stabilization of the LUMO [103, 157, 212], and, as a consequence, the HOMO–LUMO energy gap increases and a blue-shifted absorption is observed in passing from **xH** and **xF** (see Figure 4.11 on page 120).

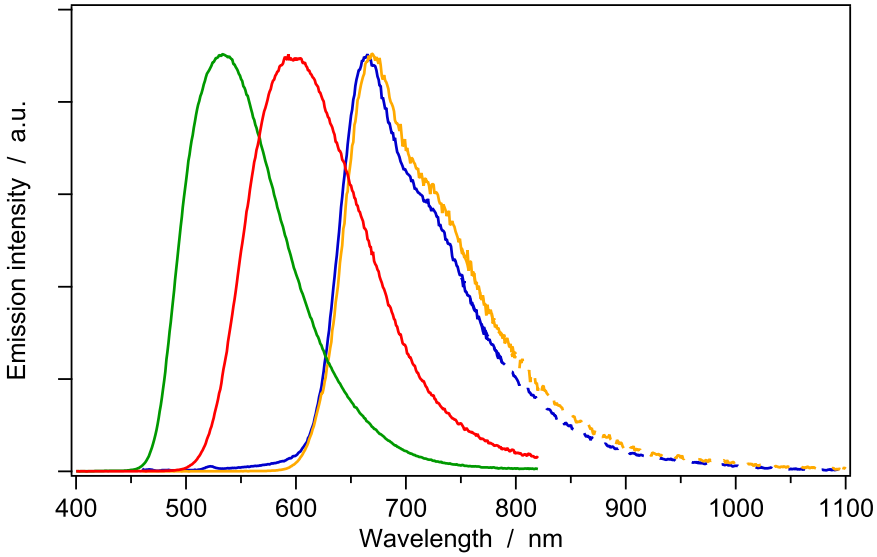

Figure 4.12: Normalized RT luminescence spectra, recorded in CH_2Cl_2, of the target complexes **GH** (orange) and **GF** (blue), compared with those of reference complexes **xH** (red) and **xF** (green); λ_{exc} = 380 nm.

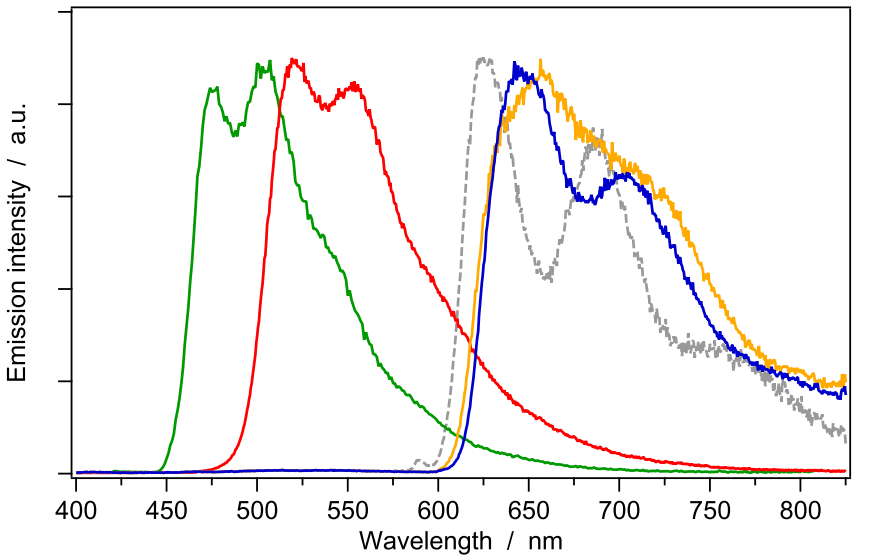

Figure 4.13: 77 K luminescence spectra of **GH** (orange) and **GF** (blue), together with reference complexes **xH** (red) and **xF** (green), all recorded in frozen CH_2Cl_2 matrix; λ_{exc} = 380 nm. The phosphorescence spectrum of the **pyr$_2$bpy** ligand is included for comparison in light gray.

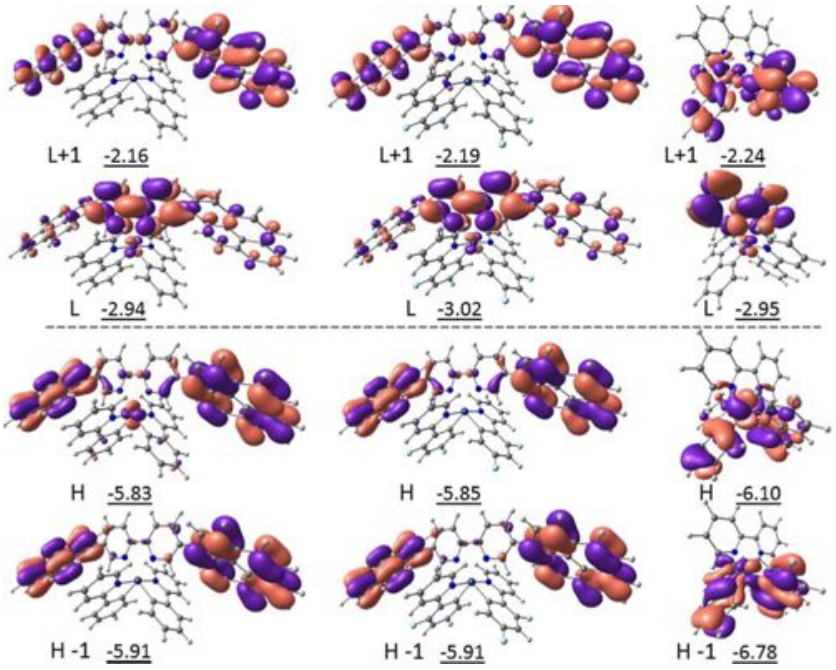

Figure 4.14: Electronic density contours (0.03 e bohr^{-3}) calculated for the HOMO, HOMO–1, LUMO and LUMO+1 (H and L denote HOMO and LUMO, respectively) of the target **GH** (left) and **GF** (middle) and the reference **xH** (right) complexes. Orbital energies are provided in eV.

The scenario is different for the pyrene-based complexes since the HOMO is located on the pyrene units and remains almost unaffected in passing from **GH** (−5.83 eV) to **GF** (−5.85 eV), whereas the LUMO is slightly stabilized (0.08 eV) owing to the direct coupling with the more positively charged $[(X_2ppy)_2Ir]^+$ environment. As a consequence, the HOMO–LUMO gap narrows from 2.89 eV (**GH**) to 2.83 eV (**GF**) and, in line with experimental data (see Figure 4.11), a red-shifted absorption is expected for **GF** compared to **GH**. This is further corroborated by TD-DFT calculations (see below).

After establishing the major orbital effects of introducing the pyr units, the excited singlet states were investigated using the TD-DFT approach. In Table 4.4 on page 126 are summarized the most important singlet states that contribute to the absorption spectrum of **GH** and **GF**. The excited singlet states of the reference complex **xH** were also calculated for comparison purposes. The lowest-energy absorptions of **GH** and **GF** (around 430 – 500 nm) are mainly described by the electronic transitions to the S_2 and S_1 states, respectively (see Table 4.4).

Both states result from the HOMO-to-LUMO excitation, and imply an electronic density charge-transfer from the lateral pyr units to the central bpy moiety of the **pyr$_2$bpy** ancillary ligand. The S_1 state in **GH** originates from the HOMO−2-to-LUMO excitation and implies a charge transfer from the [Ir(ppy)$_2$] moiety (where the HOMO−2 is located) to the bpy unit, similar to that found for the HOMO-to-LUMO S_1 state of **xH** (see Table 4.4 and Figure 4.14). The state has almost no intensity (f = 0.025) and appears at lower energies for **GH** (S_1: 2.51 eV, 494 nm) than for **GF** (S_3: 2.78 eV, 446 nm) because of the electron-withdrawing fluorine atoms attached to the cyclometalating ligands that stabilize the HOMO−2 (**GH**: −5.93 eV, **GF**: −6.25 eV). Therefore, the absorption bands in the 430 – 500 nm range (see Figure 4.11 on page 120) are ascribed to ICT pyr-to-bpy transitions. Moreover, TD-DFT calculations correctly predict the red-shift of the absorption maximum in passing from **GH** to **GF**, as the reduction of the HOMO–LUMO energy gap indicated.

To describe the triplet excited states of **GH** and **GF**, we first performed TD-DFT calculations on the ground-state fully optimized geometries (see Table 4.4). For both complexes, the lowest-energy triplet (T_1) results from a mixing of pyrene-centred and pyr-to-bpy excitations and is located 1.85 eV and 1.83 eV above S_0 for **GH** and **GF**, respectively. For the reference complex **GH**, T_1 is calculated at higher energies (2.59 eV) and implies a charge transfer from the [Ir(ppy)$_2$] environment to the bpy ligand. The corresponding [Ir(ppy)$_2$]-to-bpy triplets are found at similar energies for **GH** (T_4, 2.54 eV) and **GF** (T_5, 2.76 eV) (see Table 4.4).

In line with the photophysical study, TD-DFT calculations therefore indicate that emission in the target complexes **GH** and **GF** takes place from a charge transfer triplet state localized on the **pyr$_2$bpy** domain.

In order to further investigate the nature of the lowest-energy triplet state (T_1), we fully optimized the geometry of T_1 by means of the UDFT approach. After full-geometry relaxation, the CT state associated to the pyr-to-bpy monoexcitation is confirmed to be the most stable triplet and is calculated to lie 1.87 eV (**GH**) or 1.84 eV (**GF**) above S_0 (adiabatic energy differences), close to the values predicted by the TD-DFT results. The nature of T_1 is confirmed by the spin-density distributions shown in Figure 4.15 on page 127, which perfectly correlate with the spin density calculated for the lowest triplet state of the **pyr$_2$bpy** ligand (see Figure 4.10 on page 119, top) and differ from that computed for **xH** (see Figure 4.15, c).

Table 4.4: TD-DFT singlet and triplet excited states calculated for **GH**, **GF**, and **xH** complexes in CH_2Cl_2. Vertical excitation wavelengths (λ), oscillator strengths (f), dominant monoexcitations and nature of the electronic transition are provided. Only the singlet states with $f > 0.10$ have been included for **GH** and **GF**, and those with $f > 0.01$ for **xH**.

			GH	
state	λ (nm)	f	dominant monoexcitation	nature
S_1	494	0.03	HOMO−2-to-LUMO	$[Ir(ppy)_2]$-to-bpy
S_2	467	0.73	HOMO-to-LUMO	pyr-to-bpy (CT)
S_3	448	0.02	HOMO−1-to-LUMO	pyr-to-bpy (CT)
T_1	672	—	HOMO-to-LUMO	pyr-to-bpy (CT)
T_2	661	—	HOMO-to-LUMO+1	pyrene-centred
T_3	504	—	HOMO−2-to-LUMO	$[Ir(ppy)_2]$-to-bpy
T_4	487	—	HOMO−2-to-LUMO	$[Ir(ppy)_2]$-to-bpy
T_5	455	—	HOMO−2-to-LUMO+2	$[Ir(ppy)_2]$-to-bpy
			GF	
state	λ (nm)	f	dominant monoexcitation	nature
S_1	486	0.83	HOMO-to-LUMO	pyr-to-bpy (CT)
S_2	458	0.02	HOMO−1-to-LUMO	pyr-to-bpy (CT)
S_3	446	0.02	HOMO−2-to-LUMO	$[Ir(ppy)_2]$-to-bpy
T_1	677	—	HOMO-to-LUMO	pyr-to-bpy (CT)
T_2	664	—	HOMO-to-LUMO+1	pyrene-centred
T_3	500	—	HOMO-to-LUMO	pyr-to-bpy (CT)
T_4	456	—	HOMO−1-to-LUMO	pyr-to-bpy (CT)
T_5	449	—	HOMO−2-to-LUMO	$[Ir(ppy)_2]$-to-bpy
			xH	
state	λ (nm)	f	dominant monoexcitation	nature
S_1	471	0.00	HOMO-to-LUMO	$[Ir(ppy)_2]$-to-bpy
S_2	381	0.07	HOMO-to-LUMO+1	$[Ir(ppy)_2]$-to-bpy
T_1	478	—	HOMO-to-LUMO	$[Ir(ppy)_2]$-to-bpy
T_2	451	—	HOMO-to-LUMO+1	$[Ir(ppy)_2]$-to-bpy
T_3	446	—	HOMO-to-LUMO+2	$[Ir(ppy)_2]$-to-bpy

Theoretical calculations therefore confirm that the lowest triplet state T_1 for the target complexes is defined as a ^{3}CT state centred on the pyr_2bpy moiety, and that this state is located in energy well-below the strong [Ir(ppy)$_2$]-to-bpy emitting triplet states. An effective population is therefore expected for the pyr_2bpy-centred triplet states, explaining the low photoluminescence quantum yields observed for the target complexes when compared with those recorded for the reference complexes (see Table 4.3 on page 121).

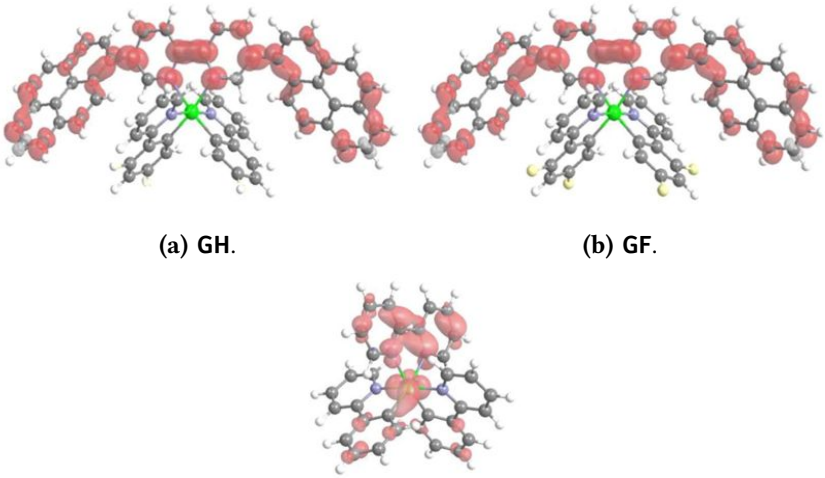

(a) **GH**. (b) **GF**.

(c) **xH**.

Figure 4.15: Spin density distributions (0.005 e bohr^{-3}) computed for the fully optimized T_1 state of the investigated complexes.

4.3 Conclusion

The synthesis and structural X-ray characterization of two novel ionic iridium(III) complexes incorporating a 2,2'-bipyridine ancillary ligand functionalized with pyrene groups in 5,5'-positions (**pyr$_2$bpy**) have been reported. A comprehensive photophysical and theoretical investigation, including comparison with model unsubstituted complexes and studies of the protonation of **pyr$_2$bpy**, has allowed elucidation of the role of the pyrene substituents in dictating the nature and sequence of electronic excited states, relative to those centered on the metal complex moiety.

An intramolecular charge transfer singlet state centered on the **pyr$_2$bpy** ligand is responsible for the intense low-energy absorption band recorded in the visible 400 – 500 nm range. Upon fluorination of the main cyclometalated ligands, this band undergoes an unexpected red-shift because of the location on the pyrene units of the HOMO level, which remains mostly unaffected, and to the electrostatic stabilization of the LUMO.

Both the photophysical and the theoretical studies establish that the lowest triplet state (T_1) of the new complexes corresponds to the lowest triplet of the **pyr$_2$bpy** ligand that is located lower in energy than the strong MLCT emitting states centered on the iTMC. The population of the pyr$_2$bpy-centred triplet levels explains the low photoluminescence quantum yield observed for the target complexes.

Noteworthy, and in contrast to what has been observed for neutral iridium(III) complexes bearing aromatic substituents, the phosphorescence of the pyr$_2$bpy-centred triplet state has been successfully recorded both at room and low temperature conditions.

These results demonstrate that, by suitable chemical design and excited state engineering [255], it is possible to make multichromophoric iridium(III) complexes whose luminescence properties are not centered on the Ir-based moiety, but where the metal center is nonetheless active in dictating the luminescence output by electrostatic interactions.

This result further widens the scope of iridium(III) complexes as versatile and tunable luminescent materials, taking advantage of thoroughly chosen chromophoric and/or luminophoric appendages on the ancillary non-cyclometallating ligand.

Chapter 5

Deeper in the device

In this last chapter, the photophysical properties of a prototypical series of charged bis-cyclometalated iridium(III) complexes have been investigated in detail. The complexes belong to the $[Ir(ppy)_2(NN)]^+$ family in which the NN ancillary ligand is a common 2,2'-bipyridine (**bpy**, for complex **tA**), the mono-substituted 6-phenyl-2,2'-bipyridine (**pbpy**, for complex **tB**), and the disubstituted 6,6'-diphenyl-2,2'-bipyridine (**dpbpy**, for complex **tC**).

The photoluminescence performance in solution decreases from **tA** to **tC** upon attachment of phenyl groups to the NN ancillary ligand. The absorption spectra recorded over time suggest that complex **tC** is less stable compared to complexes **tA** and **tB** likely due to a nucleophilic-assisted exchange of the ancillary ligand. To clarify this behavior, the temperature dependence of the experimental intrinsic deactivation rate constant has been investigated from 77 K to room temperature. Temperature-dependent studies show that non-emitting metal-centered (MC) states are accessible at room temperature for complex **tC**.

The experimental results are interpreted with the help of theoretical calculations performed within DFT approach. Calculations suggest that attachment of a phenyl group to the ancillary ligand (**tB**) promotes the temperature-independent deactivation pathways, whereas attachment of a second phenyl group (**tC**) also makes the temperature-dependent ones accessible through population of non-radiative ^{3}MC excited states.

5.1 Introduction

As already mentioned in the first chapter of this thesis, since 2004 many significant progresses in iTMC-based LECs have been made using heteroleptic cationic iridium(III) complexes (*i.e.*, color gamut, efficiency, turn-on time, stability, *etc.*). Moreover, it should be also stressed that, since LECs are based on only one active material, the most important enhancements concerning the performance of these devices have been obtained by an appropriate tuning of the photophysical and electrochemical properties of the emitting iTMCs.

Although the last breakthroughs achieved for LECs mostly result from a thorough tuning of the photophysical properties of the Ir-iTMCs, there are only a few works in which the photophysics of these complexes is studied in detail [20, 75, 90, 112, 114, 237, 256–259]. This knowledge is of the upmost importance to design efficient and stable emitters.

For this reason, in this last chapter, we investigate the photophysical properties of a series of some typical ionic iridium(III) complexes used in LECs by studying the temperature dependence of their emission properties and by performing theoretical DFT calculations. The investigated series consists of the archetype complex $[Ir(ppy)_2(bpy)][PF_6]$ (**tA**), together with and the supramolecularly caged complexes $[Ir(ppy)_2(pbpy)][PF_6]$ (**tB**) and $[Ir(ppy)_2(dpbpy)][PF_6]$ (**tC**). In Figure 5.1 are reported the structures of all these complexes and their related ancillary ligands.

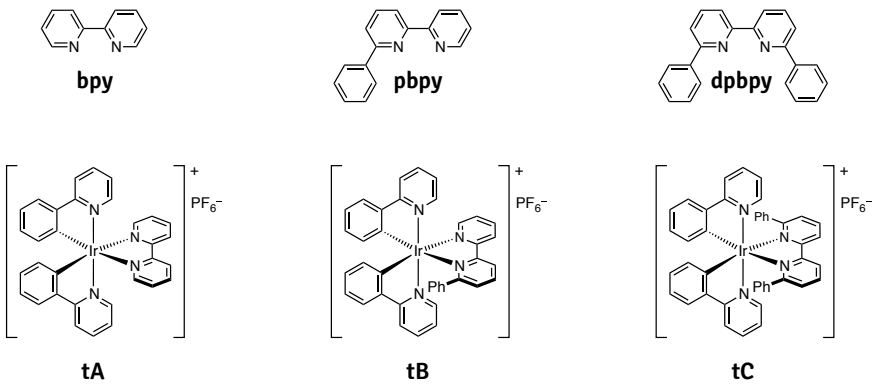

Figure 5.1: Chemical structures of the iridium(III) complexes (**tA** – **tC**) reported in this chapter, together with the respective ancillary ligands.

Although the attachment of phenyl groups usually leads to highly stable LEC devices, due to the so called "cage effect", it causes a decrease of the device efficiency especially when using complex **tC** [99]. In this chapter we successfully identified temperature-dependent deactivation pathways, via population of non-radiative metal-centered (^{3}MC) excited states, as a possible justification for such a poor photophysical behavior.

5.2 Results and discussion

5.2.1 Ground-state characterization by DFT calculations

The molecular and electronic structures of complexes **tA** – **tC** were investigated by DFT calculations at the B3LYP/(6-31G**+LANL2DZ) level considering solvent effects. The geometries of the complexes in the electronic ground state (S_0) were fully optimized, and the values obtained for selected bond lengths and dihedral angles are listed in Table 5.1 on the next page.

Theoretical values compare well with the X-ray data reported for the three complexes [37, 99, 168]. Just for the sake of clarity, the crystal structures of both the caged-complexes are reported in Figure 5.2.

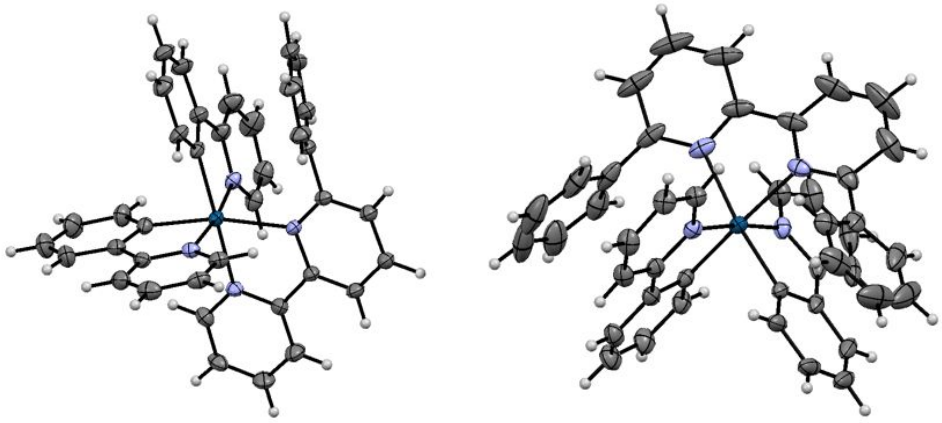

(a) Cation of **tB**. **(b)** Cation of **tC**.

Figure 5.2: X-ray crystal structures of the two caged-complexes investigated in this chapter (ellipsoids plotted at 40% probability level); solvent molecules are omitted.

Table 5.1: Selected bond distances (Å) and dihedral angle of the **bpy** ligand calculated for the cations of complexes **tA**, **tB**, and **tC** in the S_0 ground state, in the T_1 and metal-centered (^{3}MC) triplet excited states. X-ray values were taken from references [37], [168], and [99] (for **tA**, **tB**, and **tC**, respectively).

Complex	Parameter	X-ray	S_0	T_1	^{3}MC
tA	$Ir-C_{ppy}$	2.01	2.024	1.999	2.015
	$Ir-N_{ppy}$	2.05	2.082	2.081	2.505
	$Ir-N_{bpy}$	2.13	2.210	2.196	2.219
	bpy dihedral	2°	4.9°	1.5°	1.0°
tB	$Ir-C_{ppy}$	2.00/2.03	2.013/2.028	2.018/1.985	2.042/2.033
	$Ir-N_{ppy}$	2.04/2.07	2.093/2.079	2.087/2.076	2.604/2.204
	$Ir-N_{bpy}$	2.15/2.22	2.360/2.207	2.238/2.226	2.515/2.226
	bpy dihedral	18.4°	17.6°	11.6°	19.1°
tC	$Ir-C_{ppy}$	2.01	2.021/2.019	2.011/1.990	2.050/2.030
	$Ir-N_{ppy}$	2.05/2.03	2.081/2.075	2.096/2.071	2.614/2.209
	$Ir-N_{bpy}$	2.23/2.20	2.345/2.355	2.233/2.301	2.503/2.305
	bpy dihedral	20.7°	36.0°	6.0°	33.5°

In the case of **tA** both experimental and calculated Ir–C and Ir–N bond distances, together with the dihedral angle of the **bpy** ancillary ligand, suggest a near-octahedral coordination of the iridium metal core. On the other hand, complexes **tB** and **tC** (see Figure 5.2) show a more distorted octahedral coordination owing to the sequential attachment of phenyl groups to the 6- and 6'-positions of the ancillary ligand (see Figure 5.1 and Table 5.1). For both complexes, the pendant phenyl rings exhibit an intracation face-to-face π-stacking interaction with the phenyl rings of the cyclometalated ligands (calculated centroid-centroid distances of 3.60 Å). As a consequence of this interaction, the $Ir-N_{bpy}$ distances of the phenyl-substituted pyridine rings lengthen from 2.21 Å in **tA** to 2.35 Å and 2.36 Å in **tB** and **tC**, respectively. Moreover, the **bpy** dihedral angle gradually increases from 4.9° (**tA**) to 17.6° (**tB**) and 36.0° (**tC**) (see Table 5.1).

Indeed, complex **tC** shows a strongly distorted molecular structure in which the ancillary ligand can be considered to be partially decoordinated from the iridium metal core (see Figure 5.2 on the preceding page). Hence, complex **tC** seems

to be less robust in both the ground and the excited states, which increases the possibility for nucleophilic-assisted ancillary ligand-exchange reactions, leading to degradation of the complex. This behavior has been also observed in other comparable iridium complexes by Neve *et al.* [257].

Figure 5.3 on the next page displays the atomic orbital composition calculated for the HOMO and LUMO of complex **tB**, as a representative example. The same composition of the frontier molecular orbitals is also obtained for complexes **tA** and **tC**. As already reported for analogous cyclometalated Ir-iTMCs [37, 157, 237, 256], the HOMO is composed of a mixture of iridium dπ orbitals (t_{2g}) and phenyl π orbitals of the cyclometalating ligands and the LUMO resides on the neutral ancillary ligand (see Figure 5.3).

Upon introduction of phenyl groups on the ancillary ligand, the energy of the HOMO remains almost constant (-5.83, -5.82, and -5.82 eV for **tA**, **tB**, and **tC**, respectively), whereas the LUMO is gradually destabilized (-2.65, -2.61, and -2.46 eV for **tA**, **tB**, and **tC**, respectively). The destabilization of the LUMO is ascribed to the distortion of the ancillary ligand caused by the π-stacking interaction between the pendant phenyl rings and the cyclometalated ligands. As discussed above, this interaction determines a progressive increase of the internal torsional angle of the ancillary ligand (see Table 5.1 on the facing page), which reduces the conjugation between the pyridine rings with a consequent destabilization of the LUMO level and weakens the metal-ligand bond.

5.2.2 Characterization of the T_1 emitting state

Absorption spectroscopy

The electronic absorption spectra of all the complexes were recorded at room temperature in CH_2Cl_2 solution (see Figure 5.4 on page 135). The UV region (250 – 350 nm) is dominated by intense absorption bands ($10 - 55 \times 10^3$ M^{-1} cm^{-1}) that are assigned to spin-allowed ligand-centered (LC) transitions involving both the cyclometalating and the ancillary ligands. On the other hand, the weak and broader bands ($1 - 9 \times 10^3$ M^{-1} cm^{-1}) at longer wavelengths (350 – 450 nm) are attributed to charge transfer transitions with mixed metal-to-ligand (^{1}MLCT) and ligand-to-ligand (^{1}LLCT) charge transfer character (Figure 5.4, inset) [237, 256, 260, 261]. Additionally, the weak and long tail observed in the spectra above 450 nm is due to direct spin-forbidden absorption from the singlet ground state to

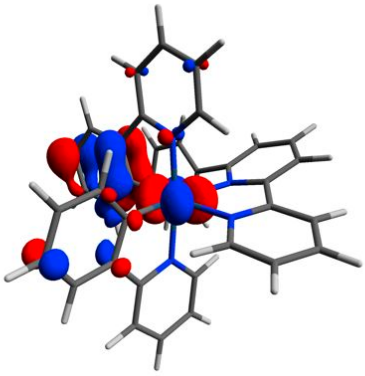

(a) HOMO of **tB**.

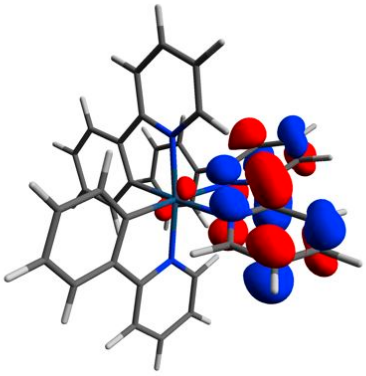

(b) LUMO of **tB**.

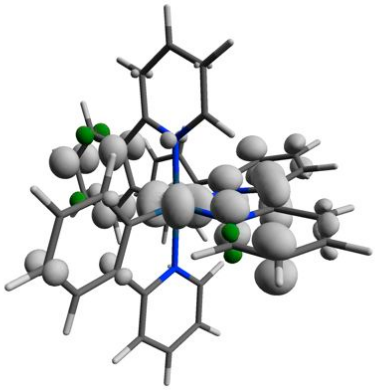

(c) Spin density of **tC** triplet.

Figure 5.3: Schematic diagram showing the electronic density contours (0.05 e bohr^{-3}) calculated for the frontier molecular orbitals of complex **tB** (a and b) and the spin density distribution (0.005 e bohr^{-3}) calculated for the emitting T_1 state of complex **tB** (c).

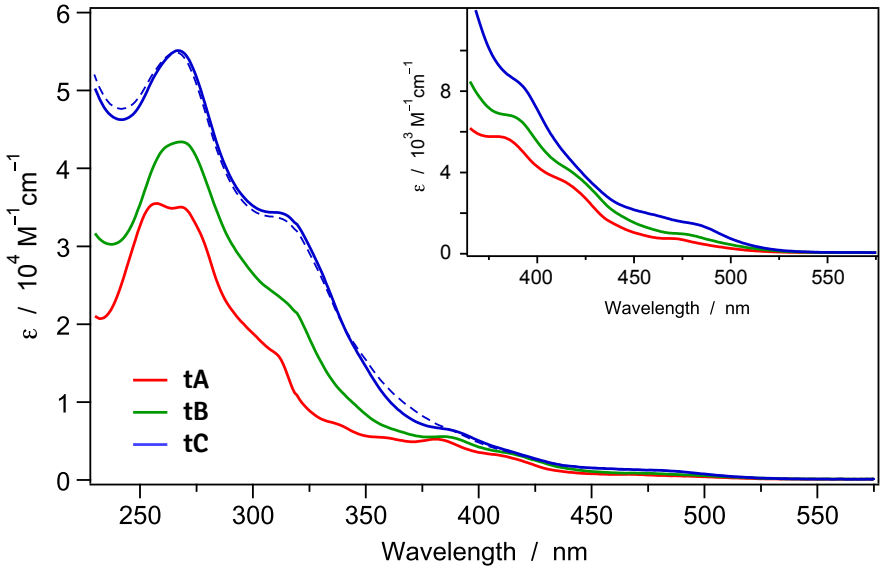

Figure 5.4: Electronic absorption spectra of complexes **tA** (red), **tB** (green), and **tC** (blue) in CH_2Cl_2 solution at room temperature; MLCT transitions are zoomed in the inset. The absorption spectrum of **tC** recorded after 24 h is reported as thin dots; those of **tA** and **tB** are unchanged.

the triplet excited states enabled by the high spin-orbit coupling constant of the iridium metal core [90]. The presence of phenyl substituents on the bipyridine ligand leads both to red spectral shifts and to higher molar extinction coefficients.

The absorption spectra of all the complexes were also recorded over time to investigate the effects of the gradual distortion of the coordination sphere on the stability of the complex upon attachment of the phenyl groups. Figure 5.4 also compares the absorption profiles obtained from fresh CH_2Cl_2 solutions (thick lines) with those after 24 h (thin lines). While the absorption profiles recorded after one day for **tA** and **tB** are completely superimposed, those of **tC** show small spectral shifts and changes in intensity, suggesting a lower stability. Indeed, after several days the absorption profile of **tC** is remarkably different compared to that from fresh solution, while those of complexes **tA** and **tB** remain unaltered. From further studies in other solvents, it can be stated that **tA** and **tB** are stable over weeks, even in highly coordinating solvents such as acetonitrile or methylethylketone, while complex **tC** shows rather rapid degradation (depending on the nucleophilicity of the solvent). Time-dependent absorption spectra

Table 5.2: Photophysical properties in CH_2Cl_2 solution (at 298 K and 77 K) and in 298 K neat film (pure compound, spin coated); λ_{exc} = 407 nm.

	oxygen-free solution, 298 K					77 K		neat film		
	λ_{max} (nm)	Φ_{em} (%)	τ (ns)	k_r (10^5 s^{-1})	k_{nr} (10^6 s^{-1})	λ_{max} (nm)	τ (µs)	λ_{max} (nm)	Φ_{em} (%)	τ (ns)
tA	595	19.6	565	3.5	1.4	521	3.5	582	20	587
tB	614	4.9	204	2.4	4.7	548	2.6	598	12	364
tC	594	3.6	131	2.7	7.4	528	4.3	593	17	505

therefore evidence the poor stability of complex **tC**, which is likely attributed to nucleophilic-assisted ancillary ligand-exchange reactions due to partial decoordination of the ancillary ligand caused by attachment of phenyl rings on the 6- and 6'-positions.

Emission spectroscopy and DFT calculations

Photoluminescence studies in different conditions were performed to elucidate the effect of phenyl substitution on the photophysical properties of all complexes. Figure 5.5 on the facing page displays the emission spectra in CH_2Cl_2 solution at room and at low temperature (77 K) together with those recorded for pure solid-state thin films at 298 K. The corresponding photoluminescence data are collected in Table 5.2. Luminescence decays are in the tenths-of-microsecond scale, indicating a phosphorescence process. As already stressed many times in all the chapters of this thesis, this is very common in cyclometalated iridium(III) complexes since the intersystem crossing process is very fast and leads to near quantitative triplet formation [20, 75, 90]. Passing from solution to the pure thin film and, finally, to the low-temperature rigid matrix, a progressive blue shift of the emission band occurs for all complexes (see Table 5.2). This trend is in line with the stabilizing effect on the lowest triplet excited state exerted by the different environments [262] and indicates that the emitting excited state has a strong CT character. The broad and structureless shape of the emission profiles (see Figure 5.5) and the radiative constants (reported in Table 5.2) also corroborate this hypothesis.

To obtain a more detailed description of the nature of the emitting triplet

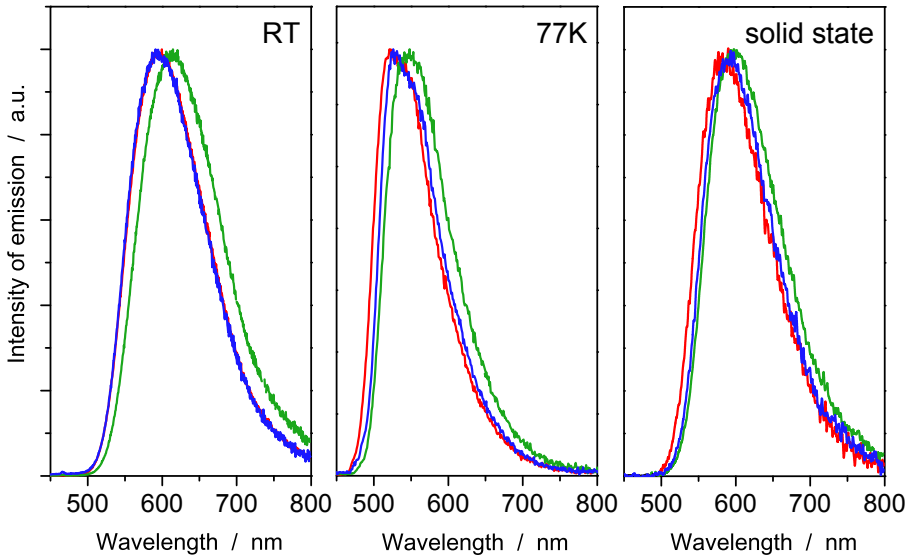

Figure 5.5: Normalized emission spectra of **tA** (red), **tB** (green), and **tC** (blue) in room-temperature CH_2Cl_2 solution (left), 77 K CH_2Cl_2 frozen matrix (middle), and pure solid-state spin-coated thin film (right). λ_{exc} = 407 nm (the emission profiles of complexes **tA** and **tC** at room temperature are almost superimposed).

state, DFT calculations at the unrestricted UB3LYP level were used to fully optimize the electronic and molecular structures of the lowest triplet state (T_1) in the presence of the solvent. The T_1 state mainly results from the HOMO-to-LUMO monoexcitation and is computed to lie 2.34 eV (**tA**), 2.31 eV (**tB**), and 2.38 eV (**tC**) above S_0 (adiabatic energy differences). Excitation to T_1 hence implies an electron transfer from the [Ir(ppy)$_2$] environment to the ancillary ligand. This is illustrated in Figure 5.3 on page 134 by the unpaired-electron spin density distribution calculated for complex **tB**, which perfectly matches the topology of the HOMO-to-LUMO excitation from which the T_1 state originates.

For the three complexes, the spin densities calculated for T_1 are very similar and confirm a mixed metal-to-ligand and ligand-to-ligand charge transfer (^{3}MLCT / ^{3}LLCT) nature of the emitting triplet state. The phosphorescence emission energy can be correlated with the vertical energy difference between T_1 and S_0 estimated by performing a single-point calculation of S_0 at the optimized minimum-energy geometry of T_1. Calculations lead to vertical emission energies

of 2.06 eV (602 nm) for **tA**, 1.98 eV (626 nm) for **tB**, and 2.00 eV (620 nm) for **tC**, in good agreement with the experimental emission wavelength values in solution (see Table 5.2 on page 136). Note that independent of the experimental conditions, the emission profiles of **tB** show a small red shift compared to those of **tA** and **tC** (see Figure 5.5). The adiabatic and vertical energy differences calculated for T_1 support this trend.

In CH_2Cl_2 solution, the luminescence performance of this series of compounds worsens on going from **tA** to **tC** (see Table 5.2). Complex **tA** shows an emission quantum yield around 20 % and a lifetime of 565 ns; these values are substantially greater than those of **tB** and **tC**, which leads to the smallest non-radiative rate constant value (1.4×10^6 s^{-1}).

As already described in of this thesis introduction, deactivation of the emitting excited states in d^6 transition-metal complexes follows three main kinetic processes [20, 75, 90].

(i) An almost temperature-independent non-radiative process, with kinetic rate constant k_{nr}, which usually occurs through direct potential energy surface crossing and/or vibrational coupling between T_1 and S_0 states.

(ii) A minor temperature-dependent radiative process, with kinetic rate constant $k_r\,(T)$, related to the thermal population of the individual triplet substates of T_1 (T_I, T_{II} and T_{III}), each of which has a unique radiative decay rate. For transition-metal complexes having significant contributions of MLCT character in their emitting excited state, the zero-field splitting (zfs) is generally less than 0.1 eV [101, 263, 264]. Thermal equilibration of the individual triplet sublevels is therefore effective at temperatures higher than 77 K, and phosphorescence can be treated as originating from a single state, having an average k_r equal to the arithmetic mean of each sublevel component.

(iii) A temperature-dependent non-radiative process, with kinetic rate constant $k_{nr}\,(T)$, comprising the thermal population of non-radiative excited states (*e.g.*, higher-lying ^{3}MC states), frequently associated with an activation energy barrier.

For practical purposes, both (i) and (ii) pathways can be regarded as substantially temperature-independent processes. Similar schemes have been proposed for neutral Ir(III) complexes and for charged Ru(II) and Os(II) complexes [20, 90,

101, 265]. According to most investigated cases, the clusters of MLCT and MC states can be considered as single MLCT and MC levels.

Following this general scenario, the stronger luminescence observed for complex **tA** compared to **tB** and **tC** (see Table 5.2) suggests that **tA** shows less effective non-radiative deactivation pathways. To confirm this notion, we correlate the structural changes predicted in passing from S_0 to T_1 with the temperature-independent deactivation (k_{nr}) pathway in a qualitative way [20, 90, 266–268].

The electron transfer associated with the excitation to the T_1 state causes a similar contraction of the coordination sphere for the three complexes (see Table 5.1). However, complex **tA** shows less-pronounced geometrical changes in passing to T_1 compared to **tB** and **tC**, which suggests that the temperature-independent deactivation pathway should be less effective than in the other two complexes.

For complex **tB**, the main structural changes upon excitation to T_1 are a shortening (0.12 Å) of the Ir–N distance of the phenyl-substituted pyridine ring with respect to that calculated for S_0, and a flattering (6°) of the ancillary ligand. These structural changes favor the temperature-independent non-radiative decay associated to vibrational deactivations and can be one of the reasons that explain the higher k_{nr} value obtained for **tB** (see Table 5.2) [20, 90, 266–268].

A second factor that contributes to the better photophysical properties of **tA** is the slightly higher energy of the T_1 emitting state compared to **tB** (see Table 5.2), which favors radiative deactivation according to the energy gap law [206]. A further reason to be considered for explaining the k_{nr} of **tB** is the population of thermally accessible non-radiative excites states, which is studied in detail in the next section.

For complex **tC**, a stronger flattering process (30°) occurs in T_1 (see Table 5.1 on page 132) and more effective vibrational deactivations should be expected in accordance with the higher value obtained for k_{nr} (see Table 5.2). However, other deactivation pathways can be likely present in **tC** as the Ir–N distance of one pyridine ring of the ancillary ligand is significantly longer (0.07 Å) than those of complexes **tA** and **tB**. The weakness of this Ir–N bond suggests that **tC** could present an effective luminescence quenching process of the T_1 state through nucleophilic-assisted ligand-exchange processes and/or population of thermally accessible non-radiative states. This hypothesis is corroborated by the low stability shown by **tC** in the absorption studies discussed above.

Further information to support the above-mentioned hypothesis is obtained from photoluminescence studies at low temperature (in 77 K rigid matrix) and in thin films. At 77 K, the PLQY is difficult to measure with acceptable accuracy but the observed lifetime can provide quantitative information thanks to the good correlation between the luminescence intensity and the relative decay [269]. The long lifetimes (microseconds time scale, see Table 5.2) measured under such conditions indicate appreciable photoluminescence performances for the three complexes. The lifetime of **tC** (4.3 µs) suffers the largest change and is the longest of the series at 77 K, supporting the aforementioned hypothesis that nucleophilic-assisted ligand-exchange processes and/or population of thermally accessible non-radiative states are present in RT solution, mainly for this complex. This hypothesis is further reinforced by the photophysical data in the solid state. In fact, whereas the PLQY of **tA** remains unchanged in passing from solution to solid state (see Table 5.2), complexes **tB** and **tC** exhibit higher quantum yields and significantly longer lifetimes. The changes are more pronounced for complex **tC** (Φ = 17 %, τ = 505 ns), which shows a luminescence intensity almost 5 times higher in a rigid environment than in the presence of solvent molecules. This suggests that the deactivation pathways are reduced in rigid matrix.

5.2.3 Following the T_1 deactivation pathways

As discussed above, one of the factors determining the change of the non-radiative constant in iTMCs is the enhancement of the temperature-independent non-radiative processes. However, they can also present other deactivation pathways related to the population of thermally accessible non-radiative states, that can be monitored following the $k_{nr}\,(T)$. This behavior is common in d^6 transition-metal complexes based on Ru(II), Os(II), and Ir(III) metal cores [20, 90, 101, 265]. For this type of complexes, a temperature dependence of k_{nr} has been observed and higher-lying, thermally accessible and reactive levels of ^{3}MC nature have proven to play an important role in photophysical patterns [20, 90, 101, 265]. On a general ground, deactivation of the emitting T_1 state is related to an activated surface crossing from the T_1 manifold to a higher-lying ^{3}MC level, which subsequently undergoes a non-radiative deactivation to the ground state S_0 (see Figure 5.6, a).

Key information about the population of thermally accessible non-radiative states can be obtained by studying the temperature dependence of the experi-

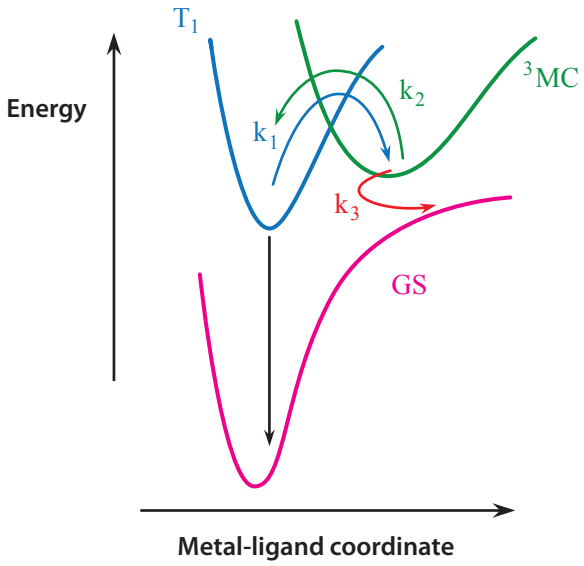

(a) General model.

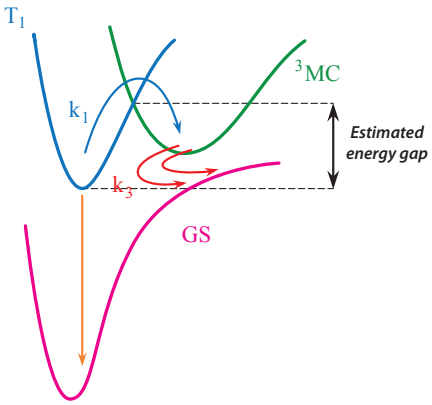

(b) Kinetic model with $k_3 \gg k_2$.

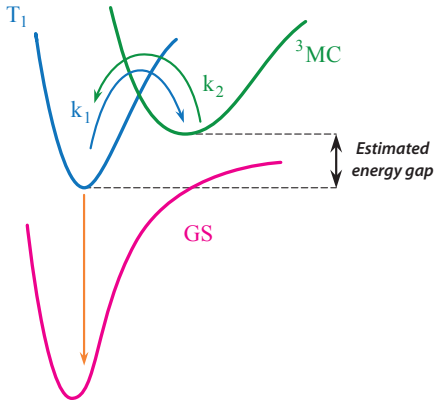

(c) Kinetic model with $k_2 \gg k_3$.

Figure 5.6: Potential energy curves illustrating a general scheme of the possible deactivation pathways to the ground state (a). Also two different kinetic cases (b and c) are depicted, depending on the involvement of ^{3}MC states in the deactivation of the T_1 emitting state.

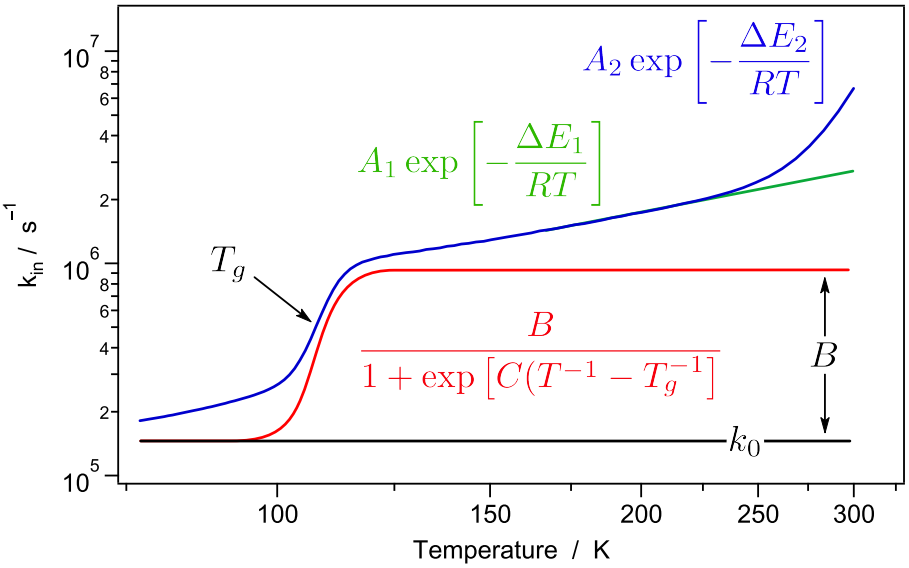

Figure 5.7: Graphical representation of the fitting function used, highlighting the contribution of the different terms in equation 5.1 and the physical meaning of some parameters.

mental intrinsic deactivation rate constant (k_{in}) that is simply the reciprocal of the excited-state lifetime (τ^{-1}). The temperature dependence of k_{in} can be fitted by the equation:

$$k_{in}\,(T) = k_0 + \frac{B}{1+\exp\left[C(T^{-1}-T_g^{-1}\right]} + \sum_i A_i \exp\left[-\frac{\Delta E_i}{RT}\right] \qquad (5.1)$$

where k_0 is a temperature-independent term, the second term takes care empirically of the effect of the rigid-fluid transition, and the third term is the usual Arrhenius expression which contains a frequency factor (A_i) and an activation energy barrier (ΔE_i) [270].

In Figure 5.7, a graphical representation of equation 5.1 is displayed, in which the contribution of each single term has been separated and highlighted. In particular, the second term describes a stepwise behavior centered at the rigid-fluid transition temperature T_g, where C is related to the smoothness of the step and B is proportional to its amplitude, while the slope of the green and blue curves is related to the activation energy of the i-th process [270].

Once the ^{3}MC state is populated, two limiting kinetic cases can be expected:

(1) when a strong coupling between the ^{3}MC level and the S_0 state takes place ($k_3 \gg k_2$), the frequency factor is predicted to be large ($A > 10^{10}$ s^{-1}) and ΔE is the activation energy barrier between the emitting level and the ^{3}MC state; the case is reported in Figure 5.6, b;

(2) when $k_2 \gg k_3$, the frequency factor is predicted to be less than 10^8 s^{-1} and ΔE is the energy separation between the emitting level and the ^{3}MC state; the case is reported in Figure 5.6, c.

In order to gain an understanding of the role played by thermally activated non-radiative decay processes on the luminescence properties of investigated series, temperature-dependent experiments were undertaken from 77 K to room temperature in degassed MeOH / EtOH 1:4 solution. Figure 5.8 displays the evolution of the k_{in} deactivation rate constant as a function of temperature. Table 5.3 on the following page summarizes the values obtained for the fitting parameters from the nonlinear iterative fitting of k_{in} data as a function of temperature using equation 5.1 with two Arrhenius terms; the corresponding χ^2 factors are 0.9982, 0.9991 and 0.9997 for **tA**, **tB** and **tC**, respectively.

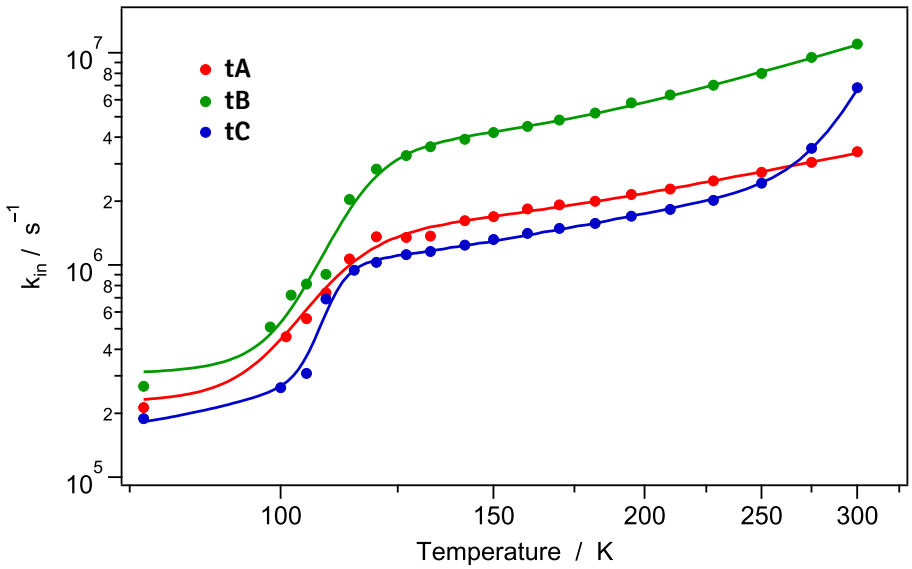

Figure 5.8: Temperature-dependent luminescent decay, as $k_{in} = \frac{1}{\tau}$, of complexes **tA**, **tB**, and **tC**. The lines are the fitting curves of the data using equation 5.1 with two Arrhenius terms and the parameters reported in Table 5.3.

Table 5.3: Kinetic parameters for excited-state decay obtained from temperature-dependent measurements.

	k_0 (10^5 s^{-1})	B (10^6 s^{-1})	C (10^3 K)	T_g (K)	A_1 (10^7 s^{-1})	ΔE_1 (eV)	A_2 (s^{-1})	ΔE_2 (eV)
tA	2.2	1.22	1.64	111.8	1.30	0.05	—	—
tB	3.0	3.30	2.10	116.3	7.60	0.06	—	—
tC	1.5	0.71	4.50	110.0	0.74	0.04	7×10^{12}	0.37

The temperature-independent term k_0 has a similar value for all the complexes (2×10^5 s^{-1}) and it is comparable to the radiative constant obtained from data at room temperature (see Table 5.3). The three complexes under investigation show a quite similar stepwise term in the temperature range between 100 K and 120 K, with $B \approx 10^6$ s^{-1} and a C value between 2 – 4 $\times$ 10^3 K; the T_g is in the range from 110 K to 116 K (seeTable 5.3). This second term in equation 5.1 corresponds to the red shift observed in the emission maxima of all complexes in the same temperature range and is associated with small rearrangements of the solvent molecules on softening of the solvent matrix and/or with reorientation of the solvent dipoles to arrange the charge displacement induced in the emitting excited state of these complexes. Solvent reorganization can only take place when the solvent has acquired the properties of a nonviscous fluid, in this case at temperatures above 120 K.

Plots of the intrinsic decay rate (k_{in}), at temperatures higher than 120 K display two distinct regimes (see Figure 5.8): one at low temperature (120 – 220 K) that corresponds to thermal redistribution between the triplet sublevels (dependent on the zfs), and the other at higher temperature (above 250 K) that involves population of the non-radiative ^{3}MC state.

Complexes **tA** – **tC** display a low-temperature activation, which corresponds to the thermal redistribution between the triplet sublevels, as suggested by the low value of the A_1 frequency factor (see Table 5.3). Accordingly, the obtained ΔE_1 values represent the zfs between the T_I and T_{III} triplet substates. The smaller splitting between sublevels T_I and T_{II} could not be resolved in the temperature range analyzed. These ΔE_1 values are in good agreement with results reported in the literature for similar complexes [20, 75, 90, 101, 263, 264]. Hence, the

decrease in lifetime observed for the investigated iridium(III) complexes upon warming from 120 K to 240 K is due to thermal population of the higher triplet sublevels, particularly the T_{III} substate, responsible for the fast radiative decay.

As the temperature increases (above 250 K), only in the case of complex **tC**, a second Arrhenius term is needed to account for the temperature dependence of k_{in}. In this case, the A_2 frequency factor is found to be 7×10^{12} s^{-1} (see Table 5.3), suggesting that the calculated value for ΔE_2 (0.37 eV) represents the activation energy for population of a high-lying non-radiative ^{3}MC excited state (case c reported in Figure 5.6 on page 141).

Investigating the deactivation pathways through DFT calculations

Metal-centered states formally result from the excitation of one electron from the occupied HOMO (t_{2g} orbitals) to the unoccupied e_g orbitals of the metal (see Figure 5.9 on the next page) [37, 97]. The geometry of the ^{3}MC states was fully relaxed starting from the optimized geometry of S_0 with Ir—N_{ppy} bond distances lengthened to 2.70 Å since the e_g orbital is σ-antibonding between the metal and the nitrogens of the cyclometalating ligands. Electron promotion to this orbital however leads to different molecular structures for the ^{3}MC state of all the complexes of the series (see Table 5.1). Whereas for complex **tA** both Ir—N_{ppy} distances lengthen to 2.51 Å (*vs.* 2.08 Å in S_0), the intramolecular π-stacking interaction present in complexes **tB** and **tC** prevents the weakening of one of the Ir—N_{ppy} bonds which lengthen to 2.60 Å and 2.20 Å (see Figure 5.9 on the following page). The pendant phenyl rings in 6- and 6'-positions thus exert a cage effect that restricts the opening of the structure of complexes **tB** and **tC** in the excited ^{3}MC state and only one of the N_{ppy} atoms is virtually decoordinated.

After geometry relaxation, the ^{3}MC states of complexes **tA** and **tB** are calculated to lie at 0.60 eV and 0.50 eV above the lowest-energy T_1 state (adiabatic energy differences), respectively. In contrast, the ^{3}MC state of complex **tC** is computed to be only 0.20 eV above the T_1 state.

These theoretical energy differences are comparable with the energies obtained from the temperature-dependent analysis (see Table 5.3 on the preceding page) for the T_{III} energy levels (ΔE_1) and the ^{3}MC activation barrier (ΔE_2). In the case of complex **tC**, the calculated ^{3}MC state is situated 0.17 eV below the activation energy barrier (ΔE_2) deduced experimentally. Hence, the calculated and experimental data are in qualitative agreement. On the other hand, the ^{3}MC

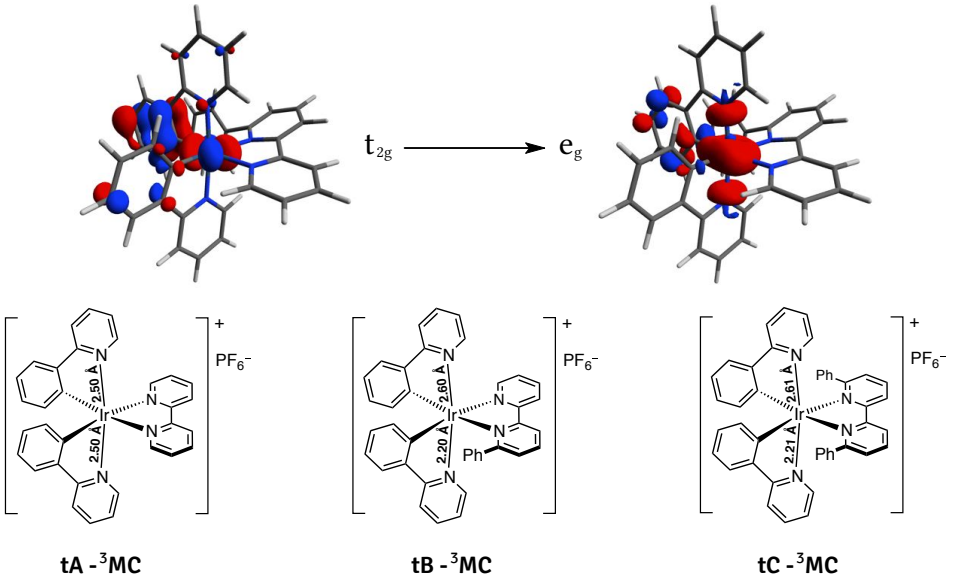

Figure 5.9: (Top) Electron density contours (0.05 e bohr^{-3}) calculated for the occupied t_{2g} and unoccupied e_g molecular orbitals of complex **tB**. The e_g orbital shows σ-antibonding interactions along the vertical $N_{ppy}-Ir-N_{ppy}$ axis. (Bottom) Sketch of the molecular structure calculated for the ^{3}MC state of complexes **tA**(left), **tB**(middle), and **tC**(right).

states of complexes **tA** and **tB** are computed to be much higher in energy with respect to the T_1 emitting state (above 0.5 eV), and no thermal activation to the non-radiative excited states is observed in temperature-dependent experiments in the range between 90 K to 400 K, which implies that they do not substantially participate in the deactivation of the T_1 emitting state. This suggests that the decrease in the photophysical performance observed in solution in passing from complex **tA** to **tB** (see Table 5.2 on page 136) is mainly related to an enhancement of the temperature-independent deactivation pathways. The situation is completely different for complex **tC** where the population of the non-radiative ^{3}MC states is an efficient pathway for radiationless processes, corresponding to case b of Figure 5.6 on page 141, as suggested by the high value of the A_2 frequency factor (7×10^{12} s^{-1}, in Table 5.3).

5.3 Conclusions

The photophysical properties of a prototypical series of charged cyclometalated $[Ir(ppy)_2(NN)]^+$, in which phenyl groups are sequentially attached to the 6- and 6'-positions of the 2,2'-bipyridine (NN ancillary ligand), have been thoroughly studied by using both experimental and theoretical approaches.

The photoluminescence properties measured in solution at room temperature worsen (lower quantum yields and shorter excited-state lifetimes) upon introduction of phenyl groups on the ancillary ligand on going from complex **tA** to **tC**. Additionally, the absorption spectra recorded over time suggest that complex **tC** presents a poor stability compared to **tA** and **tB**, likely due to a nucleophilic-assisted ancillary ligand-exchange reaction in the ground and/or in the excited states.

The study of the dependence of the experimental intrinsic deactivation rate constant ($k_{in} = 1/\tau$) on the temperature, together with the theoretical characterization of the emitting (T_1) and metal-centered (^{3}MC) excited states, help to clarify the different photophysical behavior between complexes.

Our results indicate that attachment of a phenyl group to the ancillary ligand (**tB**) enhances the temperature-independent deactivation pathways, whereas attachment of a second phenyl group (**tC**) also opens the temperature-dependent deactivation pathway through non-radiative ^{3}MC excited states. The enhancement of these deactivation pathways leads to poorer photoluminescent properties when going from complex **tA** to **tC** and is most likely the reason for the poor stability of **tC**.

The study presented in this chapter explains why LEC devices using complex **tC** are significantly less efficient than those based on **tB**, since the efficacy of the device is ultimately related to the photophysical performance of the complex used as the active component [124]. The study also suggests that the thermal population of the non-radiative ^{3}MC states is the main reason for the lower amount of light emitted during the operation lifetime of the device by LECs built up using complex **tC** [99]. For complexes **tA** and **tB**, the population of the ^{3}MC states in solution is not possible at room temperature. Nonetheless, this does not automatically imply that this is also the case in solid-state electroluminescent devices mainly because the external bias applied in the devices generates a polarization effect that can affect the relative energy of the states. Moreover

it should be stressed that, in LECs, many other factors (*e.g.*, formation of doped regions, triplet-triplet quenching, *etc.*) are playing a vital role in determining device performances. Anyway, this study further support the basic concept that the optimization in the device should start from an appropriate selection of the right active material avoiding the wrong idea that an Ir-iTMC is basically an "emitting powder".

Final remarks and outlook

In this thesis I report only a partial description of the scientific research I carried out during these last three years in the group of Dr. Nicola Armaroli. Moreover, as I already specified in the introduction, all the chapters are deliberately focused only on the investigation I performed on bis-cyclometalated iridium(III) complexes. In addition to that, the reader has to consider that, despite the CELLO project ended last January, many issues still have to be investigated and many open questions still have to be answered.

For all of these reasons, in this conclusive chapter I would like to spend time on describing few selected examples of projects that have still to be finished, rather than focusing on achievements we have accomplished in optimizing the photophysical properties of iridium(III) complexes for LEC applications.

In addition to that, in the last section of this chapter, I make an overview of some research activities in which I have been involved, which concern emitting molecules other than cyclometalated iridium(III) complexes.

Beyond CELLO

The CELLO project is over, we find reasonable answers and effective solutions to many issues concerning light-emitting electrochemical cells, not only regarding the design, the synthesis, and the optimization of the active materials, but also from the technological point of view (*i.e.*, improvements on LEC stability, turn-on time, and power efficiency; development of scaleable and roll-to-roll compatible wet processes to deposit the molecular active component and the metal contact; development of thin film flexible and large area LECs; *etc.*) ...but many other issues are still pending (*e.g.*, discovery of efficient sky-blue emitting materials showing excellent performances in LECs, a reasonable way to avoid time-dependent doping-induced quenching in the devices, *etc.*).

Florine-free blue emission

In Chapter 2 and Chapter 3, I reported selected examples of blue-emitting Ir-iTMCs but all of them display at least one drawback preventing their use in efficient LECs. In fact, carbene-based complexes (reported in Chapter 2) display a true-blue emission (around 450 nm) only in the case of the bis-fluorinated series (see Table 2.2 on page 76), consequently displaying the general problem faced by polyfluorinated cyclometalated iridium(III) complexes, *i.e.*, they usually display low stability in LECs [239–241].

On the other hand, isocyanide-based complexes (reported in Chapter 3) do not have this problem but, due to their long radiative lifetimes that may cause high sensitivity to triplet-triplet interaction and oxygen quenching, their use in efficient electroluminescent devices is most likely precluded [93].

In order to overcome all these problems we focused out attention towards new cyclometalating ligands displaying a more strong-field character. In fact, as a careful readers will have noticed, despite an almost infinite plethora of ancillary ligands (see Figure 1.12 on page 19), cationic iridium(III) complexes are based on a very limited selection of cyclometalating ligands (see Figure 1.11 on page 18). More than 10^4 papers about Ir-iTMCs are based on emitters having substituted 2-phenylpyridines as cyclometalating ligands, the pristine 2-phenylpyridine and the fluorinated 2-(3,5-difluorophenyl)pyridine being the most common [24, 212].

As already reported in the first chapter, also iridium(III) complexes based on differently substituted 1-phenylpyrazoles are quite often reported (around 10^3 papers); they have the advantage of a more blue-shifted emission despite not blue enough without the presence of fluorine-substituted cyclometalating derivatives (560 *vs* 490 nm, for the non- and bis-fluorinated complexes, respectevely) [118].

Iridium(III) complexes having other class of cyclometalating ligand are only rarely reported (see Chapter 1) and between them only a couple of cases are reporting stronger-field cyclometalating ligands.

For that reason we have synthesized and we are going to spectroscopically and theoretically investigate two new classes of efficient sky-blue emitting iridium(III) complexes having (i) carbene-based (see Figure 5.10), and (ii) phenyltetrazole as cyclometalating ligands (see Figure 5.11 on the next page). Using these different fluorine-free strong-field cyclometalating ligands we are planning to obtain a high-energy transition preserving a mainly MLCT character with a relatively short lifetime.

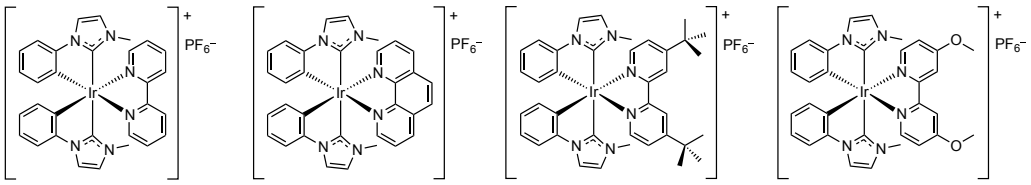

Figure 5.10: Chemical structures of some selected complexes of the carbene-cyclometalated series synthesized by Florian Kessler (EPFL, Lausanne).

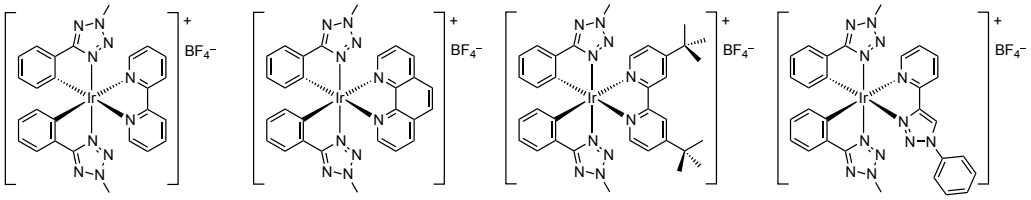

Figure 5.11: Chemical structures of some selected complexes of the tetrazole-cyclometalated series synthesized by Andrea Baschieri (UNIBO, Bologna).

Improving LEC lifetime

Another important topic we are still working on is a deeper understanding of the so-called "dynamic doping" that it is known to lead to the decrease of luminance in iTMC-based LECs [271].

In a collaboration between Sebastian Meier and Wiebke Sarfert (Siemens), and the group of Henk Bolink (University of Valencia), we are investigating the effect on temperature on the recovery of persistent doping in the devices.

As already explained in the first chapter on page 8, the formation of doped zones is essential for the process of charge injection in light-emitting electrochemical cells, but this doping zones are growing during device operation, leading to a decreasing of the intrinsic region over time and, in the end, they completely quench the device. Despite this model is able to explain the generally observed relation between the turn-on and the device lifetime [271], it is also basically predicting that, under a maybe oversimplified point of view, the same principle that allows LECs to be bright, is condemning them to a premature death.

This finding should be taken into account, not only for planning more efficient LEC driving techniques (*e.g.*, pulsed driving, alternate driving *etc.*), but

also at the very early steps of the device fabrication (*i.e.*, starting with a carefully tailored emitting iridium(III) complex).

Beyond iridium(III) cyclometalated complexes

As already described in the introduction and in Chapter 1, cyclometalated iridium(III) complexes, thanks to the huge variety of stable complexes covering the whole visible spectrum all the way from blue to red, are the most promising class of emitting materials in LECs. However, since the most relevant limitation to the use of iridium for lighting technologies is given by its low relative abundance on the Earth's crust and its high cost, a great deal of research attention has been recently devoted to find less expensive alternatives. Within this framework, promising results have been obtained with the fabrication of electroluminescent devices where copper(I) luminescent complexes have been used as emitters in place of the traditional iridium(III) luminophores (see Section 1.4.5 on page 61).

In this perspective, I am working, together with other researchers of Armaroli's group, for better understanding the basic principles that are ruling the photophysics of copper(I) complexes. Out intention is to find a good rationale that could be able to point the way to a wiser selection of organic ligands in the huge library of molecules already designed by the chemists' curiosity and ingenuity. In the case of copper, before color tuning, the main priority is intrinsic complex stability.

Appendix A

Experimental techniques

All spectroscopic measurements in solution were carried out in fluorimetric 1 cm path cuvettes using spectroscopic grade solvents.

Absorption spectra in solution were recorded with a Perkin-Elmer Lambda 950 spectrophotometer making a double baseline (*i.e.*, both at 100 % and 0 % of transmittance).

For photoluminescence experiments in solution, in the case of iridium(III) complexes, the samples were purged from oxygen by bubbling with argon. The concentration of sample solutions was adjusted to obtain absorption values < 0.15 at the excitation wavelength. All the emission spectra (both in solution and in solid state) were obtained using an Edinburgh FLS920 spectrometer equipped with a Peltier-cooled Hamamatsu R 928 photomultiplier tube (sensitive in the 185 – 850 nm range) and a Hamamatsu R 5509-72 supercooled photomultiplier tube (193 K, sensitive in the 800 – 1700 nm range). An Edinburgh Xe 900 450 W xenon arc lamp was used as the excitation source. All the reported spectra are corrected for the instrumental response using a calibration curve supplied with the instrument.

Photoluminescence quantum yields (abbreviated using the acronym PLQY, or the symbol Φ_{em}) in solution were obtained from corrected spectra on a wavelength scale (nm) and measured according to the approach described by Demas and Crosby [272] using two different standards: (i) air-equilibrated $[Ru(bpy)_3][Cl]_2$ water solution (Φ_{em} = 2.8 %) [273], (ii) air-equilibrated solution of quinine sulfate in 1 N H_2SO_4 (Φ_{em} = 54.6 %) [274].

Solid-state PLQY values were calculated by corrected emission spectra obtained from an Edinburgh FLS920 spectrometer equipped with a barium sulfate-

coated integrating sphere (diameter of 10 cm) following the procedure described by De Mello *et al.* [275]. The PMMA films containing 1 % wt. of the complex were drop-cast from dichloromethane solutions. The neat films of the complexes were spin coated from CH_2Cl_2 concentrated solutions. The thickness of the films was not controlled.

Excited-state lifetimes (τ) were determined with the single-photon counting technique by means of the same Edinburgh FLS920 spectrometer using a laser diode as the excitation source (1 MHz; λ_{exc} = 407 nm; 200 ps time resolution after deconvolution) and the above-mentioned PMT as the detector. Alternatively, the lifetimes were measured with an IBH single-photon counting spectrometer equipped either with a thyratron gated nitrogen lamp (2 to 40 kHz; λ_{exc} = 337 nm; 0.5 ns time resolution), or pulsed NanoLED excitation sources (λ_{exc} at 278, 331, and 465 nm; pulse width $\leq$ 0.3 ns); the detector was a red-sensitive (185 – 850 nm) Hamamatsu R-3237–01 PMT. Analysis of the luminescence decay profiles *vs* time was accomplished with the Decay Analysis Software provided by the instrument manufacturers, and the quality of the fit was assessed by the χ^2 value close to unity with the residuals regularly distributed along the time axis.

To record the 77 K luminescence spectra, the samples were put in quartz tubes (2 mm inner diameter) and inserted in a special quartz Dewar flask filled up with liquid nitrogen.

77 K phosphorescence spectra and lifetimes of the organic molecules were acquired using the same Edinburgh FLS920 spectrometer using a μF 920H flash lamp as excitation source.

For the temperature-dependence measurements reported in Chapter 5, all samples (oxygen-free methanol/ethanol solutions, 1:4 v/v) were degassed and put under nitrogen in a 1 cm fused quartz cell. This cuvette was placed inside a variable-temperature liquid-nitrogen Oxford OptistatDN cryostat (operating range: 77 – 500 K) and equipped with a ITC 5035 temperature controller interfaced with the same Edinburgh FLS920 spectrometer.

Experimental uncertainties are estimated to be $\pm$8 % for τ determinations, $\pm$20 % for PLQYs, $\pm$2 nm and $\pm$5 nm for absorption and emission peaks, respectively, and $\pm$2 K for the temperature in the cryostat.

Bibliography

(1) V. Smil, *Creating the Twentieth Century: Technical Innovations of 1867-1914 and Their Lasting Impact*, Oxford University Press, Oxford, 2005.

(2) J. Brox, *Brilliant: The evolution of artificial light*, Houghton Mifflin Harcourt, New York, 2010.

(3) L. S. Brown, *Plan B. Mobilizing to save the civilization*, W. W. Norton & Company, New York, 2009.

(4) *Light's Labour's Lost - Policies for Energy-efficient Lighting*, tech. rep., International Energy Agency, 2006.

(5) N. Armaroli and V. Balzani, *Energy for a sustainable world. From the oil age to a sun powered future*, Wiley-VCH, Weinheim, Germany, 2011.

(6) N. Armaroli and V. Balzani, *Energ. Environ. Sci.*, 2011, **4**, 3193–3222.

(7) E. Mills, *Science*, 2005, **308**, 1263–1264.

(8) W. J. Martin, R. I. Glass, J. M. Balbus, and F. S. Collins, *Science*, 2011, **334**, 180–181.

(9) G. Zissis and S. Kitsinelis, *J. Phys. D: Appl. Phys.*, 2009, **42**, 173001.

(10) C. J. Humphreys, *MRS Bulletin*, 2008, **33**, 459–470.

(11) M. H. Crawford, *IEEE J. Sel. Top. Quantum Electron.*, 2009, **15**, 1028–1040.

(12) C. W. Tang and S. A. Vanslyke, *Appl. Phys. Lett.*, 1987, **51**, 913–915.

(13) J. H. Burroughes, D. D. C. Bradley, A. R. Brown, R. N. Marks, K. Mackay, R. H. Friend, P. L. Burns, and A. B. Holmes, *Nature*, 1990, **347**, 539–541.

(14) *Organic Light Emitting Devices: Synthesis, Properties, and Applications*, ed. K. Mullen and U. Scherf, Wiley-VCH, Weinheim, 2006.

(15) T. Justel, in *Luminescence*, ed. C. Ronda, Wiley-VCH, Weinheim, 2008, pp. 179–190.

(16) Z. Li and H. Meng, *Organic Light-Emitting Materials and Devices*, CRC, Boca Raton, FL, 2007.

(17) *Highly efficient OLEDs with phosphorescent materials*, ed. H. Yersin, Wiley-VCH, Weinheim, 2008.

(18) S. Reineke, F. Lindner, G. Schwartz, N. Seidler, K. Walzer, B. Lussem, and K. Leo, *Nature*, 2009, **459**, 234–238.

(19) H. Yersin, *Transition Metal and Rare Earth Compounds Excited States, Transitions, Interactions III*, Springer, Berlin, 2004, vol. 241.

(20) V. Balzani and S. Campagna, *Photochemistry and Photophysics of Coordination Compounds I and II*, Springer, 2007, vol. 280.

(21) R. C. Evans, P. Douglas, and C. J. Winscom, *Coord. Chem. Rev.*, 2006, **250**, 2093–2126.

(22) A. Barbieri, G. Accorsi, and N. Armaroli, *Chem. Commun.*, 2008, 2185–2193.

(23) M. Sessolo and H. J. Bolink, *Adv. Mater.*, 2011, **23**, 1829–1845.

(24) T. Hu, L. He, L. Duan, and Y. Qiu, *J. Mater. Chem.*, 2012, **22**, 4206–4215.

(25) H.-C. Su, K.-T. Wong, and C.-C. Wu, in *WOLED and Organic Photovoltaics - Recent Advances and Applications*, ed. V. W. W. Yam, Springer-Verlag, Berlin Heidelberg, 2010.

(26) Q. Pei, G. Yu, C. Zhang, Y. Yang, and A. J. Heeger, *Science*, 1995, **269**, 1086–1088.

(27) K. M. Maness, R. H. Terrill, T. J. Meyer, R. W. Murray, and R. M. Wightman, *J. Am. Chem. Soc.*, 1996, **118**, 10609–10616.

(28) J. Slinker, D. Bernards, P. L. Houston, H. D. Abruña, S. Bernhard, and G. G. Malliaras, *Chem. Commun.*, 2003, 2392–2399.

(29) J. D. Slinker, J. Rivnay, J. S. Moskowitz, J. B. Parker, S. Bernhard, H. D. Abruña, and G. G. Malliaras, *J. Mater. Chem.*, 2007, **17**, 2976–2988.

(30) Q. J. Sun, Y. F. Li, and Q. B. Pei, *J. Disp. Technol.*, 2007, **3**, 211–224.

(31) J.-K. Lee, D. Yoo, and M. F. Rubner, *Chem. Mater.*, 1997, **9**, 1710–1712.

(32) K. M. Maness, H. Masui, R. M. Wightman, and R. W. Murray, *J. Am. Chem. Soc.*, 1997, **119**, 3987–3993.

(33) E. S. Handy, A. J. Pal, and M. F. Rubner, *J. Am. Chem. Soc.*, 1999, **121**, 3525–3528.

(34) F. G. Gao and A. J. Bard, *J. Am. Chem. Soc.*, 2000, **122**, 7426–7427.

(35) Q. B. Pei, Y. Yang, G. Yu, C. Zhang, and A. J. Heeger, *J. Am. Chem. Soc.*, 1996, **118**, 3922–3929.

(36) M. S. Lowry and S. Bernhard, *Chem. Eur. J.*, 2006, **12**, 7970–7977.

(37) R. D. Costa, E. Orti, H. J. Bolink, S. Graber, S. Schaffner, M. Neuburger, C. E. Housecroft, and E. C. Constable, *Adv. Funct. Mater.*, 2009, **19**, 3456–3463.

(38) D. A. Bernards, T. Biegala, Z. A. Samuels, J. D. Slinker, G. G. Malliaras, S. Flores-Torres, H. D. Abruña, and J. A. Rogers, *Appl. Phys. Lett.*, 2004, **84**, 3675–3677.

(39) D. A. Bernards, J. D. Slinker, G. G. Malliaras, S. Flores-Torres, and H. D. Abruña, *Appl. Phys. Lett.*, 2004, **84**, 4980–4982.

(40) J. D. Slinker, J. Rivnay, J. A. DeFranco, D. A. Bernards, A. A. Gorodetsky, S. T. Parker, M. P. Cox, R. Rohl, G. G. Malliaras, S. Flores-Torres, and H. D. Abruña, *J. Appl. Phys.*, 2006, **99**, 074502–5.

(41) J. C. deMello, N. Tessler, S. C. Graham, and R. H. Friend, *Phys. Rev. B*, 1998, **57**, 12951.

(42) J. C. deMello, *Phys. Rev. B*, 2002, **66**, 235210.

(43) G. G. Malliaras, J. D. Slinker, J. A. DeFranco, M. J. Jaquith, W. R. Silveira, Y. W. Zhong, J. M. Moran-Mirabal, H. G. Craighead, H. D. Abruna, and J. A. Marohn, *Nat. Mater.*, 2008, **7**, 168–168.

(44) D. L. Smith, *J. Appl. Phys.*, 1997, **81**, 2869–2880.

(45) I. Riess, *Phys. Rev. B*, 1987, **35**, 5740–5743.

(46) M. . J. M. de Jong and P. W. M. Blom, in *Proceedings of the 23rd International Conference on the Physics of Semiconductors, Berlin, Vol. 4*, ed. M. Scheffler and R. Zimmermann, World Scientific, Singapore, 1996, pp. 3351–3354.

(47) S. van Reenen, R. A. J. Janssen, and M. Kemerink, *Org. Electron.*, 2011, **12**, 1746–1753.

(48) V. Bychkov, P. Matyba, V. Akkerman, M. Modestov, D. Valiev, G. Brodin, C. K. Law, M. Marklund, and L. Edman, *Phys. Rev. Lett.*, 2011, **107**, 016103.

(49) J. Gao and J. Dane, *Appl. Phys. Lett.*, 2004, **84**, 2778–2780.

(50) J. H. Shin and L. Edman, *J. Am. Chem. Soc.*, 2006, **128**, 15568–15569.

(51) S. van Reenen, P. Matyba, A. Dzwilewski, R. A. J. Janssen, L. Edman, and M. Kemerink, *J. Am. Chem. Soc.*, 2010, **132**, 13776–13781.

(52) J. H. Shin, P. Matyba, N. D. Robinson, and L. Edman, *Electrochim. Acta*, 2007, **52**, 6456–6462.

(53) L. S. C. Pingree, D. B. Rodovsky, D. C. Coffey, G. P. Bartholomew, and D. S. Ginger, *J. Am. Chem. Soc.*, 2007, **129**, 15903–15910.

(54) J. D. Slinker, J. A. DeFranco, M. J. Jaquith, W. R. Silveira, Y. W. Zhong, J. M. Moran-Mirabal, H. G. Craighead, H. D. Abruña, J. A. Marohn, and G. G. Malliaras, *Nat. Mater.*, 2007, **6**, 894–899.

(55) P. Matyba, K. Maturova, M. Kemerink, N. D. Robinson, and L. Edman, *Nat. Mater.*, 2009, **8**, 672–676.

(56) D. B. Rodovsky, O. G. Reid, L. S. C. Pingree, and D. S. Ginger, *ACS Nano*, 2010, **4**, 2673–2680.

(57) Y. F. Li, J. Gao, G. Yu, Y. Cao, and A. J. Heeger, *Chem. Phys. Lett.*, 1998, **287**, 83–88.

(58) H. Rudmann, S. Shimada, and M. F. Rubner, *J. Appl. Phys.*, 2003, **94**, 115–122.

(59) Y. Shao, X. Gong, A. J. Heeger, M. Liu, and A. K. Y. Jen, *Adv. Mater.*, 2009, **21**, 1972–1975.

(60) J. Gao, Y. F. Li, G. Yu, and A. J. Heeger, *J. Appl. Phys.*, 1999, **86**, 4594–4599.

(61) J. M. Leger, D. B. Rodovsky, and G. R. Bartholomew, *Adv. Mater.*, 2006, **18**, 3130–3134.

(62) C. V. Hoven, H. P. Wang, M. Elbing, L. Garner, D. Winkelhaus, and G. C. Bazan, *Nat. Mater.*, 2010, **9**, 249–252.

(63) M. Lenes, G. Garcia-Belmonte, D. Tordera, A. Pertegas, J. Bisquert, and H. J. Bolink, *Adv. Funct. Mater.*, 2011, **21**, 1581–1586.

(64) *Current Injection in Solids*, ed. M. A. Lampert and P. Mark, Academic Press, New York, 1970.

(65) V. D. Mihailetchi, P. W. M. Blom, J. C. Hummelen, and M. T. Rispens, *J. Appl. Phys.*, 2003, **94**, 6849–6854.

(66) K. W. Lee, J. D. Slinker, A. A. Gorodetsky, S. Flores-Torres, H. D. Abruña, P. L. Houston, and G. G. Malliaras, *Phys. Chem. Chem. Phys.*, 2003, **5**, 2706–2709.

(67) P. Pachler, F. P. Wenzl, U. Scherf, and G. Leising, *J. Phys. Chem. B*, 2005, **109**, 6020–6024.

(68) O. Inganäs, *Chem. Soc. Rev.*, 2010, **39**, 2633–2642.

(69) R. H. Friend, R. W. Gymer, A. B. Holmes, J. H. Burroughes, R. N. Marks, C. Taliani, D. D. C. Bradley, D. A. Dos Santos, J. L. Bredas, M. Logdlund, and W. R. Salaneck, *Nature*, 1999, **397**, 121–128.

(70) M. A. Baldo, D. F. O'Brien, Y. You, A. Shoustikov, S. Sibley, M. E. Thompson, and S. R. Forrest, *Nature*, 1998, **395**, 151–154.

(71) H. Rudmann, S. Shimada, and M. F. Rubner, *J. Am. Chem. Soc.*, 2002, **124**, 4918–4921.

(72) C. M. Elliott, F. Pichot, C. J. Bloom, and L. S. Rider, *J. Am. Chem. Soc.*, 1998, **120**, 6781–6784.

(73) L. Flamigni, A. Barbieri, C. Sabatini, B. Ventura, and F. Barigelletti, *Top. Curr. Chem.*, 2007, **281**, 143–203.

(74) A. Juris, V. Balzani, F. Barigelletti, S. Campagna, P. Belser, and A. Von Zelewsky, *Coord. Chem. Rev.*, 1988, **84**, 85–277.

(75) C. Ulbricht, B. Beyer, C. Friebe, A. Winter, and U. S. Schubert, *Adv. Mater.*, 2009, **21**, 4418–4441.

(76) J. D. Slinker, A. A. Gorodetsky, M. S. Lowry, J. J. Wang, S. Parker, R. Rohl, S. Bernhard, and G. G. Malliaras, *J. Am. Chem. Soc.*, 2004, **126**, 2763–2767.

(77) M. Nonoyama, *Bull. Chem. Soc. Jpn.*, 1974, **47**, 767–768.

(78) M. Nonoyama, *J. Organomet. Chem.*, 1975, **86**, 263–267.

(79) K. Dedeian, P. I. Djurovich, F. O. Garces, G. Carlson, and R. J. Watts, *Inorg. Chem.*, 1991, **30**, 1685–1687.

(80) K. A. King, P. J. Spellane, and R. J. Watts, *J. Am. Chem. Soc.*, 1985, **107**, 1431–1432.

(81) L. He, J. Qiao, L. Duan, G. F. Dong, D. Q. Zhang, L. D. Wang, and Y. Qiu, *Adv. Funct. Mater.*, 2009, **19**, 2950–2960.

(82) L. He, L. Duan, J. Qiao, R. J. Wang, P. Wei, L. D. Wang, and Y. Qiu, *Adv. Funct. Mater.*, 2008, **18**, 2123–2131.

(83) B. Schmid, F. O. Garces, and R. J. Watts, *Inorg. Chem.*, 1994, **33**, 9–14.

(84) J. Li, P. I. Djurovich, B. D. Alleyne, I. Tsyba, N. N. Ho, R. Bau, and M. E. Thompson, *Polyhedron*, 2004, **23**, 419–428.

(85) C. H. Yang, J. Beltran, V. Lemaur, J. Cornil, D. Hartmann, W. Sarfert, R. Frohlich, C. Bizzarri, and L. De Cola, *Inorg. Chem.*, 2010, **49**, 9891–9901.

(86) V. Balzani, G. Bergamini, S. Campagna, and F. Puntoriero, *Top. Curr. Chem.*, 2007, **280**, 1–36.

(87) R Englman and J. Jortner, *Mol. Phys.*, 1970, **18**, 145–164.

(88) E. M. Kober, J. V. Caspar, B. P. Sullivan, and T. J. Meyer, *Inorg. Chem.*, 1988, **27**, 4587–4598.

(89) D. Kumaresan, K. Shankar, S. Vaidya, and R. H. Schmehl, *Top. Curr. Chem.*, 2007, **281**, 101–142.

(90) M. Montalti, A. Credi, L. Prodi, and M. T. Gandolfi, *Handbook of Photochemistry - Third Edition*, Taylor and Francis, 2006.

(91) M. S. Lowry, J. I. Goldsmith, J. D. Slinker, R. Rohl, R. A. Pascal, G. G. Malliaras, and S. Bernhard, *Chem. Mater.*, 2005, **17**, 5712–5719.

(92) J. Li, P. I. Djurovich, B. D. Alleyne, M. Yousufuddin, N. N. Ho, J. C. Thomas, J. C. Peters, R. Bau, and M. E. Thompson, *Inorg. Chem.*, 2005, **44**, 1713–1727.

(93) N. M. Shavaleev, F. Monti, R. D. Costa, R. Scopelliti, H. J. Bolink, E. Orti, G. Accorsi, N. Armaroli, E. Baranoff, M. Gratzel, and M. K. Nazeeruddin, *Inorg. Chem.*, 2012, **51**, 2263–2271.

(94) M. A. L. Marques and E. K. U. Gross, *Annu. Rev. Phys. Chem.*, 2004, **55**, 427–455.

(95) M. E. Casida and M. Huix-Rotllant, *Annu. Rev. Phys. Chem.*, 2012, **63**, 287–323.

(96) F. Alary, M. Boggio-Pasqua, J. L. Heully, C. J. Marsden, and P. Vicendo, *Inorg. Chem.*, 2008, **47**, 5259–5266.

(97) F. Alary, J.-L. Heully, L. Bijeire, and P. Vicendo, *Inorg. Chem.*, 2007, **46**, 3154–3165.

(98) S. Campagna, F. Puntoriero, F. Nastasi, G. Bergamini, and V. Balzani, *Top. Curr. Chem.*, 2007, **280**, 117–214.

(99) R. D. Costa, E. Orti, H. J. Bolink, S. Graber, C. E. Housecroft, M. Neuburger, S. Schaffner, and E. C. Constable, *Chem. Commun.*, 2009, 2029–2031.

(100) R. D. Costa, F. Monti, G. Accorsi, A. Barbieri, H. J. Bolink, E. Orti, and N. Armaroli, *Inorg. Chem.*, 2011, **50**, 7229–7238.

(101) T. Sajoto, P. I. Djurovich, A. B. Tamayo, J. Oxgaard, W. A. Goddard, and M. E. Thompson, *J. Am. Chem. Soc.*, 2009, **131**, 9813–9822.

(102) R. D. Costa, E. Ortí, H. J. Bolink, S. Graber, C. E. Housecroft, and E. C. Constable, *Adv. Funct. Mater.*, 2010, **20**, 1511–1520.

(103) H. J. Bolink, E. Coronado, R. D. Costa, N. Lardies, and E. Orti, *Inorg. Chem.*, 2008, **47**, 9149–9151.

(104) H. C. Su, F. C. Fang, T. Y. Hwu, H. H. Hsieh, H. F. Chen, G. H. Lee, S. M. Peng, K. T. Wong, and C. C. Wu, *Adv. Funct. Mater.*, 2007, **17**, 1019–1027.

(105) J. D. Slinker, C. Y. Koh, G. G. Malliaras, M. S. Lowry, and S. Bernhard, *Appl. Phys. Lett.*, 2005, **86**, 173506.

(106) H. Rudmann and M. F. Rubner, *J. Appl. Phys.*, 2001, **90**, 4338–4345.

(107) H.-C. Su, C.-C. Wu, F.-C. Fang, and K.-T. Wong, *Appl. Phys. Lett.*, 2006, **89**, 261118.

(108) S. Bernhard, J. A. Barron, P. L. Houston, H. D. Abruña, J. L. Ruglovksy, X. C. Gao, and G. G. Malliaras, *J. Am. Chem. Soc.*, 2002, **124**, 13624–13628.

(109) H. J. Bolink, L. Cappelli, E. Coronado, M. Grätzel, E. Ortí, R. D. Costa, P. M. Viruela, and M. K. Nazeeruddin, *J. Am. Chem. Soc.*, 2006, **128**, 14786–14787.

(110) *Colorimetry - Understanding the CIE system*, ed. J. Scahnda, John Wiley & Sons Inc., Hoboken, NJ, 2007.

(111) M. K. Nazeeruddin, R. T. Wegh, Z. Zhou, C. Klein, Q. Wang, F. De Angelis, S. Fantacci, and M. Grätzel, *Inorg. Chem.*, 2006, **45**, 9245–9250.

(112) F. De Angelis, S. Fantacci, N. Evans, C. Klein, S. M. Zakeeruddin, J. E. Moser, K. Kalyanasundaram, H. J. Bolink, M. Gratzel, and M. K. Nazeeruddin, *Inorg. Chem.*, 2007, **46**, 5989–6001.

(113) J. L. Rodriguez-Redondo, R. D. Costa, E. Orti, A. Sastre-Santos, H. J. Bolink, and F. Fernandez-Lazaro, *Dalton Trans.*, 2009, 9787–9793.

(114) S. Ladouceur, D. Fortin, and E. Zysman-Colman, *Inorg. Chem.*, 2010, **49**, 5625–5641.

(115) S. Lamansky, P. Djurovich, D. Murphy, F. Abdel-Razzaq, R. Kwong, I. Tsyba, M. Bortz, B. Mui, R. Bau, and M. E. Thompson, *Inorg. Chem.*, 2001, **40**, 1704–1711.

(116) M. Mydlak, C. Bizzarri, D. Hartmann, W. Sarfert, G. Schmid, and L. De Cola, *Adv. Funct. Mater.*, 2010, **20**, 1812–1820.

(117) B. Chen, Y. H. Li, W. Yang, W. Luo, and H. B. Wu, *Org. Electron.*, 2011, **12**, 766–773.

(118) A. B. Tamayo, S. Garon, T. Sajoto, P. I. Djurovich, I. M. Tsyba, R. Bau, and M. E. Thompson, *Inorg. Chem.*, 2005, **44**, 8723–8732.

(119) S. Ladouceur, D. Fortin, and E. Zysman-Colman, *Inorg. Chem.*, 2011, **50**, 11514–11526.

(120) C. S. Chin, M. S. Eum, S. Y. Kim, C. Kim, and S. K. Kang, *Eur. J. Inorg. Chem.*, 2007, 372–375.

(121) F. Kessler, R. D. Costa, D. Di Censo, R. Scopelliti, E. Orti, H. J. Bolink, S. Meier, W. Sarfert, M. Gratzel, M. K. Nazeeruddin, and E. Baranoff, *Dalton Trans.*, 2012, 180–191.

(122) M. Buda, G. Kalyuzhny, and A. J. Bard, *J. Am. Chem. Soc.*, 2002, **124**, 6090–6098.

(123) G. Kalyuzhny, M. Buda, J. McNeill, P. Barbara, and A. J. Bard, *J. Am. Chem. Soc.*, 2003, **125**, 6272–6283.

(124) G. G. Malliaras and J. C. Scott, *J. Appl. Phys.*, 1998, **83**, 5399–5403.

(125) J. K. Lee, D. S. Yoo, E. S. Handy, and M. F. Rubner, *Appl. Phys. Lett.*, 1996, **69**, 1686–1688.

(126) C. H. Lyons, E. D. Abbas, J. K. Lee, and M. F. Rubner, *J. Am. Chem. Soc.*, 1998, **120**, 12100–12107.

(127) A. Wu, J. Lee, and M. F. Rubner, *Thin Solid Films*, 1998, **327-329**, 663–667.

(128) A. Wu, D. Yoo, J. K. Lee, and M. F. Rubner, *J. Am. Chem. Soc.*, 1999, **121**, 4883–4891.

(129) J. A. Barron, S. Bernhard, P. L. Houston, H. D. Abruña, J. L. Ruglovsky, and G. G. Malliaras, *J. Phys. Chem. A*, 2003, **107**, 8130–8133.

(130) D. A. Bernards, S. Flores-Torres, H. D. Abruña, and G. G. Malliaras, *Science*, 2006, **313**, 1416–1419.

(131) S. Bernhard, X. Gao, G. G. Malliaras, and H. D. Abruña, *Adv. Mater.*, 2002, **14**, 433–436.

(132) D. R. Blasini, J. Rivnay, D.-M. Smilgies, J. D. Slinker, S. Flores-Torres, H. D. Abruña, and G. G. Malliaras, *J. Mater. Chem.*, 2007, **17**, 1458–1461.

(133) H. J. Bolink, L. Cappelli, E. Coronado, and P. Gavina, *Inorg. Chem.*, 2005, **44**, 5966–5968.

(134) H. J. Bolink, L. Cappelli, E. Coronado, M. Grätzel, and M. K. Nazeeruddin, *J. Am. Chem. Soc.*, 2006, **128**, 46–47.

(135) H. J. Bolink, E. Coronado, R. D. Costa, P. Gavina, E. Ortí, and S. Tatay, *Inorg. Chem.*, 2009, **48**, 3907–3909.

(136) F. G. Gao and A. J. Bard, *Chem. Mater.*, 2002, **14**, 3465–3470.

(137) A. A. Gorodetsky, S. Parker, J. D. Slinker, D. A. Bernards, M. H. Wong, G. G. Malliaras, S. Flores-Torres, and H. D. Abruña, *Appl. Phys. Lett.*, 2004, **84**, 807–809.

(138) A. R. Hosseini, C. Y. Koh, J. D. Slinker, S. Flores-Torres, H. D. Abruña, and G. G. Malliaras, *Chem. Mater.*, 2005, **17**, 6114–6116.

(139) C.-Y. Liu and A. J. Bard, *Appl. Phys. Lett.*, 2003, **83**, 5431–5433.

(140) C.-Y. Liu and A. J. Bard, *Appl. Phys. Lett.*, 2005, **87**, 061110–061113.

(141) D. L. Pile and A. J. Bard, *Chem. Mater.*, 2005, **17**, 4212–4217.

(142) H. Rudmann, S. Shimada, M. F. Rubner, D. W. Oblas, and J. E. Whitten, *J. Appl. Phys.*, 2002, **92**, 1576–1581.

(143) J. D. Slinker, J.-S. Kim, S. Flores-Torres, J. H. Delcamp, H. D. Abruña, R. H. Friend, and G. G. Malliaras, *J. Mater. Chem.*, 2007, **17**, 76–81.

(144) L. J. Soltzberg, J. D. Slinker, S. Flores-Torres, D. A. Bernards, G. G. Malliaras, H. D. Abruña, J.-S. Kim, R. H. Friend, M. D. Kaplan, and V. Goldberg, *J. Am. Chem. Soc.*, 2006, **128**, 7761–7764.

(145) W. Y. Ng, X. Gong, and W. K. Chan, *Chem. Mater.*, 1999, **11**, 1165–1170.

(146) W. Zhao, C. Y. Liu, Q. Wang, J. M. White, and A. J. Bard, *Chem. Mater.*, 2005, **17**, 6403–6406.

(147) C.-Y. Liu and A. J. Bard, *J. Am. Chem. Soc.*, 2002, **124**, 4190–4191.

(148) X. Gong, P. K. Ng, and W. K. Chan, *Adv. Mater.*, 1998, **10**, 1337–1340.

(149) N. Armaroli, G. Accorsi, M. Holler, O. Moudam, J. F. Nierengarten, Z. Zhou, R. T. Wegh, and R. Welter, *Adv. Mater.*, 2006, **18**, 1313–1316.

(150) O. Moudam, A. Kaeser, B. Delavaux-Nicot, C. Duhayon, M. Holler, G. Accorsi, N. Armaroli, I. Seguy, J. Navarro, P. Destruel, and J. F. Nierengarten, *Chem. Commun.*, 2007, 3077–3079.

(151) P. K. Ng, X. Gong, S. H. Chan, L. S. M. Lam, and W. K. Chan, *Chem. Eur. J.*, 2001, **7**, 4358–4367.

(152) W. K. Chan, P. K. Ng, X. Gong, and S. Hou, *Appl. Phys. Lett.*, 1999, **75**, 3920–3922.

(153) Y.-M. Wang, F. Teng, Y.-B. Hou, Z. Xu, Y.-S. Wang, and W.-F. Fu, *Appl. Phys. Lett.*, 2005, **87**, 233512.

(154) Q. S. Zhang, Q. G. Zhou, Y. X. Cheng, L. X. Wang, D. G. Ma, X. B. Jing, and F. S. Wang, *Adv. Funct. Mater.*, 2006, **16**, 1203–1208.

(155) R. D. Costa, D. Tordera, E. Orti, H. J. Bolink, J. Schonle, S. Graber, C. E. Housecroft, E. C. Constable, and J. A. Zampese, *J. Mater. Chem.*, 2011, **21**, 16108–16118.

(156) D. M. Roundhill, *Photochemistry and Photophysics of Metal Complexes*, Plenum Press, New York, 1994.

(157) M. S. Lowry, W. R. Hudson, R. A. Pascal, and S. Bernhard, *J. Am. Chem. Soc.*, 2004, **126**, 14129–14135.

(158) H. J. Bolink, L. Cappelli, S. Cheylan, E. Coronado, R. D. Costa, N. Lardies, M. K. Nazeeruddin, and E. Ortí, *J. Mater. Chem.*, 2007, **17**, 5032–5041.

(159) H. C. Su, H. F. Chen, F. C. Fang, C. C. Liu, C. C. Wu, K. T. Wong, Y. H. Liu, and S. M. Peng, *J. Am. Chem. Soc.*, 2008, **130**, 3413–3419.

(160) R. D. Costa, P. M. Viruela, H. J. Bolink, and E. Ortí, *J. Mol. Struct.: THEOCHEM*, 2009, **912**, 21–26.

(161) D. W. Thompson, J. F. Wishart, B. S. Brunschwig, and N. Sutin, *J. Phys. Chem. A*, 2001, **105**, 8117–8122.

(162) J. Van Houten and R. J. Watts, *J. Am. Chem. Soc.*, 1976, **98**, 4853–4858.

(163) A. W. Adamson and P. D. Fleischauer, *Concepts in Inorganic Photochemistry;* Wiley & Sons, New York, 1975.

(164) B. Durham, J. V. Caspar, J. K. Nagle, and T. J. Meyer, *J. Am. Chem. Soc.*, 1982, **104**, 4803–4810.

(165) P.-T. Chou and Y. Chi, *Chem. Eur. J.*, 2007, **13**, 380–395.

(166) I. S. Shin, H. C. Lim, J. W. Oh, J. K. Lee, T. H. Kim, and H. Kim, *Electrochem. Commun.*, 2011, **13**, 64–67.

(167) Y. Shao, G. C. Bazan, and A. J. Heeger, *Adv. Mater.*, 2007, **19**, 365–370.

(168) H. J. Bolink, E. Coronado, R. D. Costa, E. Orti, M. Sessolo, S. Graber, K. Doyle, M. Neuburger, C. E. Housecroft, and E. C. Constable, *Adv. Mater.*, 2008, **20**, 3910–3913.

(169) S. T. Parker, J. D. Slinker, M. S. Lowry, M. P. Cox, S. Bernhard, and G. G. Malliaras, *Chem. Mater.*, 2005, **17**, 3187–3190.

(170) R. D. Costa, A. Perteges, E. Orti, and H. J. Bolink, *Chem. Mater.*, 2010, **22**, 1288–1290.

(171) E. Zysman-Colman, J. D. Slinker, J. B. Parker, G. G. Malliaras, and S. Bernhard, *Chem. Mater.*, 2008, **20**, 388–396.

(172) H.-C. Su, H.-F. Chen, C.-C. Wu, and K.-T. Wong, *Chem. Asian J.*, 2008, **3**, 1922–1928.

(173) T.-H. Kwon, Y. H. Oh, I.-S. Shin, and J.-I. Hong, *Adv. Funct. Mater.*, 2009, **19**, 711–717.

(174) F. Dumur, G. Nasr, G. Wantz, C. R. Mayer, E. Dumas, A. Guerlin, F. Miomandre, G. Clavier, D. Bertin, and D. Gigmes, *Org. Electron.*, 2011, **12**, 1683–1694.

(175) D. Tordera, S. Meier, M. Lenes, R. D. Costa, E. Ortí, W. Sarfert, and H. J. Bolink, *Adv. Mater.*, 2012, **24**, 897–900.

(176) S. Graber, K. Doyle, M. Neuburger, C. E. Housecroft, E. C. Constable, R. D. Costa, E. Ortí, D. Repetto, and H. J. Bolink, *J. Am. Chem. Soc.*, 2008, **130**, 14944–14945.

(177) R. D. Costa, E. Orti, H. J. Bolink, S. Graber, C. E. Housecroft, and E. C. Constable, *J. Am. Chem. Soc.*, 2010, **132**, 5978–5980.

(178) L. He, L. Duan, J. Qiao, D. Q. Zhang, L. D. Wang, and Y. Qiu, *Chem. Commun.*, 2011, 6467–6469.

(179) L. F. Sun, A. Galan, S. Ladouceur, J. D. Slinker, and E. Zysman-Colman, *J. Mater. Chem.*, 2011, **21**, 18083–18088.

(180) R. D. Costa, E. Orti, H. J. Bolink, S. Graber, C. E. Housecroft, and E. C. Constable, *Chem. Commun.*, 2011, 3207–3209.

(181) G. Yu, Y. Cao, C. Zhang, Y. F. Li, J. Gao, and A. J. Heeger, *Appl. Phys. Lett.*, 1998, **73**, 111–113.

(182) C. Rothe, C. J. Chiang, V. Jankus, K. Abdullah, X. S. Zeng, R. Jitchati, A. S. Batsanov, M. R. Bryce, and A. P. Monkman, *Adv. Funct. Mater.*, 2009, **19**, 2038–2044.

(183) X. Zeng, M. Tavasli, I. Perepichka, A. Batsanov, M. Bryce, C.-J. Chiang, C. Rothe, and A. Monkman, *Chem. Eur. J.*, 2008, **14**, 933–943.

(184) W. J. Xu, S. J. Liu, T. C. Ma, Q. Zhao, A. Pertegas, D. Tordera, H. J. Bolink, S. H. Ye, X. M. Liu, S. Sun, and W. Huang, *J. Mater. Chem.*, 2011, **21**, 13999–14007.

(185) R. D. Costa, G. Fernandez, L. Sanchez, N. Martin, E. Ortí, and H. J. Bolink, *Chem. Eur. J.*, 2010, **16**, 9855–9863.

(186) L. He, L. A. Duan, J. A. Qiao, D. Q. Zhang, L. D. Wang, and Y. Qiu, *Org. Electron.*, 2010, **11**, 1185–1191.

(187) H. C. Su, Y. H. Lin, C. H. Chang, H. W. Lin, C. C. Wu, F. C. Fang, H. F. Chen, and K. T. Wong, *J. Mater. Chem.*, 2010, **20**, 5521–5526.

(188) H. F. Chen, C. T. Liao, T. C. Chen, H. C. Su, K. T. Wong, and T. F. Guo, *J. Mater. Chem.*, 2011, **21**, 4175–4181.

(189) C.-T. Liao, H.-F. Chen, H.-C. Su, and K.-T. Wong, *Phys. Chem. Chem. Phys.*, 2012, **14**, 1262–1269.

(190) H.-F. Chen, K.-T. Wong, Y.-H. Liu, Y. Wang, Y.-M. Cheng, M.-W. Chung, P.-T. Chou, and H.-C. Su, *J. Mater. Chem.*, 2011, **21**, 768–774.

(191) J. C. G. Bunzli and S. V. Eliseeva, *J. Rare Earths*, 2010, **28**, 824–842.

(192) S. Wang, X. Z. Li, S. D. Xun, X. H. Wan, and Z. Y. Wang, *Macromolecules*, 2006, **39**, 7502–7507.

(193) S. D. Xun, J. D. Zhang, X. Z. Li, D. G. Ma, and Z. Y. Wang, *Synth. Met.*, 2008, **158**, 484–488.

(194) C. C. Ho, H. F. Chen, Y. C. Ho, C. T. Liao, H. C. Su, and K. T. Wong, *Phys. Chem. Chem. Phys.*, 2011, **13**, 17729–17736.

(195) R. D. Costa, F. J. Cespedes-Guirao, H. J. Bolink, F. Fernandez-Lazaro, A. Sastre-Santos, E. Orti, and J. Gierschner, *J. Phys. Chem. C*, 2009, **113**, 19292–19297.

(196) R. D. Costa, F. J. Cespedes-Guirao, E. Orti, H. J. Bolink, J. Gierschner, F. Fernandez-Lazaro, and A. Sastre-Santos, *Chem. Commun.*, 2009, 3886–3888.

(197) R. D. Costa, E. Orti, D. Tordera, A. Pertegas, H. J. Bolink, S. Graber, C. E. Housecroft, L. Sachno, M. Neuburger, and E. C. Constable, *Adv. Energy Mater.*, 2011, **1**, 282–290.

(198) H. J. Bolink, L. Cappelli, E. Coronado, A. Parham, and P. Stössel, *Chem. Mater.*, 2006, **18**, 2778–2780.

(199) L. He, L. Duan, J. Qiao, G. Dong, L. Wang, and Y. Qiu, *Chem. Mater.*, 2010, **22**, 3535–3542.

(200) E. Margapoti, V. Shukla, A. Valore, A. Sharma, C. Dragonetti, C. C. Kitts, D. Roberto, M. Murgia, R. Ugo, and M. Muccini, *J. Phys. Chem. C*, 2009, **113**, 12517–12522.

(201) C.-T. Liao, H.-F. Chen, H.-C. Su, and K.-T. Wong, *J. Mater. Chem.*, 2011, **21**, 17855–17862.

(202) H. B. Wu, H. F. Chen, C. T. Liao, H. C. Su, and K. T. Wong, *Org. Electron.*, 2012, **13**, 483–490.

(203) D. Pucci, A. Bellusci, A. Crispini, M. Ghedini, N. Godbert, E. I. Szerb, and A. M. Talarico, *J. Mater. Chem.*, 2009, **19**, 7643–7649.

(204) J. C. Lepretre, A. Deronzier, and O. Stephan, *Synth. Met.*, 2002, **131**, 175–183.

(205) W. L. Jia, Y. F. Hu, J. Gao, and S. N. Wang, *Dalton Trans.*, 2006, 1721–1728.

(206) N. Armaroli, G. Accorsi, F. Cardinali, and A. Listorti, *Top. Curr. Chem.*, 2007, **280**, ed. V. Balzani and S. Campagna, 69–115.

(207) A. Lavie-Cambot, M. Cantuel, Y. Leydet, G. Jonusauskas, D. M. Bassani, and N. D. McClenaghan, *Coord. Chem. Rev.*, 2008, **252**, 2572–2584.

(208) N. Armaroli, *Chem. Soc. Rev.*, 2001, **30**, 113–124.

(209) K. Saito, T. Arai, N. Takahashi, T. Tsukuda, and T. Tsubomura, *Dalton Trans.*, 2006, 4444–4448.

(210) *A resource-efficient Europe – Flagship initiative of the Europe 2020 Strategy.*

(211) *Recycling Rates of Metals – A Status Report*, tech. rep., United Nations Environment Programme (UNEP), 2011.

(212) R. D. Costa, E. Orti, H. J. Bolink, F. Monti, G. Accorsi, and N. Armaroli, *Angew. Chem., Int. Ed.*, 2012, **51**, 8178–8211.

(213) R. J. Holmes, S. R. Forrest, T. Sajoto, A. Tamayo, P. I. Djurovich, M. E. Thompson, J. Brooks, Y. J. Tung, B. W. D'Andrade, M. S. Weaver, R. C. Kwong, and J. J. Brown, *Appl. Phys. Lett.*, 2005, **87**, 243507.

(214) C. H. Yang, S. W. Li, Y. Chi, Y. M. Cheng, Y. S. Yeh, P. T. Chou, G. H. Lee, C. H. Wang, and C. F. Shu, *Inorg. Chem.*, 2005, **44**, 7770–7780.

(215) S. Meng, I. Jung, J. Feng, R. Scopelliti, D. Di Censo, M. Gratzel, M. K. Nazeeruddin, and E. Baranoff, *Eur. J. Inorg. Chem.*, 2012, 3209–3215.

(216) Q. Zhao, M. X. Yu, L. X. Shi, S. J. Liu, C. Y. Li, M. Shi, Z. G. Zhou, C. H. Huang, and F. Y. Li, *Organometallics*, 2010, **29**, 1085–1091.

(217) B. Beyer, C. Ulbricht, D. Escudero, C. Friebe, A. Winter, L. Gonzalez, and U. S. Schubert, *Organometallics*, 2009, **28**, 5478–5488.

(218) S. Stagni, S. Colella, A. Palazzi, G. Valenti, S. Zacchini, F. Paolucci, M. Marcaccio, R. Q. Albuquerque, and L. De Cola, *Inorg. Chem.*, 2008, **47**, 10509–10521.

(219) K. Dedeian, J. M. Shi, E. Forsythe, D. C. Morton, and P. Y. Zavalij, *Inorg. Chem.*, 2007, **46**, 1603–1611.

(220) K. Nozaki, K. Takamori, Y. Nakatsugawa, and T. Ohno, *Inorg. Chem.*, 2006, **45**, 6161–6178.

(221) D. Tordera, M. Delgado, E. Orti, H. J. Bolink, J. Frey, M. K. Nazeeruddin, and E. Baranoff, *Chem. Mater.*, 2012, **24**, 1896–1903.

(222) L. He, L. A. Duan, J. A. Qiao, D. Q. Zhang, L. D. Wang, and Y. Qiu, *Appl. Phys. A: Mater. Sci. Process.*, 2010, **100**, 1035–1040.

(223) M. C. Tseng, W. L. Su, Y. C. Yu, S. P. Wang, and W. L. Huang, *Inorg. Chim. Acta*, 2006, **359**, 4144–4148.

(224) D. Sykes and M. D. Ward, *Chem. Commun.*, 2011, 2279–2281.

(225) C. S. Chin, M. S. Eum, S. Y. Kim, C. Kim, and S. K. Kang, *Eur. J. Inorg. Chem.*, 2006, 4979–4982.

(226) A. F. Ma, H. J. Seo, S. H. Jin, U. C. Yoon, M. H. Hyun, S. K. Kang, and Y. I. Kim, *Bull. Korean Chem. Soc.*, 2009, **30**, 2754–2758.

(227) A. Habibagahi, Y. Mebarki, Y. Sultan, G. P. A. Yap, and R. J. Crutchley, *ACS Appl. Mater. Interfaces*, 2009, **1**, 1785–1792.

(228) C. Wu, H. F. Chen, K. T. Wong, and M. E. Thompson, *J. Am. Chem. Soc.*, 2010, **132**, 3133–3139.

(229) X. H. Wang, J. A. Li, M. E. Thompson, and J. I. Zink, *J. Phys. Chem. A*, 2007, **111**, 3256–3262.

(230) A. A. Abdel-Shafi, J. L. Bourdelande, and S. S. Ali, *Dalton Trans.*, 2007, 2510–2516.

(231) Z. R. Bell, G. R. Motson, J. C. Jeffery, J. A. McCleverty, and M. D. Ward, *Polyhedron*, 2001, **20**, 2045–2053.

(232) C. Barolo, M. K. Nazeeruddin, S. Fantacci, D. Di Censo, P. Comte, P. Liska, G. Viscardi, P. Quagliotto, F. De Angelis, S. Ito, and M. Gratzel, *Inorg. Chem.*, 2006, **45**, 4642–4653.

(233) B. Y. Kim, J. B. Ahn, H. W. Lee, S. K. Kang, J. H. Lee, J. S. Shin, S. K. Ahn, C. I. Hong, and S. S. Yoon, *Eur. J. Med. Chem.*, 2004, **39**, 433–447.

(234) S. Sprouse, K. A. King, P. J. Spellane, and R. J. Watts, *J. Am. Chem. Soc.*, 1984, **106**, 6647–6653.

(235) L. Malatesta and F. Bonati, *Isocyanide Complexes of Metals*, Wiley- Interscience, 1969.

(236) D. A. Edwards, S. M. Tetrick, and R. A. Walton, *J. Organomet. Chem.*, 1988, **349**, 383–391.

(237) M. G. Colombo and H. U. Guedel, *Inorg. Chem.*, 1993, **32**, 3081–3087.

(238) M. G. Colombo, A. Hauser, and H. U. Gudel, *Inorg. Chem.*, 1993, **32**, 3088–3092.

(239) J. L. Kiplinger, T. G. Richmond, and C. E. Osterberg, *Chem. Rev.*, 1994, **94**, 373–431.

(240) V. Sivasubramaniam, F. Brodkorb, S. Hanning, H. P. Loebl, V. van Elsbergen, H. Boerner, U. Scherf, and M. Kreyenschmidt, *J. Fluorine Chem.*, 2009, **130**, 640–649.

(241) V. N. Kozhevnikov, K. Dahms, and M. R. Bryce, *J. Org. Chem.*, 2011, **76**, 5143–5148.

(242) R. E. Robinson, T. C. Holovics, S. F. Deplazes, D. R. Powell, G. H. Lushington, W. H. Thompson, and M. V. Barybin, *Organometallics*, 2005, **24**, 2386–2397.

(243) M. V. Barybin, *Coord. Chem. Rev.*, 2010, **254**, 1240–1252.

(244) A. A. Rachford, R. Ziessel, T. Bura, P. Retailleau, and F. N. Castellano, *Inorg. Chem.*, 2010, **49**, 3730–3736.

(245) K. Yamana, M. Takei, and H. Nakano, *Tetrahedron Lett.*, 1997, **38**, 6051–6054.

(246) M. Hariharan, S. C. Karunakaran, and D. Ramaiah, *Org. Lett.*, 2007, **9**, 417–420.

(247) J. K. Choi, S. H. Kim, J. Yoon, K. H. Lee, R. A. Bartsch, and J. S. Kim, *J. Org. Chem.*, 2006, **71**, 8011–8015.

(248) L. Liu, D. Q. Zhang, G. X. Zhang, J. F. Xiang, and D. B. Zhu, *Org. Lett.*, 2008, **10**, 2271–2274.

(249) S. N. Ding, D. Shan, S. Cosnier, and A. Le Goff, *Chem. Eur. J.*, 2012, **18**, 11564–11568.

(250) F. Spaenig, J. H. Olivier, V. Prusakova, P. Retailleau, R. Ziessel, and F. N. Castellano, *Inorg. Chem.*, 2011, **50**, 10859–10871.

(251) C. Janiak, *J. Chem. Soc., Dalton Trans.*, 2000, —, 3885–3896.

(252) J. M. Robertson and J. G. White, *J. Chem. Soc.*, 1947, —, 358–368.

(253) A. Harriman, M. Hissler, and R. Ziessel, *Phys. Chem. Chem. Phys.*, 1999, **1**, 4203–4211.

(254) A. Moissette, Y. Batonneau, and C. Bremard, *J. Am. Chem. Soc.*, 2001, **123**, 12325–12334.

(255) N. Armaroli, *ChemPhysChem*, 2008, **9**, 371–373.

(256) M. G. Colombo, A. Hauser, and H. U. Guedel, *Inorg. Chem.*, 1993, **32**, 3088–3092.

(257) F. Neve, A. Crispini, S. Campagna, and S. Serroni, *Inorg. Chem.*, 1999, **38**, 2250–2258.

(258) F. Neve, A. Crispini, S. Serroni, F. Loiseau, and S. Campagna, *Inorg. Chem.*, 2001, **40**, 1093–1101.

(259) C. Dragonetti, L. Falciola, P. Mussini, S. Righetto, D. Roberto, R. Ugo, A. Valore, F. De Angelis, S. Fantacci, A. Sgamellotti, M. Ramon, and M. Muccini, *Inorg. Chem.*, 2007, **46**, 8533–8547.

(260) J. B. Waern, C. Desmarets, L.-M. Chamoreau, H. Amouri, A. Barbieri, C. Sabatini, B. Ventura, and F. Barigelletti, *Inorg. Chem.*, 2008, **47**, 3340–3348.

(261) M. Polson, S. Fracasso, V. Bertolasi, M. Ravaglia, and F. Scandola, *Inorg. Chem.*, 2004, **43**, 1950–1956.

(262) N. J. Turro, V. Ramamurthy, and J. C. Scaiano, *Principles of Molecular Photochemistry*, University Science Book, 2009.

(263) K. Goushi, J. Brooks, J. J. Brown, H. Sasabe, and C. Adachi, *J. Photopolym. Sci. Technol.*, 2006, **19**, 181–186.

(264) W. Finkenzeller, P. Stossel, and H. Yersin, *Chem. Phys. Lett.*, 2004, **397**, 289–295.

(265) L. Yang, F. Okuda, K. Kobayashi, K. Nozaki, Y. Tanabe, Y. Ishii, and M.-a. Haga, *Inorg. Chem.*, 2008, **47**, 7154–7165.

(266) J. V. Caspar and T. J. Meyer, *J. Phys. Chem.*, 1983, **87**, 952–957.

(267) R. Englman and J. Jortner, *Mol. Phys.*, 1970, **18**, 145–164.

(268) K. F. Freed and J. Jortner, *J. Chem. Phys.*, 1970, **52**, 6272–6291.

(269) C. Schaffner-Hamann, A. von Zelewsky, A. Barbieri, F. Barigelletti, G. Muller, J. P. Riehl, and A. Neels, *J. Am. Chem. Soc.*, 2004, **126**, 9339–9348.

(270) F. Barigelletti, A. Juris, V. Balzani, P. Belser, and A. Von Zelewsky, *J. Phys. Chem.*, 1987, **91**, 1095–1098.

(271) S. B. Meier, D. Hartmann, D. Tordera, H. J. Bolink, A. Winnacker, and W. Sarfert, *Phys. Chem. Chem. Phys.*, 2012, **14**, 10886–10890.

(272) G. A. Crosby and J. N. Demas, *J. Phys. Chem.*, 1971, **75**, 991–1024.

(273) K. Nakamaru, *Bull. Chem. Soc. Jpn.*, 1982, **55**, 2697–2705.

(274) S. R. Meech and D. Phillips, *J. Photochem.*, 1983, **23**, 193–217.

(275) J. C. deMello, H. F. Wittmann, and R. H. Friend, *Adv. Mater.*, 1997, **9**, 230–236.